

UNIVERSITY OF BELGRADE

FACULTY OF CIVIL ENGINEERING

Kristina O. Kostadinović Vranešević

**VALIDATED LARGE-EDDY
SIMULATION METHOD FOR
WIND EFFECTS IN URBAN AREAS**

Doctoral Dissertation

Belgrade, 2025

УНИВЕРЗИТЕТ У БЕОГРАДУ

ГРАЂЕВИНСКИ ФАКУЛТЕТ

Кристина О. Костадиновић Вранешевић

**МЕТОДА СИМУЛАЦИЈЕ
ВЕЛИКИХ ВРТЛОГА ЗА УТИЦАЈЕ ВЕТРА
У УРБАНИМ СРЕДИНАМА**

докторска дисертација

Београд, 2025

Supervisor/ Ментор:

Asstant Professor Anina Glumac
University of Belgrade, Faculty of Civil Engineering

Committee members/Чланови комисије:

Associate Professor Vitomir Racić
University of Belgrade, Faculty of Civil Engineering

Full Professor Jasna Plavšić
University of Belgrade, Faculty of Civil Engineering

Full Professor Aleksandar Ćoćić
University of Belgrade, Faculty of Mechanical Engineering

Associate Professor Hassan Hemida
University of Birmingham, School of Civil Engineering

Assistant Professor Đorđe Romanić
McGill University, Department of Atmospheric and Oceanic Sciences

Defence date/Датум одбране: _____

To my girls

Мојим девојчицама

Acknowledgments

This has been a long journey, with many who have participated in it. Some walked alongside me, while others offered support from the sidelines. Each contributed a piece to the puzzle that shaped the work before you.

The person to whom I owe my deepest gratitude is my supervisor, Asst. Prof. Anina Glumac. Dear Anina, first and foremost, thank you for introducing me to the field of wind engineering and for your guidance and unwavering support throughout this journey. Together, we have grown both personally and professionally. As Aristotle said: “Patience is bitter, but its fruit is sweet.”

I sincerely thank the esteemed committee members for their invaluable expertise and insights, which have significantly enriched this study. Reflecting on my academic journey, it has been a decade since I attended my first lecture on computational fluid dynamics, delivered by Assoc. Prof. Hassan Hemida in Malta during the WINERCOST training school. Those inspiring lectures sparked my passion for the field and set me on the path that led to this work. I also wish to express my deep appreciation to Prof. Aleksandar Čoćić for his meticulous and selfless assistance with fluid mechanics and to Prof. Jasna Plavšić for guiding me through the complexities of statistics, revealing both its beauty and potential pitfalls. I am grateful to Assoc. Prof. Vitomir Racić for his support and constructive feedback on this dissertation. My thanks also go to Asst. Prof. Đorđe Romanić for his feedback—though we have not yet collaborated, I look forward to future opportunities to do so.

I want to express my heartfelt appreciation to Dr. Theodore Potsis from Concordia University for our fruitful discussions on computational fluid dynamics, which have been insightful and inspiring.

I am also thankful to my English teacher and friend, Ivan Ilić, for enhancing my language skills and, perhaps more importantly, for consistently challenging me to think critically and step beyond my comfort zone.

Since 2014, I have worked at the University of Belgrade, Faculty of Civil Engineering. I am profoundly grateful to Prof. Rastislav Mandić and Prof. Biljana Deretić Stojanović for warmly welcoming me to the Department of Engineering Mechanics and Theory of Structures. I thank my colleagues for fostering such a supportive and pleasant working environment. Your daily encouragement, insightful discussions, and unwavering support have enriched this study and made this journey truly enjoyable. I especially want to thank my dear friends and colleagues, Miloš Jočković and Milica Koprivica, whose continuous support and encouragement have been invaluable.

To my dear friends—Milica, Dušica, Marko, Jelena, Aleksandra, Marija and Nina—thank you for being my safe harbour amidst life’s storms. Without you, my life would be far less colourful.

The best is saved for last. My deepest gratitude goes to my family, the source of my strength, whose love and guidance have shaped me into who I am today. Мојој баки Пери, хвала за све животне мудрости кроз које живи у мом срцу. Мама, хвала ти што си увек била снажна и самоуверена жена, и пружила ми узор у животу. Тата, хвала ти што си ме научио да талент није нешто чиме треба да се хвалимо, већ одговорност да се негује и надограђује како би помагали другима којима је дато мање. Мојој сестри Јасмини и њеној породици хвала на подршци и вери у мене.

To my life partner and soulmate, Filip: thank you for walking beside me every step of this journey. Though it has been turbulent, we made it through with our little ones, Višnja and Anja. You are my rainbow on cloudy days.

Abstract

Wind is a powerful natural force that presents both challenges and opportunities in urban environments. The layout of streets and the geometry of buildings shape complex flow patterns. This dissertation explores how these patterns impact urban wind energy harvesting and wind loading on high-rise buildings, offering insights for sustainable urban planning and design.

Two approaches can be employed to study wind flow: experimental and numerical. This research focuses on the large-eddy simulation (LES) method, a leading high-precision numerical technique, used to analyse wind flow around either an isolated high-rise building or a cluster of five. Existing wind tunnel tests are employed to validate the numerical simulations. The research examines two wind angles ($0^\circ/45^\circ$) and two roof types (flat/decked).

Findings on urban wind energy reveal that decked roofs offer a higher potential of wind energy than flat ones, as they stabilise flow and create high-speed, low-turbulence zones. In building clusters, interference effects may enhance wind energy potential. Regarding turbine type, vertical-axis wind turbines prove to be optimal.

For wind loading, a validation framework for LES-based peak pressure predictions is proposed. Uncertainty analysis from 11-hour experimental data confirms that shorter LES durations (e.g., 25 min) reliably capture peak pressures. Statistical analysis identifies the Gumbel method as more reliable than the peaks-over-threshold approach. Discrepancies between LES and experimental results near upwind roof corners highlight the need for case-specific validation.

LES is confirmed as an effective method for simulating urban wind flow. Future work should refine geometry, expand to complex settings, and improve peak pressure estimation. An essential step forward in LES modelling is the development of official guidelines for creating and validating simulations.

Keywords: atmospheric boundary layer, computational fluid dynamics (CFD), large eddy simulation (LES), high-rise building, turbulent flow, interference effects, urban wind energy, wind loading, peak pressure coefficient, uncertainty quantification.

Scientific field: Civil Engineering

Scientific subfield: Engineering Mechanics and Theory of Structures

UDC:

Сажетак

Ветар је моћна природна сила која представља изазове, али и могућности у урбаним срединама. Распоред улица и геометрија зграда обликују сложене обрасце тока ветра. Ова дисертација истражује како ти обрасци утичу на убирање енергије ветра у урбаним срединама и оптерећење ветром на високе зграде, пружајући смернице за одрживо урбанистичко планирање и дизајн.

За проучавање струјања ветра могу се користити два приступа: експериментални и нумерички. Ово истраживање се фокусира на методу симулације великих вртлога (LES), високо-прецизну нумеричку технику, примењену на проучавање тока ветра око високих зграда, било изолованих или у кластеру од пет. Постојећа испитивања у аеротунелу се користе за валидацију нумеричких симулација. Анализирају се два угла ветра ($0^\circ/45^\circ$) и два типа крова (раван/закошен).

Резултати указују да закошени кровови имају већи потенцијал енергије ветра од равних, јер стабилизују ток и стварају зоне велике брзине са ниском турбуленцијом. У кластерима, утицај суседних објеката може додатно повећати енергетски потенцијал. Такође, као најпогодније су се показале ветротурбине са вертикалном осом.

За оптерећење ветром, предложен је оквир за валидацију процењених вршних коефицијената притиска из LES-а. Анализа непоузданости из 11 сати експерименталних података показује да краће LES симулације (нпр. 25 мин) поуздано предвиђају ове вредности. Статистичка анализа указује да је Гумбелов метод поузданији од методе прекорачења прага. Одступања између LES-а и експеримената у близини наветрених ивица крова истичу потребу за валидацијом сваког посматраног случаја.

LES је потврђен као ефикасан метод за симулацију струјања ветра у урбаним срединама. Будућа истраживања треба да укључе детаљнију геометрију модела, сложенија окружења и унапреде процену вршних притисака. Есенцијални корак напред у примени LES-а је развој званичних смерница за креирање и валидацију симулација.

Кључне речи: атмосферски гранични слој, рачунарска динамика флуида (CFD), симулација великих вртлога (LES), висока зграда, турбулентни ток, утицај суседних објеката, урбана енергија ветра, оптерећење ветром, коефицијент вршног притиска, анализа непоузданости.

Научна област: Грађевинско инжењерство

Ужа научна област: Техничка механика и теорија конструкција

УДК:

Contents

| | |
|--|--------------|
| Nomenclature | xviii |
| 1 Introduction | 1 |
| 1.1 Urban wind energy | 1 |
| 1.2 Wind loading on facades and roofs | 3 |
| 1.3 General methodology | 4 |
| 1.4 Formulation of the problem | 6 |
| 1.5 List of references | 7 |
| 1.6 Organisation of dissertation | 8 |
| 2 State-of-the-art | 9 |
| 2.1 Wind flow dynamics in ABL | 9 |
| 2.1.1 ABL wind profile of upstream terrain | 11 |
| 2.1.2 Local wind flow affected by urban surroundings | 12 |
| 2.2 Urban wind energy | 15 |
| 2.3 Wind loading on high-rise buildings | 17 |
| 3 Theoretical framework | 19 |
| 3.1 Turbulent flow | 19 |
| 3.2 Modelling the flow | 21 |
| 3.2.1 Basic equations of fluid motion | 22 |
| 3.2.2 LES Modelling Approach | 22 |

| | | |
|----------|--|-----------|
| 3.2.3 | Numerical modelling algorithm | 26 |
| 4 | Methodology | 31 |
| 4.1 | High-rise building models and their configurations | 31 |
| 4.2 | Wind tunnel experiments | 33 |
| 4.3 | Numerical simulations | 34 |
| 4.3.1 | Flow modelling | 34 |
| 4.3.2 | Domain and grid | 35 |
| 4.3.3 | Boundary conditions | 39 |
| 5 | Validation | 43 |
| 5.1 | Monitoring convergence | 43 |
| 5.2 | Incident wind profile | 46 |
| 5.3 | Wind flow above roof | 47 |
| 5.4 | Surface pressure statistics | 50 |
| 6 | Wind flow dynamics | 55 |
| 6.1 | Impact of the roof shape | 55 |
| 6.1.1 | Flow field around the facade | 55 |
| 6.1.2 | Flow field above the roof | 57 |
| 6.2 | Insight into the interference effects | 62 |
| 6.2.1 | Flow field | 63 |
| 6.2.2 | Velocity statistic | 69 |
| 6.2.3 | Surface pressure | 71 |
| 6.3 | Conclusions | 74 |
| 7 | Urban wind energy | 77 |
| 7.1 | Common types of wind turbines for urban environment | 77 |
| 7.2 | Wind characteristics for energy exploitation | 78 |

| | | |
|----------|--|------------|
| 7.2.1 | Isolated high-rise building: Flat vs. decked roof shapes | 79 |
| 7.2.2 | Building clusters | 84 |
| 7.3 | Conclusions | 89 |
| 8 | Wind loading on high-rise buildings | 91 |
| 8.1 | Methodology for evaluating peak pressure coefficients | 91 |
| 8.1.1 | Traditional “epochal” approach | 92 |
| 8.1.2 | Peaks Over Threshold (POT) Method | 94 |
| 8.2 | Experimental results with uncertainty quantification | 96 |
| 8.2.1 | Empirical peak pressure coefficients | 97 |
| 8.2.2 | Estimated peak pressure coefficients and corresponding uncertainties . . | 99 |
| 8.3 | LES prediction capacities of peak pressure coefficients | 105 |
| 8.3.1 | Traditional vs. POT method | 106 |
| 8.3.2 | Effect of signal duration on LES peak pressure coefficients | 108 |
| 8.4 | Conclusions | 115 |
| 9 | Concluding remarks | 117 |
| 9.1 | Summary | 117 |
| 9.2 | Main contributions | 118 |
| 9.3 | Recommendations for future work | 119 |
| | Appendices | 137 |
| A | Experimental setup: Position of the pressure taps | 139 |
| B | Numerical setup | 141 |
| B.1 | Numerical schemes: Setup from OpenFOAM® | 141 |
| B.2 | SnappyHexMesh: Creating computational grid | 142 |
| B.3 | Incoming wind profile: Modelling precursor domain | 152 |
| C | Matlab code for the estimation of the peak pressure | 155 |

| | |
|----------------------|------------|
| Biography | 159 |
| Contributions | 161 |

List of Tables

| | | |
|-----|--|----|
| 4.1 | Grid refinement zones around the principal building in C1 configuration for wind energy assessment. | 37 |
| 4.2 | Refinement zones around the principal building. | 39 |
| 4.3 | Refinement zones around the principal building. | 39 |
| 5.1 | Performance metrics for the pressure coefficient for configuration C1, simulations for wind energy assessment. | 51 |
| 5.2 | Performance metrics of the mean and RMS of pressure coefficients for the 75-minute EFS event for configurations C1 and C2, simulations for wind loading study. | 54 |
| 7.1 | The effective mean wind speed as a function of the employed velocity vector components | 79 |
| 8.1 | Scaling in the experimental and numerical part of the study. | 92 |

List of Figures

| | | |
|-----|--|----|
| 1.1 | Wind effects in the urban environment: wind loading on facades and roofs [1], bridges [2], and silos [3]; wind energy harvesting [4]; urban comfort [5] and pollution dispersion [6]. | 2 |
| 1.2 | Integrated wind turbines in between the Bahrain World Trade Center Towers: (a) towers [17] and (b) configurations: converging and diverging (adapted from [9]). | 3 |
| 2.1 | ABL wind flow in urban areas. | 10 |
| 2.2 | ABL wind tunnels at (a) the Eindhoven University of Technology, Netherlands [52] and (b) the Imperial College, London, UK [53]. | 11 |
| 2.3 | Wind flow around the isolated cubic building in the ABL, adapted from [69]. . . | 13 |
| 2.4 | Flow patterns in street canyons over building arrays of increasing density, adapted from [81]. | 14 |
| 3.1 | Idealised turbulent kinetic energy spectrum $E(\kappa)$ (adapted from [139, 140]). . . | 20 |
| 3.2 | Flow chart of the numerical modelling, adapted from [142]). | 21 |
| 3.3 | LES method: basic concept; a schematic representation of the filtering operation on the computational grid (Δ is assumed to be equal to the cell size) as well as in the frequency domain (adapted from [145]). | 24 |
| 3.4 | PISO algorithm: graphical representation with a flowchart on the left and segments of code from <i>pisoFoam</i> solver (OpenFOAM® source code). | 29 |
| 4.1 | The geometry of the high-rise building models with marked points of pressure (grey and red spots) and velocity (red spots) measurements: (a) flat roof and (b) decked roof; wooden models of the buildings (adapted from [102]): (c) flat roof models in group C2 configuration and (d) an isolated decked roof model. | 32 |
| 4.2 | Horizontal plane layout of building configurations: (a) C1, (b) C2 and (c) C3. . . | 32 |

| | | |
|-----|--|----|
| 4.3 | Pressure probes: (a) schematic representation of pressure sensor Honeywell 170 PC and (b) pressure cells with pressure tubes; (c) an isolated flat roof high-rise building model (configuration C1) mounted in the ABL wind tunnel at the Ruhr-University Bochum, Germany, adopted from [102]. | 34 |
| 4.4 | The geometry of the domain and boundary conditions, adapted from [41]. | 35 |
| 4.5 | Wind tunnel test section: experimental setup of the group configuration in the ABL wind tunnel of the Ruhr-University Bochum, Germany, on the left and computational domain for the group configuration related to LES on the right, adapted from [42, 102]. | 36 |
| 4.6 | The adopted grid around the target building: (a) xz plane through $(0, 0, 0)$; (b) xy plane through $(0, 0.5H, 0)$; (c) three-dimensional view of the building zone, adapted from [40]. | 37 |
| 4.7 | Grid adopted around the principal building in case C2 for 0° wind angle: (a) a grid through the vertical central plane; (b) perspective view on the grid on building surfaces and the ground plane near the building; (c) close view of the grid around the building; adapted from [41]. | 38 |
| 4.8 | (a) Incident wind profile at $(0, 0)$: mean velocity in the streamwise direction, turbulence intensity profiles in the streamwise and vertical directions and velocity spectrum at $(0, 0, H)$; (b) Geometry of the domain with grid description and marked boundary conditions; adopted from [42]. | 40 |
| 4.9 | Wind profiles at the middle of the turning table for wind energy assessment: (a) streamwise mean velocity component, (b) turbulence intensity profiles in the streamwise (I_u) and vertical (I_w) directions and (c) velocity spectrum at $(0, 0, H)$, adapted from [40]. | 41 |
| 5.1 | The streamwise velocity component at $(0, 0, H)$: (a) time history and (b) convergence of related statistics (adopted from [40]). | 44 |
| 5.2 | Convergence of the velocity statistics above the roof in the C2 case at 0° : (a) time history of the normalised streamwise velocity component (U_u^*/U_{ref}) above point P20 at height $z = 1.05H$, (b) sketch of the roof with marked location of point P20 and (c) percentage residuals of the velocity first (U_u) and second (U_u') order statistics. | 45 |
| 5.3 | Convergence of the surface pressure statistics on the roof in the C2 case at 0° : (a) time history of the surface pressure coefficient (C_p) at the pressure tap P20, (b) sketch of the roof with marked location of point P20 and (c) percentage residuals of the pressure first (\bar{C}_p) and second (C_p'') order statistics. | 45 |
| 5.4 | Stationarity test of the pressure signal, including the mean (\bar{C}_p), RMS (C_p''), skewness (C_p^s), kurtosis (C_p^k) and minimum C_p (\check{C}_p) on the roof for the C1 configuration at location $(-0.45B, 0, H)$ under the 0° wind angle: (a) whole signal from the experiments, (b) detailed view of the first $600t^*$ from the experiments and (c) corresponding LES results. | 47 |

| | | |
|-----|---|----|
| 5.5 | Comparison of experimental and numerical results: (a) outline of the roof with marked points of pressure (grey and red spots) and velocity (red spots) measurements; the central line is marked with the dashed red line, while the blue one represents the wind direction; (b) the velocity and (c) turbulence intensity profiles in streamwise and vertical directions above points on the central line. | 49 |
| 5.6 | Validation of the flow above the roof in the C2 case, at 0° and 45° , by comparing experimental (<i>EXP</i>) and numerical (<i>NUM</i>) results: the mean velocity and turbulence intensity profiles in streamwise and vertical directions above two points (a) P20 and (b) P36. | 50 |
| 5.7 | Scatter plots of the mean and RMS values of pressure coefficients for configuration C1, simulations for wind energy assessment: at 0° wind angle for flat (a) and decked (b) roof, and 45° for flat (c) and decked (d) roof. | 51 |
| 5.8 | Scatter plots of the mean and RMS values of the pressure coefficient for the C2 configuration, simulations for wind energy assessment: comparison of the experimental (<i>EXP</i>) and numerical (<i>NUM</i>) results at (a) 0° and (b) 45° | 53 |
| 6.1 | Streamlines of the velocity mean-field in the C1 configuration for the flat roof case in the vertical xz centre plane of the flow and horizontal xy planes in the vicinity of the bottom boundary ($z \sim 0$) and through $(0, 0, 2.25B)$ at: (a) 0° and (b) 45° , adapted from [40]. | 56 |
| 6.2 | Mean and RMS values of the surface pressure coefficient in the C1 configuration for the flat-roof case along the ring around the facade ($z = 2.25B$) at: (a) 0° and (b) 45° , adapted from [40]. | 57 |
| 6.3 | Flow structures above the flat and decked roofs in the C1 configuration at 0° : (a) sketches of the roofs; (b) velocity mean-field with streamlines in the vertical central plane of the roofs (marked with a red dashed line in (a)) complemented with profiles of mean velocity vector components in x and y direction at seven locations on the roof; (c) the surface plot of mean pressure coefficient (\bar{C}_p) on the roofs, overlapped with streamlines in the vicinity of the roofs, top view; (d) plots along the middle line of the mean and RMS values of the pressure coefficient compared with experimental values, adapted from [40]. | 59 |
| 6.4 | Flow structures above the flat and decked roofs in the C1 configuration at 45° : (a) sketches of the roofs; (b) velocity mean-field with streamlines in the vertical central plane of the roofs (marked with a red dashed line in (a)) complemented with profiles of mean velocity vector components in x and y direction at seven locations on the roof; (c) the surface plot of mean pressure coefficient (\bar{C}_p) on the roofs, overlapped with streamlines in the vicinity of the roofs, top view; (d) plots along the middle line of the mean and RMS values of the pressure coefficient compared with experimental values, adapted from [40]. | 61 |
| 6.5 | Mean velocity streamlines in vertical planes at 45° yaw angle related to the wind direction (black streamlines) and in the vicinity of the roof (white streamlines), adapted from [40]. | 62 |

| | | |
|------|---|----|
| 6.6 | Velocity mean-field overlapped with streamlines in the vertical xz central plane of the flow through $(0, 0, 0)$ and horizontal xy plane through $(0, 0, 0.8H)$ for the group configuration at 0° wind angle: (a) in the “cross” arrangement (case C2) and (b) in the “x” arrangement (case C3), adapted from [41]. | 64 |
| 6.7 | Velocity mean-field overlapped with streamlines in the vertical xz central plane of the flow through $(0, 0, 0)$ and horizontal xy plane through $(0, 0, 0.8H)$ for the group configuration at 45° wind angle: (a) in the “cross” arrangement (case C2) and (b) in the “x” arrangement (case C3), adapted from [41]. | 65 |
| 6.8 | Three-Dimensional isocontours of λ_2 invariant at $\lambda_2 = 300000$, for the “cross” shape building arrangement at 0° and 45° wind angles, adapted from [41]. | 66 |
| 6.9 | Streamlines of the velocity mean-field in the vertical xz centre plane of the flow through $(0, 0, 0)$, with an enlarged view of the area above the roof, and horizontal xy plane through $(0, 0, 0.8H)$ for three study cases: (a) C1, (b) C2 and (c) C3, adapted from [41]. | 67 |
| 6.10 | Streamlines of the velocity mean-field in the vertical xz centre plane of the flow through $(0, 0, 0)$, and horizontal xy plane through $(0, 0, 0.8H)$ complemented with an enlarged view of the zone in the vicinity of the roof in the horizontal and vertical plane, for three study cases: (a) C1, (b) C2 and (c) C3, adapted from [41]. | 68 |
| 6.11 | Velocity mean-field in the vertical xz centre plane of the flow through $(0, 0, 0)$, with an enlarged view of the area above the roof, and horizontal xy plane through $(0, 0, 0.8H)$ for three study cases: (a) C1, (b) C2 and (c) C3, adapted from [41]. . | 70 |
| 6.12 | Velocity mean-field in the vertical xz centre plane of the flow through $(0, 0, 0)$, and horizontal xy plane through $(0, 0, 0.8H)$, with an additional enlarged view of the area above the roof in the vertical central plane of the flow and four horizontal planes at height $0.125B$, $0.25B$, $0.375B$ and $0.5B$ from the rooftop (z_0), for three study cases: (a) C1, (b) C2 and (c) C3, adapted from [41]. | 71 |
| 6.13 | Turbulence intensity field in x direction overlapped with the instantaneous velocity streamlines in the vertical xz centre plane of the flow through $(0, 0, 0)$ and horizontal xy plane through $(0, 0, 0.8H)$ for three study cases at 0° and 45° : (a) C1, (b) C2 and (c) C3, adapted from [41]. | 72 |
| 6.14 | Line plots of average (\bar{C}_p) and RMS (C_p'') of the pressure coefficient at the building surface along the path over the central line of the building at 0° (a) and 45° (b), adapted from [41]. | 74 |
| 6.15 | Line plots of average (\bar{C}_p) and RMS (C_p'') of the pressure coefficients at the building surface along the rings at $z = 0.5H$ and $z = 0.75H$ for 0° (a) and 45° (b) wind angles, adapted from [41]. | 75 |
| 7.1 | Wind power density normalised with $1/2\rho U_{ref}^3$ (P^*) in configuration C1 for the flat roof case in (a) the vertical yz plane through $(-B/2, 0, 0)$ and horizontal xy plane through $(0, 0, 2.25B)$ at 0° and (b) the vertical yz plane through $(0, 0, 0)$ and horizontal xy plane through $(0, 0, 2.25B)$ at 45° . White contour lines represent the turbulence intensity in wind direction (I_u), adapted from [40]. . . . | 80 |

| | | |
|-----|--|-----|
| 7.2 | Wind power density, normalised with $1/2\rho U_{ref}^3$, overlapped with white contour lines representing the turbulence intensity in wind direction (I_u), with a line indicating $I_u = 18\%$ (the yellow dashed-dotted line), and skew angle in the central plane of the flow in configuration C1 at 0° for (a) the flat and (b) decked roof shape and at 45° for (c) the flat and (d) decked roof shape, adapted from [40]. . | 81 |
| 7.3 | Wind power density, normalised with $1/2\rho U_{ref}^3$ and overlapped with white contour lines representing the turbulence intensity in wind direction (I_u), plots above the flat roof at four heights ($z = 3.0625B, 3.125B, 3.1875B, 3.25B$) for the wind approaching at 45° , adapted from [40]. | 83 |
| 7.4 | Proposed zoning above the roof in the central plane of the flow regarding wind power density and turbulence intensity for configuration C1, adapted from [40]. . | 84 |
| 7.5 | Roof zone in the vertical (xz) centre plane of the flow through $(0,0,0)$: (a) normalised Wind power density, complemented with the shape of the separation zone (white, dashed line) and a line indicating $I_u = 18\%$ (the yellow dashed-dotted line), (b) turbulence intensities in x direction overlapped with the instantaneous velocity streamlines and (c) skew angle, for cases C1, C2 and C3, adapted from [41]. | 85 |
| 7.6 | Normalised WPD distribution regarding different effective velocities (P_{eff}^*) across the predefined lines (a) L1 and (b) L2, for 0° , 45° and 90° wind angles and three study cases (C1, C2 and C3), adapted from [41]. | 88 |
| 8.1 | Experimental results of the minimum peak pressure coefficient over the roof for various wind directions: (a) single (C1) and (b) group (C2) configurations, adapted from [42]. | 98 |
| 8.2 | Procedure for estimation of peak pressure coefficient from the experimental data using the Gumbel method in the traditional approach, demonstrated at point P4, location $(-0.45B, 0, H)$ in configuration C1, at 0° wind angle: (a) Gumbel fit using MOM, BLUE and MLE for the combination of $n_{ep} = 10$ and $\Delta t = 5$ min in EFS with conversion to $\Delta T = 15$ min in EFS and (b) Gumbel fit using MLE for all time blocks across the pressure signal with 95% confidence interval (95% CI) for the estimated peak pressure coefficient with a probability of exceedance of 20%; (c) performance metrics of MOM, BLUE and NLE method for all 64 points on the roof, adopted from [42]. | 101 |
| 8.3 | Graphical representation of performance metrics of experimental data for various combinations of n_{ep} and Δt ; each n_{ep} is marked with a different bullet symbol in the scatter plot, and data points which correspond to combinations $n_{ep}\Delta t$ equal to the specified T_{full} are connected with different line types and colours, adopted from [42]. | 102 |
| 8.4 | Graphical representation of performance metrics of experimental data for various combinations of n_{ep} , Δt and n_{bl} , resulting in $T_{full} = \{25, 37.5, 75\}$ min in EFS; each n_{ep} is marked with a different bullet symbol in the scatter plot, while points corresponding to the same T_{full} are connected with different line types and colours, adopted from [42]. | 103 |

| | | |
|------|--|-----|
| 8.5 | Graphical representation of performance metrics of experimental data for POT method in representing the 75-minute EFS event for C1 configuration at (a) 0° and (b) 45° wind angles, adopted from [42]. | 105 |
| 8.6 | Scatter plots with error bars of negative peak pressure coefficient with the table view of performance metrics for four study cases: comparison of the empirical results and corresponding estimated experimental and numerical results using (a) traditional “epochal” approach and (b) POT method, adopted from [42]. | 107 |
| 8.7 | Pressure statistics along two predefined lines on the roof for various durations of pressure signal (T_{full}) at 0° for configuration (a) C1 and (b) C2, adopted from [42]. | 109 |
| 8.8 | Pressure statistics on the roof with mean flow structures at 0° : Surface plots of mean, RMS and peak pressure coefficients overlapped with streamlines of mean velocity in the vicinity of the roof and marked pressure probes (black dots) for configuration (a) C1 and (b) C2, adopted from [42]. | 110 |
| 8.9 | Pressure statistics along two predefined lines on the roof for various durations of pressure signal (T_{full}) at 45° for configuration (a) C1 and (b) C2, adopted from [42]. | 112 |
| 8.10 | Pressure statistics on the roof with mean flow structures at 45° : Surface plots of the mean, RMS and peak pressure coefficients overlapped with streamlines of mean velocity in the vicinity of the roof and marked pressure probes (black dots) for configuration (a) C1 and (b) C2, adopted from [42]. | 113 |
| 8.11 | Pressure statistics over the ring on the facade for various durations of pressure signal (T_{full}) for configurations C1 and C2 at (a) 0° and (b) 45° wind angles; positive peak pressure coefficients are reported on the windward sides of the building (indicated with a light red background on the plot) and negative on the leeward sides, adopted from [42]. | 114 |
| A.1 | Schematic presentation of the distribution of the pressure taps on the building model in the wind tunnel experiments. | 140 |
| B.1 | OpenFOAM® fvSchemes file for wind energy assesment. | 142 |
| B.2 | OpenFOAM® fvSchemes file for wind loading. | 143 |
| B.3 | Grid refinement of the precursor domain: (a) grid 1 (G1) used in wind energy study (NUM S1) and (b) grid 2 (G2) used in wind loading study (NUM S2 and NUM S3). | 153 |
| B.4 | (a) Incident wind profile at (0,0): mean velocity in the streamwise direction, turbulence intensity profiles in the streamwise and vertical directions for the three analysed setups; velocity spectra at (0, 0, H), comparison of (b) NUM S1 and NUM S3, and (c) NUM S2 and NUM S3, with the experimental results. | 154 |

Nomenclature

| | |
|------------------|---|
| A | Area of face normal to direction of transport [m^2] |
| H | Height of building model [m] |
| B | Width of building model [m] |
| f | Frequency [1/s] |
| T | Time in full scale [s] |
| t | Time in model scale [s] |
| \boldsymbol{n} | General spatial coordinate [m] |
| xyz | Axes in Cartesian coordinate system [m] |
| \boldsymbol{I} | Unit tensor |
| n | Number of items |
| \boldsymbol{u} | Velocity vector [m s^{-1}] |
| u | Components of the velocity vector [m s^{-1}] |
| U | Components of the mean velocity vector, without a direction indicator in subscript it refers to the magnitude of the mean velocity vector [m s^{-1}] |
| P | Wind power density $P = \frac{1}{2}\rho U^3$ [W/m^2] |
| I | Turbulence intensity [-] |
| S | Spectral density function for wind velocity |
| L | Integral length scale [m] |
| E | Energy density [m^2/s^2] |
| A^+ | Van Driest dumping function |
| D | Van Dries dumping function |
| p | Pressure [Pa] |
| \boldsymbol{g} | Gravitational acceleration vector [m/s^2] |

| | |
|--------|-------------------------------|
| F | Cumulative density function |
| a, b | Estimators in the BLUE method |
| d | Threshold value |

Greek Symbols

| | |
|---------------|--|
| α | Approaching wind angle [deg] |
| β | Exponent in power law wind profile |
| Δ | Characteristic time duration |
| δ | Characteristic dimension of the grid cell [m] |
| ε | Turbulence dissipation rate [m ² /s ³] |
| κ | Wave number - proportional to inverse eddy length scale [1/m] |
| λ | Poisson process intensity function |
| μ | Dynamic viscosity [Pa · s]; in Wind loading study in Chapter 8 it also refers to the mode of the distribution or location parameter |
| ν | Kinematic viscosity $\nu = \frac{\mu}{\rho}$ [m ² /s] |
| ∇ | Nabla operator (gradient/divergence) |
| ϕ | Generic flow variable |
| ρ | Density of the fluid [kg/m ³] |
| σ | Standard deviation [m s ⁻¹]; in Wind loading study in Chapter 8 it also refers to the dispersion (spread) of the distribution or scale parameter |
| τ | Sub-grid scale stress tensor [m ² /s ²] |

Subscripts

| | |
|------------|---|
| i, j | Spatial or summation index |
| u, v, w | Direction indicators: streamwise (u), lateral (v) and vertical (w) directions |
| 0 | Distance from the rooftop |
| ∞ | Free-stream |
| ref | Value at referent location $(0, 0, H)$ in the domain without the building models |
| <i>EXP</i> | Refers to experimental results |
| <i>NUM</i> | Refers to numerical results |
| <i>ep</i> | Traditional “epochal” approach |
| <i>MC</i> | Monte-Carlo simulations |
| <i>POT</i> | Peaks over threshold method |

| | |
|------|--------------------------|
| full | Variable in a full scale |
| est | Estimated value |
| emp | Empirical value |

Superscripts

| | |
|---------------|--|
| . | Second statistical moment - root mean square - RMS |
| ' | Fluctuating component |
| ^d | Deviator part of a given tensor |
| ^k | Fourth statistical moment - kurtosis |
| ^s | Third statistical moment - skewness |
| ^T | Transpose |
| * | Dimensionless form |
| ^{UP} | Upper uncertainty bound |
| ^{DN} | Lower uncertainty bound |

Oversimbols

| | |
|-----------------------|----------------|
| $\bar{}$ | Mean value |
| $\tilde{}$ | Filtered value |
| \wedge | Positive peak |
| \vee | Negative peak |

Dimensionless Groups

| | |
|-------|---|
| C_p | Pressure coefficient $C_p = (p - p_\infty)/(\rho U_{ref}^2/2)$ |
| Re | Reynolds number $Re = (U_{ref}H)/\nu$ |
| CFL | Courant–Friedrichs–Lewy or Courant number |
| t^* | Dimensionless time $t^* = (tU_{ref})/H$ |
| y^+ | Absolute dimensionless wall distance $y^+ = yu_\tau/\nu$ (u_τ is friction velocity) |
| P^* | Normalised wind power dencity $P^* = P/(\frac{1}{2}\rho U_{ref}^3)$ |

List of Abbreviations

| | |
|------|----------------------------------|
| ABL | Atmospheric Boundary Layer |
| BLUE | Best Linear Unbiased Estimator |
| CDF | Cumulative Distribution Function |
| CFD | Computational Fluid Dynamics |

| | |
|-------|------------------------------------|
| CI | Confidence Interval |
| EFS | Equivalent Full Scale |
| HAWT | Horizontal Axis Wind Turbine |
| LES | Large Eddy Simulation |
| MLE | Maximum Likelihood |
| MNB | Mean Normalised Bias |
| MOM | Method Of Moments |
| NE | Normalised Error |
| NRMSE | Normalised Root Mean Squared Error |
| N-S | Navier–Stokes |
| WPD | Wind Power Density |
| RANS | Reynolds-Averaged Navier-Stocks |
| RMS | Root of the mean squares |
| SE | Standard Error |
| SGS | Sub-Grid Scale |
| TKE | Turbulent Kinetic Energy |
| VAWT | Vertical Axis Wind Turbine |

With my eyes closed by the seaside, as a bunch of small eddies rolls over my cheeks and tangles my hair in their joyful play, I wonder how many worlds exist around us, hidden from view. Is there any order in this wild dance of the wind? Perhaps, if we learn its moves, we can dance together. Attracted by the mystery of the unknown and filled with awakened curiosity, my journey into this world began.

1 Introduction

Wind surrounds us, from a light breeze that cools us on a hot day to a storm that overturns umbrellas and bends trees. In an urban environment, the wind brings both challenges and opportunities. The diverse topology of buildings, narrow streets that form street canyons, and numerous passages generate complex patterns of wind flow that significantly influence the urban microclimate.

Understanding these wind flow patterns at the pedestrian level is essential to enhance urban wind comfort. Thoughtful urban planning and wind-responsive architectural design can mitigate areas of excessive wind acceleration, improving the quality of life in cities. Beyond comfort, wind flow governs pollution dispersion, impacting air quality and public health. In addition, these patterns reveal the potential for wind energy harvesting in urban areas, a critical resource in the transition to sustainable cities. Wind loading is another important aspect that lies at the interface between wind flow and building envelopes. The pressure distribution across building surfaces, governed by dynamic, fluctuating wind flow, forms the basis for structural design.

Figure 1.1 captures these diverse roles of the wind in urban areas. By tackling the complexity of urban wind flow, answers to key questions about pedestrian comfort, pollution dispersion, energy generation, and structural safety can be unlocked. This dissertation focuses on two aspects of wind effects in the urban environment: the influence of wind flow patterns on wind energy harvesting potential and wind loading on the facades and roofs of high-rise buildings.

1.1 Urban wind energy

Urbanisation has increased rapidly, with more than 55% of the world's population living in urbanised areas in 2018 and projected to reach 68% by 2050 [7]. Consequently, engineers face the challenge of creating a sustainable environment that maximises the benefits of densely populated areas while minimising environmental degradation. A key question is how to meet the growing energy demands in these areas, and renewable energy sources offer a potential solution. In fact, renewable energy has become the world's leading source of new power generation capacity, with solar and wind energy ahead [8], providing a way out of the current energy crisis.

A common concept of large wind farms is unsuitable for harvesting urban wind energy due to limited land availability [9]. As an alternative, the concept of distributed energy generation has been developed. The most significant advantage of this approach is its location, as energy is produced at the point of consumption [9]. However, despite the appeal of this idea, urban wind energy faces numerous challenges in practice [10]. In 2020, concerning reports emerged from the



Figure 1.1. Wind effects in the urban environment: wind loading on facades and roofs [1], bridges [2], and silos [3]; wind energy harvesting [4]; urban comfort [5] and pollution dispersion [6].

small wind turbine market, which had almost collapsed [11]. The failure of this technology can be traced back to fundamental issues.

Traditionally, wind turbines are designed based on uniform flow assumptions, with prevailing wind direction and low turbulence, which are characteristic of open rural terrain [12]. In contrast, urban wind flow is highly complex, site-specific, and characterised by frequent changes in wind direction and high turbulence [10]. These differences have led to a misunderstanding of wind turbine performance in the urban environment, resulting in their underperformance [13].

The Bahrain World Trade Centre in Manama, Bahrain, often celebrated as a pioneering example of building-integrated wind turbines, demonstrated both the potential and the pitfalls of urban wind energy harvesting [9]. Although these turbines supply 8–10% of the building’s electricity consumption, the design lacks its full potential [9]. Specifically, based on the findings of previous studies in [14, 15], subsequent wind tunnel experiments and numerical simulations conducted by Blocken [16] revealed that the current configuration of the converging tower (see Figure 1.2 (b)) is not optimal from the point of view of wind energy. If the towers had been arranged in

a divergent configuration (Figure 1.2 (b)), the annual production of wind energy could have increased by 14%. In addition, placing the turbines further downstream in the converging configuration would have boosted efficiency by up to 31%, but it might face structural and financial constraints.

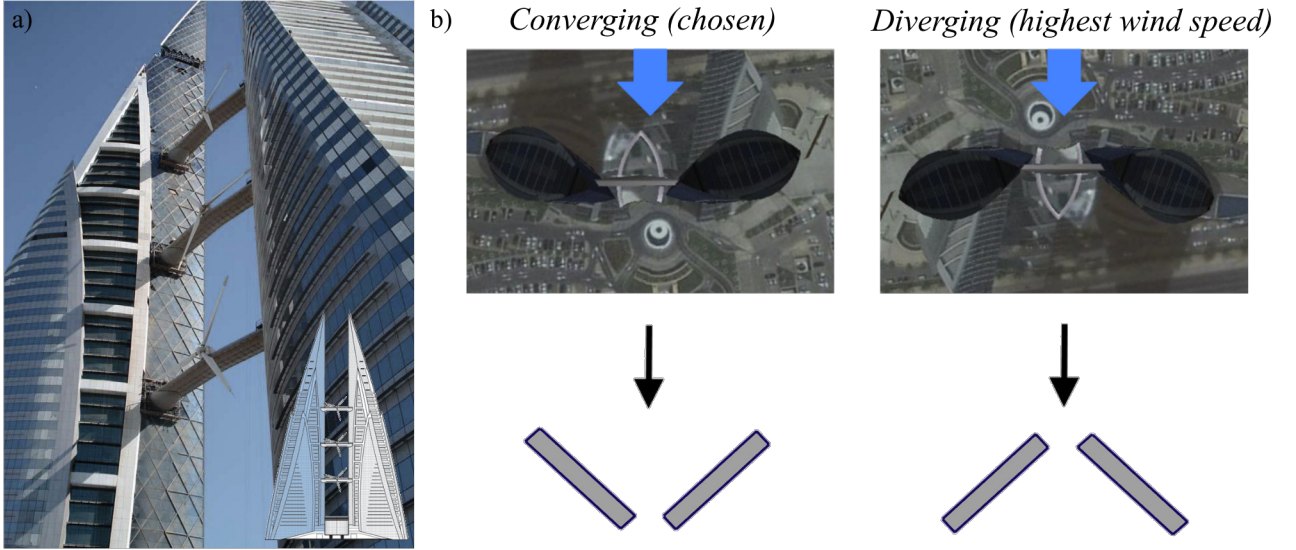


Figure 1.2. Integrated wind turbines in between the Bahrain World Trade Center Towers: (a) towers [17] and (b) configurations: converging and diverging (adapted from [9]).

Unfortunately, the Bahrain World Trade Centre is not an isolated case. Other projects, such as the Strata Tower in London, experienced failure in energy production due to the oversight of designers, who did not correctly predict the vibration and disruptive noise of the wind turbines during operation [18]. These shortcomings underscore the critical need to improve the understanding of wind flow in urban areas and develop wind turbines specifically suited to these conditions, both of which are essential to improve performance and advance the practical implementation of urban wind energy systems [9].

1.2 Wind loading on facades and roofs

The frequency and cost of weather and climate-related disasters are increasing, driven by a combination of increased exposure, vulnerability, and the intensifying effects of climate change [19]. According to the Fifth U.S. National Climate Assessment [20], climate change is amplifying the frequency of extreme events, including high-intensity winds, which contribute to billion-dollar disasters. In this context, wind loading has emerged as a critical factor in assessing and mitigating the risks posed by these increasingly severe events. Thus, understanding and addressing wind effects on structures is essential to reduce the costs of both human lives and economic losses caused by such disasters.

High-rise buildings are particularly sensitive to wind due to their height, slenderness, and exposure to strong winds at higher altitudes. Their facades are among the most economically significant components, as they often represent up to 25% of the total cost of the building [21]. However, facade damage can arise from multiple factors, from direct wind effects to windborne debris, usually originating from rooftops, such as displaced roof appurtenances or gravel. In his study on Hurricane Alicia Kareem [22] identified rooftop debris as the leading cause of

glass damage to windows in a cluster of high-rise buildings in a localised area of Houston's central business district. At the same time, the primary building structure was not corrupted and performed satisfactorily. This emphasises the need to study not only structural but also non-structural elements such as facade and roof claddings on wind loading to mitigate risks and reduce repair costs.

The instantaneous surface peak pressures determine the wind loading on the facade and roof cladding [23]. Hence, their accurate estimation is essential. However, it is not an easy task, as it is influenced by multiple factors, among which are the approaching wind flow, the relative location of the interfering buildings, and the geometry of the building [24, 25]. The wind flow pattern around the building is reflected in the surface pressure distribution, and negative pressure zones such as the separation and recirculation regions, as well as the turbulence level of the incident wind, greatly affect surface peak pressures [22].

1.3 General methodology

Two approaches are commonly employed to estimate wind effects in the urban environment: experimental and numerical. They are inevitable for understanding the complex urban wind flow and addressing engineering challenges in urban areas.

The traditional experimental approach is related to field measurements in full-scale or reduced-scale wind tunnel testing. In civil engineering, wind tunnel testing is prevalent as it is usually a tool in the design phase. Its origins trace back to 1893 when the first wind tunnel driven by a chimney draught was constructed [26]. Today, more than a hundred years later, wind tunnel testing remains a state of the art. However, it faces limitations, such as constraints in spatial scaling, test section dimensions, and challenges in capturing time-correlated data, particularly in complex urban settings.

Numerical methods, developed over the past 60 years, represent a new branch in wind engineering: computational wind engineering. Computational wind engineering leverages computational fluid dynamics (CFD) for wind engineering applications [27]. Two numerical methods are prevalent in this field: the low-fidelity Reynolds-averaged Navier-Stokes (RANS) approach and the high-fidelity large-eddy simulation (LES) method [28]. Both are based on discretised Navier-Stokes (N-S) equations.

The RANS approach resolves only the time-averaged flow, entirely modelling turbulent kinetic energy (TKE). Although cost-effective, it struggles with accurately predicting separation and recirculation zones [29, 30, 31], which are common in urban environments. Despite these limitations, RANS remains widely used in environmental applications such as urban comfort and pollution dispersion, owing to its simplicity and established best-practice guidelines [32, 33].

In contrast, the LES method resolves large-scale turbulent structures (eddies) while modelling only the effects of smaller scales. As these large-scale eddies contain over 80% of the total TKE, LES offers a more accurate and time-dependent representation of wind flow compared to RANS [34]. It provides time-resolved velocity and pressure fields, making it suitable for detailed analyses in urban wind energy harvesting and structural wind engineering [27, 35]. However, its computational demands and lack of official guidelines currently limit its widespread use.

Urban wind energy applications

In urban wind energy applications, experimental and numerical methods play an important role in their advancement and are mutually complementary. Wind tunnel measurements, in particular, are regarded as reliable but often expensive and challenging to perform. Exploring the potential for wind energy harvesting in urban areas requires high spatial resolution velocity measurements to represent wind flow accurately, and an extensive set of experimental data has to be collected [36]. Furthermore, collected velocity data may often lack time correlation, as measuring equipment cannot capture data simultaneously at multiple locations in the wind tunnel without obstructing the flow. The size of the analysed domain is bounded by the dimension of the test section and the range of spatial scaling for which a certain wind tunnel is certified. However, the measuring data collected in wind tunnel experiments are indispensable for the validation of numerical simulations.

Numerical methods aim to overcome these limitations by serving as a complementary tool to wind tunnel experiments and extending their applicability and scope in wind energy studies. The importance of numerical methods compared to experiments is reflected in the simultaneous availability of a large number of high-resolution parameters, both temporal (in high-fidelity methods like LES, data are available in all time intervals) and spatial (data are available at any point in the computational domain). Data are correlated in time and collected under strictly controlled conditions. Moreover, the possibilities regarding the geometry of the domain and the models that can be examined using numerical methods are unlimited. Confronting two numerical methods, preference should be given to the LES method due to the inaccuracy of the RANS approach in predicting the size and location of the separation regions around buildings, which is important to improve the efficiency of wind turbines [35].

Wind loading studies

Wind loading studies also rely on the synergy between experimental and numerical techniques to assess wind effects on structures. Wind tunnel testing has long been the primary tool for determining wind loading, forming the basis of the structural design codes. However, the codes are developed based on isolated building tests and offer conservative estimates to ensure safety across diverse designs, often failing to reflect the specific aerodynamic characteristics of individual structures [24, 37]. This limitation highlights the need for advanced tools and methods to refine predictions of wind loads, in particular surface peak pressure, as there is no consensus among different design codes on the methods used to predict these values. The implementation of wind tunnel experiments in determining the surface peak pressure, in addition to the constraints already mentioned (such as the size of the analysed domain, spatial scaling, and the geometry of the models), is limited by the number of pressure sensors that can be installed and, sometimes, the impossibility of their placement.

On the other hand, high-fidelity numerical methods, particularly LES, do not face such limitations, offering a detailed insight into the time-varying pressure field. Moreover, an association between the wind flow and the pressure field can be established, which facilitates the identification of the origins of specific phenomena. However, to date, the use of CFD for the evaluation of wind loads in the final design stage is still not permitted under most code provisions worldwide, and the validation of numerical simulations against experiments remains imperative [38]. Despite this, in the preliminary design phase, it is undoubtedly a powerful tool, as demonstrated in [39]. This study employs CFD in the preliminary design of the Bologna Stadium roof to identify critical wind directions, high-pressure zones, and the impact of structural damping. The insights gained from the numerical simulations helped narrow the scope of subsequent wind tunnel tests,

thus reducing overall project costs. In addition, the simulations indicated the zones of interest for optimal pressure tap placement during wind tunnel measurements.

As computational power advances, the landscape of numerical modelling in environmental and civil engineering is likely to shift. The growing availability of high-performance computing and cloud-based simulation platforms is expected to reduce the computational burden associated with LES. This will enable its broader adoption in both research and practical applications, particularly in areas where detailed, time-resolved predictions of wind flow and pressure statistics are required. As best practice guidelines for LES develop, the gap between RANS and LES applications in engineering practice may narrow further, leading to a future where LES becomes the standard for high-precision numerical modelling [38]. This research is motivated by the desire to contribute to this ongoing evolution, working towards the full integration of CFD into engineering practice.

1.4 Formulation of the problem

The research in this dissertation is guided by the exploration of wind effects in the urban environment using numerical simulations, in particular, LES. The key questions that form the basis for the dissertation are:

- How accurately can LES predict wind flow patterns around high-rise buildings in an urban environment?
- How can these wind flow patterns be used to determine the urban wind energy harvesting potential?
- How accurately can LES predict surface peak pressures on building envelopes, and what is the appropriate validation procedure for these predictions?

The findings presented in this dissertation represent a thorough investigation of these issues based on four journal articles and three conference papers published between 2020 and 2024. The main issues associated with numerical modelling are its accuracy and reliability. Therefore, the main objective of this research is to evaluate the accuracy of the LES method through the validation of velocity and pressure statistics with available wind tunnel measurements and to enhance its reliability.

A scaled-down numerical model of the urban atmospheric boundary layer (ABL) is developed, replicating wind tunnel conditions. The study concentrates on local wind flow around isolated high-rise buildings and group configurations of five buildings in clusters at two approaching wind angles (0° and 45°). The capabilities of LES are assessed through three main topics:

- **Wind flow dynamics:** The complex dynamics of wind flow around high-rise buildings are investigated, focusing on identifying characteristic mean flow structures and mechanisms of their formation. First, the isolated high-rise building has been analysed with two roof shapes: flat and decked, published in [40]. The study is then extended to account for the interference effects only in the flat roof case. Two group arrangements with the varied positions of the four buildings surrounding the central one were investigated, and the findings have been published in [41].
- **Urban wind energy:** Based on the wind flow patterns obtained, the potential for wind energy harvesting around an isolated building and building in clusters has been assessed.

The primary focus is on the roof zone, with two roof types included (flat and decked) in the isolated building case [40] and only a flat one for group arrangements [41]. Optimal locations for wind turbine placement have been provided with specific zoning based on the characteristics of the wind flow. Furthermore, the link between the wind energy potential and the choice of wind turbine type has also been provided.

- **Wind loads on high-rise buildings:** The study examines the ability of LES to predict peak pressure coefficients on high-rise buildings. Factors such as the methodology for estimating peak pressure, the duration of pressure signals, and the flow complexity have been explored. A set of guidelines has been proposed for the peak pressure validation procedure when long-duration experimental and short-duration LES pressure signals are confronted. Here, the role of uncertainty quantification in experimental measurements is underlined. These findings have been published in [42].

By integrating these topics into a unified framework, this dissertation addresses key challenges regarding wind effects in the urban environment, focusing on the capability and reliability of the LES method.

1.5 List of references

The research presented in this dissertation has been disseminated through four peer-reviewed journal articles and three conference papers (presented by the author at their respective conferences). These publications have been integral to the development and validation of the methodologies and findings presented herein.

- Journal articles:
 - [43] H. Hemida, G. Vita, **K. Kostadinović Vranešević**, R. Hoffer, A. Šarkić Glumac, “*On the Flow over High-rise Building for Wind Energy Harvesting: An Experimental Investigation of Wind Speed and Surface Pressure*”, Applied Sciences 10.15 (2020), p. 5283, doi: 10.3390/app10155283.
 - [40] **K. Kostadinović Vranešević**, G. Vita, S.P.A. Bordas, A. Šarkić Glumac, “*Furthering knowledge on the flow pattern around high-rise buildings: LES investigation of the wind energy potential*”, Journal of Wind Engineering and Industrial Aerodynamics 226 (2022), p. 105029, doi: 10.1016/j.jweia. 2022.105029
 - [41] **K. Kostadinović Vranešević**, S. Ćorić, A. Šarkić Glumac, “*LES study on the urban wind energy resources above the roof of buildings in generic cluster arrangements: Impact of building position*”, Journal of Wind Engineering and Industrial Aerodynamics 240 (2023), p. 105503, doi: 10.1016/j.jweia.2023.105503.
 - [42] **K. Kostadinović Vranešević**, A. Šarkić Glumac, “*Peak pressures on high-rise buildings roof: A dual approach through validated LES and wind tunnel experiments with uncertainty quantification*”, Journal of Wind Engineering and Industrial Aerodynamics 250 (2024), p. 105784, doi: 10.1016/j.jweia.2024.105784.
- Conference papers:
 - [44] **K. Kostadinović Vranešević**, A. Šarkić Glumac, S. Bordas, “*The influence of exposure on wind flow characteristics around a high-rise building*”, *The 8th European-African conference on wind engineering (8EACWE)*, Bucharest, Romania, 2022, ISBN: 978-973-100-532-4.

- [45] **K. Kostadinović Vranešević**, A. Šarkić Glumac, “*Impact of surroundings on the local peak pressure in high-rise building clusters*”, *The 16th International Conference on Wind Engineering (ICWE16)*, Florence, Italy, 2023.
- [46] **K. Kostadinović Vranešević**, A. Šarkić Glumac, “*Peak Pressure Evaluation on High-Rise Buildings: Insights from Experimental and LES Analyses*”, *The 9th International Colloquium on Bluff Body Aerodynamics and Applications (BBAA9)*, Birmingham, UK, 2024.

1.6 Organisation of dissertation

Chapters 2 and 3 provide literature reviews, with a gradual shift from general research trends to the theoretical principles relevant to this study. Chapter 2 reviews the current state of research in CFD and its application across various fields of interest, highlighting key developments and challenges. Chapter 3 then presents the theoretical background, covering the basics of turbulent flow and numerical modelling algorithms. The governing equations of motion are presented, along with details of their numerical solution and the principles of the LES method.

Chapter 4 outlines the methodology employed in the study. It introduces the model of the building and configurations, followed by a description of the wind tunnel setup used in the validation process. Finally, details of the numerical setup are provided, including the computational domain, grid and boundary conditions. Chapter 5 presents validation of the numerical simulations with the available wind tunnel measurements. The first part examines the convergence of the main quantities of interest (velocity and pressure statistics). Then, the validation of the incoming wind profile, flow above the roof, and surface pressure is discussed.

The following three chapters focus on the numerical outcomes and their interpretation. Chapter 6 offers a detailed analysis of the wind flow in the studied configurations, after which the results have been interpreted in terms of urban wind energy in Chapter 7 and wind loading on high-rise buildings in Chapter 8. Each of these three chapters ends with concluding comments. The dissertation concludes with an overall summary and recommendations for future research in Chapter 9.

2 State-of-the-art

During the past six decades, substantial progress has been made in computational wind engineering. This chapter provides an overview of the current state of research in this field, structured into four sections. First, Section 2.1 discusses the phenomenology of wind flow in ABL, emphasising its characteristics in urban environments where most engineering structures are located and challenges in its numerical modelling. Next, Section 2.2 reviews the achievements in implementing CFD in wind energy, particularly in assessing the wind energy potential in urban areas. Finally, Section 2.3 focuses on the application of CFD in structural engineering, specifically addressing wind loads on the facades and roofs of high-rise buildings.

2.1 Wind flow dynamics in ABL

The ABL is the lowest part of the troposphere and is mainly influenced by the Earth's surface [47]. It plays a crucial role in wind engineering and environmental sciences. The thickness of the ABL varies from several tens of metres under stable stratification to several kilometres under unstable stratification or convection conditions [28]. Two important phenomena occur within the Atmospheric Boundary Layer (ABL): thermals and mechanical turbulence, including wake flows [48]. Thermals are pockets of air that become heated by the surface and ascend due to positive buoyancy. In contrast, mechanical turbulence, driven by wind shear, is primarily a result of the roughness of the earth's surface, such as terrain variations and buildings. Wake flows are a subset of mechanical turbulence created when obstacles disrupt the local flow, inducing reversed flow patterns and shear layers. While both thermals and mechanical turbulence contribute to turbulence generation in the ABL, this research focuses solely on mechanical turbulence, as thermal effects are beyond the scope of this dissertation and will not be further considered.

Figure 2.1 illustrates the ABL wind flow in urban areas, where the height of the ABL is around 1–2 km [49]. Above this height lies the free atmosphere, distinguished by the characteristics of the wind profile. Within the ABL, the typical mean wind velocity profile (represented with the continuous blue line in Figure 2.1) increases with height, starting from zero on the ground. In contrast, in the free atmosphere, in wind engineering applications, it is commonly assumed that the wind velocity remains relatively uniform with height, with little vertical gradient. For the turbulence intensity (profile presented with the red line in 2.1), the ABL wind flow is characterised by the high turbulence, which, in contrast to the velocity profile, reaches its maximum near the ground and decreases with height, unlike in the free atmosphere, where they are significantly lower.

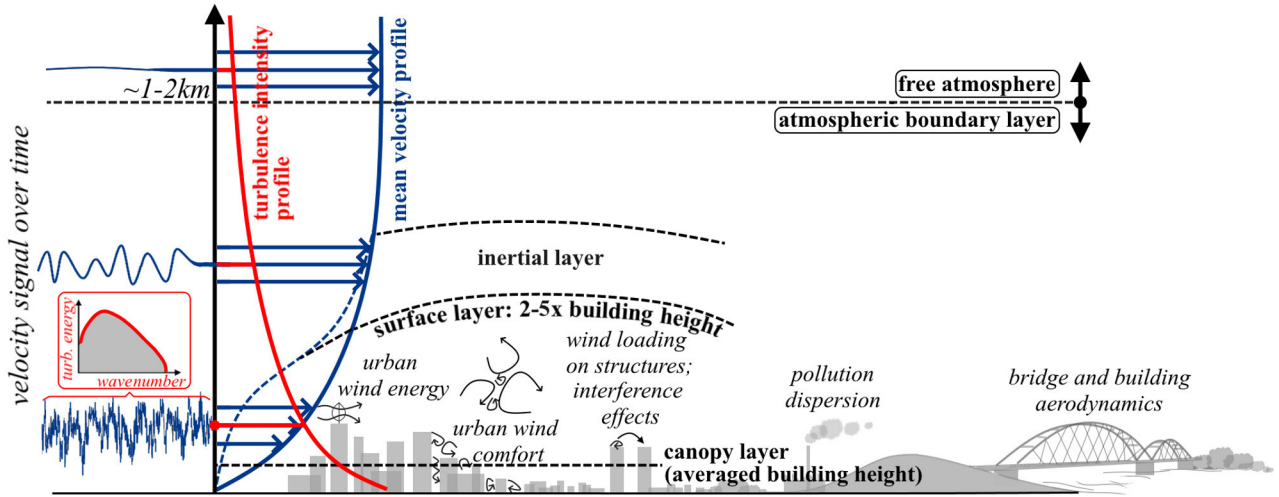


Figure 2.1. ABL wind flow in urban areas.

In an urban environment, the vertical structure of the ABL wind flow has its specifics. Due to surrounding buildings and other structures, the typical mean velocity profile is modified, resulting in a shape that more closely resembles the dashed blue line than the continuous one in Figure 2.1. Hence, urban ABL can be divided into four sub-layers, according to [49]:

- **Canopy layer:** Extending from the ground to the average building height, this layer is important for pedestrian wind and urban comfort.
- **Surface layer:** With a depth that varies between 2-5 times the average building height, this layer experiences significant drag due to the diverse topology of the buildings in urban areas, which modifies the ABL mean velocity profile from the upstream terrain, leading to also inhomogeneous turbulence; this layer is critical for applications in wind engineering, such as urban wind energy, wind loading and pollution dispersion.
- **Inertial layer:** This layer is characterised by nearly constant turbulent fluxes with height. Unlike the surface layer, the turbulence is more homogeneous in the inertial layer, and a logarithmic-like vertical wind velocity profile is typically observed.
- **Classical ABL flow:** Above the inertial layer, the urban ABL exhibits a classical ABL structure: under convective conditions, a mixed layer forms, while at night, a residual layer develops above a ground-based stable layer.

To obtain the urban atmospheric boundary layer (ABL) wind profile (represented by the dashed blue line in Figure 2.1) at a specific location in an urban environment, two key elements must be considered:

- ABL wind profile of the upstream terrain and
- local wind flow influenced by urban surroundings.

While the ABL wind profile of the upstream terrain is generally well-defined through design codes, the situation becomes more complex when considering the local wind flow. Wind effects at the local scale are site-specific and, thus, not defined in the design codes. That is why, to model the urban ABL wind flow, the design codes have to be complemented with experimental wind tunnel measurements and/or numerical modelling to capture wind effects at the local scale. Subsections 2.1.1 and 2.1 discuss the characteristics and challenges associated with modelling the

ABL wind profile of the upstream terrain (Subsection 2.1.1) and the local wind flow influenced by urban surroundings (Subsection 2.1).

2.1.1 ABL wind profile of upstream terrain

The upstream terrain ABL wind flow is typically described with the mean velocity profile following the logarithmic or power law. This velocity profile defines the surface roughness of the upstream terrain and presents different exposures classified into terrain categories in the design codes. According to Eurocodes [50], these categories are descriptive, ranging from terrain category 0, which denotes low surface roughness (“sea and coastal area exposed to the open sea” [50]), to terrain category IV (“area in which at least 15% of the surface is covered with buildings and their average height exceeds 15 m” [50]). The higher terrain category is related to the larger power law exponent α in the expression of the normalised vertical mean velocity profile $U/U_{ref} = (z/z_{ref})^\alpha$ where z_{ref} indicates the reference height (usually the height of the principal building). The design codes specify mean velocity and turbulence intensity profiles for different terrain categories. However, they are not easy to replicate in wind tunnel experiments and numerical simulations.

In wind tunnel experiments, these target profiles are developed by air passing through the upstream precursor domain (i.e. driving domain) in front of the turning table, supplied with the elements that generate turbulence, such as barriers, spires, and roughness fields. The technique is known as the traditional spire-roughness technique and is a widely adopted method [51]. Figure 2.2 presents examples of the two ABL wind tunnels.

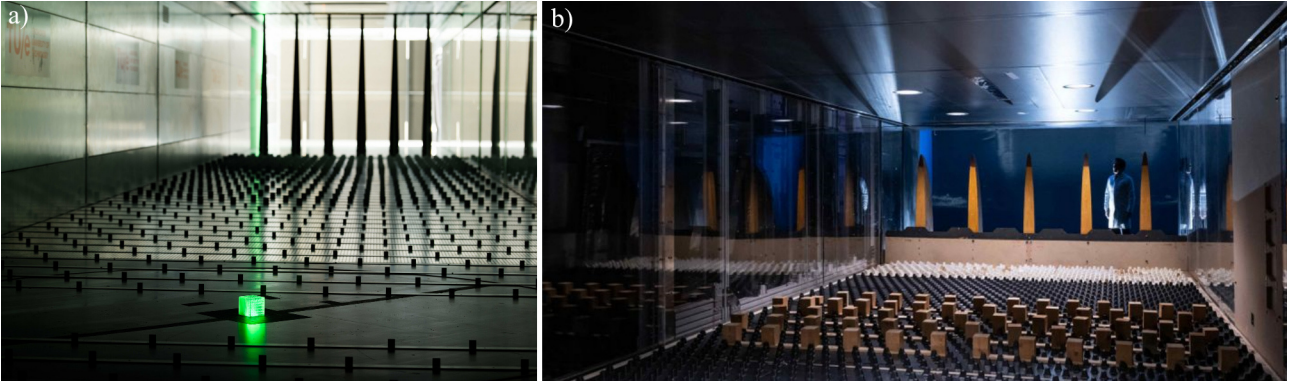


Figure 2.2. ABL wind tunnels at (a) the Eindhoven University of Technology, Netherlands [52] and (b) the Imperial College, London, UK [53].

In numerical modelling, however, the complexity of developing the target wind profile for the upstream terrain category largely depends on the choice of the numerical method. Different methods may require varying levels of computational effort and model sophistication to achieve profiles consistent with those specified in the design codes.

For the RANS approach, this process is relatively straightforward. The target profiles are implemented through the definition of inlet boundary conditions, where the velocity and turbulence intensity profiles from the design codes are directly prescribed. Unlike methods that require a precursor domain to develop these profiles, RANS does not necessitate such a domain, making it computationally efficient. Additionally, the RANS method allows for the specification of other turbulence parameters, such as turbulent kinetic energy and dissipation rate, providing flexibility in tailoring the inlet conditions to match the desired wind flow characteristics.

On the other hand, in the LES method, this is one of the most challenging tasks, and various approaches have been developed, overviewed in [54, 55]. Four main methods were identified in [54]:

- **The wind tunnel replication:** The most straightforward method and requires an accurate replica of the driving section of the physical wind tunnel in the computational domain with all elements that generate turbulence [56]. The turbulent boundary layer is reproduced in the same way as in the experiments, and turbulence develops as the wind passes through the replicated upstream fetch length. The precision of this method is highly dependent on the grid resolution [54]. In [55], a particular method is described as reliable and easy to achieve a good match between the experimental and numerical results. As a drawback, the required computational expenses are higher than those of the other methods.
- **The recycling method:** Method is based on simulating an auxiliary domain—an infinitely long fetch of upstream wind flow—by recycling a portion of the domain. This process generates a turbulent inflow that is applied as a time-dependent boundary condition in the test domain. The method was initially proposed by Lund et al. [57] and demonstrated a high precision in replicating surface pressures on buildings, as shown in [58, 59]. However, this method usually lacks a detailed description of the procedure to be repeated [55].
- **The precursor database method:** It is a combination of the first two methods. Namely, it employs an auxiliary domain, as in the recycling method, but it replicates the driving section of the physical wind tunnel, like in the wind tunnel replication method. Values at the outlet are sampled, creating a database that can be reused as the turbulent-inflow data. Clear guidelines for using this method are provided in [54]. This method (as well as the recycling) requires storing and loading new values on-fly at the inlet boundary in each time step, which can be a limitation in terms of computer memory.
- **The synthetic turbulence generator method:** Method computationally generates upstream wind flow, either in advance or during simulation, making it highly efficient [54]. The target is the alignment with the theoretical von Karman velocity spectrum, as described in [60, 61]. However, criticisms arose regarding its mismatch with the spectrum and lack of coherence in vortex structures. Subsequent advancements exposed in [62, 63], enhanced its ability to maintain coherent vortex structures and accurate time correlation. The remarkable match of the numerically obtained velocity spectrum with the experimental ones, even in the high-frequency range, was achieved by the method presented in [64]. It is also worth mentioning a recent method presented in [65, 66] that has a ready-to-use OpenFOAM® boundary condition.

Modelling the urban ABL wind flow requires replicating upstream conditions. While wind tunnel experiments rely on physical turbulence generators, numerical methods, particularly LES, require advanced inflow techniques, which come at notable computational costs.

2.1.2 Local wind flow affected by urban surroundings

The local wind flow in an urban environment is site-specific. The flow patterns around an isolated building provide a basis for further analyses of more complex building configurations. It has been extensively studied, revealing key features such as flow separation and reattachment, vortex shedding, recirculation zones, and wake formation [67]. The first studies were experimental wind tunnel measurements, most of which are presented in [68].

Figure 2.3, adapted from [69], illustrates the mean flow pattern around an isolated cubic building immersed in the ABL wind flow, with a wind perpendicular to the front facade. As the flow approaches the building, a stagnation point with maximal pressure occurs on the front facade, typically in the upper third of the building height. Its exact position depends on the height-to-width ratio, shifting higher as this ratio increases [70]. From the stagnation point, the flow splits—moving downward, upward, and around the sides of the building—creating a cavity zone. In front of the building, a horseshoe vortex forms due to downward deflection. At the windward edges, the flow separates, leading to low-speed, high-turbulence zones on the roof and sides. Whether reattachment lines on the roof and sides occur depends on the building's size and the turbulence intensity of the incoming wind [67]. In the near wake region, an arch vortex recirculation zone develops in the low-pressure area behind the building. Beyond the cavity zone, after its mean reattachment line, the flow gradually resumes the original direction but with decreased speed and increased turbulence over a considerable distance.

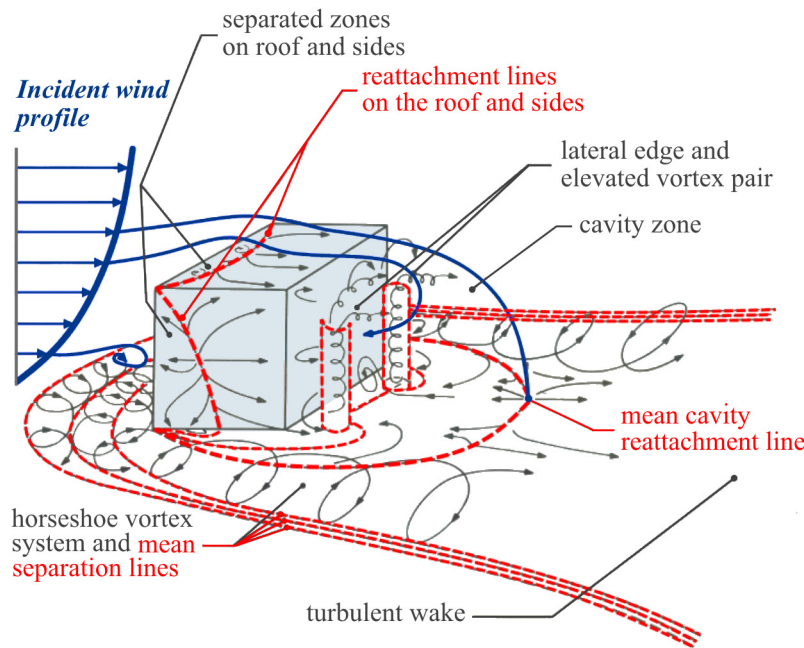


Figure 2.3. Wind flow around the isolated cubic building in the ABL, adapted from [69].

These flow patterns around an isolated building are strongly influenced by the building's geometry, orientation, and the characteristics of the approaching wind flow. Particularly interesting is the case when the wind approaches at a 45° angle, as it generates a characteristic pair of conical vortices on the roof, as detailed in experimental studies [71, 72, 73]. For other wind angles, the flow pattern above the roof is a combination of those observed for 0° and 45° wind angles, as shown in [74]. A comprehensive review of studies on the wind flow around isolated buildings is provided in [67].

In urban environments, however, wind flow is shaped by various interacting factors, including street canyons, building arrangements, and the orientation of structures with respect to the approaching wind. Flow pattern within street canyons depends on their aspect ratio and the prevailing wind direction [75, 76, 77, 78, 79, 80]. When the wind is orthogonal to the street canyon, three distinct flow patterns can develop—isolated flow, wake interference flow, and skimming flow—depending on the building height (H), length (L), and street canyon width (W), as illustrated in Figure 2.4, adapted from [81]. In contrast, longitudinal wind can induce channelling, leading to increased wind speeds [75, 78]. A similar acceleration occurs due to the Venturi effect when airflow is constricted between buildings [14].

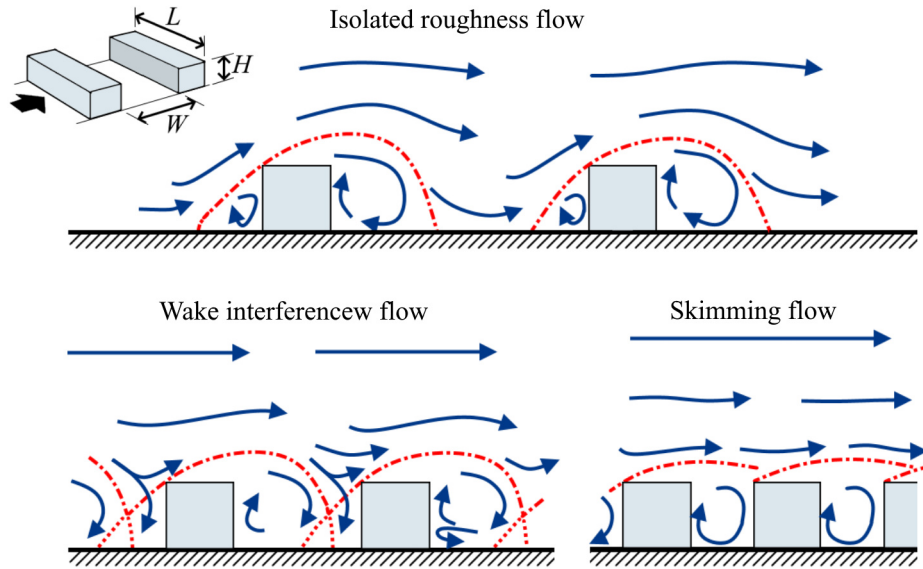


Figure 2.4. Flow patterns in street canyons over building arrays of increasing density, adapted from [81].

High-rise buildings significantly influence the surrounding flow field, often generating strong downwash effects that elevate wind speeds at the pedestrian level [82]. At the same time, they contribute to wind sheltering, the extent of which depends on the height difference between neighbouring buildings [83, 84, 85] and their spacing [86]. Beyond these individual effects, detailed interactions of the flow around buildings are described through the interference effects, a specific research topic. Studies in this area generally fall into two categories: those investigating interactions between two buildings and those examining the flow dynamics within larger building clusters.

The first category investigates how a principal building is affected by an interfering building in three typical configurations: tandem (aligned with varying longitudinal distances), side-by-side (separated by different transverse distances), and staggered (a combination of the first two). Notable studies in this area include [24, 87, 88, 89, 90, 91, 92]. The second category explores wind flow in idealised building clusters [74, 93, 94, 95, 96, 97].

A large body of research on urban wind flow focuses on pedestrian-level wind comfort and pollution dispersion, with comprehensive reviews available in [98, 99, 100]. However, these studies typically do not address wind flow above high-rise rooftops, which is strongly influenced by roof shape and the configuration of surrounding buildings. This aspect is more commonly studied in wind energy assessments, with a review provided in Section 2.2.

Unlike the well-documented wind effects around idealised, isolated buildings, the influence of urban surroundings on local wind flow requires a combination of experimental wind tunnel measurements and numerical simulations, each presenting specific challenges and constraints. The size of the domain included in the analysis depends greatly on the specific problem being investigated and can range from an isolated object to the entire city [28].

In wind tunnel studies, this challenge arises due to limitations in spatial scaling. The physical constraints of the wind tunnel limit the extent of the urban area that can be modelled, often necessitating compromises in representing the larger urban context. In addition, wind tunnel experiments are limited in their ability to evaluate the effects of varying geometric parameters of

structures, as adjustments to physical models can be time-consuming and costly. Furthermore, achieving a detailed representation of the flow field is challenging, as the resolution and extent of the measurements are limited by the measuring equipment.

It is worth mentioning two open-access sets of experimental data that remain the basis of the knowledge for urban flows: measurements in the wind tunnel of the Architectural Institute in Japan [32] and CEDVAL [101]. In [32], field measurements around isolated and grouped buildings were included, as well as models of building complexes in actual urban areas, while data in [101] provided flow measurements for cubic and prismatic buildings placed stand-alone or in a regular array. Both databases offer detailed insight into the flow field around building facades, particularly at the pedestrian level, though data on flow above rooftops remain scarce. To address this gap, a series of experiments were conducted in the wind tunnel of the Ruhr University in Bochum, Germany, as part of COST action TU1304. These experiments generated a substantial database of wind flow in the rooftop zones of both low- and high-rise buildings, whether isolated or in groups [102]. Some of these results are presented in [43, 74, 95]. All the datasets mentioned serve as a basis for validating numerical simulations.

In contrast, numerical modelling addresses many of these limitations by allowing the simulation of large domains without the constraints imposed by physical space. These methods accommodate complex and detailed urban geometries while offering the flexibility to modify building configurations and geometric parameters easily. Additionally, numerical modelling provides a comprehensive representation of the flow field across the entire computational domain. However, the accuracy and reliability of these simulations rely on validation against experimental data to ensure that the predicted wind flow accurately reflects physical conditions. Furthermore, the choice of numerical method, whether RANS or LES, significantly influences the results. A comparison of these approaches, along with their specific advantages and limitations, is presented in Section 1.3.

Eventually, a comprehensive analysis of urban ABL wind flow requires the integration of the design codes, experimental wind tunnel tests, and numerical modelling. By combining these approaches, an exhaustive understanding of wind behaviour in urban environments can be achieved.

2.2 Urban wind energy

Urban wind energy research focuses on understanding unique wind flow characteristics within built environments to optimise wind energy harvesting and turbine performance. Key parameters for assessing wind energy potentials and wind turbine efficiency and operation include wind speed, turbulence intensities, and skewness (inclination) of the flow [35]. Wind energy density is directly proportional to the cube of wind speed, so any increase in wind speed is of great importance. Tall buildings have been identified as having the greatest potential for wind energy harvesting in urban areas [9]. Zones above rooftops and around facades are of particular interest due to flow acceleration in these areas [9]. Considering turbulence intensities, values above 18%, which are usually indicators of separation regions, are not recommended for the installation of most types of wind turbines and should be avoided [103].

Regarding the methodology, experimental studies on urban wind energy are limited due to high costs and practical challenges [36]. The available open-access studies on wind flow, already discussed in Section 2.1, provide valuable insights, but most of them are not specifically focused

on wind energy applications. Given these limitations, CFD is widely regarded as a powerful tool for studying urban wind energy potential due to its capacity to provide detailed results in the entire computational domain and flexibility in varying the models themselves [38]. Comprehensive reviews of work in this area are provided in [35, 96, 104, 105]. It is evident from these reviews that the RANS method is the most commonly used. The focus in these studies is mainly on determining wind acceleration around objects, though it is limited in assessing turbulence intensities accurately [29]. Moreover, much of the published work relies on limited validation of the data [30, 106, 107, 108, 109]. This could lead to potential inaccuracies in assessing the size of separation and re-circulation regions on the roof and around the facade, which is critical for evaluating wind energy potentials and determining the optimal location for wind turbines. Nevertheless, RANS remains an unskippable tool in urban wind energy [29] and, by following the available best practice guidelines in [32, 33], it can yield satisfactory results for the mean flow statistics [29].

Studies using RANS modelling primarily focus on optimising building shapes to improve aerodynamics and enhance wind energy potential. Most of these studies concentrate on the roof zone, which is exposed to more stable wind conditions and higher wind speeds than facades. The surrounding environment is another important factor. As isolated high-rise buildings become less common in urban areas, the impact of surrounding structures significantly affects flow behaviour and wind energy harvesting potential.

The effects of the various roof shapes on the flow acceleration have been extensively studied [30, 106, 108, 110, 111, 112]. Gabled roofs have been analysed primarily in studies of low-rise buildings [110, 111], while studies on tall buildings typically focus on flat roofs [96, 109, 113]. In [106], a wide range of simple geometric roof shapes were examined. It was concluded that the best results were achieved on the top of a vaulted roof. An empirical optimisation for urban wind energy on more complex building-roof shapes, including wall-roof coupling and the effect of the roof-edge shape, is presented in [114]. While certain roof shapes offer higher wind energy harvesting potential, Larin et al. [115] emphasised the importance of synergy between buildings and wind turbines in harnessing the available energy. Using the combined numerical model of a building and a Savonius wind turbine, the optimal configuration reached a 450% improvement in the power coefficient. Another example of synergy between building and wind turbines is found in [109], where a case study of shrouded diffuser casing for turbines is presented.

Regarding the influence of neighbouring tall buildings, Juan et al. [96] analysed a generic cluster formed by four tall buildings and explored the possibility of placing wind turbines in the passage between them. Other studies, like [106, 108, 116], have investigated the impact of varying heights of neighbouring buildings. Wind resource assessment in realistic urban environments was analysed in [117, 118, 119]. However, this area remains less explored in the context of urban wind energy. The impact of neighbouring buildings, or the interference effect, is more thoroughly studied in fields such as wind loads or pedestrian wind comfort. Additionally, the zone above rooftops has not been the primary focus of these studies.

In contrast to RANS, there is a notable lack of studies applying the LES method in urban wind energy, despite its clear advantages in predicting urban wind flow and more accurately identifying separation zones [35]. Only a few researchers have explored the flow around buildings with respect to the roof region [120, 121, 122], and these studies often lack robust validation strategies and provide only limited flow statistics. In [120, 121], the wind energy resource above the roof of isolated buildings were examined, considering prism-shaped buildings, with the height-to-width ratio of 2:1, at 0° wind angle [121], and analysed the influence of the horizontal aspect ratios under varying wind directions [120]. When LES was combined with the

interference effects, there was only one significant investigation by Millward-Hopkins et al. [122], which examined idealised urban arrays, both uniform and heterogeneous in height, in relation to rooftop turbine placement. Across these studies, flow behaviour around the side walls of buildings was not analysed, and the available flow statistics were minimal.

A critical gap in urban wind energy research lies in the scarcity of studies employing high-fidelity methods like LES to examine the flow patterns above the roof regions thoroughly. The majority of existing research offers only limited and often unverified insights into flow characteristics. Bridging this gap is essential for improving the accuracy of wind energy resource predictions and increasing the efficiency of wind turbines in urban environments.

2.3 Wind loading on high-rise buildings

Unlike research focused on urban wind energy, the analysis of wind loads has a much longer history, making it a broader and more diverse field of study. To accurately predict wind-induced effects on high-rise buildings, an initial understanding of the dynamics of urban wind flow is essential. Numerous experimental and numerical studies, summarised in [123], have addressed this issue and provided robust data for determining global wind impacts, as well as mean pressure values on individual elements. However, studies focused on peak pressure are notably fewer.

In wind tunnel experiments, there are physical limitations to positioning measurement devices near sharp, separating edges, where the highest peak pressure values are expected to occur [37]. A recent experimental study on facade peak pressures in [124] concentrated around 100 taps near the top corner and 100 taps closest to the edge at mid-height, offering the highest density of pressure taps in a specific region in wind tunnel measurements to date.

Experimental limitations can be overcome by complementing them with numerical simulations. However, determining surface peak pressure remains one of the most challenging tasks in CFD. As a time-resolved solution, the LES method is more suitable and, therefore, preferred over RANS [125]. The performance of LES in predicting peak pressures on the facade was demonstrated in [37]. The excellent agreement with experimental results from [124] was reached, justifying the high expectations of the LES method and confirming its potential. This topic was also addressed in [126, 127], focusing primarily on the facade, while the roof zone was not analysed. In general, the roof zone of high-rise buildings has received less attention despite its importance, highlighted in [22]. More research in this zone has been conducted on low-rise buildings [128, 129, 130]. Overall, few numerical studies address wind loads on high-rise buildings, especially regarding peak pressure evaluation, and this area requires further investigation.

In addition to the difficulties of capturing peak pressure experimentally and modelling it numerically, determining peak pressure from a pressure signal is also problematic. Researchers have developed various methodologies to address this, but no consensus has been reached. A thorough literature review in [131] provides both a historical and a current state of practice in estimating peak pressures, emphasising the importance of uncertainty quantification associated with applied statistical treatment. Studies addressing this uncertainty are given in [131, 132, 133]. In [132], the uncertainties related to various peak pressure estimation methods were reported. The authors included different translation methods, as well as the Gumbel method, which showed remarkable results. Study in [131] explored in detail the uncertainties related to peak pressure estimates using the Gumbel method, with a focus on the influence of time series

duration and the number of subsets employed for observing peaks. The study offers valuable insights into the trade-offs between the length of the time series and the resulting uncertainty in peak pressure estimates. Research presented in [133] examined the influence of the duration of a wind tunnel test on the uncertainty of the estimated mean peak pressure and wind load factors. While these studies provide guidelines for evaluating peak pressures, they were conducted solely on experimental pressure signals from the roofs of low-rise buildings and have not yet been tested using numerical results.

The importance of addressing uncertainty resulting from statistical treatment of the peak pressures for numerical simulations is reflected in the validation process. The well-known Prof. Theodore (Ted) Stathopoulos, from Concordia University, Canada, made the following observations in his papers [134]: “It should be stressed, however, that LES as a procedure of turbulence modelling is going to be truly useful only if it reaches the stage of producing peak instantaneous pressure coefficients, with some reasonable accuracy.” This quote prompts two fundamental inquiries: Can LES effectively replicate instantaneous pressure coefficients, and what constitutes a reasonable level of accuracy? These queries are inherently linked; resolving the former necessitates addressing the latter.

Pressure signals from wind tunnel experiments are typically long-duration signals, providing a solid statistical foundation, while pressure signals from LES are shorter due to high computational costs. For proper validation, the duration of the pressure signals for peak pressure estimation should be the same in both the experiments and LES. However, variability arises when different time windows are extracted from experimental signals, introducing uncertainty. This uncertainty is critical when assessing the performance of LES. This issue has not been extensively explored in the literature, marking a clear gap in current research.

The literature review highlighted key gaps in urban ABL wind flow research. While a comprehensive understanding requires integrating design codes, wind tunnel experiments, and numerical modelling, several challenges persist. Notably, there is a scarcity of high-fidelity LES studies, particularly regarding flow patterns above the rooftops of high-rise buildings, which are important for assessing wind energy harvesting potential, as well as more complex building configurations. Additionally, there is a lack of detailed validation procedures for numerical simulations, especially when comparing signals of different durations. Addressing these gaps is essential for improving predictions of wind energy potentials in urban areas and enhancing the reliability of LES in wind loading studies.

3 Theoretical framework

This chapter aims to provide a theoretical background on the research topic. An introduction to the subject is given through a brief description of turbulent flow in Section 3.1, with basic characteristics of turbulence and wind profile. Section 3.2 provides details of the numerical modelling. It starts with a mathematical description of the problem and moves on to the modelling principles and numerical algorithm that lead to the solution.

3.1 Turbulent flow

Turbulent flow is the basic flow in nature and can be observed in various phenomena, such as solar winds, ocean currents or even simple cigarette smoke. According to Tennekes and Lumley [135], laminar flow is the exception in fluid dynamics, not the rule. While each turbulent flow is unique and dependent on its environment, certain fundamental characteristics can be identified. In particular, turbulent ABL wind flow can be described by the following characteristics specified in [135]:

- **Randomness:** Turbulent flow is very unsteady and chaotic in a way that small initial differences will undergo amplification and yet result in completely uncorrelated fields, making the deterministic prediction of turbulent flow practically impossible.
- **Diffusivity:** Turbulence facilitates the mixing and dispersion of momentum, heat, and other atmospheric properties, leading to enhanced transport and diffusion processes within the ABL.
- **Three-dimensionality:** Turbulent motion occurs in all three spatial dimensions; it is rotational motion and contains a great deal of vorticity, resulting in turbulent eddies across various time and length scales.
- **Dissipation:** This is the essential characteristic of all turbulent flows. The turbulent kinetic energy (TKE) of the flow is continuously dissipated into smaller scales through viscous effects, converting kinetic energy into internal energy of the fluid.

Osborne Reynolds set the fundamentals for understanding turbulence in experimental work [136]. He demonstrated the dependence of the ratio of inertial and viscous forces (Reynolds number) on the flow regime. The work of Lewis Fry Richardson made the next noticeable improvement in the field. He defined turbulence as a complex collection of eddies with different length scales (l), where “big whirls have little whirls that feed on their velocity, and little whirls have lesser whirls and so on to viscosity in the molecular sense” [137]. An important discovery came from the work of Andrey Kolmogorov [138] on the phenomenological prediction of the distribution of small-scale eddies (Kolmogorov’s law).

Figure 3.1 illustrates the idealised TKE spectrum adapted from [139, 140] in which eddies are represented by their wavenumber κ (directly proportional to the inverse length scale of the eddy). Most of the TKE is accumulated in large, energy-containing eddies. Their formation mechanism depends on the environment, and no theoretical approach to this mechanism is available. These eddies exhibit the vortex stretching process in which two energy transfers occur. First, the kinetic energy of the main flow is extracted and converted into TKE because of the mean velocity gradient (energy production). Second, the TKE from the large eddies is transferred to smaller ones, which forms the energy cascade (transfer of energy). Interestingly, unlike the large ones, these smaller eddies, primarily responsible for energy transport, are isotropic and tend to be independent of the formation mechanism. This simplifies their statistical treatment as they depend only on turbulent dissipation rate ε (the rate at which TKE transforms into internal thermal energy) and κ and obey Kolmogorov's law. At scales smaller than κ_d (the Kolmogorov scale), the molecular viscosity of the fluid (ν) starts to dominate and dump small-scale eddies, destructing turbulence. This part of the energy spectrum is characterised by a steep energy decrease and depends on ε and ν . In summary, turbulence can not maintain itself; without feeding it, it will eventually dissipate in the end.

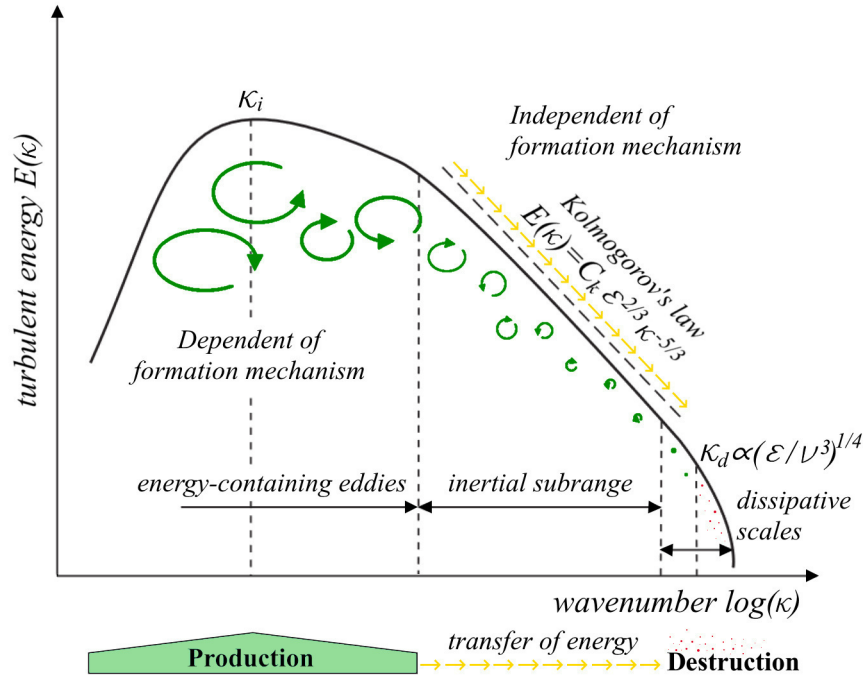


Figure 3.1. Idealised turbulent kinetic energy spectrum $E(\kappa)$ (adapted from [139, 140]).

The idealised energy spectrum in Figure 3.1 is characteristic of turbulent flows developed from instabilities in the free-shear flows. However, in wall-bounded flows, instabilities occur through the viscous process due to the presence of a boundary. In such cases, the energy-containing eddies are small-scale with large κ and anisotropic, but energy transfer to the core flow still follows Kolmogorov's law through the reversed energy cascade.

Recent developments in the study of turbulence have focused on examining turbulent structures, providing a more comprehensive understanding of eddies as coherent structures that are correlated by the flow dynamic as summarised in [141]. This is an ongoing research area, and there is still much to discover about the vortex dynamics.

3.2 Modelling the flow

This section describes a path from the “engineering” problem to the solution. The set of actions on this path is graphically represented in Figure 3.2, adapted from [142]. The first step is the definition of the mathematical model. This includes the mathematical description of the problem using differential equations, examined in Subsection 3.2.1, and establishing computational domain with boundary conditions. Next, the choice of the turbulence model is made, with basic principles of the LES method exposed in Subsection 3.2.2. Details of the following numerical algorithm in order to reach a numerical solution are provided in Subsection 3.2.3, referring to OpenFOAM®, an open-source software platform. An indispensable part of numerical modelling is the verification and validation of the model. The current level of development of CFD is not sufficient to use numerical simulations as a stand-alone tool. Hence, validation with the field (full-scale) data or wind tunnel (scaled-down model) measurements is mandatory [28].

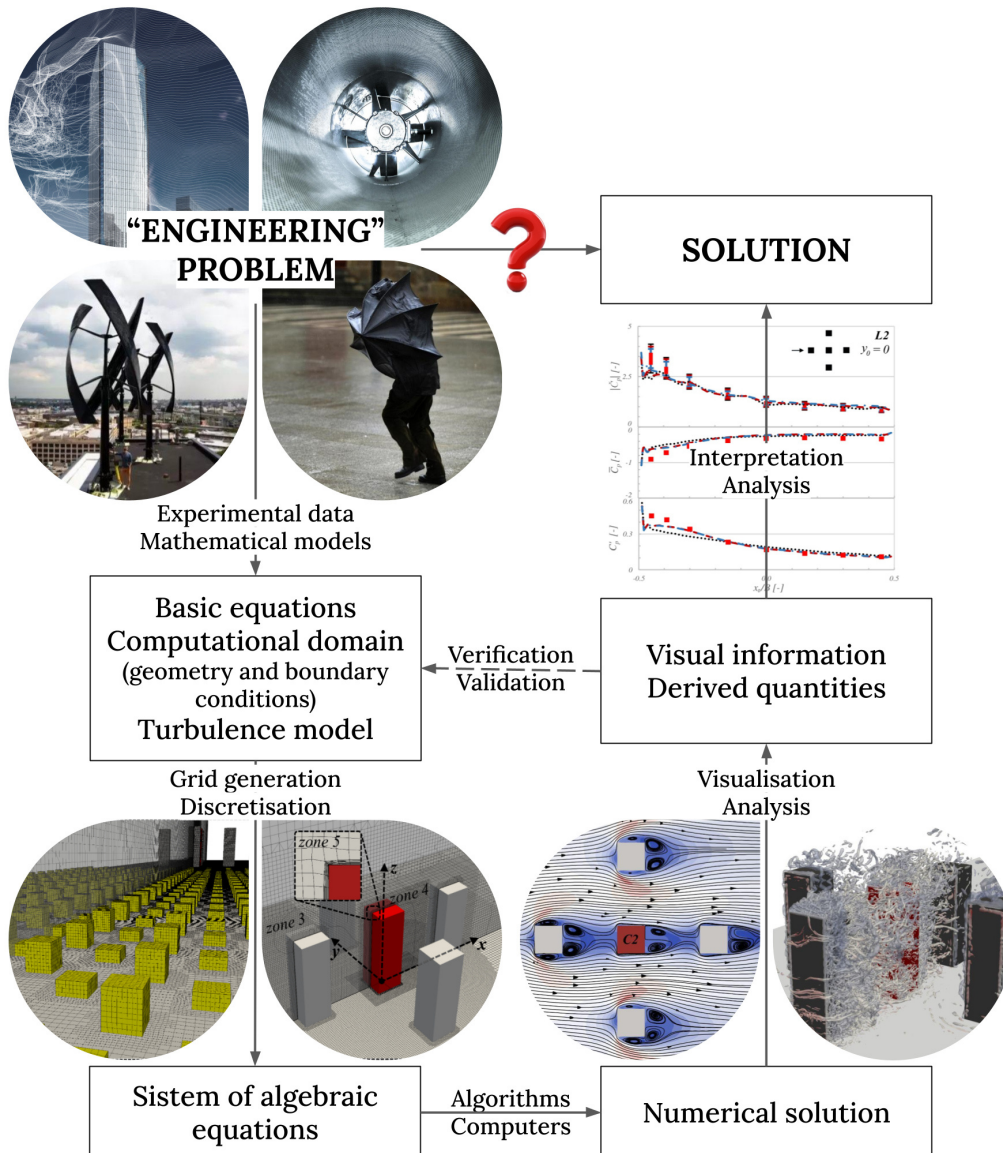


Figure 3.2. Flow chart of the numerical modelling, adapted from [142]).

3.2.1 Basic equations of fluid motion

The basic definition of fluids is that “fluids are substances whose molecular structure offers no resistance to external shear forces: even the smallest force causes deformation of a fluid particle” [143]. Fundamental approximations on fluid flow used in most cases in wind engineering are presented in [143] and summarised here. First, fluid is regarded as a continuous, homogeneous and isotropic medium. Furthermore, fluid can be treated as incompressible for March numbers (ratio between wind speed and speed of sound) lower than 0.3, which is fulfilled in this research. Regarding viscosity, fluid is considered Newtonian and obeys Newton’s law of viscosity.

The governing equations which describe the fluid flow are the three conservation laws of physics:

- Conservation of mass
- Conservation of momentum (Newton’s second law)
- Conservation of energy (first law of thermodynamics)

While these laws form the foundation of fluid dynamics, it’s important to note that the third law, governing energy conservation, is resolved primarily in scenarios involving heat transfer. However, in the context of the present research, which focuses on incompressible fluid flow without significant heat exchange, fluid flow is defined by the first two conservation laws, expressed as:

$$\nabla \cdot \mathbf{u} = 0 \quad (3.1)$$

$$\frac{\partial \mathbf{u}}{\partial t} + \nabla \cdot (\mathbf{u}\mathbf{u}) = -\frac{1}{\rho} \nabla p + \nabla \cdot \left[\nu \left(\nabla \mathbf{u} + \nabla \mathbf{u}^T \right) \right] \quad (3.2)$$

Equations (3.1) and (3.2) are the Navier–Stokes (N-S) equations for incompressible fluid. These equations are nonlinear second-order equations and form a system of four equations in four independent variables—three components of velocity vector \mathbf{u} and pressure p . Interestingly, there is no pressure equation, but it is coupled in Equation (3.2). Regarding the mathematical classifications of N-S equations for incompressible flow, they are incompletely parabolic problems, a combination of parabolic and elliptic type [143]. It comes from the fact that the flow can advance in both directions in space, like in recirculation regions, which is characteristic of the elliptic type. However, advancement in time is always forward, giving the parabolic character to the problem. The N-S equations are mathematically unsolved problems and are one of six active Millennium Prize Problems [144]. As computational resources and numerical methods continue to advance, various approaches tailored to specific fluid dynamics problems have emerged. CFD is the scientific discipline dedicated to this goal. Section 3.2.2 gives more details on the specific numerical method used in the present study—the LES modelling approach.

3.2.2 LES Modelling Approach

After determining basic equations which describe fluid motion (Equations (3.1) and (3.2)) and summarising the characteristics of the ABL wind flow, this subsection gives the principles of the LES modelling approach.

LES is a numerical method for solving N-S equations. The main idea behind LES is to directly resolve the large-scale, energy-containing turbulent structures while modelling the effects of

the small-scale turbulent structures (with large κ in Figure 3.1). LES can be judged as a balance between RANS and direct numerical simulations—DNS—by modelling only smaller-scale turbulence, unlike RANS, which models the entire turbulence spectrum. On the other hand, DNS resolves the entire spectrum of turbulence. Nevertheless, it can be computationally over-expensive for engineering problems since Reynold's number is usually too high and geometry complex, making LES a more affordable and reasonable alternative [143].

Filtering operation in LES

The background of the LES method is a filtering operation. Its role is to separate resolved from modelled scales on the TKE spectrum in Figure 3.1. In each flow variable ϕ , there are two parts to consider: the primary part, which is affected by the larger, resolved scales ($\tilde{\phi}$) and is an output of the LES method, and the secondary part, which results from the smaller, modelled, sub-grid scales (SGS) ϕ' . This can be expressed as:

$$\phi = \tilde{\phi} + \phi' \quad (3.3)$$

A filtering operator is a local spatial averaging operator over a certain volume, eliminating high-frequency range fluctuations from flow variables. It is accomplished through the low-pass filter kernel function $G(\mathbf{x}, \mathbf{x}', \Delta)$, which is a function of location $(\mathbf{x}, \mathbf{x}')$ and filter width (Δ) . Δ represents a characteristic length scale above which flow is fully resolved and is also proportional to the wave number (κ) of the smallest resolved eddies. The most common definitions of filter kernel function in LES are the Gaussian filter, box or top-hat filter, and the sharp spectral Fourier filter [145]. While the Gaussian filter is smooth and differentiable, the sharp spectral Fourier filter defines the cut-off frequency (wave numbers κ) above which frequencies are filtered out. The box filter is the most common choice when the finite volume method is used because it performs the averaging over a specific volume, which is typically adopted equal to the volume of the grid cell. The filter width Δ is a local filter and can be calculated as a cube root of the cell volume (OpenFOAM® function `cubeRootVol`). The filtered variable $\tilde{\phi}$ and kernel function G for the box filter are:

$$\tilde{\phi}(\mathbf{x}, t) = \oint G(\mathbf{x}, \mathbf{x}', \Delta) \phi(\mathbf{x}', t) d\mathbf{x}' \text{ and } \oint G(\mathbf{x}, \mathbf{x}', \Delta) d\mathbf{x}' = 1 \quad (3.4)$$

$$G(\mathbf{x}, \mathbf{x}', \Delta) = \begin{cases} 1/\Delta^3 & \text{if } |\mathbf{x} - \mathbf{x}'| \leq \Delta/2 \\ 0 & \text{otherwise} \end{cases} \quad (3.5)$$

A graphical representation of the filtering operation in LES is given in Figure 3.3, with illustrations of resolved and modelled (SGS) scales in the computational grid and frequency domain. The LES is considered well-resolved if over 80% of the flow's TKE is resolved [34].

Applying filtering to Equations (3.1) and (3.2), one obtains the following filtered N-S equations:

$$\nabla \cdot \tilde{\mathbf{u}} = 0 \quad (3.6)$$

$$\frac{\partial \tilde{\mathbf{u}}}{\partial t} + \nabla \cdot (\widetilde{\mathbf{u}\mathbf{u}}) = -\frac{1}{\rho} \nabla \tilde{p} + \nabla \cdot \left[\nu \left(\nabla \tilde{\mathbf{u}} + \nabla \tilde{\mathbf{u}}^T \right) \right] \quad (3.7)$$

The filtered non-linear convective term in Equation (3.7) can be decomposed into two parts to express it as a product of filtered velocities rather than a filtered product of velocities since $\widetilde{\mathbf{u}\mathbf{u}} \neq \tilde{\mathbf{u}}\tilde{\mathbf{u}}$, expressed as:

$$\widetilde{\mathbf{u}\mathbf{u}} = \tilde{\mathbf{u}}\tilde{\mathbf{u}} + \boldsymbol{\tau} \quad (3.8)$$

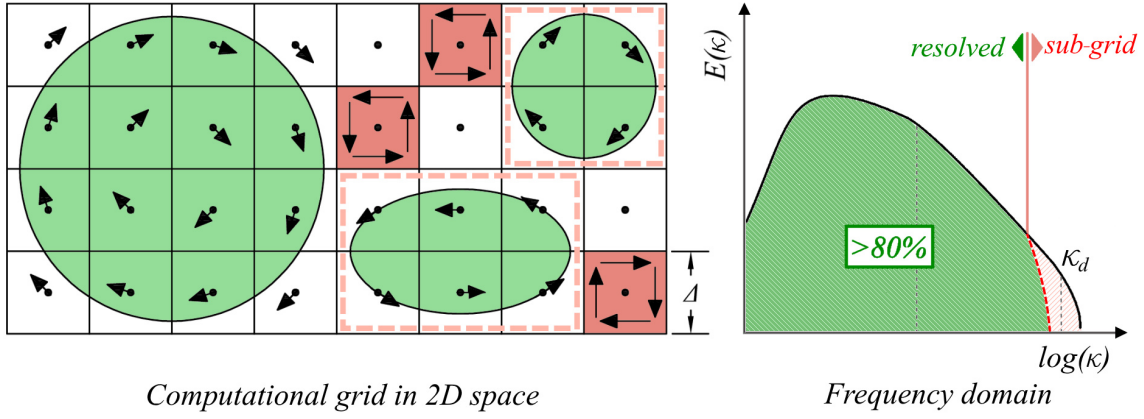


Figure 3.3. LES method: basic concept; a schematic representation of the filtering operation on the computational grid (Δ is assumed to be equal to the cell size) as well as in the frequency domain (adapted from [145]).

τ is commonly referred to as the SGS stress tensor, which is a fictional “residual stress tensor” and ensures that the filtered equation retains the same form as the original Navier–Stokes equation. It can be further reconstructed into three parts by applying decomposition in Equation (3.3) to \mathbf{u} :

$$\tau = \widetilde{\mathbf{u}\mathbf{u}} - \widetilde{\mathbf{u}}\widetilde{\mathbf{u}} = \left(\widetilde{\mathbf{u}\mathbf{u}} - \widetilde{\mathbf{u}}\widetilde{\mathbf{u}}\right) + \left(\widetilde{\mathbf{u}}\mathbf{u}' + \mathbf{u}'\widetilde{\mathbf{u}}\right) + \mathbf{u}'\mathbf{u}' \quad (3.9)$$

Each of the three terms in Equation (3.9) illustrates the impact of filtering on different scales in a flow. The first term is related to the interaction among resolved scales, whereas the second term links the resolved and unresolved scales (SGS). The last term describes the interaction among unresolved scales, commonly known as the SGS Reynolds stress. It is important to note that the portion of TKE in SGS is much smaller than the resolved one, unlike in RANS, where the whole turbulence spectrum is modelled. Therefore, SGS models in literature tend to be relatively simple in LES, compared to RANS, and model all terms in Equation (3.9) together due to the smaller error potential.

Modelling the sub-grid scales

The issue with the filtering process is that the TKE is locked in the resolved eddies, which are just larger than the grid cell (marked with dashed, light red rectangles in Figure 3.3). One needs to find a way to remove these resolved scales from the grid because there are no smaller scales to break them down and drain the energy, and viscous effects are not strong enough. It can be achieved by artificially increasing the turbulence dissipation rate (ε) by introducing eddy viscosity (ν_{SGS}), which is just enough to mimic the breakdown process of small resolved eddies. The turbulence dissipation rate is proportional to the product of the velocity gradients, and smaller eddies experience higher velocity gradients. Hence, it leads to an increase in dissipation rate ε associated with a decrease in eddy length scale until the viscous effects prevail. Returning to the SGS stress tensor (τ), ν_{SGS} can be interpreted as its controller, which properly doses its strength and dissipates only the scales just larger than the grid cell size. Instead of modelling τ , one needs to model only ν_{SGS} .

An important assumption in eddy-viscosity models is isotropy, implying that only the size of the eddy needs to be considered, not the shape. This simplifies the ν_{SGS} definition since it can be expressed through a single scalar value dependent on the size of the eddy and not any shape parameter. As δ reflects the cell size, it means that the coarser grid requires higher values of ν_{SGS} .

to break down larger resolved eddies compared to a finer grid. Here, the criteria for resolving 80% of total TKE is particularly important for LES quality assessment as grid independence study is impossible to perform in LES. However, the isotropic turbulence assumption leads to the following expression of the SGS stress tensor:

$$\boldsymbol{\tau} = -2\nu_{SGS}\tilde{\mathbf{S}} + \frac{1}{3}\text{tr}(\boldsymbol{\tau})\mathbf{I} \quad (3.10)$$

where $\tilde{\mathbf{S}} = 1/2 (\nabla \tilde{\mathbf{u}} + \nabla \tilde{\mathbf{u}}^T)$ is the strain rate tensor of the resolved flow. Different methods exist in the literature for determining ν_{SGS} in LES. Smagorinsky [146] proposed the first solution for the case of isotropic turbulence away from the wall. The solution came from simple dimensional analyses of the SGS viscosity, which is measured in $[\text{m/s} \cdot \text{m}]$ or $[\text{velocity} \cdot \text{length}]$. It suggests that the SGS viscosity can be expressed in terms of one characteristic SGS length scale l_{SGS} (due to the assumption of isotropic turbulence) and velocity scale. The SGS length scales are proportional to Δ , but smaller as these eddies are smaller than the cut-off filter width. To account for this, the Smagorinsky constant C_S is introduced to reduce Δ . The velocity scale is taken equal to the product of the SGS length scale and the averaged $\tilde{\mathbf{S}}$ of the resolved flow, calculated as $\sqrt{2\tilde{S}_{ij}\tilde{S}_{ij}}$ where $\tilde{S}_{ij}\tilde{S}_{ij} = \tilde{\mathbf{S}} : \tilde{\mathbf{S}}$. The resulting Smagorinsky model for the SGS viscosity is:

$$\nu_{SGS} = (C_S\Delta)^2 \sqrt{2\tilde{S}_{ij}\tilde{S}_{ij}} \quad (3.11)$$

The only parameter that needs to be defined in Equation (3.11) is the Smagorinsky constant C_S . It can range between 0 and 1, but it is usually adopted between 0.18 and 0.23, determined from the isotropic TKE decay rate in the inertial subrange (Kolmogorov's law) [34].

The main drawback of the Smagorinsky model is that it does not consider walls since the eddy length scale decreases as it approaches the wall. Analysing the Equation (3.11), one can conclude that it can not equal zero since Δ is a function of grid size and $\tilde{\mathbf{S}}$ will have terms different than zero as long as there is any velocity gradient. This means that even in the vicinity of the wall, where the tiny viscous layer occurs, the Smagorinsky model would add SGS viscosity to the system. There are three options to overcome this. The first option is to change the SGS model from simple algebraic to more complex ones. Numerous different SGS models are available, including the differential one with additional transport equations for one or more turbulence properties, scale-similarity and more advanced dynamic models in which coefficients are calculated based on the energy content of the smallest resolved eddies rather than an input itself. However, with the increasing complexity of the SGS models, the computational cost is rising, too, compared to the Smagorinsky model. Hence, the next two options are related to improving the Smagorinsky model by modifying the SGS length scale ($l_{SGS} = C_S\Delta$) or velocity scale ($u_{SGS} = \Delta\sqrt{2\tilde{S}_{ij}\tilde{S}_{ij}}$) to decrease ν_{SGS} in the close-wall zone.

The commonly adopted modification of the SGS length scale in the Smagorinsky model is the Van Driest dumping function D [147, 148]. It decreases the size of the SGS eddies as they approach the wall by introducing a new criterion for determining the SGS length scale l_{SGS} :

$$l_{SGS} = \min\{\kappa y D, C_S\Delta\}, \quad D = \sqrt{1 - \exp\left(-\frac{y^+}{A^+}\right)} \quad (3.12)$$

where y is an absolute wall distance, and y^+ is a dimensionless wall distance, which can also be interpreted as a local Reynolds number since it equals $y^+ = yu_\tau/\nu$ (u_τ is friction velocity). Parameter A^+ controls the shape of D and equals 26 from empirical resources. The Van Driest

dumping function is the most straightforward modification of the standard Smagorinsky model. More advanced dynamic methods (Dynamic Smagorinski) were proposed in [149, 150] but also computationally more expensive due to the dynamic procedure.

The Wall-Adapting Local Eddy-viscosity (WALE) model [151] is another algebraic SGS model, which targets the modification of the velocity scale in Equation (3.11) to handle the effects of the wall. The SGS viscosity is defined relative to the strain rate tensor of the resolved scales $\tilde{\mathbf{S}}$ and its deviatoric part $\tilde{\mathbf{S}}^d$ as follows:

$$\nu_{SGS} = (C_w \Delta)^2 \frac{(\tilde{S}_{ij}^d \tilde{S}_{ij}^d)^{3/2}}{(\tilde{S}_{ij} \tilde{S}_{ij})^{5/2} + (\tilde{S}_{ij}^d \tilde{S}_{ij}^d)^{5/4}} \quad (3.13)$$

where C_w is a model constant, and in OpenFOAM®, which default value is 0.325. If one needs to calculate the TKE of SGS or ε , two additional constants need to be specified, which do not affect ν_{SGS} , and they are C_k (which is actually the Smagorinski constant) and C_e . Compared to the Smagorinsky model with the Van Driest dumping function, WALE includes the rotation rate based on the filtered velocity in ν_{SGS} calculations. Due to the favourable numerical behaviour of the WALE SGS model in the wind engineering applications [55], it has been implemented in the present research.

3.2.3 Numerical modelling algorithm

After defining the basic principles for modelling the flow using the LES modelling approach in Subsection 3.2.2, this subsection provides details of the numerical algorithm. Essentially, three phases can be identified: pre-processing, processing and post-processing. More information about each of these phases is given below.

Pre-processing

This is the most important phase in flow modelling, as it encompasses the essential process of discretisation in both temporal and spatial domains. In that way, the set of partial differential Equations (3.1) and (3.2) is approximated by the system of algebraic equations for flow variables. These equations are then solved at each discrete location in time and space (in the processing phase).

Among the various spatial discretisation methods, the finite volume method stands out as it satisfies the conservation of mass by its construction compared to the finite element and finite difference methods. At the centroid of each cell, the flow variables are calculated, applying the integral form of N-S equations. In the finite volume method, the numerical domain is divided into a finite number of control volumes—cells—forming a computational grid. This is a particularly challenging task as there are no strict rules on how it should be done, but rather guidelines about the minimum requirements provided in [33, 152]. Furthermore, it is tied to the choice of the time step. Namely, the adopted time step should be small enough to capture the velocity passing through the individual grid cell. The parameter which quantifies that is called Courant–Friedrichs–Lewy or just Courant number (CFL) and represents the ratio between two distances: the distance which a fluid particle passes in on time step ($U\Delta t$) and a cell length in the direction of the velocity vector. In LES, a general recommendation is CFL below 1. This underlines the importance of adapting grid refinement to the velocity field as well as the choice of Δt .

Regarding the topology of control volumes, it is a general polyhedron, giving freedom to grid generation. Grids typically fall into two categories: structured, including regular, block-structured and overlapping (also called composite or Chimera) grids and unstructured grids [143]. All these types are suitable for use with the finite volume method. Important parameters of the grid quality are the aspect ratio of the cells, orthogonality and skewness, which can cause noticeable numerical errors. Nevertheless, these errors are inevitable with the complex geometries, but they can be greatly reduced with the adequate choice of the discretisation schemes.

This brings another important task in pre-processing phase, and that is the selection of discretisation schemes (specified in the `fvSchemes` dictionary in OpenFOAM®) and solvers with tolerances for various flow variables (specified in the `fvSolution` dictionary in OpenFOAM®). The discretisation schemes have to:

- ensure the stability and convergence of the numerical simulation,
- maintains boundedness of physical quantities and
- achieve accuracy.

These properties are intertwined, often requiring a compromise between them. The example is boundedness and accuracy. Boundedness is hard to provide with higher-order schemes, but these schemes are essential for reducing errors in the numerical solution and gaining accuracy. This brings to light another important aspect—the error analysis. A comprehensive investigation of the errors associated with the finite volume method is given in [153].

Numerous schemes are available in commercial CFD codes, and deciding on a particular one is tedious. As a guideline, a detailed description of the finite volume method and discretisation schemes for each part of the momentum equation can be found in [143]. The final goal when choosing schemes is to reach the solution with the desired accuracy and minimal resources [143]. In general, it is advised to use second-order numerical schemes, as they offer a good balance between accuracy and computational cost [154].

Processing

In the processing phase, a system of algebraic equations on flow variables obtained through the discretisation is solved using numerical algorithms. The two most common algorithms are SIMPLE (Semi-IMplicit Pressure Linked Equations) [155] and PISO (Pressure-Implicit Splitting of Operators) [156]. Both are iterative, pressure-based algorithms. The former is typically used to obtain steady solutions (averaged in time—RANS simulations), and the latter for transient solutions. Since LES simulates an unsteady flow, the PISO algorithm is applied in the present research and examined in more detail in the following.

An illustration of the PISO algorithm flowchart, including the implementation of key components in the OpenFOAM®, is presented in Figure 3.4, based on [154, 157]. To distinguish between the OpenFOAM® implementation and the mathematical formulations in the text, sections of the OpenFOAM® source code are highlighted in gray. These code selections serve as informative notes to illustrate the connection between the equations and their implementation in OpenFOAM®. However, the syntax of the C++ programming language is not the subject of this analysis; for further details on C++ syntax in OpenFOAM®, see [158]. The algorithm is performed in every time step. Two essential stages of the PISO algorithm can be distinguished:

- **Momentum predictor:** After the initialisation of the velocity and pressure fields (initial \mathbf{u} and p), the momentum matrix \mathbf{M} —noted as `UEqn` in OpenFOAM® source code—is created (the mass flux ϕ from the previous time step is used for evaluating the nonlinear convection term `fvm::div(phi, U)` in `UEqn`). The discretised equation of conservation of momentum ($\mathbf{M}[\mathbf{u}] = -\nabla p$) is solved in the momentum predictor stage, bringing the new, intermediate velocity field. This stage is computed only once in the PISO algorithm, which is the basic difference between the PISO and SIMPLE algorithms (in the SIMPLE algorithm, this step is included in the pressure corrector loop, why it is called *outer pressure loop*).
- **Pressure corrector—PISO loop:** The velocity field from the momentum predictor stage does not satisfy the continuity equation (unless initial p is correct). In order to obtain the corrected pressure field, first, the mass fluxes (ϕ) at the cell faces are computed from decomposed \mathbf{M} matrix as explained in Figure 3.4. Next, the non-orthogonal pressure corrector loop solves the pressure correction equation (`pEqn`) and correct the mass fluxes with the obtained pressure field for the number of non-orthogonal corrections (`nNonOrthogonalCorrectors`). The pressure correction equation is derived from coupling continuity and conservation of momentum equations ($\nabla \cdot (\mathbf{A}^{-1} \cdot \nabla p) = \nabla \cdot (\mathbf{A}^{-1} \cdot \mathbf{H})$). After finishing the non-orthogonal pressure corrector loop, the explicit velocity correction is performed using the corrected pressure field and mass fluxes ($\mathbf{u} = \mathbf{A}^{-1} \cdot \mathbf{H} - \mathbf{A}^{-1} \cdot \nabla p$). This is the final step in the PISO loop. However, the corrected pressure field is calculated using the velocity field (intermediate for the first and corrected after the second PISO loop iteration), which does not fulfil the continuity criteria (unless it is the correct velocity field). As a result, the pressure field needs to be corrected again in the new PISO loop, resulting in the new corrected velocity field as well until the number of `nCorrectors` is reached.

It is important to note that the number of pressure corrector iterations (`nCorrectors`) is prescribed by the user. General advice is to use `nCorrectors` equal to 2. Another parameter explicitly defined by the user is the number of non-orthogonal corrector iterations (`nNonOrthogonalCorrectors`). The number of these iterations depends on the grid quality. For good quality, an orthogonal grid with a non-orthogonality of less than 60 can be set to 1. However, with increased grid non-orthogonality, the number of non-orthogonal corrector iterations should be increased (to 2 or 3), too [154].

Post-processing

Post-processing is the final stage in reaching the solution. It further processes the raw numerical results using code and visualisation programs. The output data from the OpenFOAM® depends on the function objects run. A great variety of function objects is available in OpenFOAM®. Nevertheless, they are an extra load to the already demanding LES simulation, which is why they should be selected carefully. It is especially important for statistical, field function objects like the mean and standard deviation of certain variables. These function objects have to be run during the simulation and executed in every time step, providing derived quantities in the whole computational domain. A compromise can be made with function objects that collect data only at discrete locations. A good example is function object `probes` which records a certain variable at the specified point in the computational domain, over the desired time interval. It is computationally less expensive and allows further manipulation of the collected signal over time.

However, the amount of output data in OpenFOAM® is usually large and requires the use of developed code for processing. In particular, Matlab programming language and numeric computing environment is used in the present research. ParaView is employed to visualise the

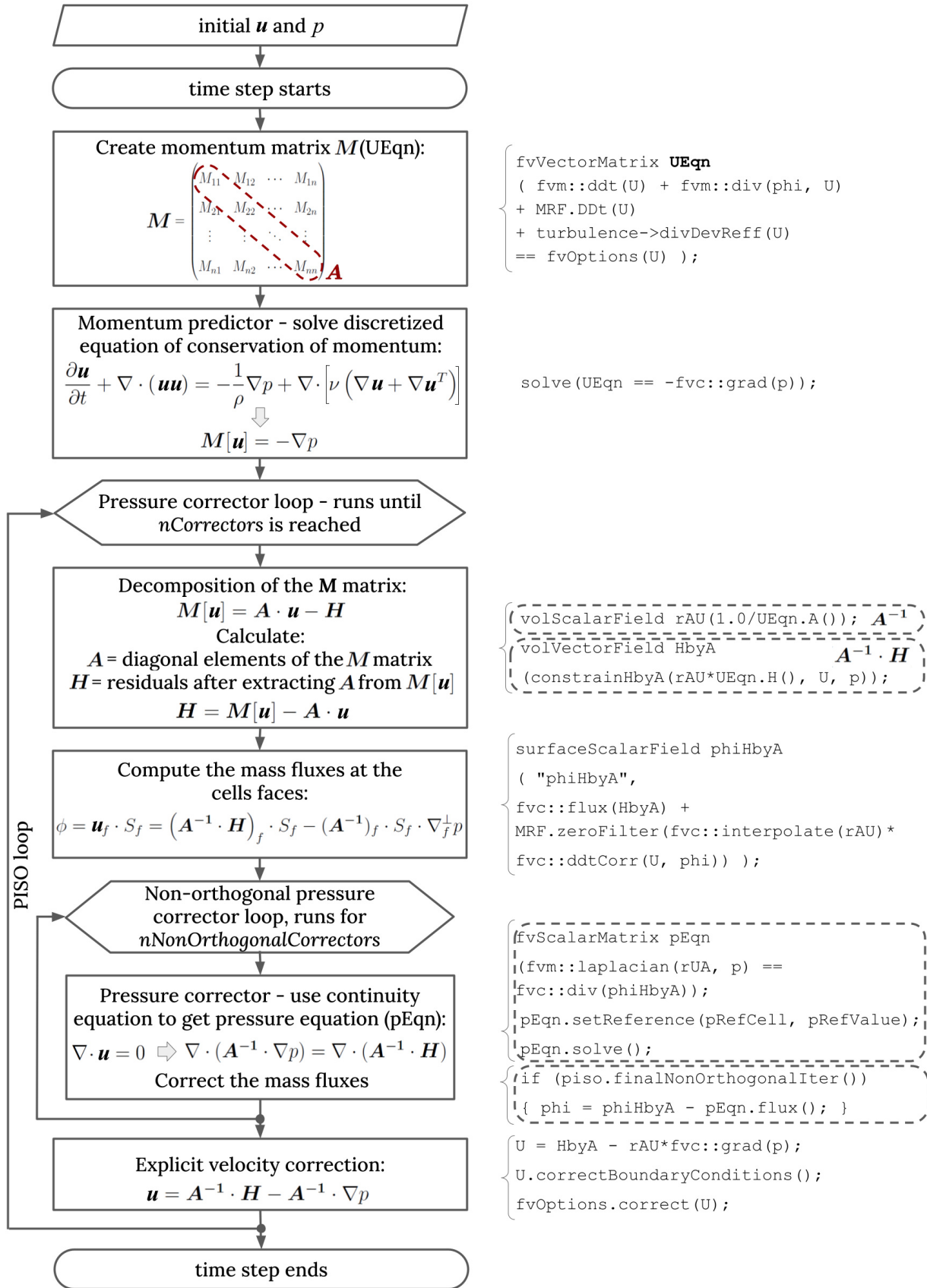


Figure 3.4. PISO algorithm: graphical representation with a flowchart on the left and segments of code from *pisoFoam* solver (OpenFOAM® source code).

collected field data, which can help further clarify certain phenomena. ParaView is a leading

open-source multiple-platform application for visualisation and data analyses, and it is a native reader for OpenFOAM®. It has numerous filters available to create stunning figures.

After post-processing the OpenFOAM® output data, the next step towards the solution is the validation of the numerical results with available experimental data. This is a vital part of numerical modelling, as already explained at the beginning of Subsection 3.2. In the end, interpretation of the obtained numerical results leads to solving the initial “engineering” problem.

4 Methodology

This chapter summarises the numerical and experimental methodologies employed in carrying out and validating numerical simulations of the wind flow around high-rise buildings in this research. Section 4.1 describes the models and configurations of the buildings used in the available wind tunnel experiments and the present numerical study. Section 4.2 briefly describes the experimental procedure, while Section 4.3 reports the setup for LES.

4.1 High-rise building models and their configurations

The geometry of the high-rise building models is illustrated in Figure 4.1. The square-base models with a height ($H=0.4$ m) to width ($B=0.1333$ m) ratio of 1:3 and a length scale of 1:300 is adopted. It corresponds to a 120 m height of the high-rise building in a full scale. Two roof shapes are investigated: flat roof (Fig. 4.1(a,c)) and decked roof with slopes inclining 30° relative to the horizontal plane (Fig. 4.1(b,d)). The coordinate system origin is set in the middle of the turning table in the experiments (at the centre of the central building base), and it is also retained in numerical simulations.

The building configurations included in the study are the following:

- A single configuration with an isolated high-rise building, further referred to as C1 configuration (Figure 4.2(a)), with flat and decked roof shapes,
- Group configurations of five geometrically identical high-rise buildings with flat roofs in a regular circular cluster arrangement of four buildings around the central one in:
 - the “cross” shape, marked as configuration C2 (Figure 4.2(b)) and
 - the “x” shape, marked as configuration C3 (Figure 4.2(c)).

The available wind tunnel experiments, reported in [102], addressed only configurations C1 and C2 at four approaching wind angles (α): 0° , 15° , 30° and 45° . However, the numerical investigation presented in this research includes all three configurations at two approaching wind angles, 0° and 45° . The selection of particular wind angles is made based on the published experimental results [43, 74]. Namely, it was found that 0° and 45° wind angles were associated with the highest wind energy harvesting potential in terms of wind speed and turbulence characteristics but also identified as having distinct flow behaviour, as well as surface pressure patterns.

The flow around the buildings and the study on wind energy are conducted on three configurations (C1, C2 and C3) for the flat-roof high-rise building model. However, the influence of roof shape

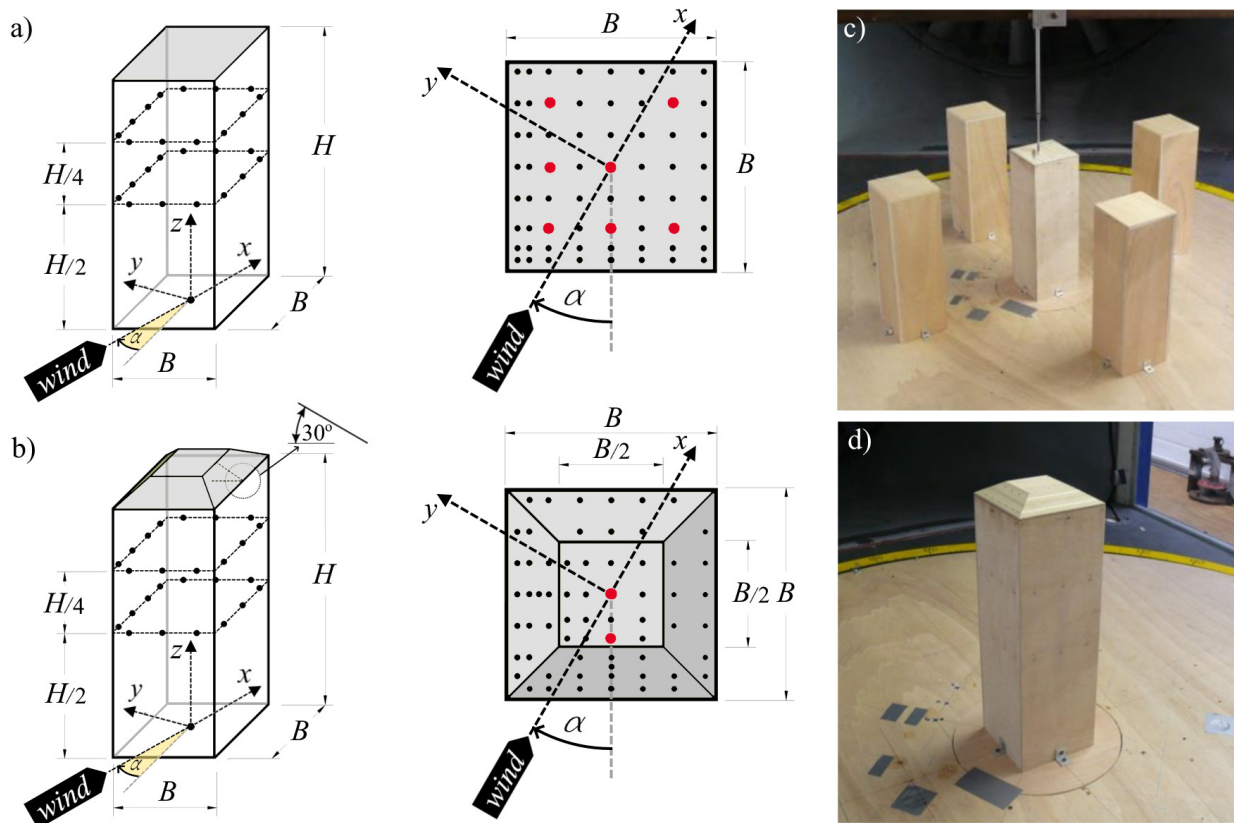


Figure 4.1. The geometry of the high-rise building models with marked points of pressure (grey and red spots) and velocity (red spots) measurements: (a) flat roof and (b) decked roof; wooden models of the buildings (adapted from [102]): (c) flat roof models in group C2 configuration and (d) an isolated decked roof model.

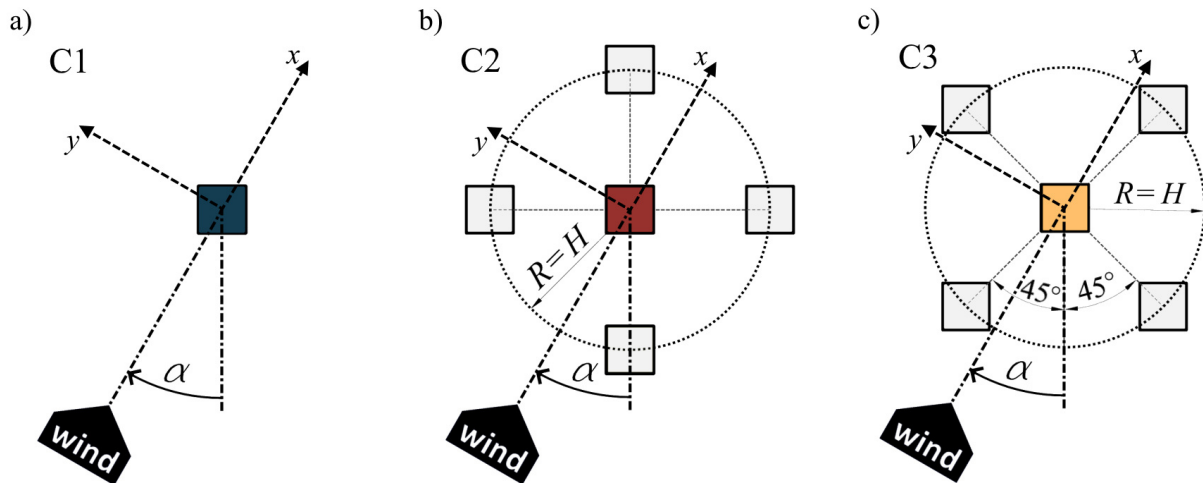


Figure 4.2. Horizontal plane layout of building configurations: (a) C1, (b) C2 and (c) C3.

is analysed only in configuration C1. Regarding wind load, only configurations C1 and C2 are considered due to the availability of experimental data, with the flat-roof model exclusively used.

4.2 Wind tunnel experiments

Experimental results were obtained during the Short-Term Scientific Mission as a part of the WINERCOST COST Action TU1304. A series of experiments were carried out in the ABL wind tunnel of the Ruhr-University Bochum, Germany. This open circuit wind tunnel features a test section measuring 9.3 m in length, 1.8 m in width, and 1.6 m in height. The incident wind profile, defined as the profile at the middle of the turning table in the domain without models of the building (at location $(0, 0)$), was developed by applying the traditional spire-roughness technique (illustration of turbulent elements mounted in the wind tunnel are shown in Figure 4.3(c)). The resulting mean velocity profile is aligned to a power law with an exponent of 0.20 (see Figure 4.8 and 4.9). It is a representative of the terrain category II [50], simulating realistic conditions of the flow around isolated high-rise buildings, which can be used to approximate the flow pattern in urban areas with a dominant high-rise building surrounded by sparse low-rise buildings. The particular arrangement is common on the outskirts of large cities, university campuses displaced from city centres, etc., all representing potential locations for efficient wind energy harvesting.

At the height of the building model (coordinates $(0, 0, H)$), the reference mean wind speed ($U_{ref,EXP}$) is 16 m/s. The reference turbulence intensities in the windward and vertical directions are $I_{u,ref,EXP} = 13\%$ and $I_{w,ref,EXP} = 11\%$, respectively, calculated as:

$$I_u = \frac{\sigma_u}{U_u} \quad I_w = \frac{\sigma_w}{U_u} \quad (4.1)$$

The resulting Reynolds number (Re) in the experiments is $Re \sim 4.2 \cdot 10^5$, based on the $U_{ref,EXP}$ and H .

The experimental study comprised two main types of measurements: wind velocity and surface pressure. Wind velocity was recorded using a hot-wire anemometer operating at a sampling frequency of 2000 Hz. The streamwise and vertical components of the velocity vectors were measured above the centre of the turning table to capture the incident wind profile and at various points (marked in Figure 4.1 with red circles) and heights above the roof of the central building in configurations C1 and C2. The estimated maximum uncertainty for time-averaged streamwise velocity equalled 5.6%, while for turbulence intensities, it reached 9.6% and 9.4% in the streamwise and vertical directions, respectively, based on a 95% confidence interval. These results are used in the validation process.

The surface pressure data were collected using piezoresistive pressure sensors with a frequency of 1000 Hz. Two differential pressure sensors were used: the Honeywell 170 PC and the AMSYS 5812-0001-D-B. Both sensor models measure the voltage difference corresponding to the differential pressures between the model surface and the static pressure within the Prandtl tube. The schematic representation of the Honeywell 170 PC sensor and pressure cells is given in Figure 4.3(a,b), while their exact locations on the roofs and facades are provided in Appendix A. The number of pressure taps in the experiments is very limited, totalling 90 taps overall—26 on the facades (over two rings at heights of $z = 0.5H$ and $z = 0.75H$, with 13 taps per each ring) and 64 on the roof—marked with black and red dots in Figure 4.1(a,b)). The maximum uncertainty of pressure measurements determined from five sets of repeated measurements was estimated to be around 2.5%.

A detailed description of the experimental procedure and the signal processing can be found in a published report [102]. Furthermore, detailed analyses of the velocity and pressure measurements

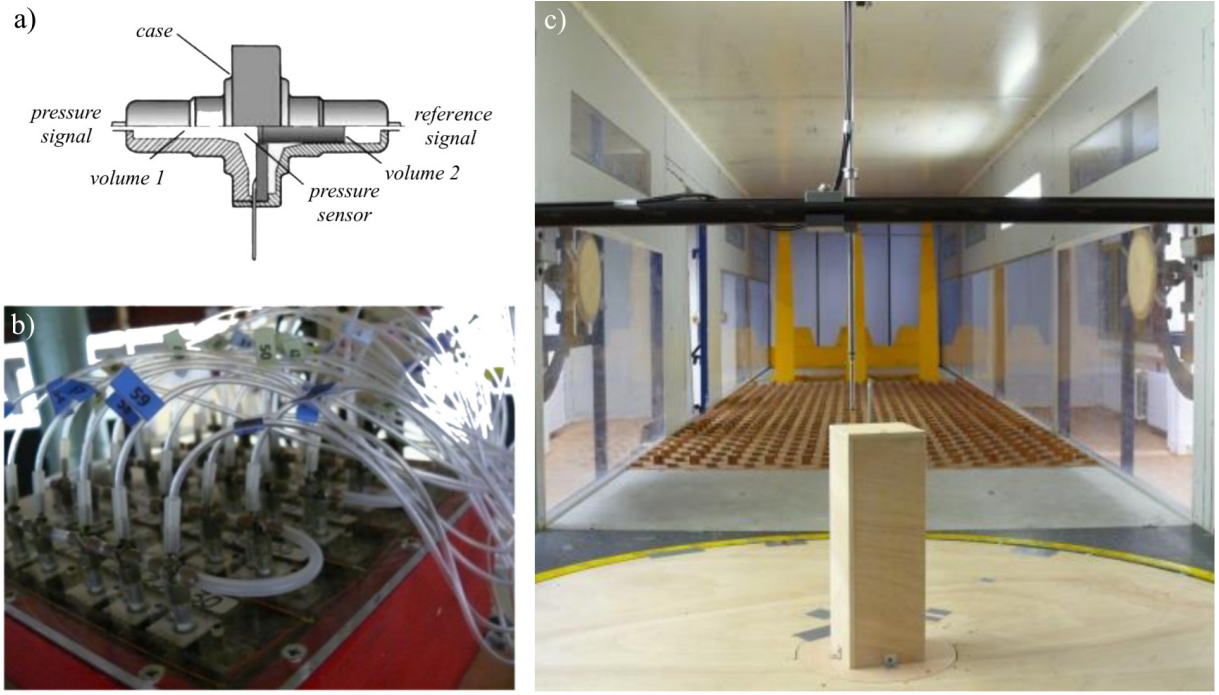


Figure 4.3. Pressure probes: (a) schematic representation of pressure sensor Honeywell 170 PC and (b) pressure cells with pressure tubes; (c) an isolated flat roof high-rise building model (configuration C1) mounted in the ABL wind tunnel at the Ruhr-University Bochum, Germany, adopted from [102].

obtained are published in [43, 74]. In addition, the datasets are publicly available in Mendeley Data [159, 160].

4.3 Numerical simulations

This subsection is divided into three parts. The first part is dedicated to flow modelling, describing the numerical setup adopted for LES (Section 4.3.1). The second part provides information on the computational domain and grid (Subsection 4.3.2). The third part (Subsection 4.3.3) elaborates boundary conditions used.

4.3.1 Flow modelling

The flow dynamic is simulated using the LES method (examined in more detail in Subsection 3.2.2), solving the time-dependent filtered Navier-Stokes equations for incompressible fluid given in Equations (3.6) and (3.7). The filter width is adopted as the cubic root of the volume of the grid cell. In order to mimic the interaction between SGS turbulence and resolved large-scale turbulent motion and overcome the closure problem, the WALE SGS model by Nicoud and Ducros [151] (outlined in Subsection 3.2.2) is used with model coefficients set as $C_e = 1.048$, $C_k = 0.094$ and $C_w = 0.325$. Finally, the coupling between pressure and velocity was facilitated using the PISO (Pressure Implicit with Splitting of Operators) algorithm, initially introduced by Issa [156] (the flowchart of the algorithm is provided in Figure 3.4, Subsection 3.2.3). To ensure accessibility and reproducibility, all numerical simulations were performed using OpenFOAM®, a widely used open-source CFD software platform.

Regarding the numerical schemes used to discretise each term in Equations (3.6) and (3.7), all adopted schemes are second-order accurate. A backward implicit scheme is employed for temporal discretisation. Considering spatial discretisation, the convective, nonlinear term in Equation (3.7) is discretised using the Linear Upwind Stabilised Transport (LUST) scheme. This particular scheme is a fixed blend between linear upwind and centred linear, and in this case, the blend of 0.75 linear and 0.25 linear upwind has been used as recommended by Weller [161]. The scheme was shown to perform well, particularly for LES in complex geometries, offering a good trade-off between low dissipative behaviour and numerical stability [161]. The `fvSchemes` file with discretisation schemes of other terms in Equations (3.6) and (3.7) is given in Appendix B.1. A slight scheme modification is made between wind energy and wind loading simulations, outlined in Appendix B.1.

4.3.2 Domain and grid

The adopted computational domain in all simulations represents a replica of the wind tunnel test section used in the experiments, taking into account turbulence generators. The framework of the problem is creating a numerical wind tunnel, aiming to reproduce an analogous wind flow around the target model of the building obtained in the experiments. This method is known as the wind tunnel replication method described in Section 2.1.

The geometry of the computational domain is illustrated in Figure 4.4. It is a cuboid, $34.5H$ in length with a rectangular across-wind section, $4.5H$ wide and $4H$ high. The cross-section and precursor domain dimensions are retained from the wind tunnel test section as recommended in COST “Best Practice Guidelines” [33]. However, the computational region behind the building is expanded to the distance of $10H$ as suggested by Tominaga et al. [152]. The original geometry of the turbulence generators (castellated barrier, spires and roughness field) is replicated in the driver section (i.e. precursor domain). Figure 4.5 shows both experimental and computational domains.

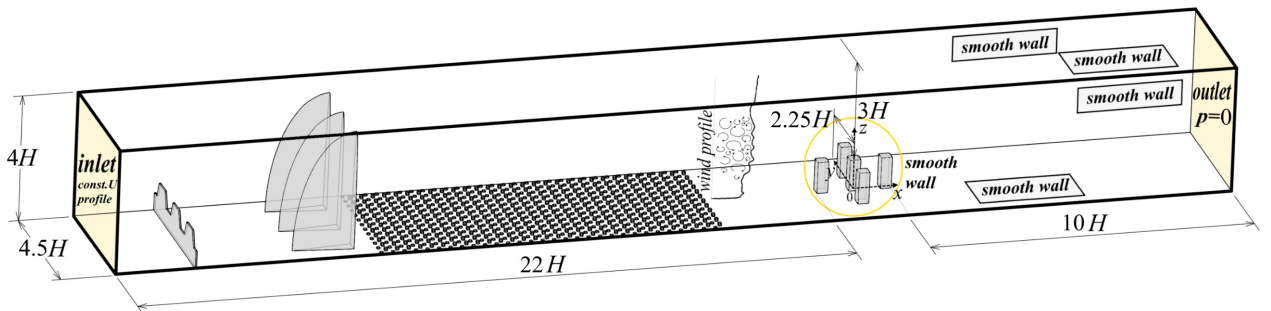


Figure 4.4. The geometry of the domain and boundary conditions, adapted from [41].

Building models and approaching wind angles defined in Subsection 4.1 result in the maximum blockage ratio equal to 2.7% for isolated configuration C1 and therefore remains below 3%, as suggested in [33, 152]. However, this 3% threshold is exceeded in group configurations C2 and C3, with the worst case being the C2 configuration at a 45° wind angle, where the maximum blockage ratio reaches 7.9%. According to the literature, in [162, 163], authors indicated that the permissible blockage threshold for squat models (cubes) or prisms was approximately 8–10%. Since the blockage ratio in the present research remains below 8% in all analysed cases, no further corrections have been made.



Figure 4.5. Wind tunnel test section: experimental setup of the group configuration in the ABL wind tunnel of the Ruhr-University Bochum, Germany, on the left and computational domain for the group configuration related to LES on the right, adapted from [42, 102].

Spatial discretisation of the computational domain is performed using the grid of finite volumes, which are predominantly hexahedrons (over 97%). Grids for all analysed building configurations, as well as the simulations without the building model, are block-structured and created using SnappyHexMesh, a grid generation tool part of the OpenFOAM® open-source software. While the same refinement strategy, based on cell splitting in predefined regions (blocks), is applied across all grids, each grid has specific characteristics. Therefore, they will be reported chronologically in three separate groups chronologically, with these specifics highlighted. The first two groups consist of grids for wind energy assessment. The first group addresses the grids for configuration C1, an isolated building with a flat and decked roof, while the second is dedicated to group configurations C2 and C3. The third group describes grids for C1 and C2 configurations for the wind loading study.

Additionally, Appendix B.2 reports details on creating a grid using snappyHexMesh. It provides basic steps in this process and an example of the snappyHexMeshDict file. Moreover, details of the modelling of the precursor domain grids are reported in B.3.

Group 1: Grid for wind energy assessment - Configuration C1

The initial grid consists of purely cubic cells with edge $\delta/H = 8.75 \cdot 10^{-2}$ to provide a suitable starting point for further refinement. The precursor domain grid is created following the guidelines in [54]. Aiming to preserve as many physical processes as possible and provide the desired wind profile, refinement from zone 1 at Fig. 4.6 has been propagated through the whole domain to height $6B$. Regarding the grid around the building, additional levels of refinement are used in zones 2, 3 and 4, as shown in Fig. 4.6 and reported in Table 4.1. The finest zone 4, in the building nearby, has a cell size of $\delta/H = 5.47 \cdot 10^{-3}$. The resulting grid resolution is higher than the minimum required by Tominaga et al. [152].

Furthermore, at the model walls, a body-fitted structured grid of 15 boundary layers is adopted, with the first layer height $\delta/H = 5 \cdot 10^{-4}$ and an expansion ratio of 1.05, as suggested in [164]. The resulting mean dimensionless wall distance y^+ is around 5 in all cases, while the maximum values are 15 and 12 for the flat and decked roof models, respectively. An example of a similar refinement procedure can be found in [165]. The final grid of the simulation without

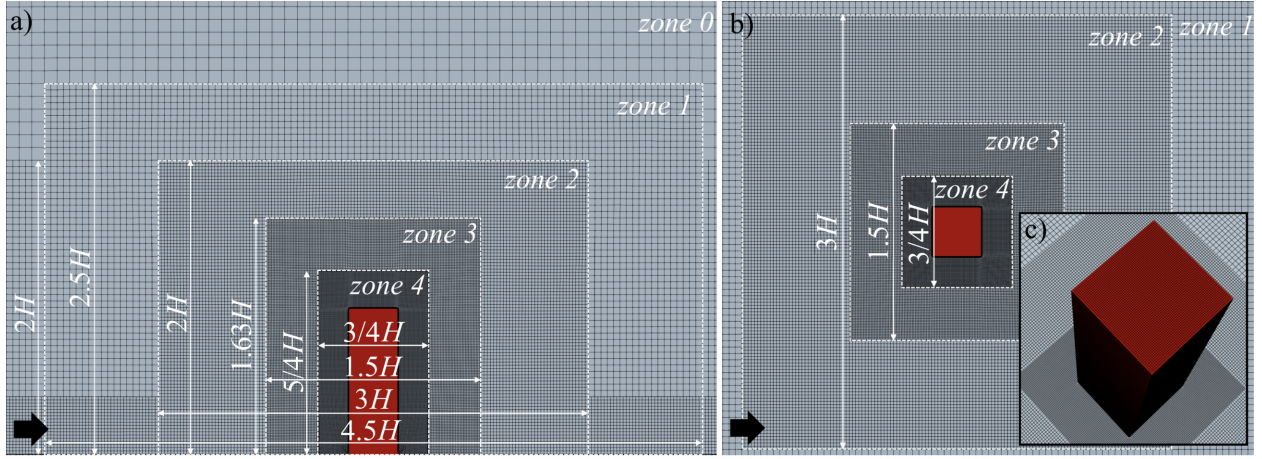


Figure 4.6. The adopted grid around the target building: (a) xz plane through $(0, 0, 0)$; (b) xy plane through $(0, 0.5H, 0)$; (c) three-dimensional view of the building zone, adapted from [40].

Table 4.1. Grid refinement zones around the principal building in C1 configuration for wind energy assessment.

| Zone | Cell size | Upstream | Downstream | Width | Height |
|------|-----------------------|------------------------|------------|-----------------|---------|
| 0 | $0.0875H$ | base grid—whole domain | | | |
| 1 | $0.0437H$ | $-9/4H$ | $9/4H$ | width of domain | $5/2H$ |
| 2 | $0.0219H$ | $-3/2H$ | $3/2H$ | $3H$ | $2H$ |
| 3 | $0.0109H$ | $-3/4H$ | $3/4H$ | $3/2H$ | $1.63H$ |
| 4 | $5.47 \cdot 10^{-3}H$ | $-3/8H$ | $3/8H$ | $3/4H$ | $5/4H$ |

the building’s model contains about $22 \cdot 10^6$ cells, while those with the target building have around $27 \cdot 10^6$ cells.

Group 2: Grid for wind energy assessment - Configurations C2 and C3

Slight modifications in the grid refinement are made in group configurations C2 and C3, compared to C1. Namely, the base grid and the grid in the precursor domain are the same as in configuration C1. The differences occur in the refinement of the region around the principal building. Two additional refinement levels are introduced, resulting in a total of six refinement zones, and, also, the dimensions of the refinement regions (blocks) are changed to better match the velocity field dynamic. All zones are illustrated in Fig. 4.7 for the group configuration in the “cross” shape arrangement (case C2) at 0° , while a table view of details for each refinement zone is given in Table 4.2. Again, like in configuration C1, a body-fitted structured grid of 10 boundary layers is generated on the principal building walls, with an expansion ratio of 1.05. The height of the first layer is $\delta/H = 2 \cdot 10^{-4}$, and the resulting mean and max dimensionless wall distance y^+ on the surface of the principal building are around 1.5 and 5, respectively. A similar refinement strategy is applied in [56]. The final grids of the group configurations C2 and C3 have around $46 \cdot 10^6$ cells.

Group 3: Grid for wind loading study - Configurations C1 and C2

The previous two groups are large grids, above $20 \cdot 10^6$ cells in the C1 configuration and even above $45 \cdot 10^6$ cells in the C2, the group ones. One can notice an increase in cells moving from the first to the second group. It can easily become a trap, entering a cycle of continuous refinement and grid enlargement, moving towards direct numerical simulation and away from the engineer’s

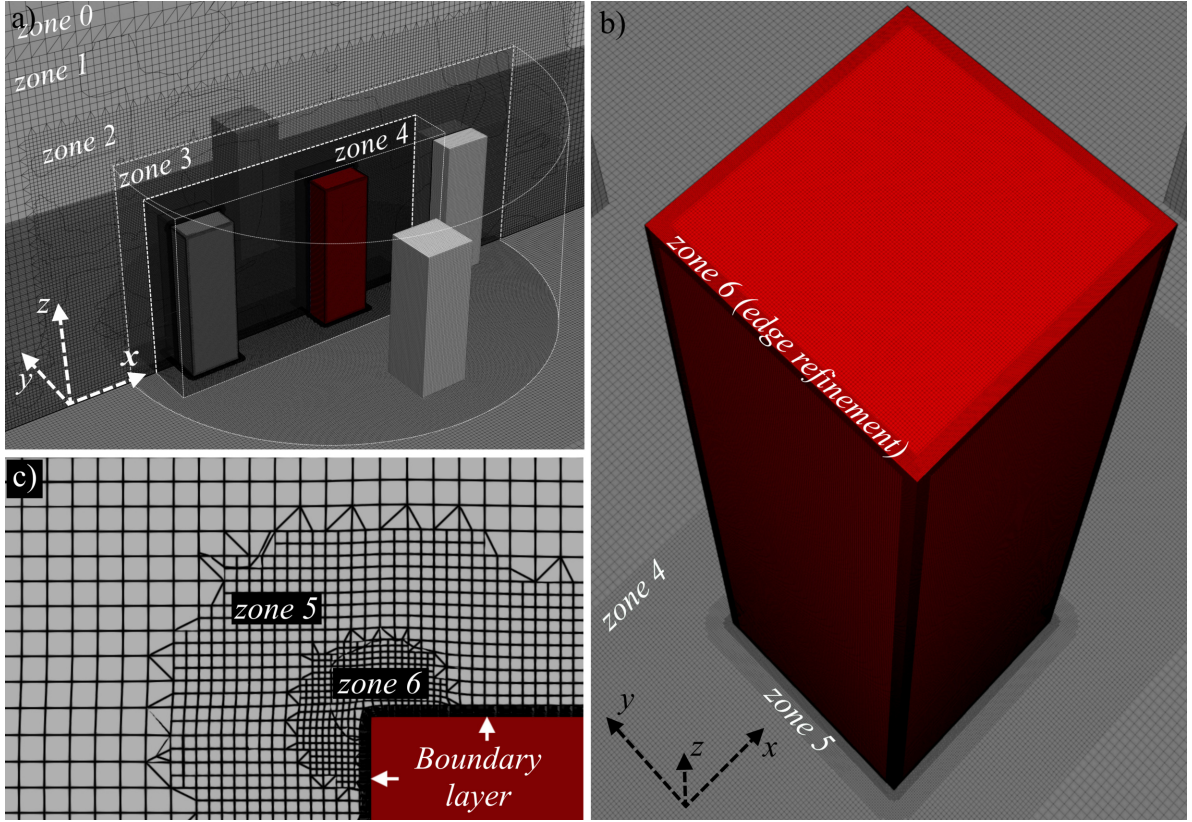


Figure 4.7. Grid adopted around the principal building in case C2 for 0° wind angle: (a) a grid through the vertical central plane; (b) perspective view on the grid on building surfaces and the ground plane near the building; (c) close view of the grid around the building; adapted from [41].

desk as the primary aim. These grids are computationally highly demanding. With available resources, simulating one second takes two to three weeks using 160 cores of an Intel Xeon E5345 @2.33GHz CPU on the High-Performance Computing (HPC) cluster at the Institute of Physics, Belgrade. At this point, the research takes a twist. The decision is made to reduce the number of cells in the grids for the wind loading study. The reasons are decreasing the maximal Courant number and, at the same time, obtaining a longer signal duration, enabling statistical treatment of surface peak pressure.

The cell size of the base grid is almost doubled, compared to the first two groups, and equals $\delta/H = 16.67 \cdot 10^{-2}$. The refinement regions in the precursor domain and around the building are shown in Figure 4.8(b) and correspond to those in the two previous groups. The region around the principal building has five levels of refinement, and the characteristics of each level are reported in Table 4.3. The additional structured, body-fitted grid is applied to the principal building surface with ten boundary layers. The height of the first layer is set to $\delta/H = 2 \cdot 10^{-4}$, and the expansion ratio is 1.05, resulting in an overall height of the boundary layers of $\delta_{all}/H = 2.5 \cdot 10^{-3}$. The maximum dimensionless wall distance y^+ on the principal building's surface is around 5, while it is 1.5 on average. The final grids for the group configurations contain around $10 \cdot 10^6$ cells, which is more than four times smaller grid than in the group configuration for wind energy assessment, the second group. The snappyHexMeshDict file for configuration C2, at 0°, is given in Appendix B.2.

Table 4.2. Refinement zones around the principal building.

| Zone | Cell size | Upstream | Downstream | Width | Height |
|------|-----------------------|--|------------|-----------------|----------|
| 0 | $0.0875H$ | base grid—whole domain | | | |
| 1 | $0.0437H$ | $-9/4H$ | $3H$ | width of domain | $2H$ |
| 2 | $0.0219H$ | $-2H$ | $2H$ | $4H$ | $5.5/3H$ |
| 3 | $0.0109H$ | cylindrical zone, $R = 1.5H$, center at $[0,0,0]$ | | | |
| 4 | $5.47 \cdot 10^{-3}H$ | $-H/3$ ($-4H/3$ in C2) | $2H/3$ | $2H/3$ | $5/4H$ |
| 5 | $2.73 \cdot 10^{-3}H$ | surface refinement around the building—10 rows | | | |
| 6 | $1.37 \cdot 10^{-3}H$ | edge refinement—10 rows | | | |

4.3.3 Boundary conditions

Boundary conditions are chosen in a way that completely mimics the experimental setup in the wind tunnel. Recommendations given in [33, 152] are followed, and a brief sketch of the adopted conditions is provided in Fig. 4.4. All solid surfaces are modelled as smooth walls, including the wind tunnel floor, sides and top, as well as the building surfaces. The outlet is treated as a pressure outlet with a constant relative pressure equal to zero and a zero-gradient boundary condition for the other flow variables. This setup is consistent across all simulations. However, the definition of the inlet velocity is distinct for wind energy and wind loading studies, clearly separated and reported in the following. Aiming to obtain the simulated incident wind profile, an additional LES without the building models but with the same precursor domain and grid topology is performed.

To reduce computational time and speed up the convergence process, the velocity and pressure fields are initialised by mapping the mean fields obtained from LES on a coarser grid for all simulations.

Wind energy assessment

In the simulations for wind energy assessment, a uniform, constant velocity of 15 m/s is prescribed. The imposed inlet velocity entails the incident wind profile shown in Fig. 4.9, at location $(0,0)$. Mean wind speed, $U_{ref,NUM}$, and turbulence intensities $I_{u,ref,NUM}$ and $I_{w,ref,NUM}$ at the building height H are 14.4 m/s, 14% and 12%, respectively. Resulting Reynolds number is $Re \sim 3.8 \cdot 10^5$, based on the $U_{ref,NUM}$ and H .

Additional simulation with the inlet velocity of 8 m/s in the case of the decked roof building at 0° has been conducted to investigate the flow's sensitivity to the change in wind speed. The resulting mean flow pattern matches well for these two cases. Furthermore, a tolerance range of

Table 4.3. Refinement zones around the principal building.

| Zone | Cell size | Upstream | Downstream | Width | Height |
|------|-----------------------|--|------------|-----------------|----------|
| 0 | $H/6$ | base grid—whole domain | | | |
| 1 | $H/12$ | $-9/4H$ | $3H$ | width of domain | $2H$ |
| 2 | $H/24$ | $-2H$ | $2H$ | $4H$ | $5.5/3H$ |
| 3 | $H/48$ | cylindrical zone, $R = 1.5H$, center at $[0,0,0]$ | | | |
| 4 | $H/96$ | $-H/3$ ($-4H/3$ in C2) | $2H/3$ | $2H/3$ | $5/4H$ |
| 5 | $2.73 \cdot 10^{-3}H$ | surface refinement around the building—5 rows | | | |

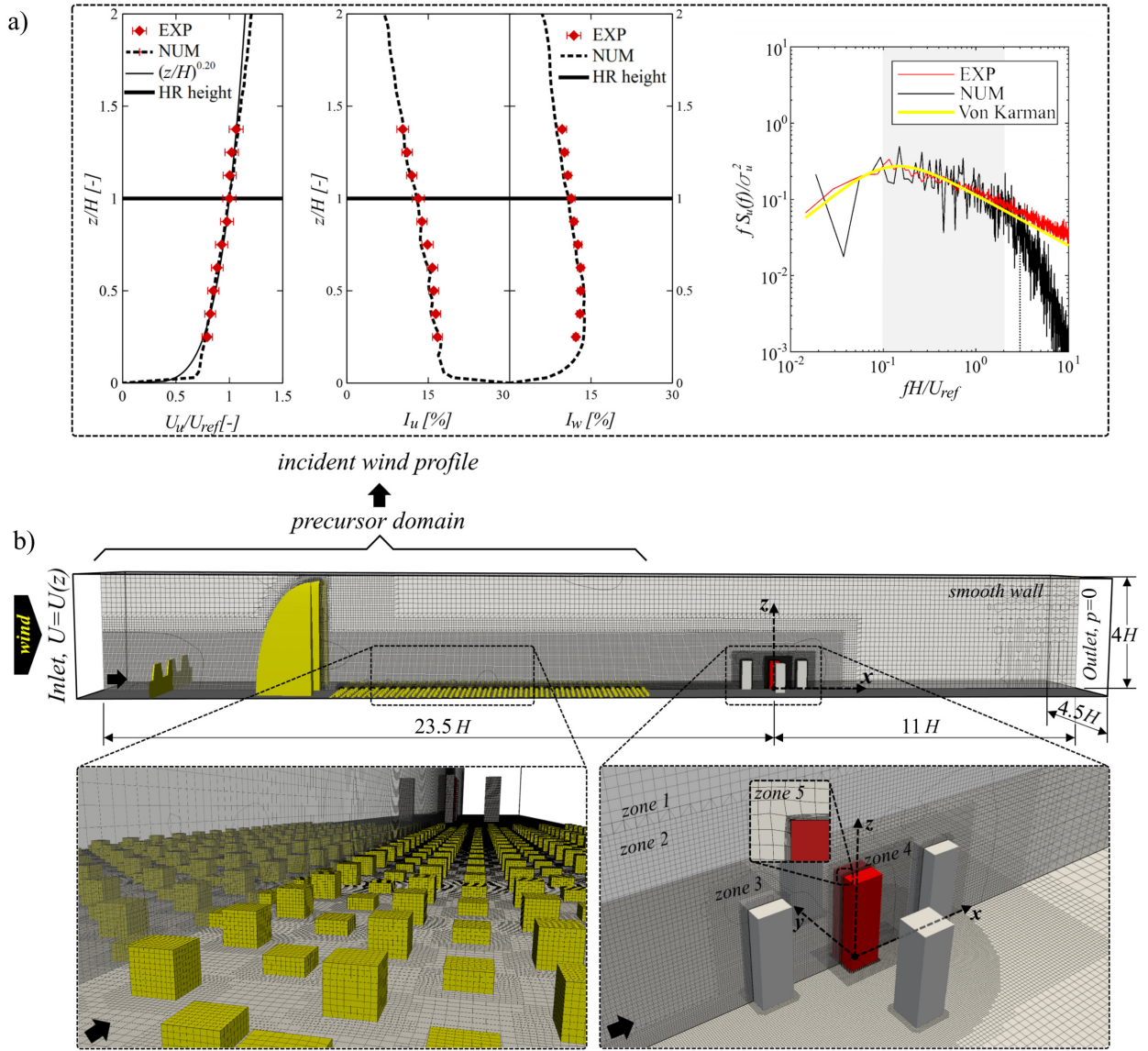


Figure 4.8. (a) Incident wind profile at $(0,0)$: mean velocity in the streamwise direction, turbulence intensity profiles in the streamwise and vertical directions and velocity spectrum at $(0,0,H)$; (b) Geometry of the domain with grid description and marked boundary conditions; adopted from [42].

5%, according to [166], regarding normalised mean velocity above the roof and mean pressure coefficient is accomplished, confirming Re independency in the particular case.

The non-dimensional time step, based on building width B and velocity at the building height $U_{ref,NUM}$, is set to $\Delta t^* = \Delta t U_{ref,NUM}/B = 7.15 \cdot 10^{-4}$ leading to the maximum and mean Courant number in all wind energy assessment simulations equal to 4 and 0.05, respectively.

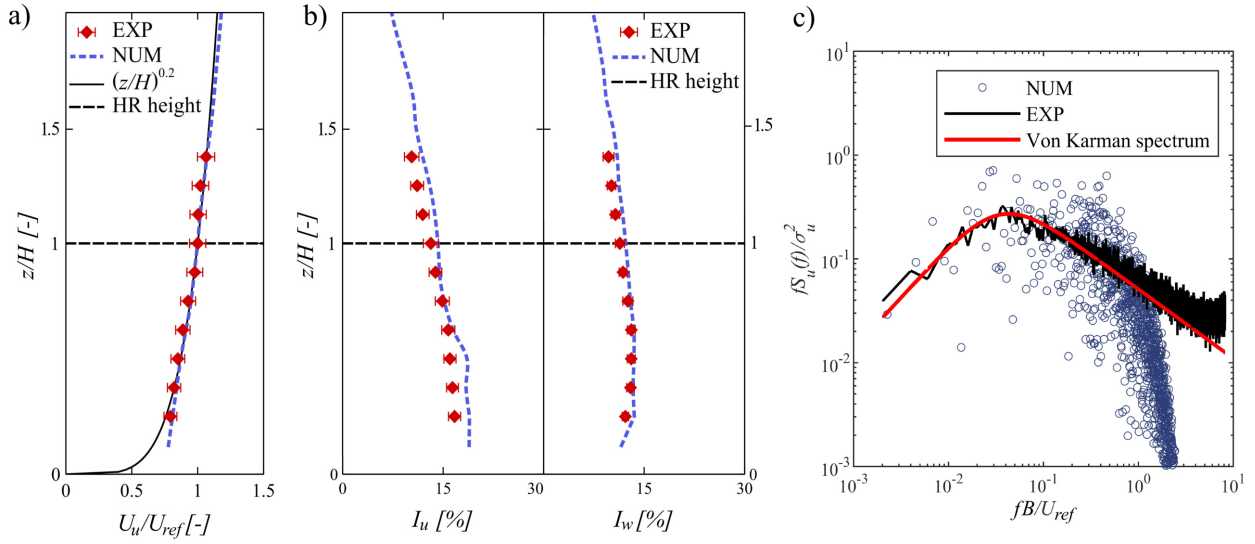


Figure 4.9. Wind profiles at the middle of the turning table for wind energy assessment: (a) streamwise mean velocity component, (b) turbulence intensity profiles in the streamwise (I_u) and vertical (I_w) directions and (c) velocity spectrum at $(0, 0, H)$, adapted from [40].

Wind loading study

In the wind loading study, at the inlet, the experiment's incident mean velocity profile (i.e. without turbulence) is prescribed with a scaled-down velocity of 25% to reduce the Courant number. The change from uniform value to mean velocity profile is made. A detailed comparison of two inlet definitions, as well as two grid refinements in the precursor domain, is given in Appendix B.3. The resulting incident wind profile, considering the mean streamwise velocity component, turbulence intensities in the streamwise and vertical directions and streamwise velocity spectrum at $(0, 0, H)$ are shown in Figure 4.8(a). The reference flow characteristics in the LES are: $U_{ref,NUM} = 12.6$ m/s, $I_{u,ref,NUM} = 13\%$ and $I_{w,ref,NUM} = 11\%$. Reynolds number in the LES is $Re \sim 3.3 \cdot 10^5$, based on the $U_{ref,NUM}$ and H . The non-dimensional time step $\Delta t^* = \Delta t U_{ref,NUM}/H = 3.2 \cdot 10^{-4}$ is adopted, ensuring the maximal Courant number below 1.5.

5 Validation

Validation is a vital and indispensable part of any numerical modelling. In this research, the LES results are compared against the data from the wind tunnel experiments described in Section 4.2. At the very beginning, Section 5.1 presents the convergence of the numerical simulations, focusing specifically on wind velocity and surface pressure. This is assessed through the convergence of higher-order statistical moments of velocity (up to the second order) and pressure (up to the fourth order). Next, two stages of the validation process are reported. The first stage involves validation of the incident wind profile, provided in Section 5.2, to ensure that the flow at the building location is adequately modelled, which is one of the biggest challenges in LES. The second stage includes validation of the wind flow around the central high-rise building for six LES cases: configuration C1 with flat and decked roof building model and configuration C2 with only flat roof building models, all at 0° and 45° . It compounds the analyses of the wind profiles above the roof, processed in Section 5.3, and surface pressure prediction at the building's facade and roof in Section 5.4.

5.1 Monitoring convergence

To assure that the duration of the numerical simulations is large enough to provide converged velocity and pressure field, as well as their first and second-order statistics, a common approach of tracking residuals described in [167] is used. This approach has been effectively utilised in numerous numerical studies, including those in [126, 165, 168]. The procedure described in [168] is followed in this research with certain modifications, according to [165].

The core of the method is dividing the recorded velocity or pressure signal into n time windows (T) and calculating related statistics for increasing extents of the sampling window nT . This is accompanied by monitoring the percentage residual that is defined for the i -th sampling window as $\phi_{res}^i = |\phi_{iT} - \phi_{(i-1)T}| / |\phi_{iT}| \cdot 100$ [%]. The adopted time window T represents the length of ten integral time scales ($T = 10t^* \approx 10T_{ux}$). T_{ux} is determined from the time auto-correlation function at the building's height in the simulation without the building.

Regarding the convergence of the incident wind profile, the velocity signal recorded at model height ($z = H$) is used to check its first and second-order statistics. The graph in Figure 5.1 provides information about the convergence of the streamwise velocity component. Throughout the first $100t^*$, a significant drop in residuals to less than 5% is notable. A steady decrease is further observed, reaching values lower than 1% after $220t^*$.

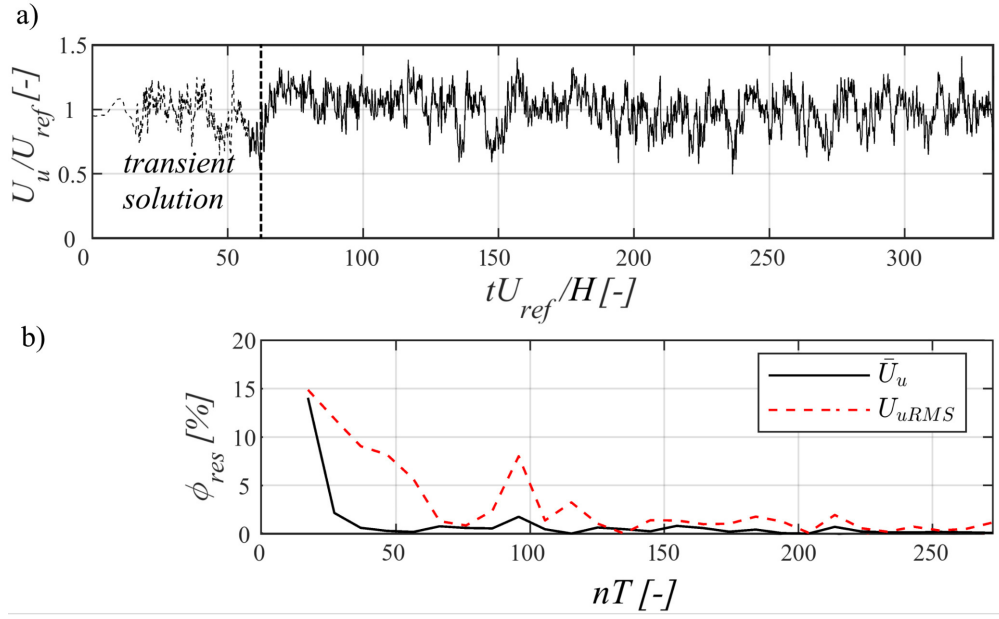


Figure 5.1. The streamwise velocity component at $(0, 0, H)$: (a) time history and (b) convergence of related statistics (adopted from [40]).

The same convergence check is repeated for the velocity signals above the roof of the central building in simulations with building models, as well as the pressure signals collected at the roof surface, for both wind energy assessment simulations and wind loading study. Figures 5.2 and 5.3 illustrate the convergence checks in the C2 case, at 0° , simulation for wind energy assessment. The location of velocity recording is placed just above the rooftop point P20, positioned at $(-0.33B, 0, 1.05H)$ (Figure 5.2), while, for pressure, point P20 is chosen (Figure 5.3). The first $60t^*$ of both signals (velocity and pressure) are removed from the analysis as a transient solution. Pressure is analysed in terms of pressure coefficient C_p defined as:

$$C_p = \frac{p - p_\infty}{0.5\rho U_{ref}^2} \quad (5.1)$$

with p_∞ denoting the free-stream pressure, set to the value of 0 in the LES, and ρ the air density.

Similar results are obtained for the statistics of the streamwise velocity component and surface pressure coefficient. A significant drop of the residuals of first- and second-order velocity and pressure statistics, below 2%, is noted after $150t^*$. Therefore, the duration of all simulations for wind energy assessment is kept around $300t^*$, excluding the first $60t^*$.

Regarding the numerical simulations for the wind loading study, a more robust convergence check of the pressure signal is performed. Namely, the stationarity of the pressure signal is a requirement from the employed statistical methods and is examined consistently from both experiments and numerical simulations. According to [129], a model's duration is considered optimal when it is the shortest time necessary for all full-time histories to pass a stationarity (or convergence) test satisfactorily and when the peak pressure coefficient values have reached a stable state within an acceptable uncertainty range. In light of this, the stationarity test of the surface pressure signals in the wind loading study is conducted using the previously described method of tracking residuals through analysis up to the fourth statistical moment of C_p .

Figure 5.4 illustrates the stationarity test of the pressure coefficient (C_p) for the C1 configuration at location point P4 $(-0.45B, 0, H)$, under a 0° wind angle, but obtained results are also verified at various other locations, wind angles, and configurations. The figure includes the mean (\bar{C}_p),

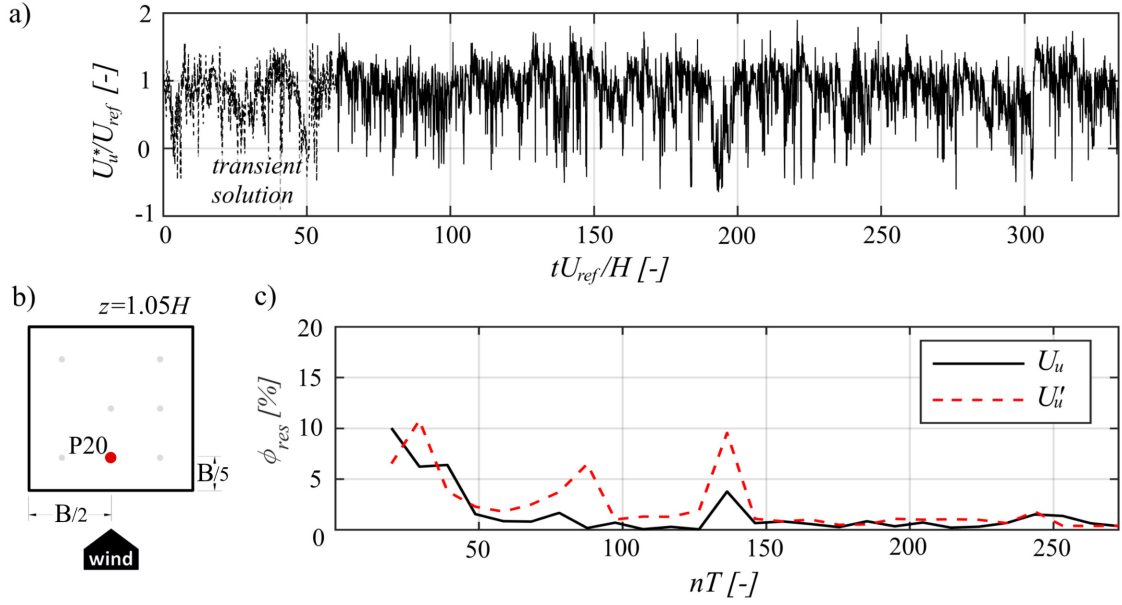


Figure 5.2. Convergence of the velocity statistics above the roof in the C2 case at 0° : (a) time history of the normalised streamwise velocity component (U_u^*/U_{ref}) above point P20 at height $z = 1.05H$, (b) sketch of the roof with marked location of point P20 and (c) percentage residuals of the velocity first (U_u) and second (U'_u) order statistics.

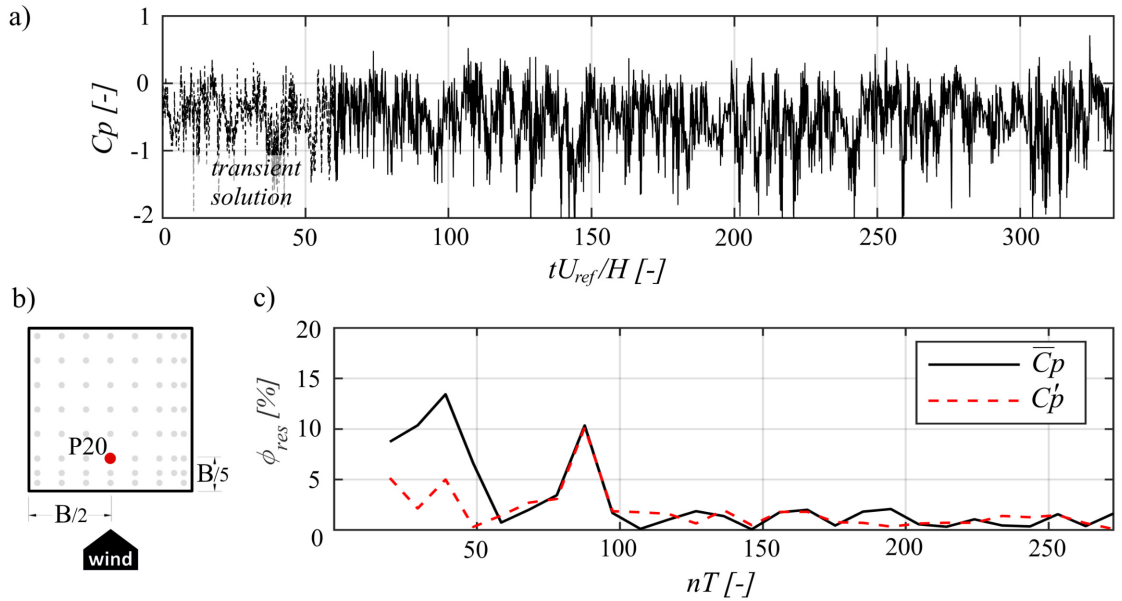


Figure 5.3. Convergence of the surface pressure statistics on the roof in the C2 case at 0° : (a) time history of the surface pressure coefficient (C_p) at the pressure tap P20, (b) sketch of the roof with marked location of point P20 and (c) percentage residuals of the pressure first (\bar{C}_p) and second (C_p') order statistics.

root mean square—RMS (C_p''), skewness (C_p^s), kurtosis (C_p^k) and monitoring of the minimum C_p (\check{C}_p). Study in [167] recommended an alternative calculation of residuals for statistical moments close to zero, suggesting the use of the simple difference ($\phi_{res}^{*i} = |\phi_{iT} - \phi_{(i-1)T}|$), without normalisation by ϕ_{iT} . This modification is particularly relevant for tracking the residuals of the third statistical moment, or skewness, due to its typically small values and is implemented in this research.

In Figure 5.4(a), for the experimental measurements, a noticeable decline in residuals below 10^{-2} is observed after $600t^*$ for mean and RMS values, whereas kurtosis shows occasional spikes above this threshold until $1400t^*$. Skewness follows a similar pattern. Given that residuals below 10^{-2} are challenging to achieve, a residual error threshold of 10^{-2} is set for stationarity criteria, with $600t^*$ being the minimal signal length meeting this criteria. Analysis of \check{C}_p directly derived as the minimal signal value indicates stability after $1400t^*$. A detailed view of the first $600t^*$ from the experimental measurements is provided in Figure 5.4(b).

Figure 5.4(c) shows corresponding LES results at the same location. Residuals below 10^{-2} for all four statistical moments are reached after a duration of $600t^*$ (from $60t^*$ to $660t^*$, the first $60t^*$ is excluded as a transient solution), representing a 75-minute equivalent full-scale (in the rest of the dissertation, the abbreviation EFS will be used to refer to the equivalent full-scale time) event. Therefore, this duration is maintained across all numerical simulations. However, increasing the residual limit from 10^{-2} to $2 \cdot 10^{-2}$ results in meeting the stationarity criteria after a duration of $300t^*$ for all statistical moments of C_p except the third one. Moving it to $5 \cdot 10^{-2}$, stationarity criteria is fulfilled after only $150t^*$. Given the high cost associated with long-duration pressure signals, particularly in numerical simulations, the peak pressure values obtained for a specific time window should be considered with corresponding uncertainty bounds [132]. Consequently, durations of $150t^*$, $200t^*$, $300t^*$, $400t^*$ and $600t^*$ after the transient solution, equivalent to $T_{full} = \{18.5, 25, 37.5, 50, 75\}$ min EFS, will be used for evaluating peak pressure coefficients with uncertainty quantification, as a part of wind loading study in Chapter 8.

All wind loading simulations are run for $700t^* = 700tU_{ref,NUM}/H$, and the first $60t^*$ is excluded from the statistics as a transient solution.

5.2 Incident wind profile

To check the incident wind profile, the domain shown in Figure 4.5 has been tested without the building model. A sampling of the results over height (z) has been performed at the building location, i.e. at the centre of the turning table $(0, 0)$.

Figures 4.9 and 4.8(a) show the resulting profiles of mean streamwise velocity and turbulence intensities from two grid refinements of precursor domain (see Appendix B.2 for more details) for wind energy assessment and wind loading study, respectively. The profiles are compared with the experimental ones. In addition, the uncertainty estimates of the experimental data, corresponding to a 95% confidence interval, have been considered and marked with vertical ticks from both marker sides. Graphs for both grid refinements indicate a good agreement between experimental and numerical data. A slight discrepancy of around 10% is noticeable in streamwise turbulence intensities on the grid for wind energy assessment at elevations below $z = H/2$.

Considering the velocity spectra at $(0, 0, H)$, presented in Figures 4.9(c) and 4.8(a), both numerical and experimental ones fit well with the Von Karman spectrum [169]. In the high-frequency range, energy in the LES drops as expected due to the filtering. Special attention is paid to the results from the wind loading study simulations in Figure 4.8(a) and frequency range of $0.1 < fH/U_{ref} < 2$. The particular range is marked as a crucial part of the spectrum for pressure fluctuations according to [129, 170]. Moreover, the reduced frequency of 3 has been the cut-off frequency in the present study at the high-frequency range of the velocity spectrum. It would be more thorough that the quality assessment of LES regarding the share of the resolved

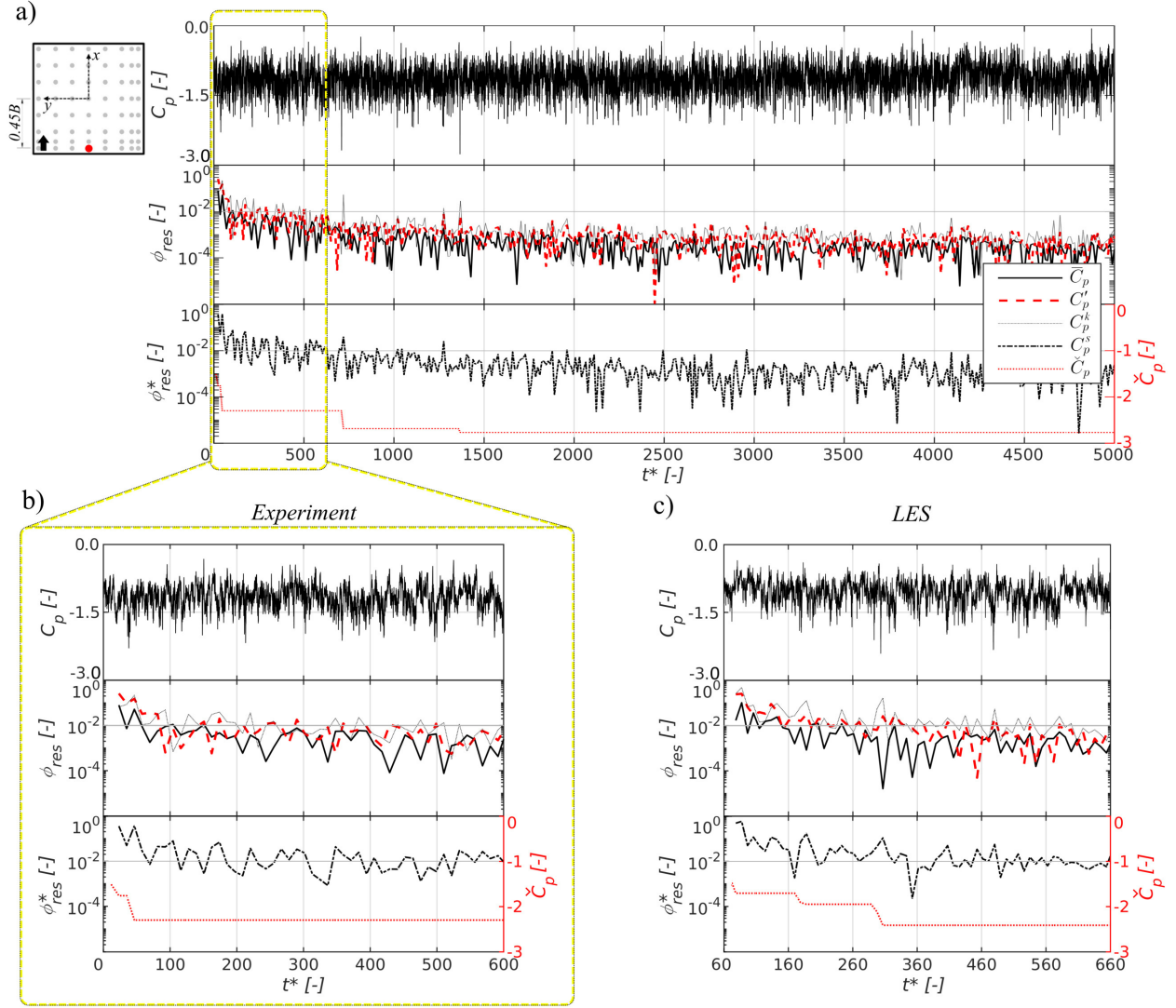


Figure 5.4. Stationarity test of the pressure signal, including the mean (\bar{C}_p), RMS (C_p''), skewness (C_p^s), kurtosis (C_p^k) and minimum C_p (\check{C}_p) on the roof for the C1 configuration at location $(-0.45B, 0, H)$ under the 0° wind angle: (a) whole signal from the experiments, (b) detailed view of the first $600t^*$ from the experiments and (c) corresponding LES results.

part in total turbulent kinetic energy proposed by Pope [34] is checked, but the averaged SGS turbulent kinetic energy field was not calculated during the numerical simulations.

5.3 Wind flow above roof

Wind flow above the roof of the central building is investigated in terms of mean velocity vector components and turbulence intensities in windward and vertical directions. Profiles are normalised with reference values from both numerical simulations (subscript *NUM*) and experiments (subscript *EXP*). First validation of the isolated building (configuration C1) with the flat and decked roof is examined, and then the group configuration C2. Results from simulations for wind energy assessment are presented, while the same validation has been conducted for simulations for wind loading study with comparable results.

Figures 5.5 and 5.6 provide a comparison of profiles above two points, P20 and P36 for the flat roof and P50 and P58 for the decked roof, over the central line in two building configurations at 0° and 45° wind angles. In configuration C1, both flat and decked roofs are analysed (Figure 5.5), while in configuration C2, only the flat roof is considered. The lighter tone of markers at graphs in Figure 5.5(b,c) illustrates the sampling locations with streamwise turbulence intensity higher than 30% in the experiments. The following data cannot be treated as reliable due to the inaccuracies in hot-wire measurements [171]. In Figure 5.6, these locations are excluded from the graphs. Nevertheless, such high values of turbulent intensities confirm the existence of a separated flow.

Considering the C1 configuration, velocity profiles from the numerical simulations in Figure 5.5(b) agree well with the experimental results, especially for the flat roof cases. For the particular roof type in the streamwise direction, a nearly perfect match is achieved above both points at 0° , whilst at 45° , a slight mismatch occurs above point P20. Specifically, the along-wind velocity is over-predicted by the numerical simulations at higher locations for approximately 10%. Regarding the decked roof model, a gradual increase in along-wind velocity for both wind angles is notable at higher locations, reaching the maximum discrepancy of around 15%. Profiles in the vertical direction fit well with the experimental ones in all four cases.

As far as the turbulence intensities are concerned, the modelled levels in the streamwise direction are a bit higher than the experimental ones. Such discrepancy is observed in the vicinity of the roof. Namely, a slight shift in the vertical direction of the whole profile is noticeable above almost all points compared to the experiments (see Figure 5.5(c)). It suggests a slight increase in the height of the separation zone. Again, in the vertical direction, almost no mismatch takes place.

Results for configuration C2, given in Figure 5.6 show a similar trend regarding the velocity profiles as for the C1 configuration. A good match between the numerical and experimental profiles in both directions above points P20 and P36 is achieved. However, the results of turbulence intensities above these points show the discrepancy.

At 0° , numerical simulations tend to overpredict the streamwise turbulence intensities by an average of around 22%, with a slightly lower overprediction of around 16% in the vertical direction. A similar pattern was observed in the C1 case with the isolated building but with a lower discrepancy of up to 15% in both directions. The same trend is observed at a 45° wind angle, where turbulence levels near the rooftop are also overpredicted by LES, while, at elevations exceeding $z = 1.1H$, they perfectly match the experimental data in both the streamwise and vertical directions.

There is an apparent counter-intuition between the overestimation of turbulence intensities above the roof in LES and the simultaneous underestimation of the high-frequency flow component (as shown in Fig. 4.9(c) in the simulation without the building model, at $(0, 0, H)$). The underestimation of the high-frequency flow component is a well-known limitation of the LES methodology. Yet, it is interesting to note that the incident turbulence intensity profiles illustrated in Fig. 4.9(b) align flawlessly with the experimental data at building height despite the missing part of the spectrum. This may suggest that the overestimation of turbulence intensities above the roof in simulations with building models can be attributed to the modelling of more complex flow around the buildings compared to the flow in the domain without the building model. In particular, the flow above the roof is dominated by separation, and the numerical prediction of turbulence intensity profiles suggests a slight increase in the size of the separation zone compared to the experiments.

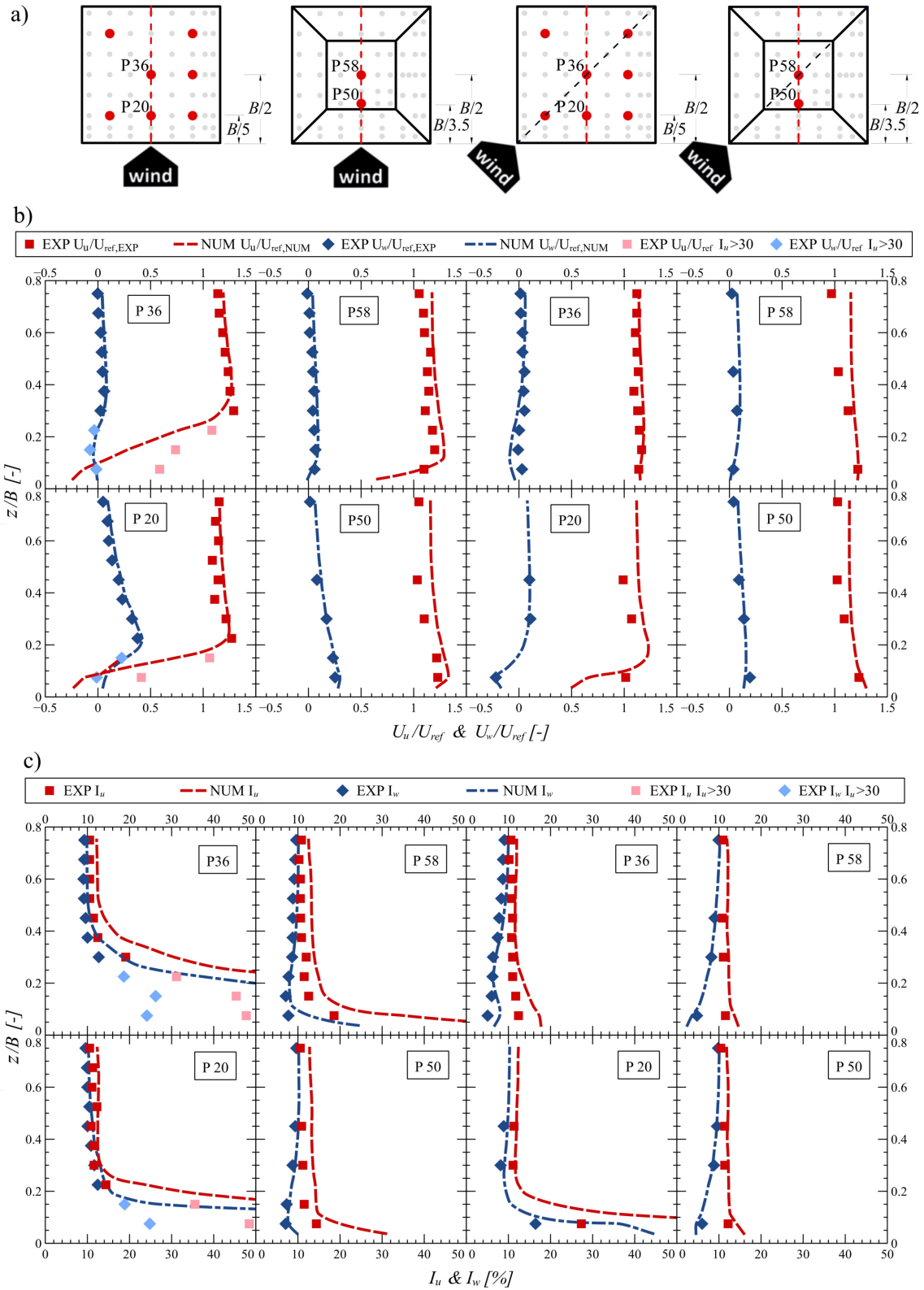


Figure 5.5. Comparison of experimental and numerical results: (a) outline of the roof with marked points of pressure (grey and red spots) and velocity (red spots) measurements; the central line is marked with the dashed red line, while the blue one represents the wind direction; (b) the velocity and (c) turbulence intensity profiles in streamwise and vertical directions above points on the central line.

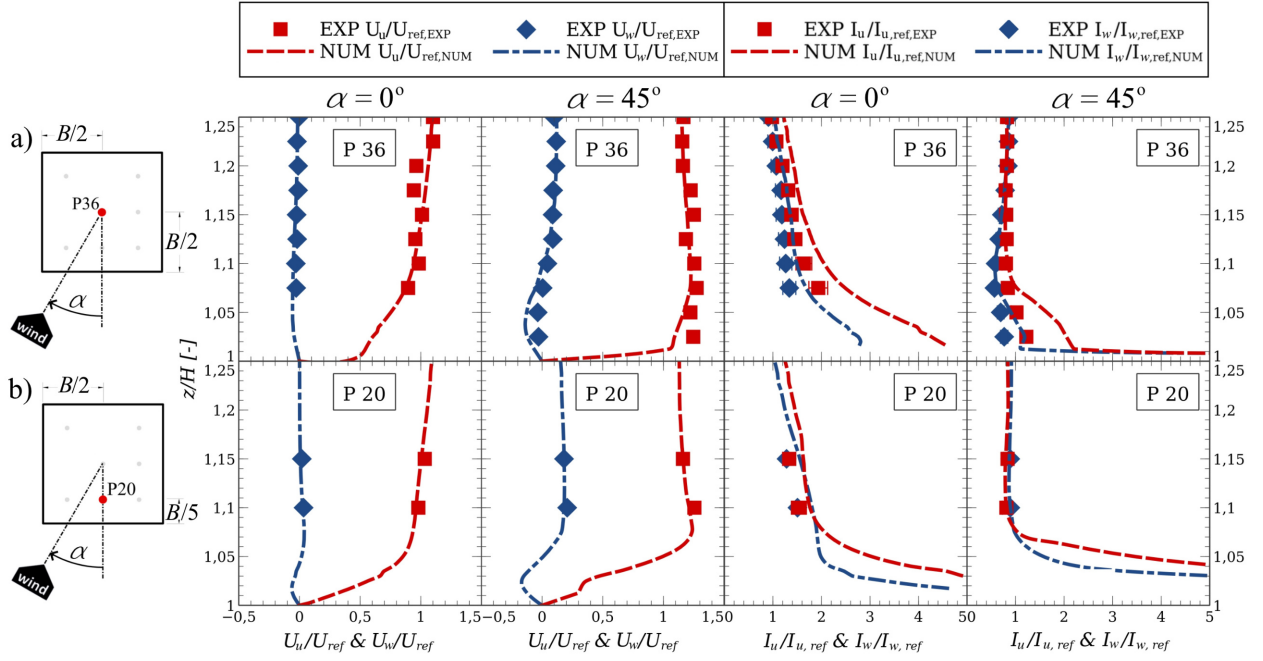


Figure 5.6. Validation of the flow above the roof in the C2 case, at 0° and 45° , by comparing experimental (*EXP*) and numerical (*NUM*) results: the mean velocity and turbulence intensity profiles in streamwise and vertical directions above two points (a) P20 and (b) P36.

Furthermore, when considering the C1 and C2 configurations, an even higher discrepancy in turbulence intensity profiles is observed in the group arrangement (C2). Specifically, the complexity of the flow is here related to the accuracy of predicting the shear layer flow, which develops as the flow interacts first with the upstream building and then with the principal building in the wake. Further investigation can be conducted by adjusting modelling parameters in LES, such as the SGS model.

Overall, there is an acceptable agreement between the numerical and experimental data regarding the first- and second-order velocity statistics for both configurations and approaching wind angles. The mean velocity profiles show an almost perfect match, with certain deviations in the streamwise direction, which do not exceed 15%. The turbulence intensities are overpredicted by approximately 20% on average, in both directions with LES, but these results are considered satisfactory given the uncertainty of the experimental data, which is around 10%.

5.4 Surface pressure statistics

To investigate the surface pressure prediction in LES, comparisons with the experiments of the mean (\bar{C}_p) and RMS (C_p'') values of pressure coefficient C_p are made. Scatter plots in Figures 5.7 and 5.8 demonstrate results for wind energy assessment simulations. Experimental data from 64 pressure taps distributed over the roof and 26 on the facade, shown in Figure 5.5(a), are plotted along the horizontal axis, while corresponding numerical data are plotted along the vertical axis. The perfect match between the modelled and observed values indicates a red 45° line. Furthermore, zones of difference less than 10%, 20% and 30% are highlighted in plots. Complementary to the graphic presentation in Figure 5.7 for configuration C1, a table view of tolerance ranges is given in Table 5.1 with the Mean Normalised Bias (MNB) included. For configuration C2, tables with performance metrics are already included in Figure 5.8.

The MNB is a measure of the average relative error between numerical and experimental data, calculated as follows:

$$MNB = \frac{1}{N} \sum_{i=1}^N \left(\frac{q_{i,NUM} - q_{i,EXP}}{q_{i,EXP}} \right) \cdot 100[\%] \quad (5.2)$$

where N is the number of pressure taps, and $q_{i,NUM}$ and $q_{i,EXP}$ are corresponding numerical and experimental data. It is used as an index that can synthetically characterise the scatter plots [165].

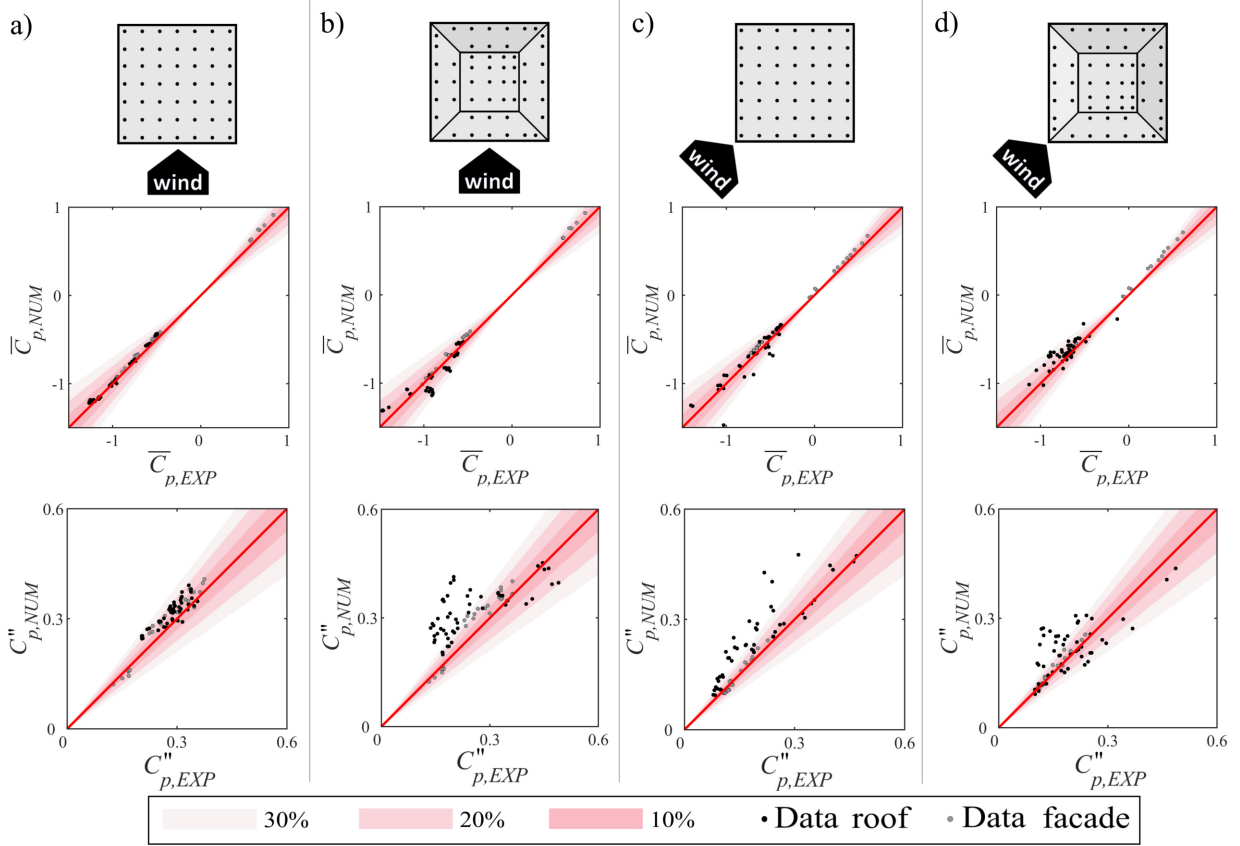


Figure 5.7. Scatter plots of the mean and RMS values of pressure coefficients for configuration C1, simulations for wind energy assessment: at 0° wind angle for flat (a) and decked (b) roof, and 45° for flat (c) and decked (d) roof.

Table 5.1. Performance metrics for the pressure coefficient for configuration C1, simulations for wind energy assessment.

| Performance metrics [%] | Flat roof building | | | | Decked roof building | | | |
|----------------------------|--------------------|---------|-------------|---------|----------------------|---------|-------------|---------|
| | 0° | | 45° | | 0° | | 45° | |
| | \bar{C}_p | C_p'' | \bar{C}_p | C_p'' | \bar{C}_p | C_p'' | \bar{C}_p | C_p'' |
| 10% tolerance | 77.33 | 46.67 | 45.33 | 45.33 | 47.78 | 27.78 | 46.67 | 44.44 |
| 20% tolerance | 97.33 | 90.67 | 84.00 | 60.00 | 86.67 | 51.11 | 74.44 | 63.33 |
| 30% tolerance | 100.00 | 100.00 | 86.67 | 64.00 | 100.00 | 62.22 | 90.00 | 72.22 |
| <i>MNB</i> | 3.59 | -9.21 | 3.93 | -18.47 | -0.30 | -29.12 | 5.97 | -13.35 |

Analysing the results in Figure 5.7 for the C1 configuration impact of the complexity of the roof geometry on numerical prediction of surface pressure coefficient is revealed. Considering the mean pressure coefficients, LES results agree well with the corresponding experimental ones. At 0° , for both flat and decked roof cases, all points fall within a 30% tolerance range. At 45° ,

approximately 90% of the points are within the specified range. Additionally, the simulations for the flat roof achieve better predictions than those for the decked roof at the same wind angles. The MNB values are lower than 6% and positive, indicating a slight tendency of the numerical models to underestimate the mean surface pressure.

The second-order pressure statistics are more difficult to predict. Hence, the differences in the C_p'' pressure coefficients are more pronounced. At 0° , all points are in the 30% tolerance range only in the flat roof case. In other cases, it is significantly smaller. For the same roof type at 45° , it is 64% of points, whilst for the decked roof, 62% and 72% of points at 0° and 45° , respectively. The same tendency is reflected in the MNB values. Both minimum and maximum values occur at 0° , minimal -9.2% for the flat roof model, whereas maximal -29.1% for the decked roof. The negative sign of the MNB depicts the overestimation of the RMS pressure coefficient, mainly on the roof. Such behaviour can be addressed to the roof's more complex geometry than the flat roof case, resulting in second-order statistics being more challenging to predict numerically. Another explanation may lie in the y^+ values. Achieving the maximum $y^+ \sim 5$ at the building surface may lead to a better match of the second-order statistics, as this represents the upper bound of the linear sublayer [172]. Based on this study, the consistent mesh topology results in different tolerance ranges with respect to the experimental measurements. It is important to notice that all simulations have similar y^+ values, which may indicate that different flow features need different mesh sensitivity. Nevertheless, a good fit is achieved for the flat roof at 0° and satisfying for others. Furthermore, the acceptable level of agreement between numerical and experimental results is obtained compared to the results in [165].

Pressure statistics for group configuration C2 are given in Figure 5.8. Considering the 0° wind angle, the numerical and experimental values of the mean pressure coefficient coincide very well, as in the C1 configuration. It is important to note that such a result is obtained even though most of the values are relatively small and concentrated around 0. This means that even the slightest disagreement could result in a significant per cent deviation. Yet, more than 90% of the data falls within the range of less than 20% discrepancy. In addition, the error represented by MNB is low, 2.13%. At the 45° wind angle, there is a comparable level of agreement between experimental and LES data, mirroring the results observed at 0° . Specifically, for the mean pressure coefficient \bar{C}_p , 73% of the data yields a discrepancy of less than 20%, while 90% of the data fits within a 30% discrepancy range.

When the RMS of the pressure coefficient is analysed, at 0° , 67% of numerical results have a deviation from the experimental ones of less than 20%, while 97% is in a range of up to 30%. The absolute value of the MNB is higher compared to the result for \bar{C}_p , and the negative sign expresses the tendency of LES to overestimate the C_p'' . The obtained results show the link between the velocity and pressure second-order statistics. Namely, the RMS of the pressure coefficient is more sensitive to the inaccuracies in the flow prediction, and the overestimation noticed in turbulence intensity profiles is reflected in the C_p'' values as well. The same trend is noticed in the C1 configuration for the flat roof building model. A similar level of accuracy is achieved at a 45° wind angle.

Overall, considering simulations for wind energy assessment, a satisfactory agreement between numerical simulations and experiments is achieved in terms of pressure statistics. The discrepancy is kept within the limits of the maximal absolute MNB values less than 6% for mean and 30% for RMS of the pressure coefficient, having similar values as reported in [165].

The validation of the surface pressure statistics on the roof for simulations for the wind loading study is summarised in Table 5.2. The mean (\bar{C}_p) and RMS (C_p'') of the pressure coefficients are

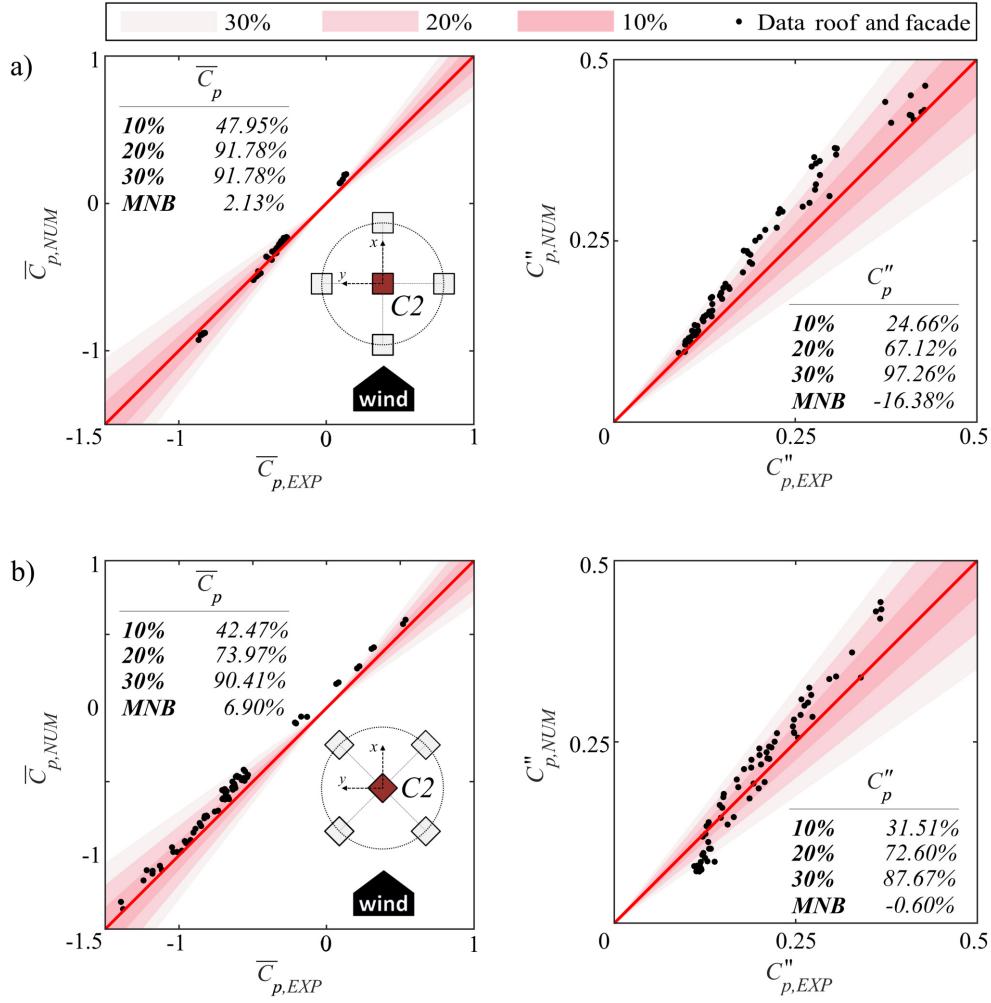


Figure 5.8. Scatter plots of the mean and RMS values of the pressure coefficient for the C2 configuration, simulations for wind energy assessment: comparison of the experimental (*EXP*) and numerical (*NUM*) results at (a) 0° and (b) 45°.

examined for the 75-minute EFS event. Results across both configurations and approaching wind angles in Table 5.2 report a very good match between experimental and numerical data on both \bar{C}_p and C''_p . Nearly 100% of the numerical results fall within a range of up to 30%, with over 80% of the results showing a discrepancy of less than 20%. An exception is noted for configuration C2 at 0° wind angle, where performance metrics for \bar{C}_p are notably lower. It is attributed to the relatively small values of \bar{C}_p on the roof for this case, which are concentrated around 0. Consequently, even minor disagreements between results lead to significant per cent deviations. In terms of the effects of the approaching wind angle, a slightly lower performance in predicting C''_p is observed at 45° compared to 0°. Compared to the results for wind energy assessment simulations, the performance metrics obtained for first- and second-order pressure statistics align with those reported in Table 5.1 and Figure 5.7.

Table 5.2. Performance metrics of the mean and RMS of pressure coefficients for the 75-minute EFS event for configurations C1 and C2, simulations for wind loading study.

| Perf. metrics [%] | C1, $\alpha = 0$ | | C2, $\alpha = 0$ | | C1, $\alpha = 45$ | | C2, $\alpha = 45$ | |
|----------------------|------------------|---------|------------------|---------|-------------------|---------|-------------------|---------|
| | \bar{C}_p | C_p'' | \bar{C}_p | C_p'' | \bar{C}_p | C_p'' | \bar{C}_p | C_p'' |
| 10% tolerance | 83.67 | 61.22 | 0 | 81.63 | 40.82 | 42.86 | 22.45 | 55.1 |
| 20% tolerance | 100 | 93.88 | 14.29 | 93.88 | 89.8 | 71.43 | 81.63 | 85.71 |
| 30% tolerance | 100 | 100 | 51.02 | 100 | 100 | 81.63 | 95.92 | 95.92 |
| <i>MNB</i> | 5.72 | -3.54 | 28.29 | 2.27 | 6.6 | -12.2 | 14.53 | -0.43 |

6 Wind flow dynamics around high-rise buildings

A local flow pattern around the target building is dominantly influenced by the building's shape and nearby objects. This chapter first aims to study the impact of the roof shape on the wind flow in Section 6.1, considering the isolated building in the C1 configuration and two cases: a building with a flat roof and a decked roof, illustrated in Figure 4.1. Next, the focus in Section 6.2 is moved to the group configurations C2 and C3, shown in Figure 4.2, analysing the effects of certain buildings' arrangements in the cluster on the flow around the target, central one. All analyses encompass two approaching wind angles: 0° and 45° . The flow is visualised in ParaView, an open-source multiple-platform application for interactive, scientific visualisation [173], using various filters, like surface plots for velocity and pressure fields, streamlines for main flow structures, calculator, etc. Results presented in this chapter are from simulations for wind energy assessment and are already published in [40, 41].

6.1 Flow around the isolated high-rise buildings: Impact of the roof shape

Numerical results on the flow structures around the high-rise building in configuration C1 are visualised using streamlines of the velocity mean field. Figure 6.1 shows the topology of the mean flow in the vertical xz plane through $(0, 0, 0)$ and horizontal xy planes in the vicinity of the bottom boundary ($z \sim 0$) and through $(0, 0, 2.25B)$ for the flat-roof building case at 0° and 45° . Two zones of the flow field can be identified regarding distinct flow structures, flow around the facade and above the roof. Hence, this section is divided into two subsections. Subsection 6.1.1 discusses the flow around the building facade, as it is not affected by the roof type. Then, Subsection 6.1.2 focuses on the flow structures above the roof with an overview of both flat and decked roof shapes.

6.1.1 Flow field around the facade

To investigate the flow around the facade, the main flow structures marked in Figure 6.1 are analysed. The immersed building model causes a disturbance in the incoming boundary layer wind flow. Upstream of the building, the flow reaches a stagnation point, marked with the letter A in Figure 6.1, after which it diverges around the building. The well-known horseshoe vortex, which forms between the stagnation point A and the building model, is not conspicuous in the

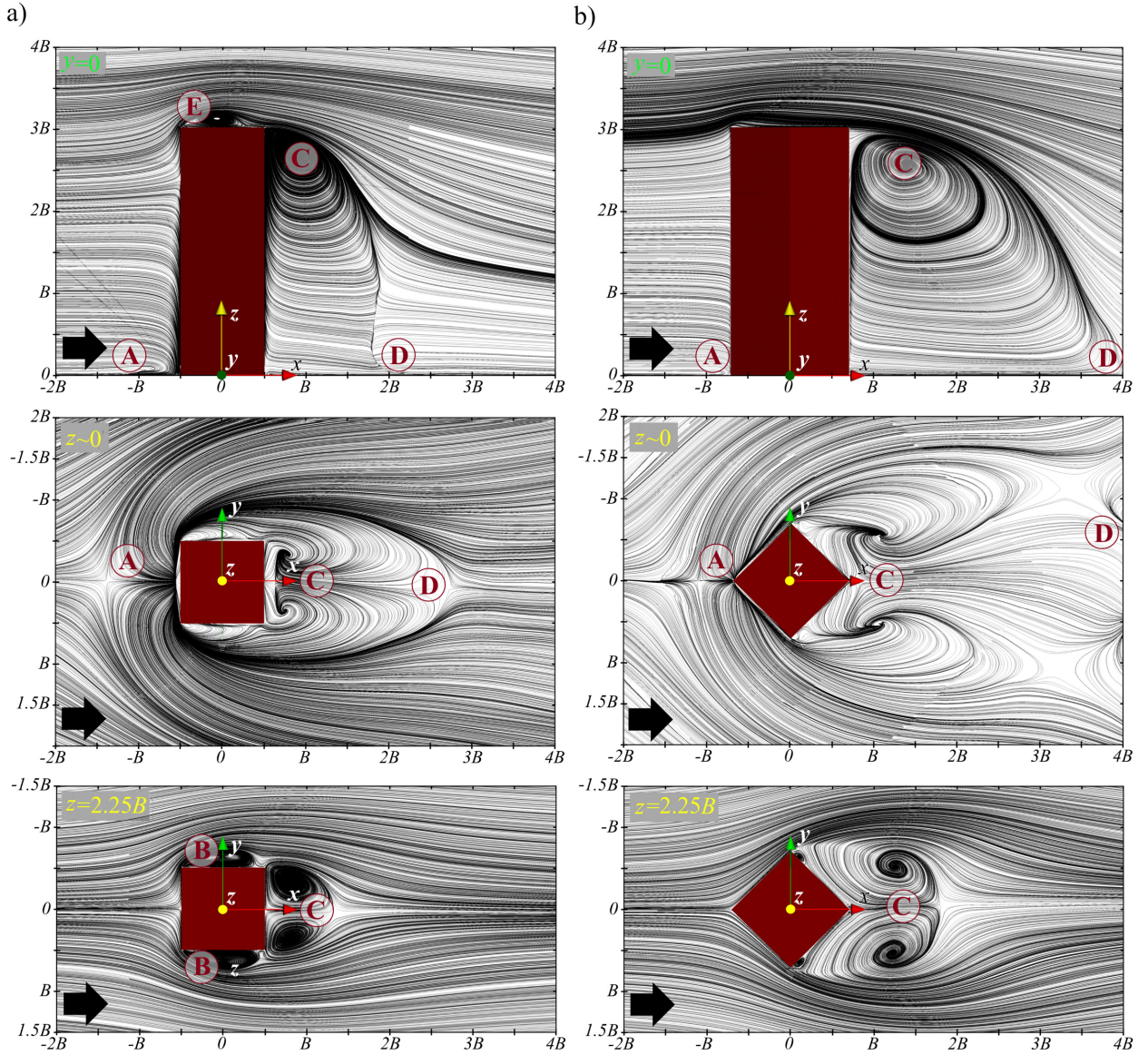


Figure 6.1. Streamlines of the velocity mean-field in the C1 configuration for the flat roof case in the vertical xz centre plane of the flow and horizontal xy planes in the vicinity of the bottom boundary ($z \sim 0$) and through $(0, 0, 2.25B)$ at: (a) 0° and (b) 45° , adapted from [40].

vertical xz plane for either angle of attack. This may be due to the extended time required to capture certain structures. The location of the vortex core can be anticipated at approximately $x/B = -0.9$ at 0° and $x/B = -0.8$ at 45° .

Considering the flow field around lateral walls, for the 0° angle of attack, the separation zone on each side (marked with letter B in Figure 6.1) is clearly visible in the horizontal plane $z = 2.25B$ and flow is detached from the model surface. In contrast, at 45° , flow is completely attached to the two windward faces of the model and fully separates at the lateral edges, combining with the wake region behind the building.

In the lee of the building, the arch vortex (marked with the letter C in Figure 6.1) is indicated by two zones of recirculating flow, noticeable in the horizontal xy plane, and the head of the vortex, visible in the vertical xz plane. The vortex size and shape prediction differ for two wind directions. Namely, at 0° , the flow reattaches at $x/B = 2$ (marked with the letter D), and the arch vortex is relatively flat, as shown in Figure 6.1(a) in the vertical xz plane. Unlike

the previous one, the wake region at 45° is broader and more extended to the average flow reattachment location (marked with the letter D) at $x/B = 4$, and the shape is quite oblique (Figure 6.1(b)).

The previously described flow pattern is reflected in surface pressure distribution as well. Figure 6.2 shows numerical results for the mean (\bar{C}_p) and RMS (C_p'') values of the surface pressure coefficient along the ring around the facade at $z = 2.25B$ in C1 configuration, for the flat-roof case and two considered approaching wind angles. Additionally, graphs are complemented with corresponding experimental data, demonstrating a good agreement between the numerical and experimental data, as they almost overlap. Regarding the pressure distribution at 0° , large suction at side walls maps out the separation region. The maximum negative mean pressure coefficient is located at approximately $0.4B$ from the leading edge, after which pressure recovery occurs. The absence of a plateau after the recovery zone [168] distinguishes the separated-type flow, confirmed in streamlines in Figure 6.1(a). In addition, the maximum RMS value C_p'' occurs in the recovery region, which is consistent with findings in [168]. However, at 45° , flow separation is delayed up to the model lateral corners, indicated by positive \bar{C}_p values on two windward surfaces. The rear surfaces for both wind angles are in suction due to the reversed flow in the wake.

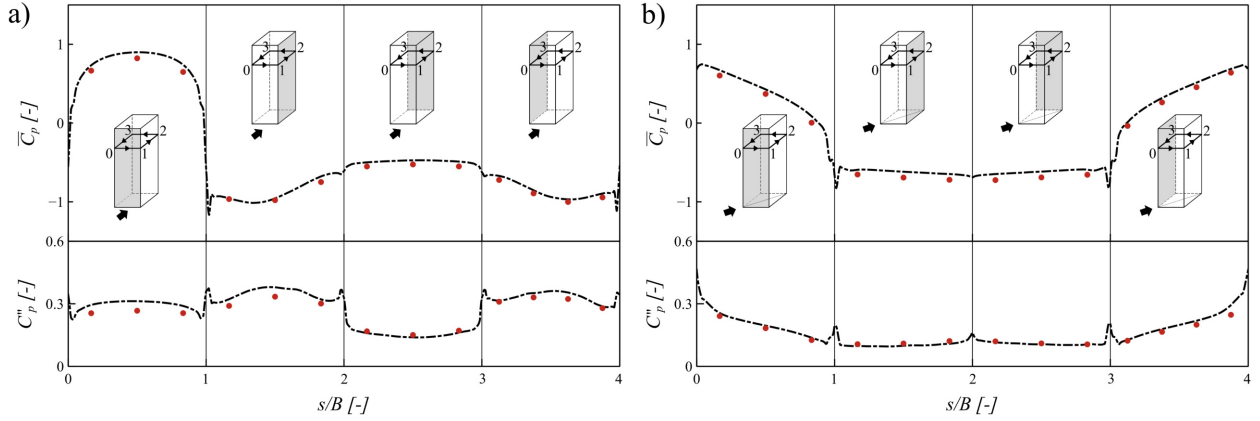


Figure 6.2. Mean and RMS values of the surface pressure coefficient in the C1 configuration for the flat-roof case along the ring around the facade ($z = 2.25B$) at: (a) 0° and (b) 45° , adapted from [40].

6.1.2 Flow field above the roof

Regarding the flow above the roof, detailed analyses of mean flow structures for both roof types are presented. These structures are illustrated in Figure 6.3 for wind approaching 0° , and Figure 6.4 for wind approaching 45° . The velocity mean-field surface plots in the vertical plane, marked with a red dashed line on a sketch of the roof (see Figure 6.3(a) and Figure 6.4(a)), are presented in Figure 6.3(b) and Figure 6.4(b). They are complemented with profiles of mean velocity vector components in x and y directions at seven locations on the roof. Furthermore, the contour line of velocity magnitude (U) equal to the free stream velocity (U_{ref}) is marked with a white dash-dot line. Figure 6.3(c,d) and Figure 6.4(c,d) illustrate a more profound view of the flow on surface pressure distribution. It is also compared to the experimental data, confirming their satisfactory agreement. Surface plots in Figure 6.3(b,c) and Figure 6.4(b,c) are overlapped with the streamlines in order to visualise and distinguish the most dominant mean flow structures. Flow topology is strongly dependent on the wind angle, and first, it will be analysed flow above two different roof types at 0° and than at 45° . All flow structures are symmetrical concerning the wind direction, suggesting the converged results.

The angle of attack: 0°

At 0° , the point of separation on the flat roof is predefined by the sharp front edge facing the incoming flow, visible in Figure 6.3(b). The mean reattachment point in the central flow plane is located at $\sim 0.8B$. Furthermore, the mean separation region can be divided into specific zones, according to [168]. The study by [168] is mainly related to the bridges and the 2D flow phenomena, but a similar separation pattern is observed in the present investigation in the centre plane of the flow. Nevertheless, the 3D effects of the flow should not be neglected, and they are more pronounced as moving closer to the lateral edges of the roof, resulting in a characteristic “bubble shape” of the separation region.

The most dominant zone is the primary vortex zone (marked with letter E in Figure 6.1 and Figure 6.3, with its core located at $\sim 0.43B$ from the leading edge and the height of the separation bubble of $\sim 0.2B$). A thin recirculation region (marked F) is noticed close to the roof surface, between the separation point and the primary vortex. The zone in between the previous two is defined as the inner region and noted by G. The streamlines plot in the vicinity of the roof (Figure 6.3(c)) reveals the reattachment line of two recirculation regions across the roof marked with H (for primary vortex) and I (for thin recirculation region).

The velocity profiles in Figure 6.3(b) in the streamwise (U_u) direction show the characteristic reversal flow in the separation zone. The vertical velocity vector component (U_v) indicates the inclination of the flow, which reaches its maximum above the front part of the roof as the flow must overcome the obstacle by lifting above it. Negative values point out the flow tendency to attach to the roof.

The mean pressure coefficient distribution manifests a characteristic “hump shape” described in [174], typical for separated flow with the reattachment. A more detailed analysis, connecting the patterns of the mean and RMS values of the pressure coefficient, follows conclusions from [168]. Namely, four zones identified by [168] can be recognised. The first zone is defined between the separation point and the top of the inner region, and the plateau of \bar{C}_p and low C_p'' values characterise it. The second one is followed by the highest mean suction values with an increase in the RMS values of the pressure coefficient. The pressure recovery zone is marked as a zone with a gradual increase in the mean and maximum RMS value of the pressure coefficient. The previous is consistent with the findings in [175] that the maximum C_p'' value is located just upstream of the mean reattachment position. Finally, another plateau of \bar{C}_p values indicates the reattachment zone.

The roof change from the flat to the decked one alters the flow physics above the roof significantly. From the streamlines plot in Figure 6.3(b), the flow separates at the upstream edge, but the slope of the roof prevents the development of the large separation bubble, unlike in the flat roof case. Namely, the flow managed to attach to the slope (reattachment is marked with L) after a small separation region marked with J. The second separation point is located at the windward edge of the flat part of the roof. The approaching flow in the vicinity of the roof is already inclined due to the slope, resulting in a less pronounced separation region on the top (marked with the letter K) followed by the reattachment (M). The height of this region is $\sim 0.05B$ and length $\sim 0.25B$ from the separation point. Again, the streamline plot in Figure 6.3(c) shows the reattachment line of the two separation regions. The third recirculating zone is visible at the leeward part of the roof, and it coalesces with the wake behind the building.

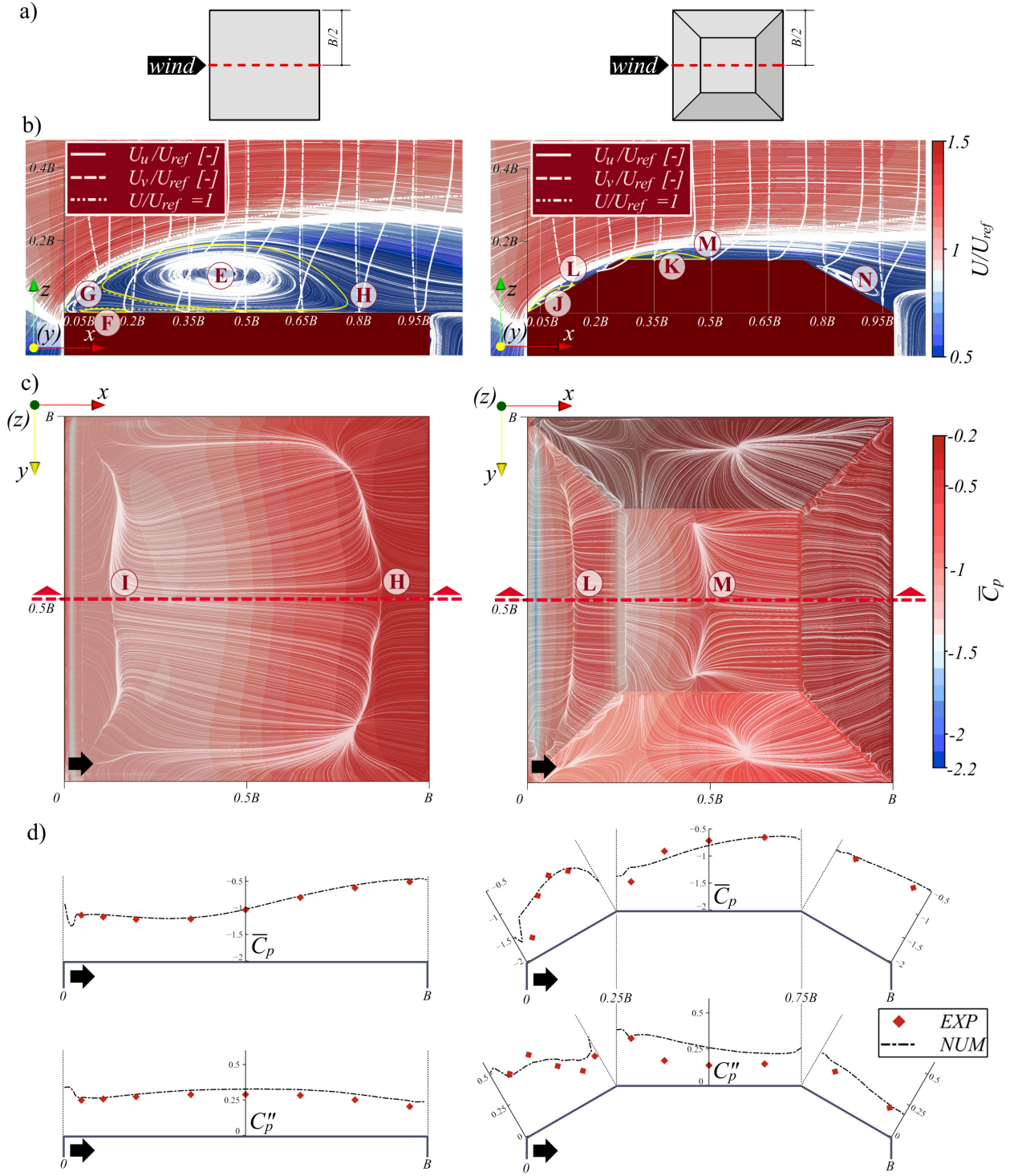


Figure 6.3. Flow structures above the flat and decked roofs in the C1 configuration at 0° : (a) sketches of the roofs; (b) velocity mean-field with streamlines in the vertical central plane of the roofs (marked with a red dashed line in (a)) complemented with profiles of mean velocity vector components in x and y direction at seven locations on the roof; (c) the surface plot of mean pressure coefficient (\bar{C}_p) on the roofs, overlapped with streamlines in the vicinity of the roofs, top view; (d) plots along the middle line of the mean and RMS values of the pressure coefficient compared with experimental values, adapted from [40].

Velocity profiles confirm the previous flow description. The vertical velocity profile (U_v) manifests the flow's inclination close to the upwind slope, while the reversal flow can be noticed in separation regions.

The mean pressure coefficient in Figure 6.3(d) on the windward slope and flat part of the roof has a “hump shape” in the separation region, as observed in the flat roof case. However, it is hard to identify all four zones described by [168] due to the scale of the separation zone compared to the roof size and mesh refinement. It is particularly challenging to determine reliable RMS values of the pressure characteristics since the discrepancy with the experimental results is strongly pronounced. The average overestimation by numerical simulations is $\sim 30\%$, and it may be attributed to the complex geometry of the roof and the change in aerodynamic characteristics compared to the flat roof. Namely, separation zones are less pronounced above the decked roof, resulting in two smaller separation bubbles in contrast to the big one above the flat roof. The mesh around both roofs is of the same refinement level and prevents the capture of second-order statistics with the same accuracy in both cases. Furthermore, subgrid-scale modelling can affect such behaviour [165] as it plays an important role in a zone close to the surface.

Regarding the roof shape at 0° , it is evident that the disturbance of the flow is substantially smaller for the decked roof. It is interesting to note that the height of the separation region above the flat roof is even larger than the compound height of the decked roof and the separation region above it. Furthermore, the velocity magnitude above the decked one reaches the free stream value (U_{ref}) at lower heights relative to the upstream corner of both roofs.

The angle of attack: 45°

The wind direction of 45° promotes the consequential change in the flow structures above the roof. As expected, a pair of conical vortices occur near the leading edges instead of one big separation bubble. To reveal their characteristics, the mean velocity field in Figure 6.4(a) is considered. Two zones of swirling flow are noted: the dominant one, the primary vortex zone (denoted by the letter E), and the less pronounced one, the secondary vortex zone, closer to the separation edge (marked with F). The same structures can be found in the work of [176].

From the streamlines plot in Figure 6.4(b,c), the traces representing the reattachment lines of these two zones are inferred and identified with a yellow dash-dotted line in Figure 6.4(b). The yaw angles of these traces, relative to the eave, are $\phi_r = 26^\circ$ and $\phi_s = 10^\circ$ for primary and secondary vortex zones, respectively. Moreover, the mean vortex core trace is marked with a yellow dotted line at $\phi_c = 16^\circ$, which is close to the values obtained in [72] on a top surface of the cube ($\phi_c = 14^\circ$) and [177] on low rise building model ($\phi_c = 14.4^\circ$), both in a turbulent flow. Above the main diagonal on the roof in wind direction, velocity profiles show fully attached flow and slightly accelerated due to the narrow space between two cone vortices, which produce the Venturi effect. Spatial visualisation of the mean flow with recognised structures is presented in Figure 6.5 using streamlines.

The impact of the flow field on the surface pressure is demonstrated in Figure 6.4(c,d). From the line plots in Figure 6.4(d), the close similarities in the shape of the graphs and the occurrence of extreme pressure characteristics with results in the flat roof case at 0° are evident. Namely, the characteristic hump shape is identified in the line plot. The maximum negative mean pressure coincides with the main vortex core trace, as reported in [71] and [177]. Regarding the RMS values of the pressure coefficient, the maximum is located between the traces described by ϕ_c and ϕ_r (Figure 6.4(c)) in the mean pressure recovery zone. The plateau in the mean pressure

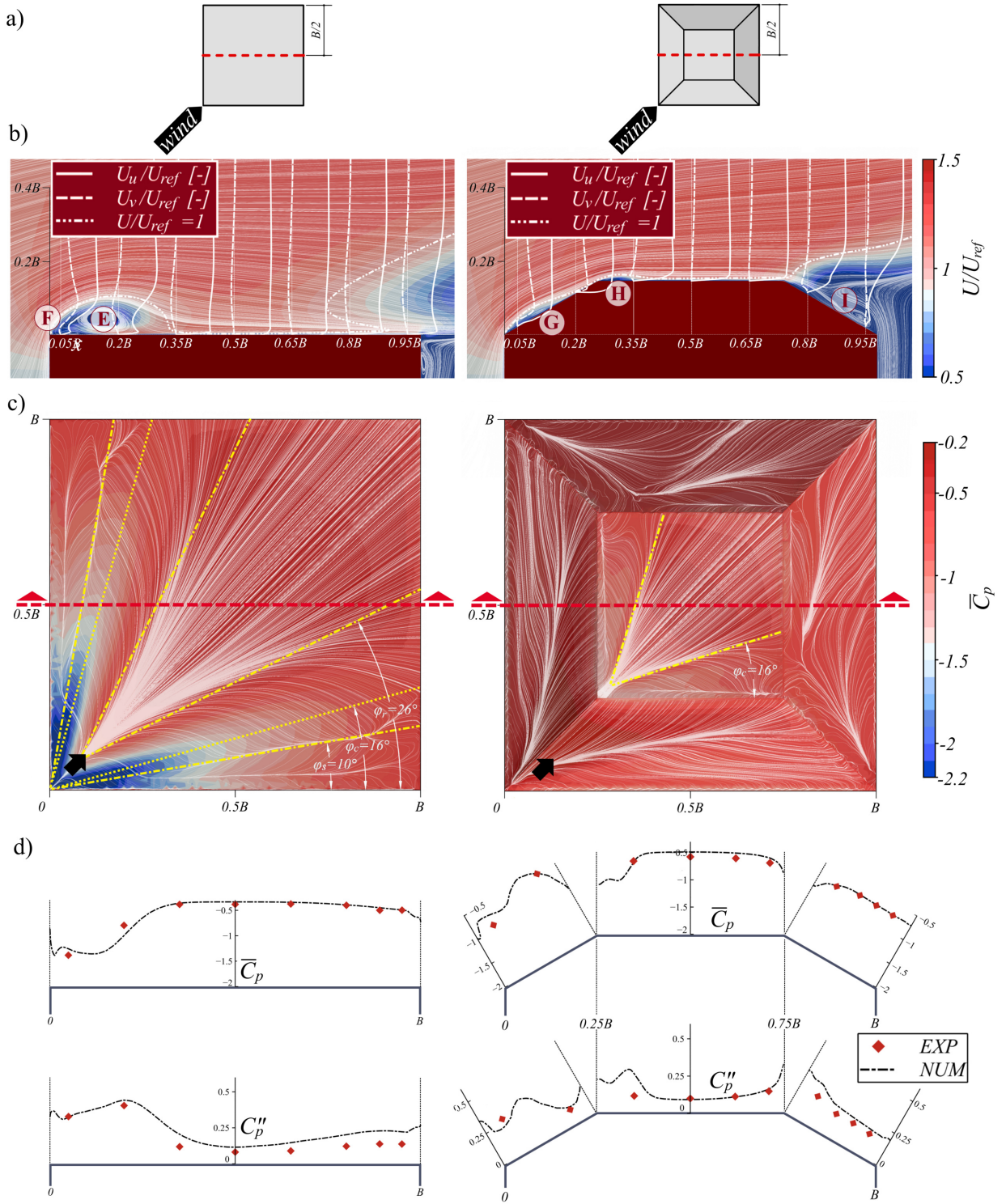


Figure 6.4. Flow structures above the flat and decked roofs in the C1 configuration at 45°: (a) sketches of the roofs; (b) velocity mean-field with streamlines in the vertical central plane of the roofs (marked with a red dashed line in (a)) complemented with profiles of mean velocity vector components in x and y direction at seven locations on the roof; (c) the surface plot of mean pressure coefficient (\bar{C}_p) on the roofs, overlapped with streamlines in the vicinity of the roofs, top view; (d) plots along the middle line of the mean and RMS values of the pressure coefficient compared with experimental values, adapted from [40].

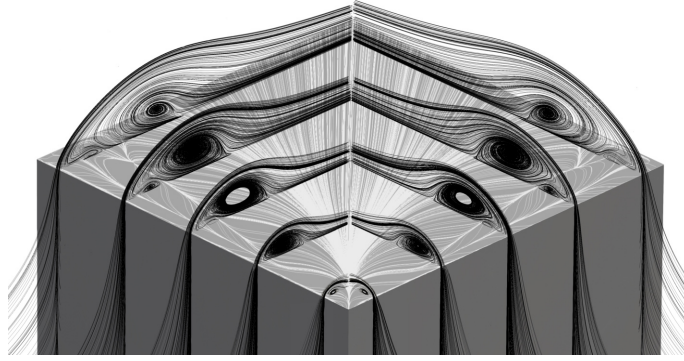


Figure 6.5. Mean velocity streamlines in vertical planes at 45° yaw angle related to the wind direction (black streamlines) and in the vicinity of the roof (white streamlines), adapted from [40].

coefficient indicates the flow attached to the roof. It is worth noting that the connection between mean flow structures and four pressure zones in the separation region defined by [168] can be mapped to this case in the plane normal to the leading edge, even though the nature of the vortices is not the same.

Switching from the flat to the decked roof, two sharp windward corners can be observed instead of one. That promotes the flow to separate, first, from the two leading edges, rolling up and forming a pair of cone vortices above the windward slopes of the roof, and secondly, from the edges on the flat part of the roof, creating another pair of cone vortices above the flat part of the roof. Both pairs of vortices are not distinct as in the flat roof case, especially the one on the flat part of the roof. Namely, wind velocity profiles show only a slight disturbance above this part because the separation zones are spread over the less confident area. Moreover, the reduction of the reattachment line inclination (ϕ_r) to 16° is present, as shown in Figure 6.4(c). Separations above the leeward slopes are in the wake zone behind the building.

The same pressure distribution characteristics over the flat part of the decked roof, only less pronounced, can be noticed from the line plots (Figure 6.4(d)) compared to the flat roof case.

Considering the wind approaching 45°, flow mainly attached to the roof above its main diagonal is observed for both roof types. Again, as previously shown for 0° angle of attack, the decked roof case results in a less disturbed flow above the roof, and the free stream velocity has been achieved from the height of $0.05B$ relative to the roof surface.

6.2 Flow field in the building clusters: Insight into the interference effects

In this section, the results of the numerical simulations considering the impact of the interference effects on the flow behaviour and surface pressure distribution in two group configurations C2 and C3, for two wind angles (0° and 45°) are presented. Special attention is given to the zone above the roof, as it is a potential installation site for a future wind turbine. The section starts with Subsection 6.2.1 describing the flow field in two arrangements in the group configuration. Then it moves on to the description of characteristic flow structures in three study cases illustrated in Figure 4.2 and defined as:

- The isolated high-rise building in configuration C1, directly exposed to the wind—case **C1**,
- The central building in group configuration C2, placed between four surrounding buildings in the “cross” shape arrangement—case **C2** and
- The central building in group configuration C3, surrounded by buildings in the “x” shape arrangement—case **C3**.

It continues with the representation of velocity first- and second-order statistics for the defined cases in Subsection 6.2.2. Finally, the section closes with an overview of the surface pressure distribution on the roof and facade of the principal buildings in Subsection 6.2.3.

6.2.1 Flow field

In order to tackle the interference effects, an overview of the flow field in the group configuration for two building arrangements is presented in the beginning (Subsection 6.2.1.1). It is followed by an enlarged view of the basic flow structures around the buildings in three study cases (Subsection 6.2.1.2). In addition, particular flow structures are visualised using mean velocity streamlines.

6.2.1.1 Flow field in different building arrangements in group configuration

Figures 6.6 and 6.7 represent the normalised mean velocity field overlapped with mean velocity streamlines for the “cross” and “x” shape arrangements at 0° (Figure 6.6) and 45° (Figure 6.7) wind angles. The normalisation is done with the reference mean velocity (U_{ref}), and plots in the vertical central plane of the flow and the horizontal plane at height $z = 0.8H$ are included.

Wind approaching at 0°

Considering the “cross” shape arrangement, the disturbance in the incoming boundary layer flow, produced by the immersed buildings, and resulting flow structures are illustrated in Figure 6.6(a). The well-known horseshoe vortex is captured in front of the upstream building in the vertical plane. The incoming flow separates at the windward edges of the building, resulting in recirculation regions above the roof and around the facade. In the lee of the first building, the wake forms the arch vortex, indicated by two zones of swirling flow, which can be seen in the horizontal plane, and the head of the vortex, visible in the vertical plane. The flow then manages to reattach to the base plane in the inner region between the front building and the central one (case C2), resulting in the formation of a second horseshoe vortex upstream of the C2. However, the front building shades the central one, producing a “sheltering effect” that damps the separation around the central building. At the same time, the wake zone retains a similar shape as observed around the front building. Moreover, a similar flow behaviour is observed around the third downstream building. In the case of lateral buildings, a slight deviation from the central symmetry line shows that the flow in the passage between the central and side buildings is biased toward the lateral boundaries. Additionally, the denser streamlines in the passage and the flow acceleration suggest the presence of the Venturi effect.

The second, “x” shape, arrangement shows different flow behaviour compared to the previous one, as illustrated in Figure 6.6(b). Namely, similar flow structures to those around two side buildings in the “cross” shape arrangement are observed around two upstream side buildings.

The incoming flow hits the two upstream side buildings first, causing separations from their windward edges and creating a wake behind them. Yet, the asymmetric flow around the buildings is even more pronounced than in the first (“cross” shape) arrangement. The separation zones closer to the side boundaries of the domain are larger and more rounded compared to the flatter and more skewed ones closer to the central plane of the flow, which is due to the position of the central building (building in the C3 case). On the other hand, the flow around the central building is completely different in these two arrangements. Instead of being shaded by the upstream building in the C2 case, the central building here is hit by the flow that passes through the passage between the two upstream side buildings. Interestingly, due to the position of the four surrounding buildings, the flow pattern around the central one resembles the shape of a cylinder. Specifically, the separation zones above the roof and around the facade are strongly pronounced and rounded, i.e. wider in the y and z directions, but with a shorter wake zone, indicating that the whole zone around the building is compressed. The two downstream buildings have smaller separations on the side walls than the upstream ones. However, they are not shielded by the buildings in front, and almost no deviation of the flow toward the lateral boundaries is observed.

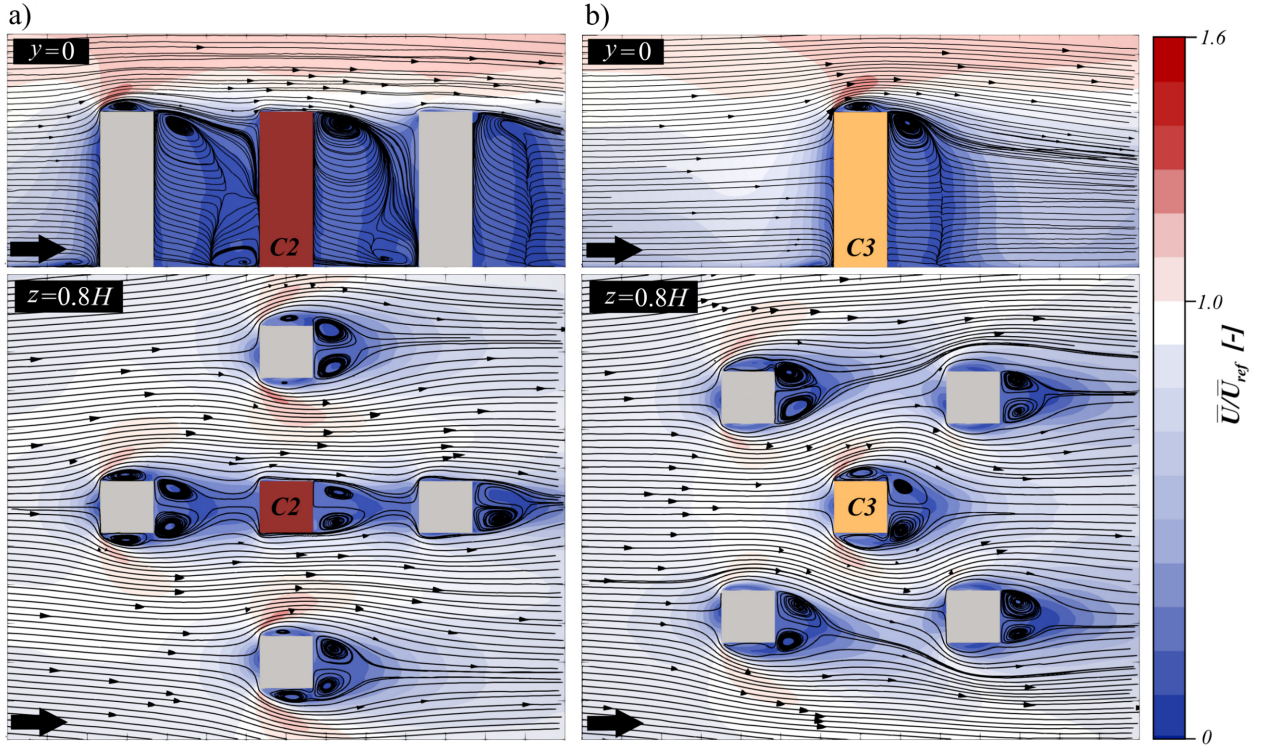


Figure 6.6. Velocity mean-field overlapped with streamlines in the vertical xz central plane of the flow through $(0,0,0)$ and horizontal xy plane through $(0,0,0.8H)$ for the group configuration at 0° wind angle: (a) in the “cross” arrangement (case C2) and (b) in the “x” arrangement (case C3), adapted from [41].

Wind approaching at 45°

The shift in wind direction notably modifies flow behaviour across both building arrangements. In the “cross” shape arrangement, represented in Figure 6.7(a), the incoming flow initially encounters the windward corner of the two upstream buildings. These corners split the flow, directing it along the windward sides until it reaches the lateral corners. At these points, the flow separates, forming an arch vortex in the wake zone. The asymmetric flow is distinctly biased towards the lateral sides of the domain as a consequence of the unique arrangement of the buildings. The central building (case C2) faces the incoming flow in a similar manner to the

“x” shape arrangement at 0° . Specifically, the wake regions from the two upstream buildings circumnavigate the central one while the incoming flow passes through a passage even narrower than that observed at 0° . This produces a pronounced Venturi effect. Again, the flow appears compressed due to the position of the surrounding buildings. Looking at the vertical central plane of the flow, the flow above the roof of the central building is completely attached, owing to the cone vortices, which are flow structures typically seen above the flat roof at the 45° wind angle. More details on this will be provided in Subsection 6.2.1.2. The wake zone is flat, in line with expectations. An interesting observation can be made regarding the flow around the two downstream side buildings. These buildings, not being overshadowed by their upstream counterparts, display a wake zone biased towards the central plane of the flow. This bias appears to result from the strong stream forming between the buildings.

In the “x” shape arrangement, shown in Figure 6.7(b), the front building directly faces the oncoming wind. This leads to pronounced separation at the two lateral edges, consequently generating a wake behind the building. Compared to the “cross” shape arrangement at 0° , the increased frontal projection of the upstream building in this setup, as well as the wind direction, result in a more extensive and elongated wake. In contrast to the “cross” arrangement at 0° , where the wake reattaches to the base plane, the wake in this setup reattaches to the windward sides of the central building (case C3). The flow around the central building is strongly influenced by the incoming wake, manifesting as a reduced size of separation behind it. Subsequently, a secondary wake zone forms and manages to reattach to the base plane before reaching the third downstream building. A distinct horseshoe vortex is visible in the vertical plane in front of the third building. In terms of the flow around two lateral buildings, it appears largely undisturbed by the central cluster of three buildings, yielding an almost perfectly symmetric flow around them.

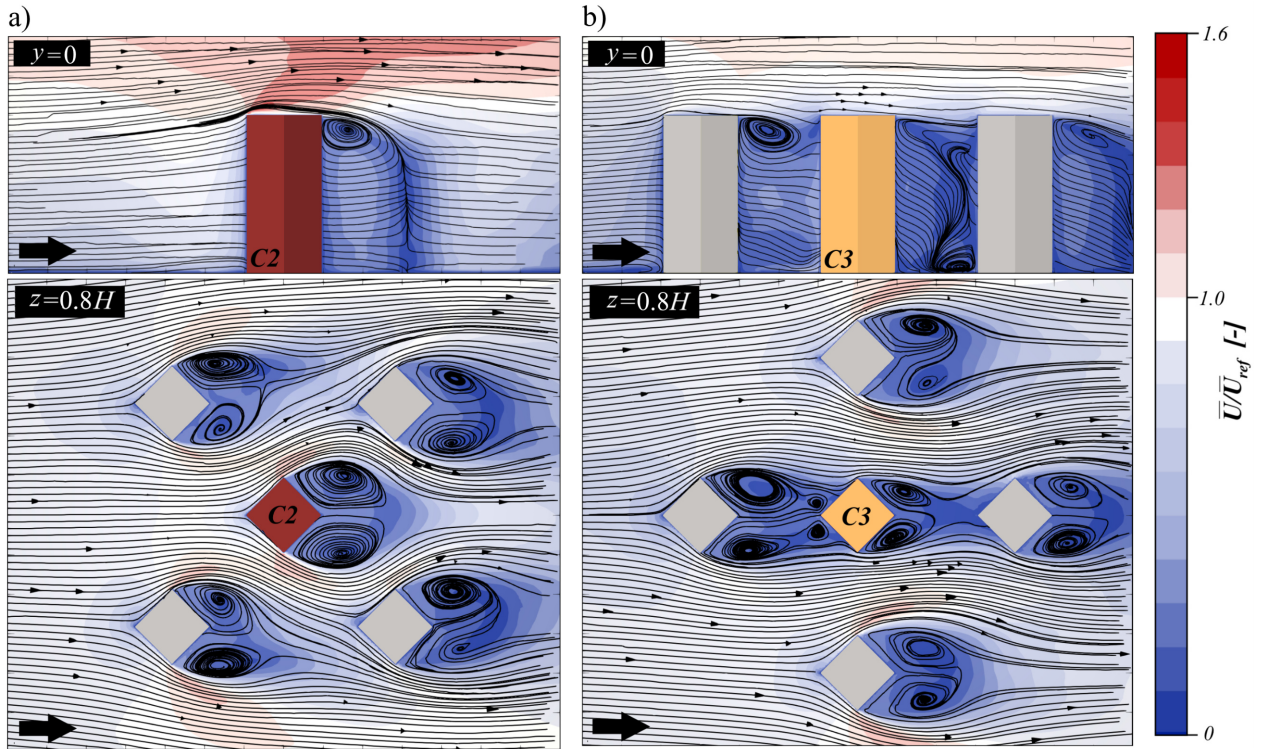


Figure 6.7. Velocity mean-field overlapped with streamlines in the vertical xz central plane of the flow through $(0, 0, 0)$ and horizontal xy plane through $(0, 0, 0.8H)$ for the group configuration at 45° wind angle: (a) in the “cross” arrangement (case C2) and (b) in the “x” arrangement (case C3), adapted from [41].

Supplementing the earlier flow descriptions, Figure 6.8 offers a detailed visualisation of the vortical structures in the “cross” shaped building arrangement at both 0° and 45° angles of attack. The figure displays isocontours of the invariant λ_2 , as defined by [178], with colouration representing pressure.

In the 0° scenario, it is clear that the incoming boundary layer separates upon encountering the windward edges of the high-rise buildings, with the formation of the horseshoe vortex visible upstream. In contrast, the 45° wind angle brings about a significant modification in wind flow structures. This shift in wind direction influences the emergence of paired cone vortices above the flat roofs of the buildings. Also noteworthy is the flow separation at the lateral edges of the clustered buildings.

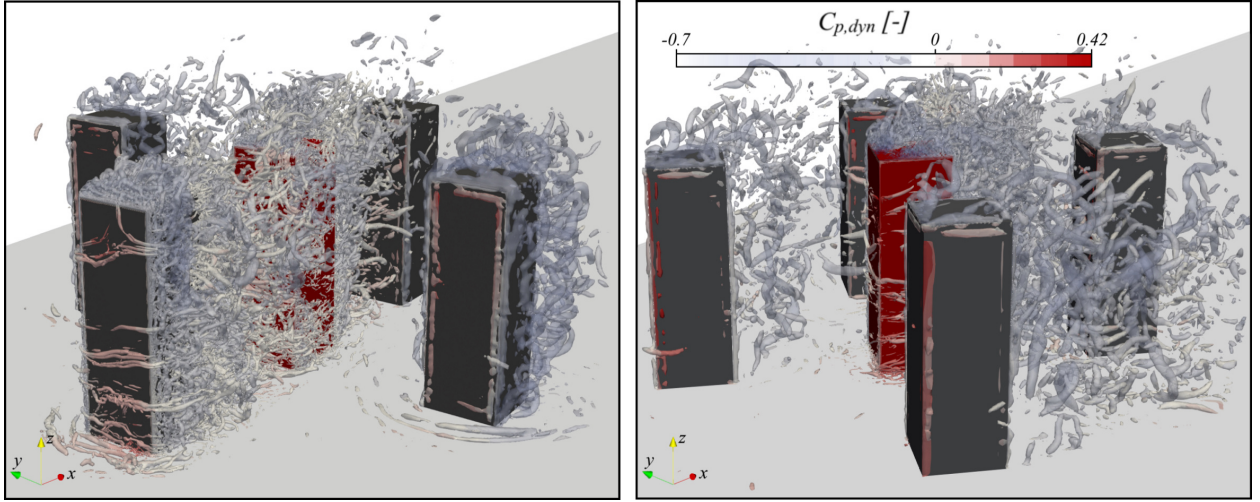


Figure 6.8. Three-Dimensional isocontours of λ_2 invariant at $\lambda_2 = 300000$, for the “cross” shape building arrangement at 0° and 45° wind angles, adapted from [41].

6.2.1.2 Flow structures for three study cases

The following part focuses on the flow structures for three study cases, taken out of the context of the overall flow field. An accent is on the zones above the roof and around the facade. Figures 6.9 and 6.10 give a cross-sectional view of mean velocity streamlines in the horizontal plane at $z = 0.8H$ and the vertical central plane of the flow. Each figure offers an enlarged view of the region above the roof for each study case at 0° (Figure 6.9) and 45° (Figure 6.10) wind angles. An additional plot focusing on the vicinity of the roof at a 45° wind angle is included to account for the unique nature of the flow structures present in this wind direction.

Wind approaching at 0°

Analysing the flow above the roof, a separation zone followed by reattachment is evident in Figure 6.9 in all three cases. In the case of C1, where the building is isolated and directly exposed to the wind, a distinct separation bubble with a length of approximately $\sim 0.29H$ and a height of $\sim 0.06H$ can be observed. On the other hand, the flow in case C2, with the building shielded by the one in front, demonstrates barely noticeable separation over a limited length of roughly $\sim 0.06H$, with the flow primarily parallel to the roof. In the context of the “x” shape arrangement (case C3), the size of the separation zone increases by approximately 10% in both horizontal and vertical directions relative to case C1. This results in a separation zone of approximately $\sim 0.31H$ length and $\sim 0.07H$ height.

Around the facade, the flow separates at the windward edges without reattachment in the C1 and C3 cases at $z = 0.8H$. Namely, separated flow merges with the recirculation region behind the building. The shape of the wake region in case C1, visible in the vertical plane, is oblique, with the $H/2$ length in the x direction, and flow manages to reattach in the inter-obstacle region at around $x = 2/3H$. Nevertheless, in the C3 case, the wake zone is rather flat in the z direction, with the $H/3$ length in the x direction and a bit broader in the y direction, reflecting the effects of the surrounding buildings. Similarly to the observation above the roof, flow in case C2 is almost parallel to the side walls, with limited separation zones. The wake behind the building matches the building's width and has a length in the x direction equivalent to that observed in case C1.

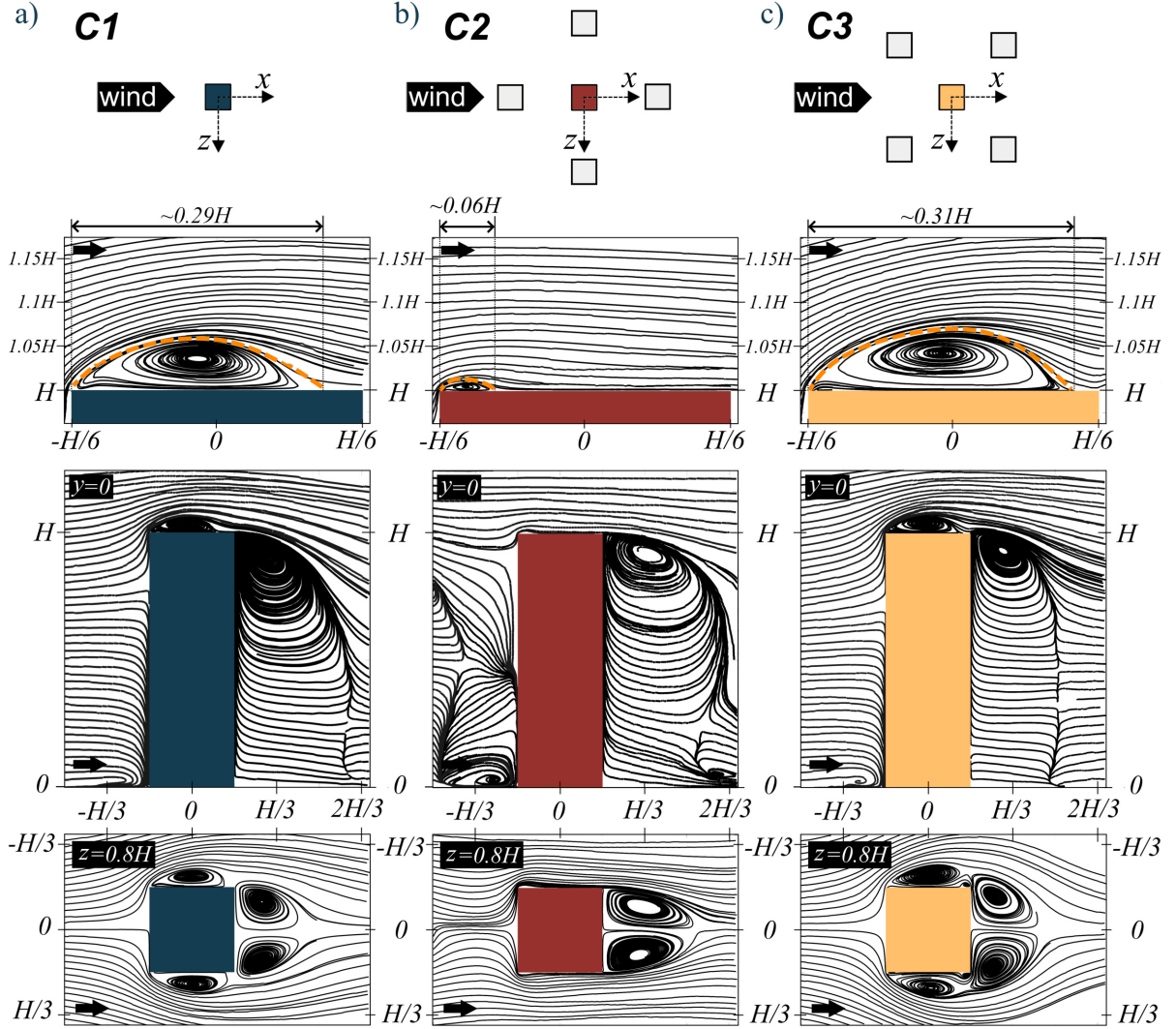


Figure 6.9. Streamlines of the velocity mean-field in the vertical xz centre plane of the flow through $(0, 0, 0)$, with an enlarged view of the area above the roof, and horizontal xy plane through $(0, 0, 0.8H)$ for three study cases: (a) C1, (b) C2 and (c) C3, adapted from [41].

Wind approaching at 45°

A change in wind direction triggers a significant transformation in the flow structures above the roof, as shown in Figure 6.10. As expected, in cases C1 and C2, a pair of cone vortices replace the single separation bubble observed at a 0° wind angle. The wind flow in case C1 presents two distinct zones of swirling flow: a primary, dominant vortex zone and a less pronounced secondary vortex zone closer to the separation edge, also reported in [176] and in previous Subsection

6.1.2. The flow in the central plane remains parallel to the roof. The presence of surrounding buildings in case C2 encourages stronger separation and larger cone vortices compared to case C1. Interestingly, the secondary vortex is absent in the mean velocity streamlines plot presented in Figure 6.10(c). In contrast, case C3 demonstrates modestly developed cone vortices close to the windward edges, while most of the flow is attached to the roof.

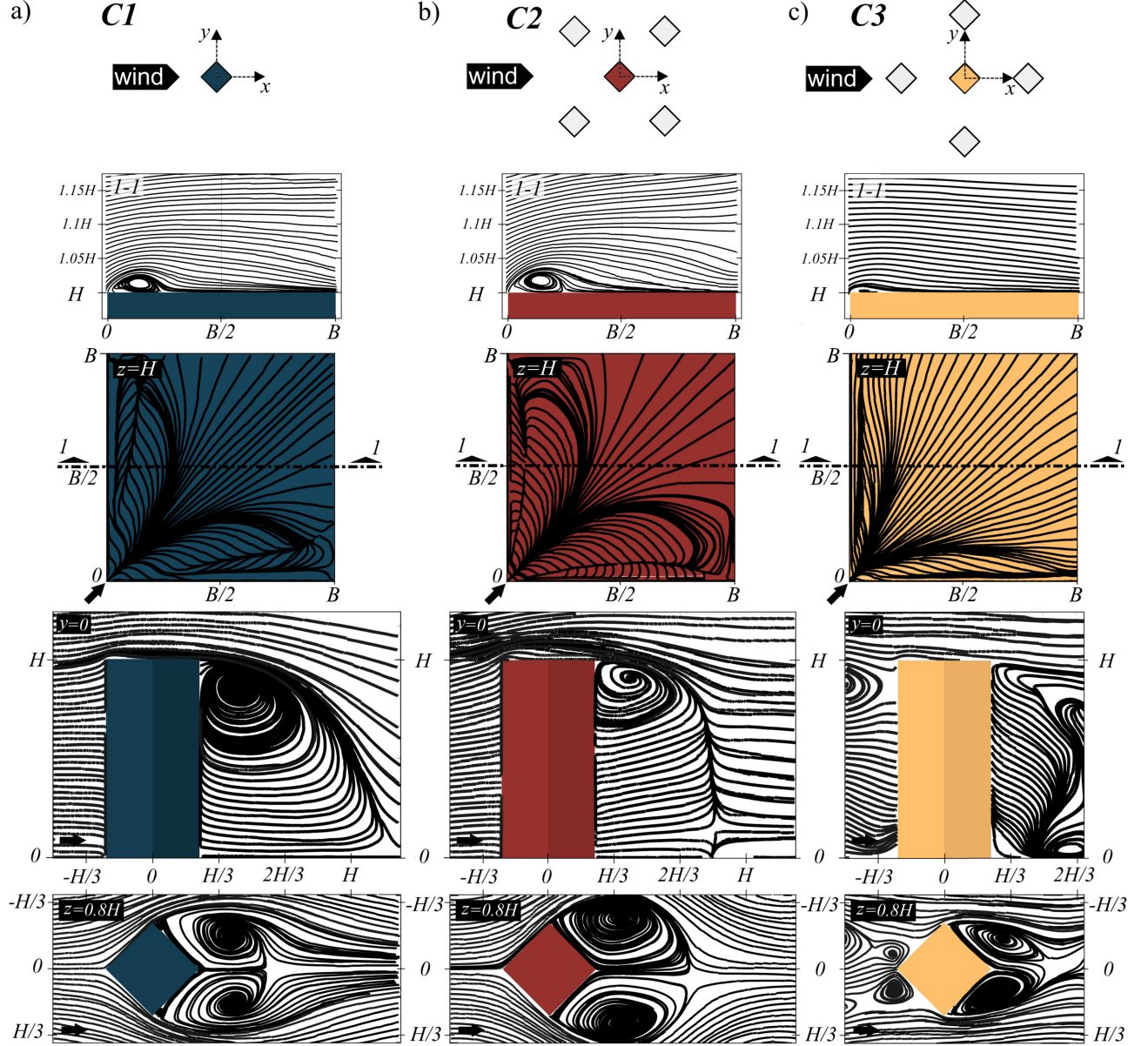


Figure 6.10. Streamlines of the velocity mean-field in the vertical xz centre plane of the flow through $(0, 0, 0)$, and horizontal xy plane through $(0, 0, 0.8H)$ complemented with an enlarged view of the zone in the vicinity of the roof in the horizontal and vertical plane, for three study cases: (a) C1, (b) C2 and (c) C3, adapted from [41].

In the context of the flow around the facade at a 45° wind angle, unique patterns arise in each case (Figure 6.10). For the isolated building (C1), the flow is attached to the windward building's sides and entirely separates at the lateral edges, forming the arch vortex in the lee of the building. The wake zone's form is oblique, with reattachment occurring near $x = 1.2H$. The wake's breadth in the y direction slightly exceeds the building's projection on a plane perpendicular to the wind at $z = 0.8H$, approximating $1.7B$. In contrast, case C3 reveals the wake zone from the upstream building reattaching to the windward sides of the central building. This results in a second, milder separation at the lateral edges, reattaching upstream of the

third building within the inter-obstacle region. A distinctive horseshoe vortex forms ahead of this third building. Lastly, case C2 exhibits the most extensive wake zone, reaching widths of about $2.3B$. Its flat profile results in a consistent size in the z direction. Reattachment to the base plane happens at $x = 0.8H$, suggesting notable wake zone dynamics influenced by the surrounding buildings.

6.2.2 Velocity statistic

This subsection aims to link flow structures from Subsection 6.2.1 with the mean velocity field described in Subsection 6.2.2.1 and turbulence intensities given in Subsection 6.2.2.2 in specific zones around three considered cases.

6.2.2.1 Mean wind velocity

Normalised velocity mean wind speed (U/U_{ref}) around the buildings in three study cases is shown in Figure 6.11 for wind approaching at 0° and Figure 6.12 for wind approaching at 45° . Red shades on the surface plots indicate an increase in wind speed, white represents equality, and blue indicates a decrease compared to U_{ref} . In addition, the view of the roof zone is complemented with streamwise (U_u) and vertical (U_w) profiles of the mean velocity vector components, and the red horizontal line on the graphs marks an equality between the observed and reference wind speed.

Wind approaching at 0°

In light of the previously defined flow structures, zones of low wind speed are detected inside the recirculating regions, as shown in Figure 6.11. It is also confirmed by the reversal flow recorded in streamwise (U_u) profiles above the roof. Furthermore, the vertical components (U_w) have the highest positive values close to the windward edge, above the separation point, in all three cases, indicating the inclination of the flow as it has to overcome the obstacle by lifting above it. On the other hand, negative values of (U_w) represent the mean velocity vectors pointing down and the flow tendency to reattach the roof. The speed-up effect is observed outside the regions of low wind speed (above the separation zones marked with the white dashed lines in Figure 6.11). The most conspicuous acceleration compared to the U_{ref} is recorded in the vicinity of the windward edge in the C1 case, up to 30%, with a slightly lower value in the C3 case. It follows the shape of the separation zone downstream. Around the facade, the maximal increase of approximately 20% is observed in the same cases. As for the C2 case, no acceleration takes place due to the building in front.

Wind approaching at 45°

Directing our focus to the wind angle of 45° (illustrated in Figure 6.12), previously examined flow structures (refer to Subsection 6.2.1.2) cause corresponding alterations in the velocity fields. While zones of low wind speed persist within the recirculating regions, the flow profiles present a distinct behaviour compared to 0° . For all three cases, the velocity profiles above the roof's main diagonal, aligned with the wind direction, confirm an entirely attached flow and the absence of a vertical (U_w) component. The latter is only noticeable near the windward corner, where the flow is compelled to elevate to overcome the building. With respect to flow acceleration in this plane, an increase in wind speed, relative to U_{ref} , reaches up to 30% in case C1 and even escalates

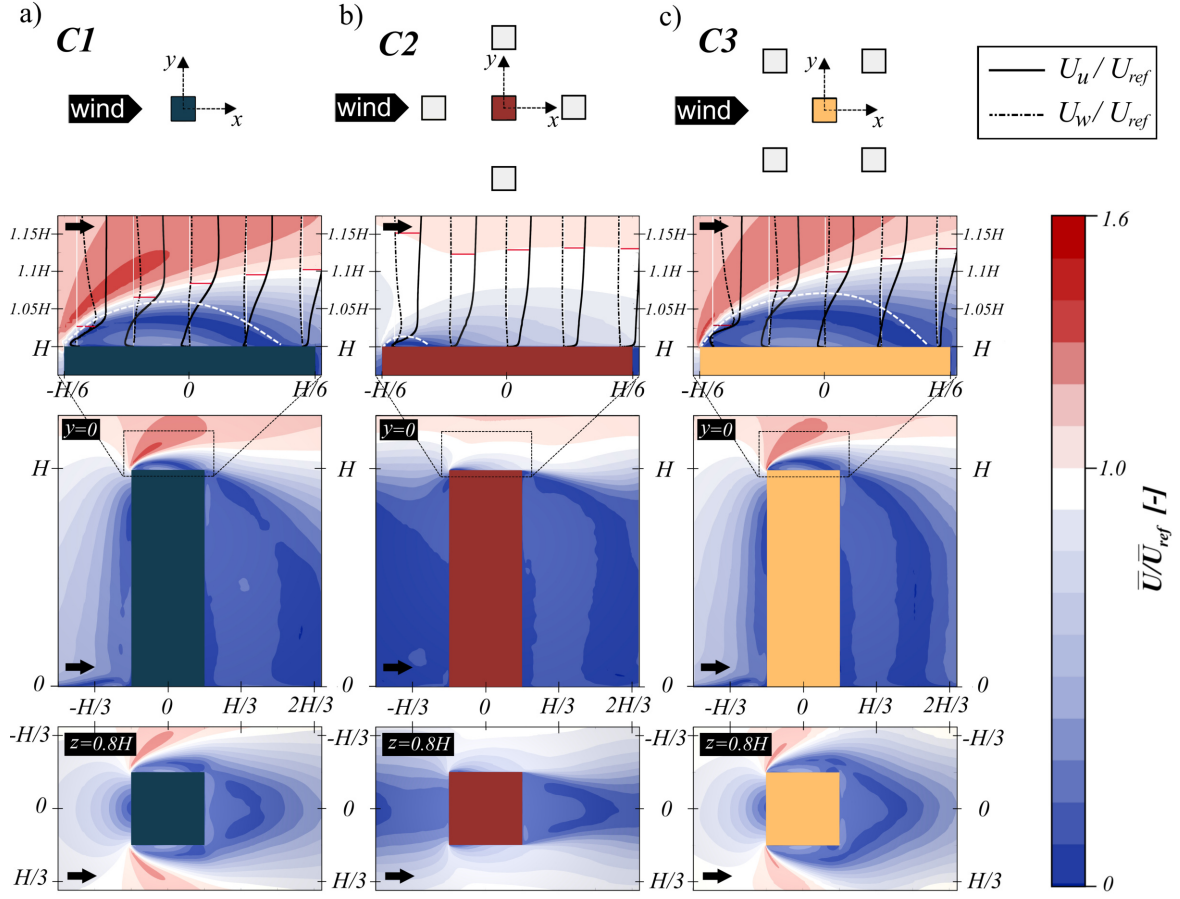


Figure 6.11. Velocity mean-field in the vertical xz centre plane of the flow through $(0, 0, 0)$, with an enlarged view of the area above the roof, and horizontal xy plane through $(0, 0, 0.8H)$ for three study cases: (a) C1, (b) C2 and (c) C3, adapted from [41]

to 50% in case C2. Conversely, it is completely absent in the C3 case. Interestingly, wind speed across the entire central plane of the flow above the roof in cases C1 and C2 is increased. However, outside this plane, the influence of the cone vortices is conspicuous, as demonstrated in four horizontal planes above the roof in Figure 6.12. Specifically, in cases C1 and C2, the influence of these structures wanes above the windward half of the roof, starting at the height of $0.25B$ from the rooftop (z_0). Beyond $z_0 = 0.5B$, their influence no longer persists across the roof. Near the building facades, wind speed increases in cases C1 and C2, though these increases are somewhat more modest than those above the roof, reaching up to 20% relative to U_{ref} near the separation edges. Once again, case C3 shows no acceleration, underlining the pronounced effect of the building located upwind.

6.2.2.2 Turbulence intensities

Regarding second-order velocity statistics, surface plots of the turbulence intensities in the x direction overlapped with the instantaneous velocity streamlines are shown in Figure 6.13 for both wind angles.

At 0° , in all study cases, the zone around the building is highly turbulent with I_u above 30%, characteristic for separation regions. The horizontal plane at $z = 0.8H$ reveals the effects of the surrounding buildings. Considering the generated shear layer around the facade, a broad layer

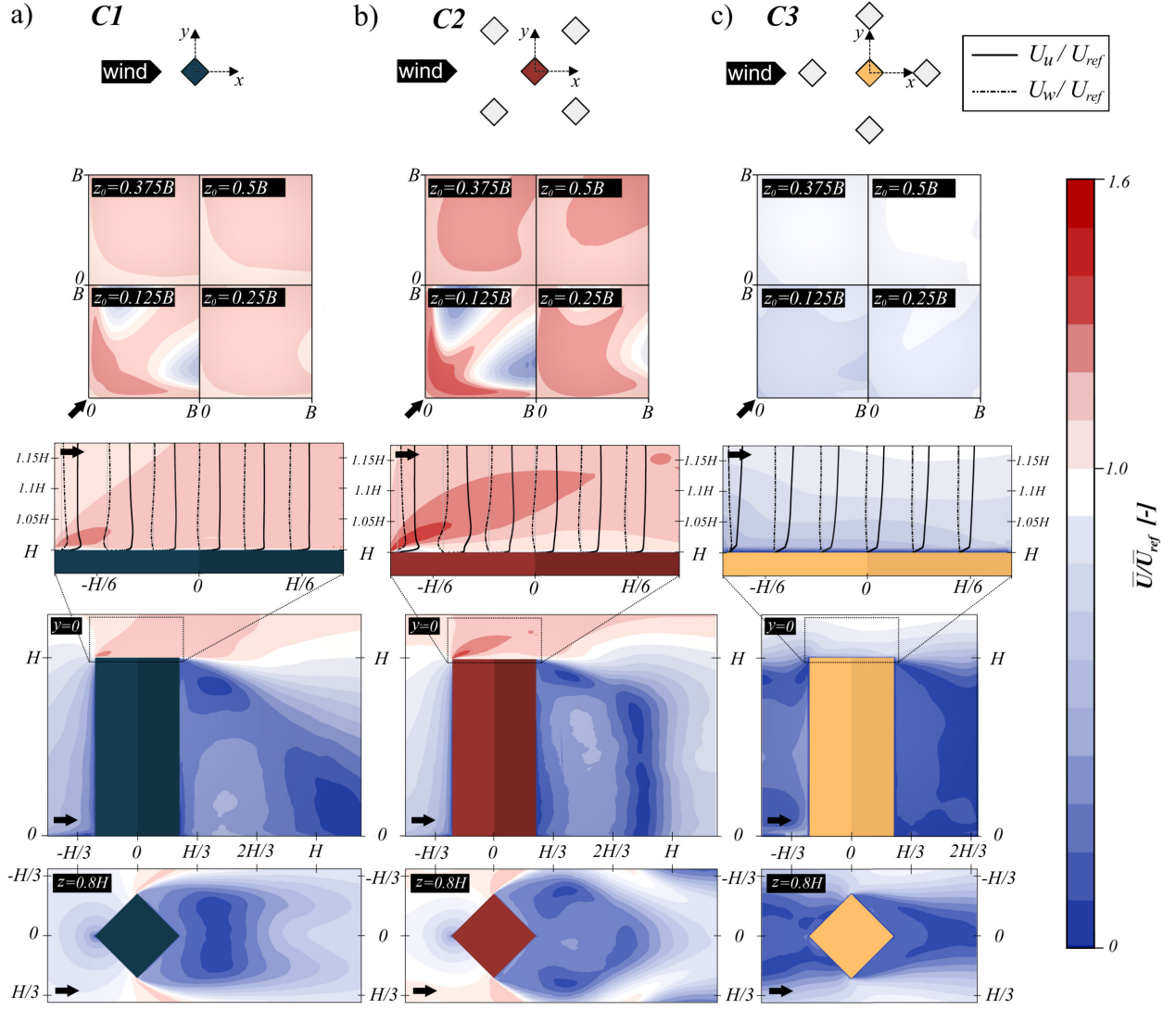


Figure 6.12. Velocity mean-field in the vertical xz centre plane of the flow through $(0,0,0)$, and horizontal xy plane through $(0,0,0.8H)$, with an additional enlarged view of the area above the roof in the vertical central plane of the flow and four horizontal planes at height $0.125B$, $0.25B$, $0.375B$ and $0.5B$ from the rooftop (z_0), for three study cases: (a) C1, (b) C2 and (c) C3, adapted from [41].

is reported in the C1 case, while case C2 is overwhelmed by the turbulence generated from the upstream building. The C3 case again depicts a tendency of the surrounding buildings in the “x” shape arrangement to compress the flow around the central one.

Turning to the 45° wind angle scenario, a noticeable difference in turbulence levels above the roof is observed. Specifically, in cases C1 and C3, turbulence levels above the main diagonal of the roof are not only below 30% but are also comparable to free stream values. Around the facade, case C2 exhibits a broader shear layer compared to case C1, appearing more rounded due to the positioning of surrounding buildings. Flow around the building in case C3 show high turbulence across all zones surrounding the building.

6.2.3 Surface pressure

At the end of Section 6.2, an insight over the surface pressure distributions by means of mean and RMS pressure coefficient is presented in order to link the previous flow observations. For

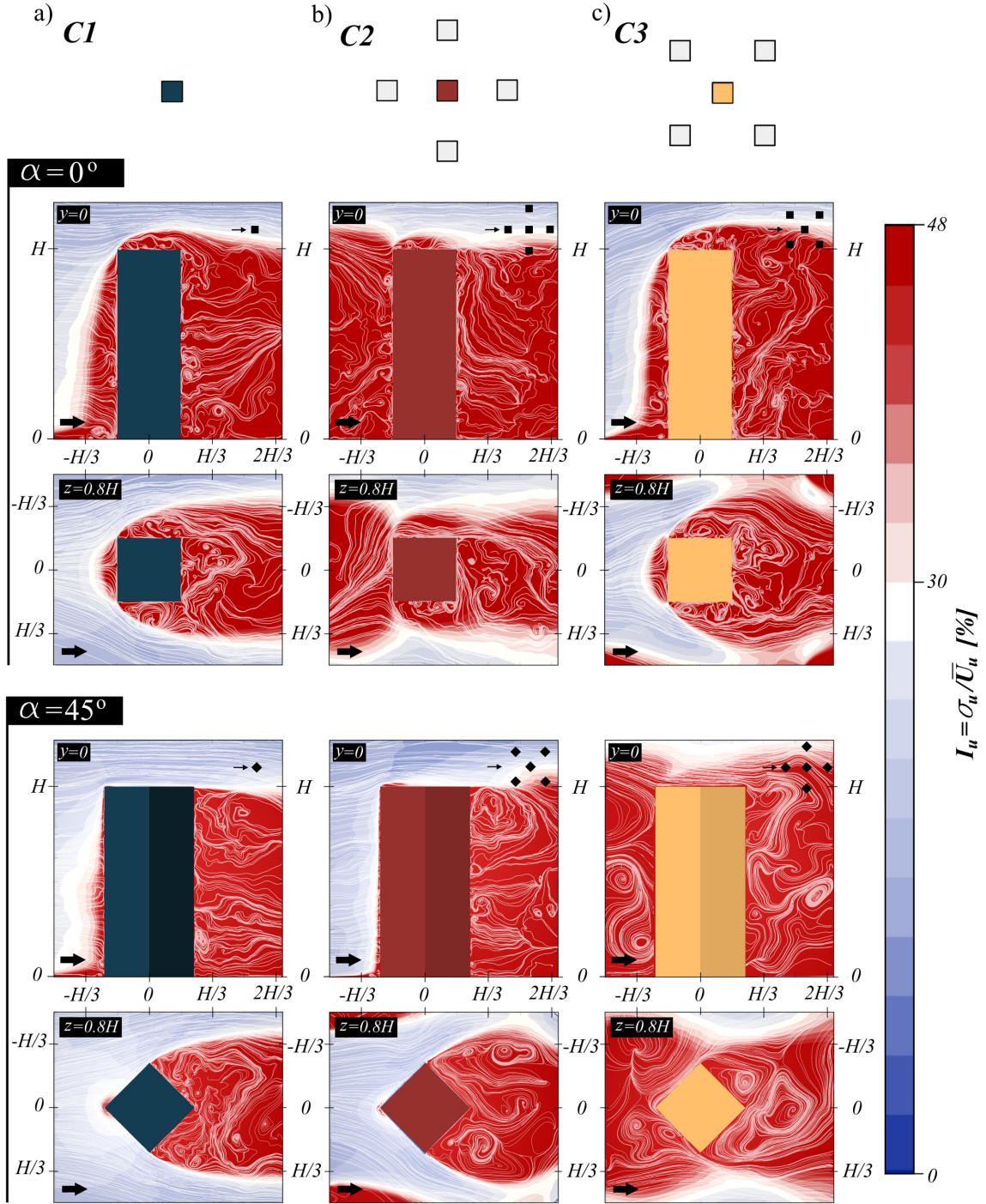


Figure 6.13. Turbulence intensity field in x direction overlapped with the instantaneous velocity streamlines in the vertical xz centre plane of the flow through $(0, 0, 0)$ and horizontal xy plane through $(0, 0, 0.8H)$ for three study cases at 0° and 45° : (a) C1, (b) C2 and (c) C3, adapted from [41]

each study case, plots of both mean (\bar{C}_p) and RMS (C_p'') pressure coefficients over the predefined paths are reported. This includes plots across the central line of the building in the vertical plane (Figure 6.14) and two rings around the facade (Figure 6.15) for both wind angles.

Wind approaching at 0°

In all three cases, positive values of \bar{C}_p in Figs. 6.14 and 6.15 are associated with the front facade that faces the incoming flow. In fact, this is also recorded in the C2 case, which agrees with the findings in Subsection 6.2.1. Namely, the shear flow from the upstream building hits

the building behind without overshooting it. The stagnation point on the front facade in the C2 case is located at $\sim 0.95H$. This point indicates the upward-moving fluid that separates at the top leading edge of the building, resulting in a short recirculating region above the roof, as reported in Subsection 6.2.1. The same behaviour was detected by Martinuzzi and Havel [88] for two cubes in a tandem arrangement, with the longitudinal distance between the centres of $4h$, where h denotes the cube's height. Nevertheless, \bar{C}_p values in the C2 case are much smaller than those reported in the other two cases owing to the “sheltering effect”. For case C1, the stagnation point is located at $z = 0.85H$, while for case C3, it is slightly lower at $z = 0.8H$.

Regarding negative values of the mean pressure coefficient in Figures 6.14 and 6.15, they are detected over the rest of the building surfaces. In particular, detected separation regions are governed by the large suction. At the rooftop of all three cases, a characteristic “hump shape” is detected in plots of \bar{C}_p over the central line in Figure 6.14. This particular shape is typical for separated flow followed by the reattachment [174]. Maximal suction in the C1 and C3 cases is found at a distance of $0.4B$ relative to the leading edge on the rooftop. This is followed by the pressure recovery zone downstream and a less pronounced plateau, typical for the reattachment zone [168]. Furthermore, the maximum C_p'' is recorded in the pressure recovery zone, also confirmed in [168]. In the C2 case, the maximal suction is found in the vicinity of the leading edge. Moreover, a plateau after the pressure recovery is strongly pronounced, confirming that the flow is parallel to the roof, as observed by the streamlines and mean velocity plots.

At the lateral walls, a notable shift in the distribution of \bar{C}_p at different heights is observed in cases C1 and C2, as depicted in Figure 6.15. This behaviour aligns with the findings reported by Ricci et al. [165]. Namely, in the region just behind the stagnation point, the reattachment length reaches the maximum in terms of the distance from the upwind side corner of the high-rise building. Above that height, the flow is deviated upwards by the high suction occurring at the top part of the building. In contrast, at lower heights, the reattachment length starts decreasing, reaching a minimum at the bottom of the side wall. This trend, however, is not evident in the C3 case, where the distribution of both \bar{C}_p and C_p'' shows no discrepancy at different heights. This is in accordance with the flat shape of the wake zone in Figure 6.9. All three cases have an almost uniform distribution of pressure coefficients on the leeward back facade, as shown in Figs. 6.14 and 6.15.

Wind approaching at 45°

Analysing the distribution of the \bar{C}_p and C_p'' above the roof at 45° wind angle, similarities with observations at 0° are notable. Namely, in cases C1 and C2, the zones where the cone vortices emerge are followed by a characteristic “hump” shape in the line plots in Figure 6.14. Furthermore, the maximum negative values of \bar{C}_p are related to the core of the primary vortex (consistent with the findings in [71, 177]), followed by the pressure recovery zone. A pronounced plateau in the \bar{C}_p plots symbolises the flow attached to the roof. It is noteworthy to contrast the sizes of the cone vortices in the C1 and C2 cases. A larger separation in the C2 case is manifested through the less steep recovery zone and shorter plateau. Regarding the C3 case, the plateau is strongly pronounced, with indications of minor separation near the windward edge.

The windward facades in all three cases are associated with the positive \bar{C}_p values and their slight decrease towards the separation edges (as shown in Figure 6.15), indicating the flow parallel to the facade. On the other hand, the leeward faces in all three cases experience suction, with both the \bar{C}_p and C_p'' displaying an almost uniform distribution. In the C3 case, the C_p'' plots reveal high fluctuations on the windward facades, as well as the reattachment location of the wake generated from the upstream building and indicated by maximal C_p'' .

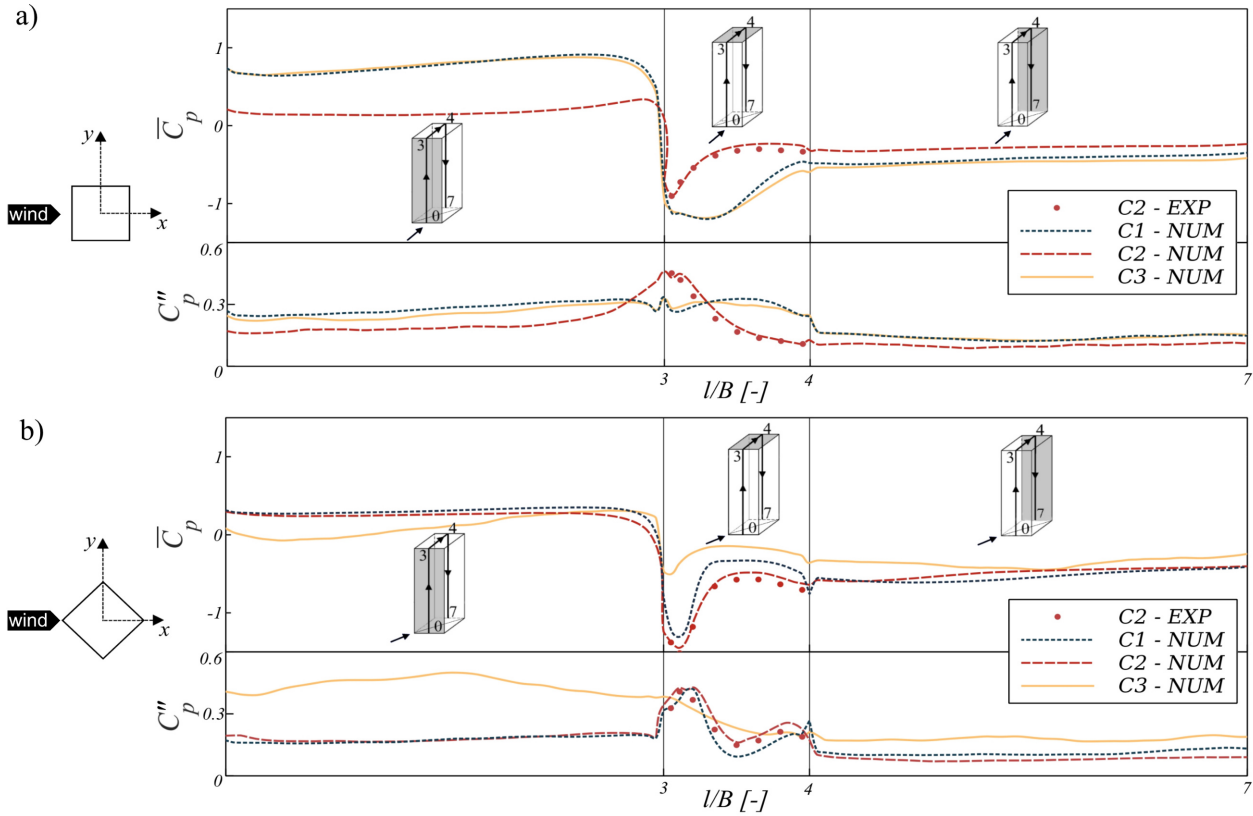


Figure 6.14. Line plots of average (\bar{C}_p) and RMS (C_p'') of the pressure coefficient at the building surface along the path over the central line of the building at 0° (a) and 45° (b), adapted from [41].

One should notice an almost perfect match of the experimental and numerical results in Figure 6.15 for the C2 case at both wind angles. That implies the accurate prediction of the velocity field around the facade since no other experimental measurements are available in a certain zone. Lastly, it can be seen that the prediction of the C_p'' on the rear corners of the buildings shows the well-captured high fluctuations, also noted in [179].

6.3 Conclusions

To close this section, an extensive description of the wind flow in three analysed configurations (C1, C2 and C3) is given. Additionally, specifics regarding two roof shapes, flat and decked, in configuration C1 are provided.

Results on the flow field reveal the complex nature of aerodynamic interactions in urban environments. The switch from flat to decked roof type dumps the separation above the roof. Furthermore, decking the roof shows insensitivity to the change in wind direction.

Regarding group configurations, building arrangement and wind direction significantly influence the emerging flow behaviour. For example, in the “cross” shape building arrangement (configuration C2) at 0° , the front building creates a “sheltering effect” on the central one. This effect causes suppressed separation around the building, a reduction in wind speed and an increase in turbulence levels. Conversely, at a wind angle of 45° , the positioning of the two upstream buildings initiates the Venturi effect, which accelerates flow around the central building, thereby increasing the mean wind velocity above the roof in the vertical central plane of the flow up to

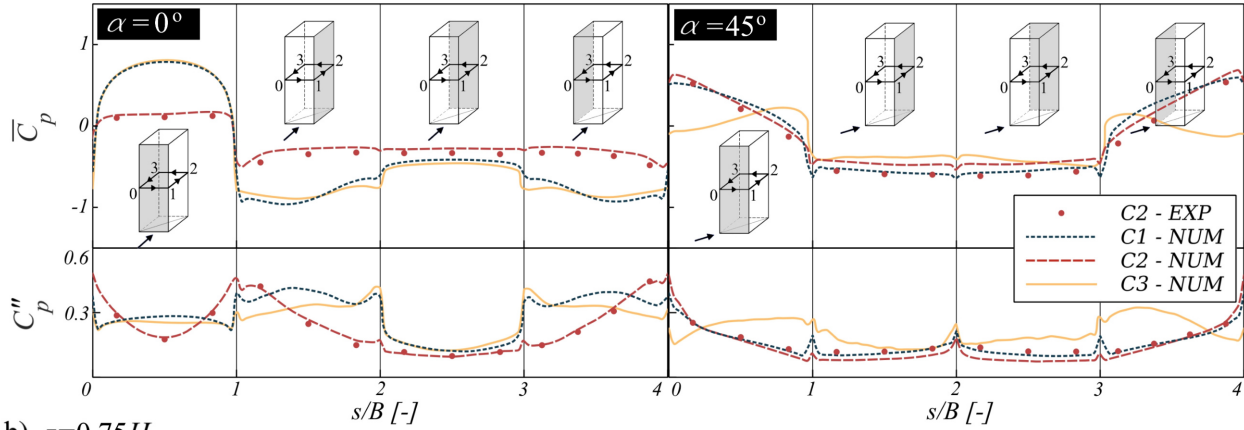
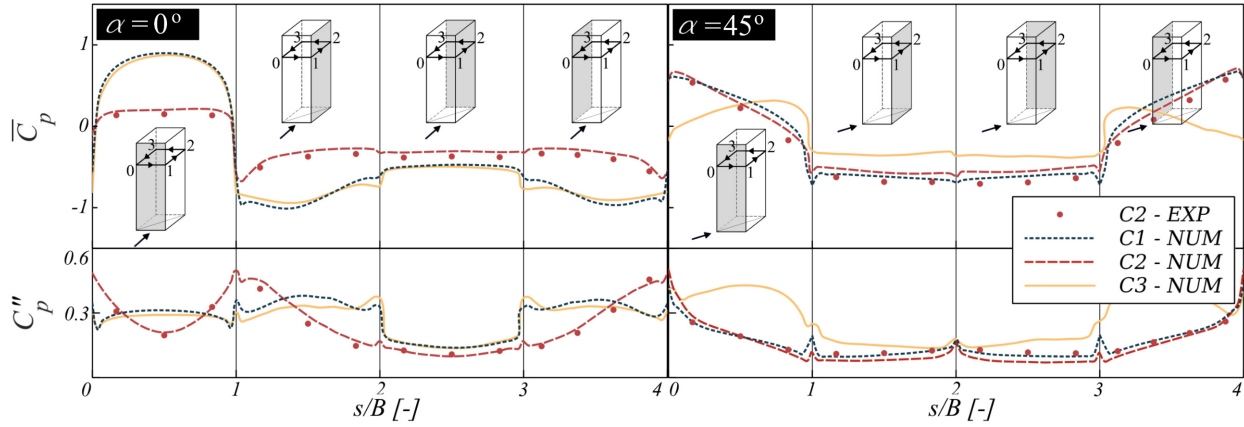
a) $z=0.5H$ b) $z=0.75H$ 

Figure 6.15. Line plots of average (\bar{C}_p) and RMS (C_p'') of the pressure coefficients at the building surface along the rings at $z = 0.5H$ and $z = 0.75H$ for 0° (a) and 45° (b) wind angles, adapted from [41].

50% compared to the reference free-stream velocity. This arrangement, in conjunction with the two downstream buildings, compresses the flow around the central building. As a result, the separation zones around the central building appear more rounded and broader in the lateral direction compared to the isolated building configuration C1. The wake zone's shape over the building height is flattened, and the separation zones above the roof and around the facade are approximately 10% larger. A similar pattern is observed for the “x” shape arrangement, configuration C3, but for the opposite wind angles.

7 Wind energy harvesting potential around high-rise buildings

The previous chapter provided details of the flow around the high-rise building in terms of separation zones, their location, dimensions, and nature. The aim of this chapter is to provide details on the local characteristics of the flow, which are thought to be crucial in determining the potential for wind energy harvesting and choosing the wind turbine's optimal type and position. Section 7.1 provides a short overview of common types of wind turbines in urban areas. Section 7.2 is revising the wind flow characteristics for energy exploitation, presented in the same manner as the previous chapter. First, the influence of the roof shape on wind energy potentials is addressed in Subsection 7.2.1. Second, analyses for three study cases of the central building in three different configurations are exposed in Subsection 7.2.2. Overall conclusions on results exposed in this chapter are given in Section 7.3.

7.1 Common types of wind turbines for urban environment

Typically, wind turbines are installed in locations with strong, steady winds and low turbulence levels. These conditions can be found in coastal and rural areas with open, flat terrain. In contrast, urban areas often have lower average wind speeds and higher turbulence levels due to the buildings' presence and rapidly changing wind direction [10]. That clearly has a significant effect on the design of wind turbines for urban wind harvesting. Various literature reviews summarise the research studies of common types of small wind turbines used in the urban environment [10, 12, 35, 104, 180].

Wind turbines are generally classified as Horizontal Axes Wind Turbines (HAWTs) and Vertical Axes Wind Turbines (VAWTs). HAWTs are still the most common type of wind turbine due to their aerodynamic performance. Nevertheless, high turbulence and skewed flow in urban areas were found to affect their efficiency and operability, since the inherited design is primarily for open terrain applications [35]. They need to be installed outside the flow separation zones around buildings, including the roof separation zone [35]. In addition, Carpmann [181] highlighted the increased strain and loading that wind turbines experience in highly turbulent environments, as well as the frequent changes in wind direction.

On the other hand, VAWTs were reported to cope better with high turbulence and the change in wind direction and might even benefit from it using the appropriate design [182]. A study in

[183] reported such behaviour, showing the improved power output for a specific type of VAWTs in the skewed flow, in contrast to the power output decrease of HAWTs. Moreover, skew angle values between 15° and 35° can promote energy yield up to 12% by applying a particular type of VAWTs as exposed in [107]. Regarding the social acceptance aspects, VAWTs evoke lower noise levels and tend to be more aesthetically pleasing [9]. The review paper by Tasneem et al. [12] gave a table view of the advantages and disadvantages of HAWTs, VAWTs (Lift based), VAWTs (Drag type) and H-Rotor. They concluded that VAWTs were the preferable choice for urban application due to their omnidirectional and lower sensitivity to high turbulence, as well as better social acceptance (less noisy and environmentally friendly). Furthermore, the reported studies showed that H-blade rotors performed better than the conventional Darrieus and Savonius designs [12]. A detailed summary of the advantages and disadvantages of certain types of urban wind turbines based on the Wineur project report is given in [184].

The International Electrotechnical Commission, Standard 61 400–Part 1 [185] is a set of guidelines for designing wind turbines that consider factors such as safety, durability, and performance. These standards proposed two categories of wind turbines for use in urban areas: those designed for high-turbulence environments (categories A and A+) and those designed for moderate-turbulence environments (category B). However, the highest levels of turbulence (16–18%) were defined for turbines in categories A and A+. This underlined the necessity for a new category of wind turbines that can handle turbulence levels higher than 18%, as can commonly be found in urban environments. Wind turbines exposed to these conditions are currently labelled as class S turbines. Turbines in that class are designed to meet the unique requirements, whether it is turbulence higher than 18% of other specifics, removing borders of standard classes. The design values for these wind turbines are directly given by a manufacturer. Furthermore, turbulence intensity greater than 18% is not necessarily a non-favourable situation and can improve the performance of small VAWT [182]. A detailed account of the approach adopted in standards for urban wind turbines is given in [10]. A detailed account of the approach adopted in standards for urban wind turbines is given in [10].

In order to distinguish the wind energy resources at potential installation sites by taking into account the type of wind turbine, three types of wind turbines are chosen for further analyses in Subsection 7.2.2, similar to [96]:

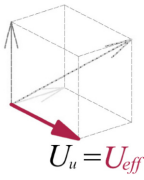
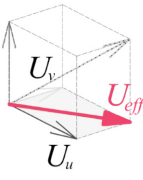
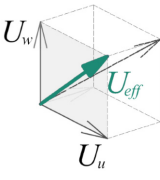
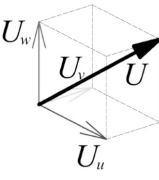
- The most common HAWTs,
- The Darrieus (lift-based) VAWTs, and
- The horizontally-mounted Darrieus VAWTs.

These different types of wind turbines have different effective wind velocities. For example, the WPD calculation for HAWTs only considers the streamwise (U_u) mean velocity vector component. For lift-based wind turbines, such as the Darrieus VAWTs, both the streamwise (U_u) and vertical (U_w) components of the mean velocity vector are used. For horizontally-mounted Darrieus VAWTs, the streamwise (U_u) and lateral (U_v) components are considered. Table 7.1 summarised these effective wind velocities (U_{eff}).

7.2 Wind characteristics for energy exploitation

It is well-known that knowledge of the wind flow at a building's micro-location is crucial for determining the potential for using wind energy around the building [9]. The flow pattern

Table 7.1. The effective mean wind speed as a function of the employed velocity vector components

| Effective velocity vector |  |  |  |  |
|---------------------------|---|---|--|---|
| Effective wind speed | U_u | $\sqrt{(U_u^2 + U_v^2)}$ | $\sqrt{(U_u^2 + U_w^2)}$ | $\sqrt{(U_u^2 + U_v^2 + U_w^2)}$ |
| U_{eff} | | | | |
| Type of wind turbine | HAWTs | Hor.-mount. VAWTs | VAWTs (lift-based) | total wind energy |

changes radically across potential installation locations of future wind turbines due to the change of wind angle or arrangement of neighbouring buildings. In Chapter 6, flow amplifications and zones of high turbulence occur in certain configurations, which have an influence over the entire operational lifetime of a turbine [35]. In [35], the impact of skew angle on rotor performance was also emphasised.

In the present research, the focus of further investigation of available wind energy resources is on the zone above the roof of the principal building, with a scarce review of the zone around the facade only in the C1 configuration. The particular choice of the roof zone is made with regard to the highest recorded acceleration around the building in all three configurations. Apart from the flow acceleration, two other quantities of interest are identified: turbulence intensities and skew angle. Each of them can affect the efficiency and operability of wind turbines in a positive or negative way, as described in the previous Subsection 7.1. The wind energy potential is evaluated using the normalised wind power density (P^*), calculated as follows:

$$P = \frac{1}{2}\rho U^3; P^* = P / (\frac{1}{2}\rho U_{ref}^3) \quad (7.1)$$

$$P_{eff}^* = U_{eff}^3 / (U_{ref}^3) \quad (7.2)$$

Here, U represents the mean velocity magnitude, U_{eff} effective mean velocity defined in Table 7.1 and ρ is the air density. The wind power density is normalised using $\frac{1}{2}\rho U_{ref}^3$.

The presentation of wind characteristics for energy exploitation is organised into two subsections. Subsection 7.2.1 provides results for configuration C1, including two roof shapes. The second investigation unit, exposed in Subsection 7.2.2, concentrates on the roof zone above the central (principal) building in three configurations, referred to as three study cases: C1, C2 and C3, in Section 6.2.

7.2.1 Isolated high-rise building: Flat vs. decked roof shapes

This subsection presents wind flow characteristics and potentials for wind energy harvesting expressed through wind power density around the isolated high-rise building, configuration C1. It encompasses zones around the facade in Subsection 7.2.1.1 and above the roof in Subsection 7.2.1.2. The target is on confronting results for the flat and decked roof shapes.

7.2.1.1 Wind energy resource around the facade

The building model induces flow accelerations, which might represent an opportunity for wind energy exploitation. Figure 7.1 indicates such zones around the facade through the WPD plots in the horizontal plane at $z = 2.25B$ for two wind directions, 0° (Figure 7.1(a)) and 45° (Figure 7.1(b)), and relevant vertical planes (marked with a red dashed line in the horizontal plane) for the flat roof case. Results are also applicable to the decked roof.

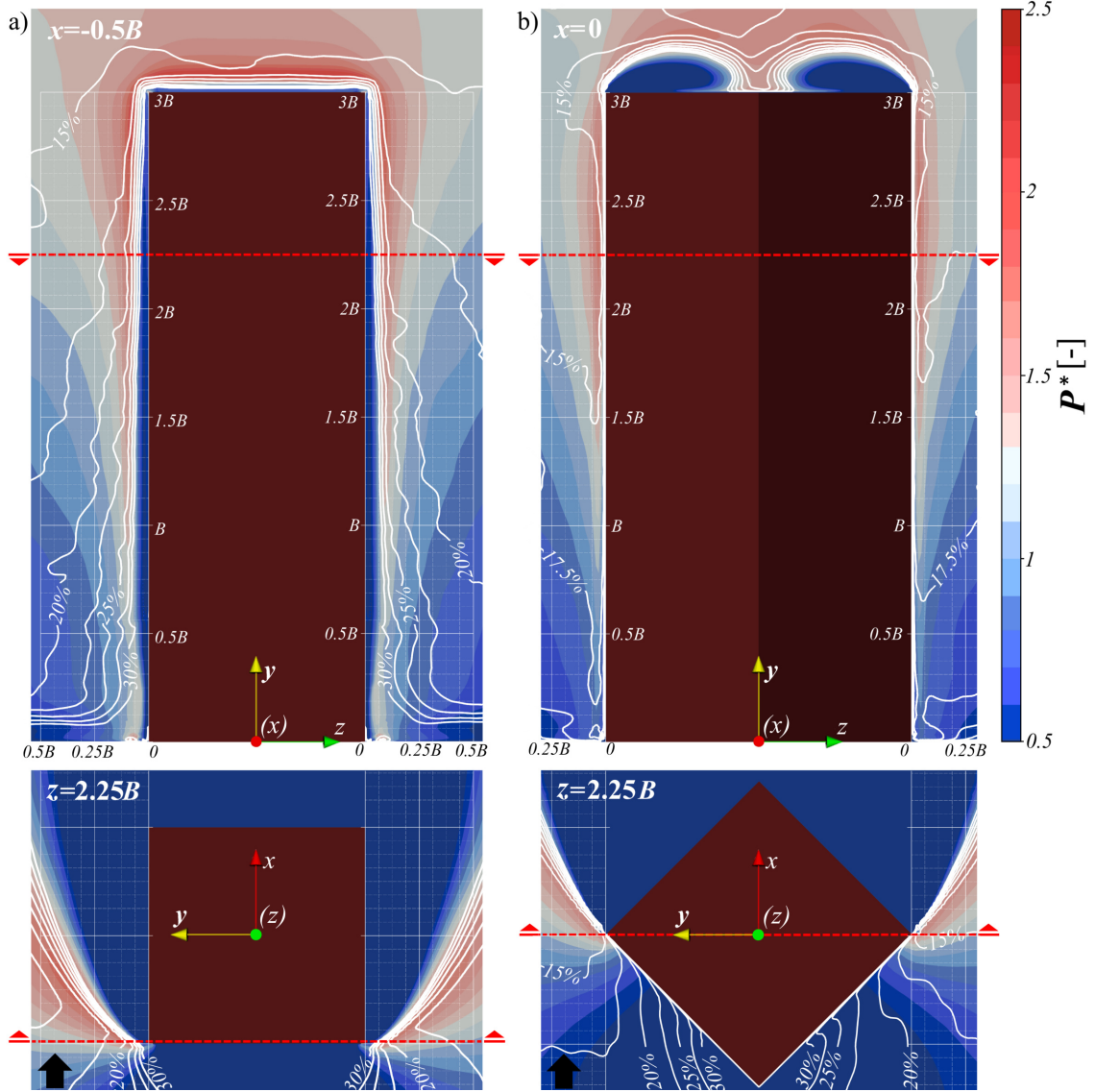


Figure 7.1. Wind power density normalised with $1/2\rho U_{ref}^3$ (P^*) in configuration C1 for the flat roof case in (a) the vertical yz plane through $(-B/2, 0, 0)$ and horizontal xy plane through $(0, 0, 2.25B)$ at 0° and (b) the vertical yz plane through $(0, 0, 0)$ and horizontal xy plane through $(0, 0, 2.25B)$ at 45° .

White contour lines represent the turbulence intensity in wind direction (I_u), adapted from [40].

At 0° , the zone with normalised WPD > 1 occurs near two leading edges, as shown in the horizontal plane in Figure 7.1(a). Since these edges are also the separation points of the flow, the following zones behind them have low WPD and high turbulence intensity due to the separation bubble and wake region. Therefore, the accelerated flow is located more than $0.2B$ away from the lateral walls, which is why they do not represent promising candidates for potential wind turbine location, as well as the lee of the building. Preferable locations are separation edges. Moreover, the plot in the vertical yz plane through $(-0.5B, 0, 0)$ reveals the trend of increasing

the WPD with height accompanied by a decrease in turbulence intensity. Above $z = 2B$, a favourable region regarding wind energy resources is placed at distance $< 0.075B$ from the leading edges with $P^* > 1.5$ and $I_u < 20\%$.

As regards the 45° wind angle (Figure 7.1(b)), the normalised WPD > 1 is found close to the separation edges, like at 0° , with the difference in turbulence intensity levels that are lower in this case. It is evident from the plot in the vertical plane that the same improvement in WPD with height is retained, analogous to the 0° case. Namely, above $z = 2B$, P^* is ~ 1.5 , and I_u is not greater than 15% in the vicinity of the building.

7.2.1.2 Wind energy resources above the roof

Above the roof, the flow pattern affects the WPD distribution in a way similar to the flow around the facade. The separation regions are related to WPD less than 1 and high turbulence intensities, as presented in Figure 7.2 on plots in the central plane of the flow.

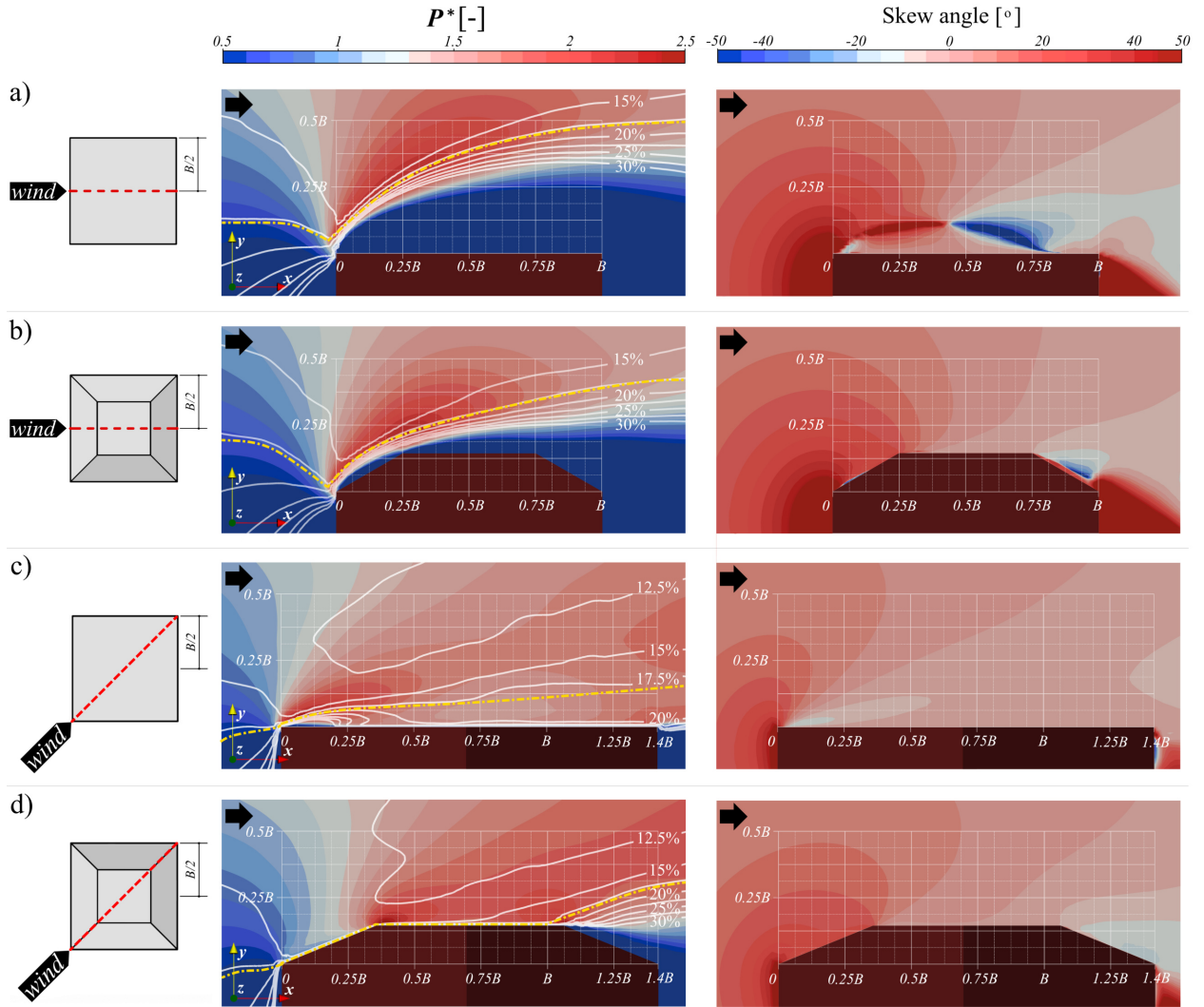


Figure 7.2. Wind power density, normalised with $1/2\rho U_{ref}^3$, overlapped with white contour lines representing the turbulence intensity in wind direction (I_u), with a line indicating $I_u = 18\%$ (the yellow dashed-dotted line), and skew angle in the central plane of the flow in configuration C1 at 0° for (a) the flat and (b) decked roof shape and at 45° for (c) the flat and (d) decked roof shape, adapted from [40].

The angle of attack: 0°

At 0° , the region with WPD values higher than 2.0, reaching up to 2.3, is noticed above the upwind half of the roof. The lowest points of this region are located just above the upstream separation corner at height $z_0 = 0.05B$ (z_0 represents height from the rooftop) for both roof shapes. Moving downstream, the zone of high WPD ($P^* > 2$) follows the shape of the separation zone, resulting in maintaining these high values with increasing height. Above the central roof point, it reaches the height of $z_0 = 0.35B$ in the flat roof case and only $z_0 = 0.125B$ in the decked roof case. Turbulence intensity in this region is lower than 25% and drops with height.

The skew angle plots in Figure 7.2 show that relatively high values occur in the core of the separation region in the flat roof case. It can be attributed to the reversal flow above the roof and the change in wind direction inside the separation bubble (see profiles of velocity component in the x direction in Figure 6.3(b)). In contrast, above the decked roof, this phenomenon has not been observed, as the separation zones are significantly less pronounced. Outside the separation region, the flow is highly skewed in both cases close to the upstream edge as it must overcome the obstacle and gradually becomes parallel to the roof, following the borders of the separation region.

The angle of attack: 45°

Focusing on the 45° wind angle, flow acceleration, reflected through $P^* > 1.5$, is recorded above the flat part of both roof types over the whole central line of the flow. Furthermore, the turbulence intensity levels are lower than 18% close to the surface. These imply the flow attached to the roof, which is also confirmed by the skew angle, which is almost equal to the roof inclination.

To tackle the impact of the cone vortices in the flat roof case, Figure 7.3 presents the plots of the WPD and I_u in the horizontal xz plane at four different heights above the roof (z_0). It is clear from the figure that the channel formed between two conical vortices shrinks at lower heights ($z_0 = 0.0625B$) and spreads with increasing distance from the roof, following the shape of the separation zone. It can be concluded that from $z_0 = 0.25B$, the effect of cone vortices is negligible to the WPD, and values are higher than 1.5 at the majority area of the roof. The same trend is reflected in the turbulence intensity distribution where I_u is lower than 15% at $z_0 = 0.25B$ above 2/3 of the roof area. In the decked roof case, the separation region on the flat part of the roof is quite small. Hence, this effect is limited to the height of $z_0 = 0.05B$.

Fig. 7.4 introduces performance maps above the roof depending on WPD and the turbulence intensity I_u and classifies zones above the roof from unfavourable to most favourable zone for wind turbine positioning. Four zones in the central xz flow plane are detected. Zone 0 is characterised by no amplification of the wind speed ($P^* < 1$), and it should be avoided as a suitable location. Zone 1 is characterised by $I_u > 18\%$ in the windward direction, with $P^* > 1$. This zone can be considered as an installation place of specially designed turbines (class S according to the [185]) that perform well in turbulence. The most favourable zones for placing wind turbines are Zones 2 and 3, as $P^* > 1$ with $I_u < 18\%$. In Zone 3, $P^* > 1.5$ occurs closer to the roof surface, while Zone 2 lies in the buffer zone between the unobstructed flow and the disturbed flow around the building (with P^* between 1.0 and 1.5).

At 0° , the separation zones above the roof, described through Zones 0 and 1, are strongly pronounced, especially above the flat roof. Zone 3, the most desired one for wind energy harvesting, is spread above the height of $0.125B$ relative to the upstream edge. The lowest

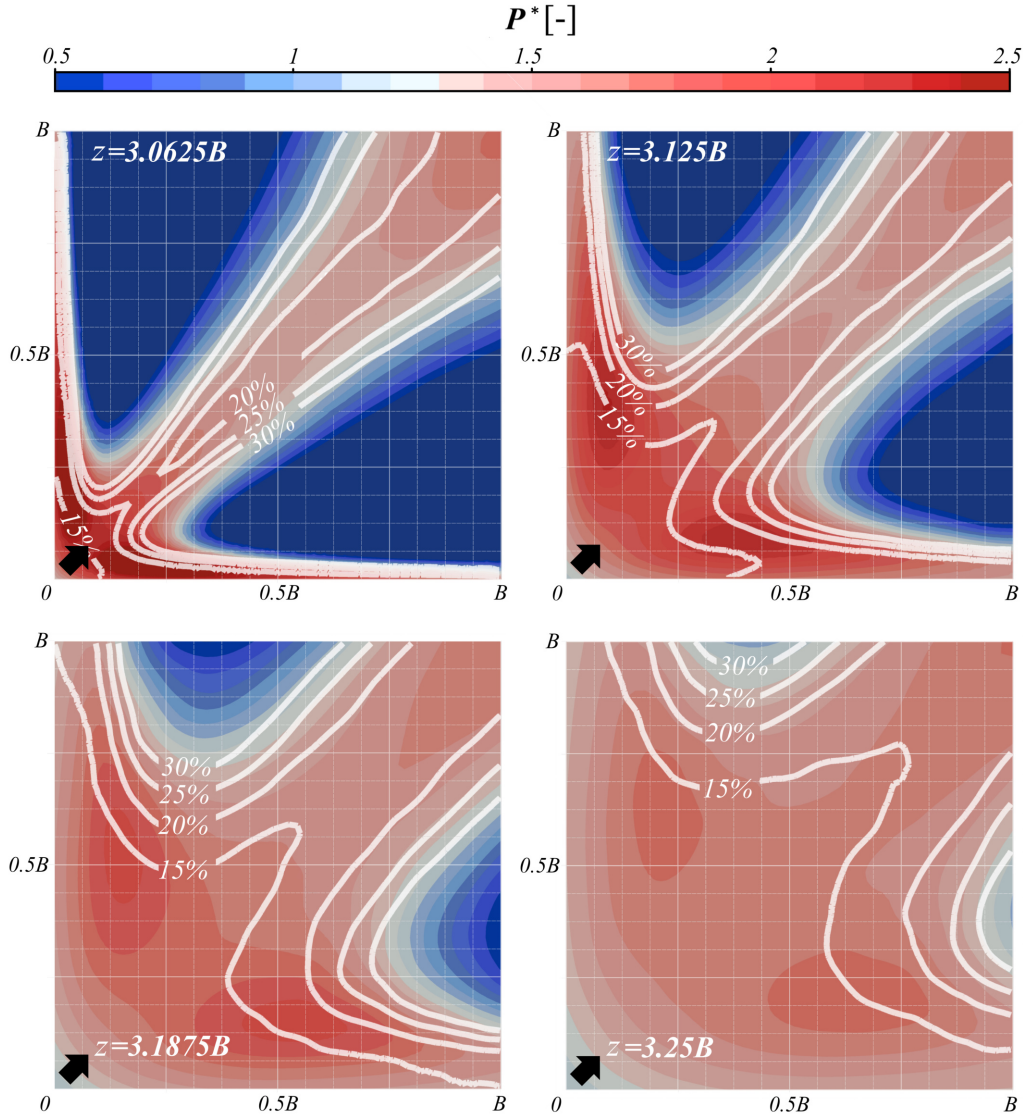


Figure 7.3. Wind power density, normalised with $1/2\rho U_{ref}^3$ and overlapped with white contour lines representing the turbulence intensity in wind direction (I_u), plots above the flat roof at four heights ($z = 3.0625B, 3.125B, 3.1875B, 3.25B$) for the wind approaching at 45° , adapted from [40].

locations are above windward edges and the height of the zone lower bound increases almost linearly with the increase in the distance downstream. A steeper increase occurs above the flat roof, and it reaches the height of $0.375B$ above the centre of the flat roof. In the decked roof case, when the relative distance from the roof surface is considered, values lower than $0.188B$ are present above the upwind half of the roof. That is a significant benefit of the decked roof shape since the mounting height of wind turbines is halved compared to the flat roof. Regarding the most favourable Zone 3, it is interesting that the area increases by decking the roof.

At 45° , unfavourable Zone 0 and Zone 1 are somewhat limited in the central plane. They occur in the vicinity of the flat roof and above the leeward slopes of the decked roof. Zone 2 is present at higher locations above the upwind half of the flat roof, while it is the dominant one above the windward slopes of the decked roof. The prevailing zone above the flat roof from the height of $0.061B$ on the upstream half and $0.125B$ on the downstream half is Zone 3. This particular zone is retained in the whole area above the flat part of the decked roof and at higher locations above the leeward slopes.

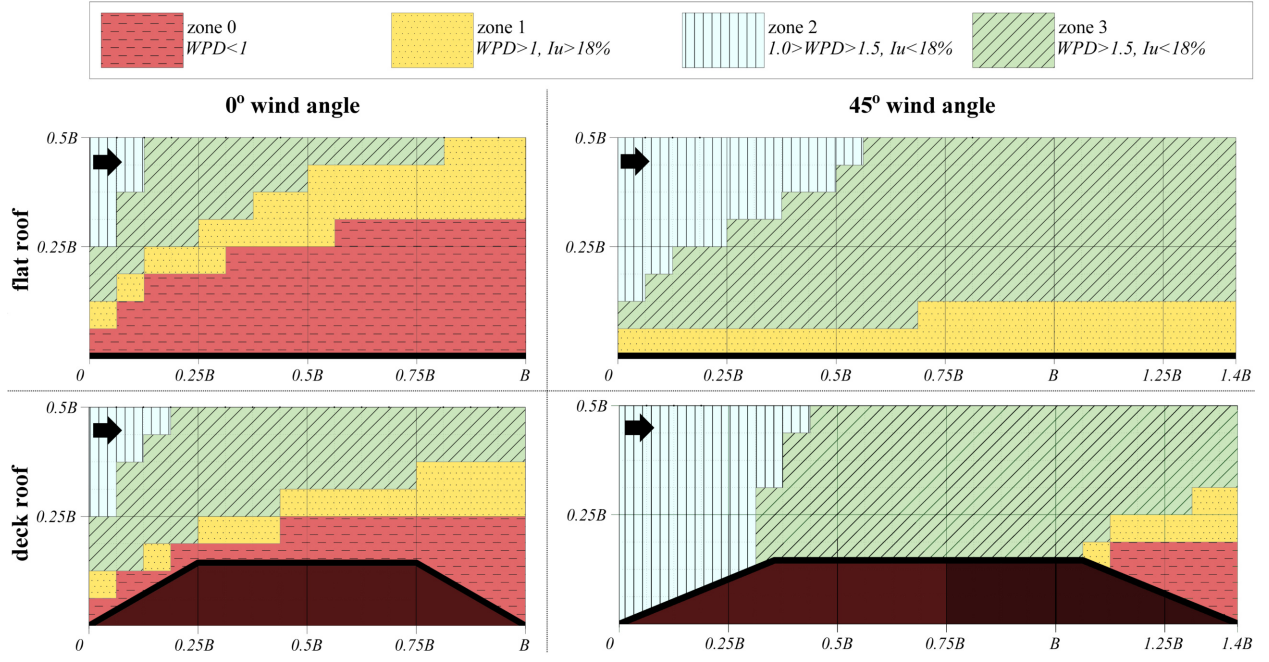


Figure 7.4. Proposed zoning above the roof in the central plane of the flow regarding wind power density and turbulence intensity for configuration C1, adapted from [40].

The highest potential for wind energy harvesting is observed at a 45° angle, particularly along the main diagonal of the roof, for both roof shapes. However, the influence of cone vortices has a detrimental effect when moving further in the lateral direction, as illustrated in Fig. 7.3.

7.2.2 Building clusters

This subsection analyses the wind energy resources above the roof for three study cases. It revises the wind flow characteristics in three study cases and highlights the potential wind energy resources and turbulence levels above the roof in Subsection 7.2.2.1. In addition, possible installation locations for wind turbines, depending on their type, are defined and analysed in Subsection 7.2.2.2.

7.2.2.1 Wind energy resources above the roof of building in three study cases

Figure 7.5 provides the normalised WPD marked as P^* above the roof in the central plane of the flow for two wind angles. Surface plots are complemented with the shape of the separation zone, a white dashed line, and the yellow dash-dotted line indicating $I_u = 18\%$, which is the maximum recommended level of turbulence for A+ class wind turbines according to the IEC Standard [185]. Besides, Figure 7.5 shows the turbulence intensities in the streamwise direction in the same plane (overlapped with the instantaneous velocity streamlines) and the skew angle. The skew angle is defined as an angle between the streamwise mean velocity vector component (U_u) and the component in the z direction (U_w).

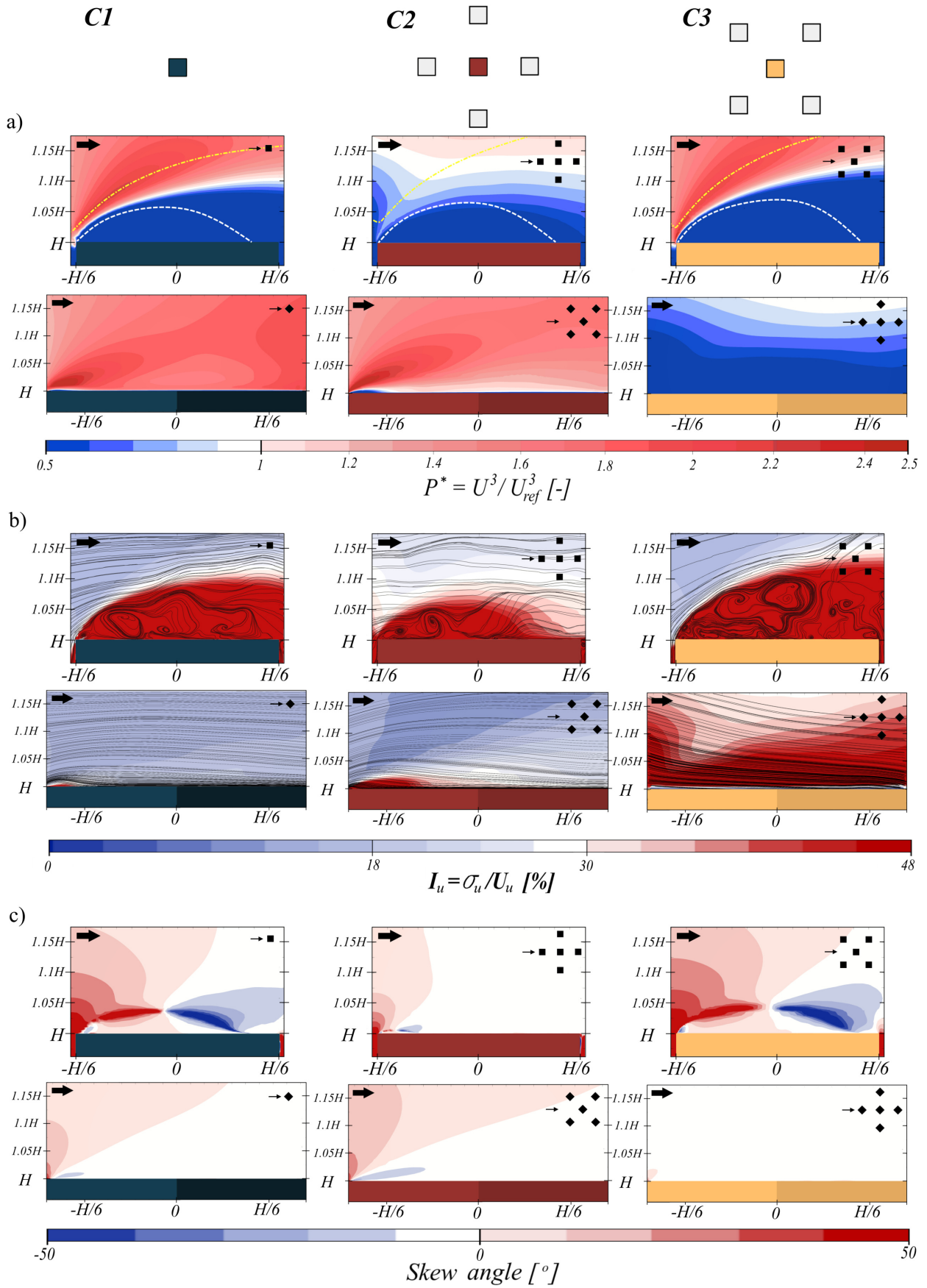


Figure 7.5. Roof zone in the vertical (xz) centre plane of the flow through $(0,0,0)$: (a) normalised Wind power density, complemented with the shape of the separation zone (white, dashed line) and a line indicating $I_u = 18\%$ (the yellow dashed-dotted line), (b) turbulence intensities in x direction overlapped with the instantaneous velocity streamlines and (c) skew angle, for cases C1, C2 and C3, adapted from [41].

Wind approaching at 0°

The most conspicuous normalised WPD of 2.3 is recorded in the C1 case at the height $z_0 = 0.025H$ (relative to the rooftop) above the windward edge ($x = -B/2$), as already reported in Subsection 7.2.1. The particular value is retained up to $x = -B/4$, with a gradual increase in height, which follows the shape of the separation zone and reaches $z_0 = 0.1H$. Likewise, in the C3 case, maximal normalised WPD occurs above the upwind edge of the roof at the same height and propagates downstream in the same way up to $x = -B/4$ ($z_0 = 0.1H$), reaching a slightly lower maximal value of 2.2. Conversely, the C2 case records normalised WPD around 1.0 above the height $z_0 = 0.15H$ over the whole central line on the rooftop, labelling this case as the least desirable for wind energy harvesting for wind approaching 0°.

Turbulence intensities in the windward direction at locations where maximal P^* takes place in the C1 and C3 cases match the maximal recommended 18% (marked with a yellow line in the plots). Increasing the height, turbulence intensities drop until they reach the free stream value ($I_{u,ref} = 14\%$). In contrast, in the C2 case, I_u exceeds 18% in the whole zone above the roof.

Regarding the skew angle, in all three cases, highly skewed flow is observed above the separation point at the windward edge. This results from the flow tending to lift above the building as it flows over it. As the flow moves downstream, it follows the shape of the separation zone, and the skew angle gradually decreases. In the C1 and C3 cases, the skew angle reaches zero at approximately $x = 0$ and $z_0 = 0.05H$, indicating flow parallel to the roof above the centre of the separation bubble. Downstream of this point, negative values of the skew angle show the flow's tendency to reattach to the rooftop. The core of the separation region is also characterised by highly skewed flow due to the reversal of flow direction. However, in the C2 case, the skew angle is close to zero already after $x = -0.1H$. Considering the regions where the highest values of P^* (in the C1 and C3 cases) are recorded, the skew angle in these regions ranges from around 50 degrees above the windward edge to approximately 15 degrees at $x = -B/4$.

Wind approaching at 45°

Focusing on the 45° wind angle, a significant flow acceleration above the roof in the central plane of the flow, observed in cases C1 and C2, results in normalised WPD exceeding 1.5 across the entire area. Maximum values, reaching up to 2.5, are detected in both cases. However, one should not neglect the impact of the cone vortices on the WPD in planes deviating from the central one, as outlined in Subsection 6.2.2 and illustrated in Figure 6.12. With WPD values falling below 1, case C3 is not a viable option for wind energy harvesting at the 45° wind angle.

Turbulence levels in the central plane of the flow for cases C1 and C2 are highly desirable for wind energy harvesting, given that nearly the entire region exhibits turbulence intensities in the x direction below 18%. Moreover, within the regions where cone vortices occur, turbulence levels drop below 18% above the height of $z_0 = 0.25B$ on the windward half of the roof. This trend is observed in both the C1 and C2 cases. However, the picture is different in the C3 case, where turbulence levels throughout the entire roof zone are substantially high.

Considering the skew angle, values in the central plane of the flow are near zero in all three cases, pointing out the flow parallel to the roof. Only near the windward corner does a slight increase occur, resulting from the upward deflection of the flow needed to overcome it.

Summing up the wind characteristics for energy harvesting, two lines along the roof width (B) located in the zone of high normalised WPD occurring at both wind angles are distinguished as

potential installation places for wind turbines in three study cases. The first line (L1) is above the windward edge for 0° wind angle at $z_0 = 0.025H$ since it is located closest to the rooftop but with high values of the skew angle at 0° wind angle. The second line L2 is parallel to the L1, at $x = -B/4$ (defined for 0° wind angle) and $z_0 = 0.1H$, where a low value of skew angle ($\sim 15^\circ$) is recorded at 0° and also the absence of influence of cone vortexes at 45° wind angle. The particular low values of skew angle are desirable for HAWTs. In the following subsection (Subsection 7.2.2.2), a more profound view of these locations is given.

7.2.2.2 Sensitivity of the wind energy prediction to the effective mean velocity

The ability to extract wind energy at a specific location depends on the wind turbine's characteristics. In Subsection 7.1, three types of wind turbines are depicted based on their effective mean velocity for wind energy harvesting. Profiles of normalised effective WPD are plotted in Figure 7.6 along the roof width (B) for two favourable line locations above the roof (defined in Subsection 7.2.2.1) at three wind angles. Namely, in addition to previously analysed 0° and 45° , the results for the 0° are used to demonstrate the distribution at the 90° wind angle. The normalised effective WPD profiles are defined by $P_{eff}^* = \frac{1}{2}\rho U_{eff}^3 / (\frac{1}{2}\rho U_{ref}^3)$, where U_{eff} is the effective wind speed determined by the wind turbine harvesting mechanism, presented in Table 7.1. Additionally, for comparison, Figure 7.6 depicts the total wind energy P^* (i.e. full potential) based on the magnitude of the mean velocity vector as well. Profiles over the width of the building (B) intend to give an insight into the lateral flow deviations. Namely, the separation bubbles above the roof represent a three-dimensional formation creating the non-uniform wind profile across the roof. Moreover, the representation used in Figure 7.6 is suitable for determining the optimal position or considering installing multiple small-scale wind turbines in the defined lines.

Distribution over the first line (L1)

In the C1 case, plots over the first line (marked L1 in Figure 7.6) reveal a dramatic change in the effective WPD depending on the utilised mean velocity vector component at wind angles of 0° and 45° . Specifically, the normalised total wind energy (P^*) is approximately two over the entire line at 0° , with this value also being achieved at 45° at certain locations. However, when employing only U_u or the combination of U_u and U_v , the normalised effective WPD value substantially decreases, even falling below one at 0° . In contrast, when combining the U_u and U_w components, P_{eff}^* is almost equal to P^* at both wind angles, highlighting the significant contribution of the vertical (U_w) component. That is in line with the findings in Subsection 7.2.2.1 related to highly skewed flow close to the upstream edge. The non-uniform distribution of the P_{eff}^* across the line L1 emphasises the spatial character of the flow. At a wind angle of 90° , almost no wind power is accessible, barring a small region close to the windward end of line L1, where a peak of $P^* = 2$ is noticed.

The C2 case demonstrates pronounced influences from both the surrounding buildings and the approaching wind angle. Specifically, the building arrangement, in this case, leads to a considerable decrease in total wind energy (P^*) at 0° when compared to the C1 case. However, at the 45° wind angle, P^* exhibits notably higher values than in the C1 case, recording above 1.5 over the entire line and peak values of 2.5. Nevertheless, the volume of potentially exploitable wind energy also depends on the type of wind turbine used. As in the case C1, the skewness of the flow vertically in the C2 case makes the combination of the U_u and U_w components the most

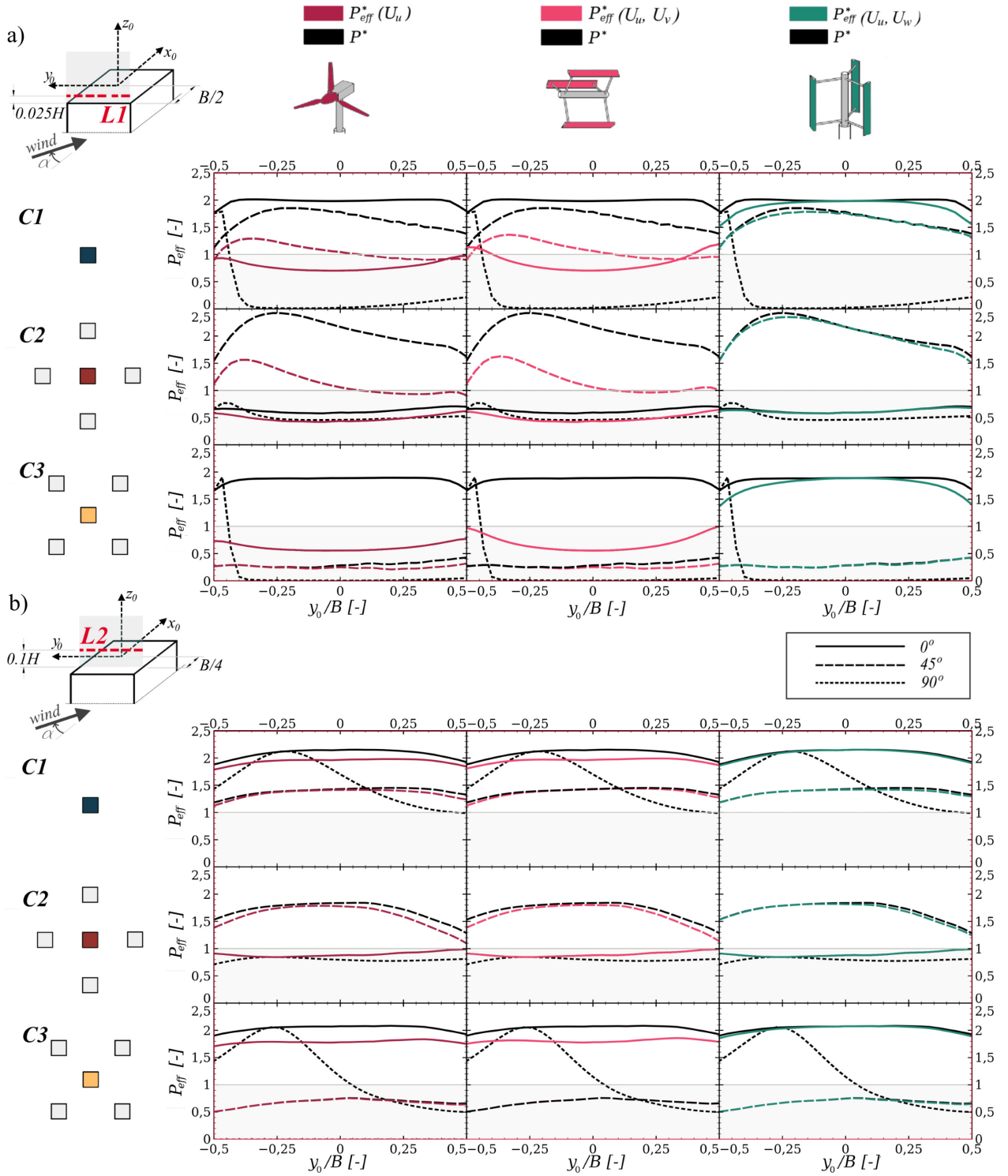


Figure 7.6. Normalised WPD distribution regarding different effective velocities (P_{eff}^*) across the predefined lines (a) L1 and (b) L2, for 0° , 45° and 90° wind angles and three study cases (C1, C2 and C3), adapted from [41].

desirable, with the highest values of P_{eff}^* . At 90° , an almost uniform distribution of $P^* = 0.5$ is recorded with a slight increase on the windward end.

Similar to the C2 case, the C3 case also underlines the effects of the neighbouring buildings. However, in this arrangement, the most favourable angle for wind energy harvesting is 0° . Additionally, no increase in P^* has been recorded compared to the C1 case, and a conspicuous

drop of P^* at 45° expresses the influence of the front building. Again, the contribution of the U_w component in the P^* is strongly emphasised. For wind approaching 90° , a peak is observed close to the windward edge, while over the rest of the line, L1 exhibits the P^* close to 0.

Distribution over the second line (L2)

Considering the plots over the second line (marked L2 in Figure 7.6(b)), the C1 case reveals the most pronounced contribution to the WPD from the horizontal U_u component across all three wind angles. However, at a wind angle of 0° , the inclusion of the U_w component leads to an observable increase in P_{eff}^* by up to 20%, whereas the U_v component shows no noticeable impact on P_{eff}^* . As over line L1, the highest values of P^* are recorded at the wind angle of 0° (exceeding 2.2), whereas these values are lower at 45° , ranging between 1.2 and 1.4. An interesting observation is notable at the wind angle of 90° . Namely, P^* exceeds one over the entire L2, even reaching values comparable to those at 0° at $y/B = -0.25$.

In the C2 case, P^* for wind angles of 0° and 90° closely align, concentrating around 0.9. As seen over line L1, the most favourable wind angle is 45° , with P^* varying between 1.5 and 2. The smooth distribution of WPD across the line suggests that line L2 is situated above the cone vortices. Moreover, the absolute dominance of the U_u component is evident across all wind angles.

Finally, in the C3 case, outcomes comparable to those in the C1 case are observed at wind angles of 0° and 90° . However, a distinction arises at the 45° wind angle, where the presence of the front building leads to a drop in P^* to below 0.5. The influence of different velocity vector components on WPD is found to be consistent with the conclusions drawn in the previous two cases.

In light of the defined types of wind turbines, preference should be given to lift-based VAWTs for installation above the windward edge (over line L1). That results from the domination of the U_w and, thus, highly skewed flow. However, over the line L2, both HAWTs and lift-based VAWTs could be considered, as the higher aerodynamic performance of HAWTs can overcome the difference in P_{eff}^* for these two types. Conversely, all analysed cases have shown unfavourable flow conditions for horizontally mounted Darrieus VAWTs.

7.3 Conclusions

In summarising the findings in this chapter, certain conclusions can be drawn. When comparing two roof shapes, decking the roof results in less disturbed flow above the roof since Zone 0 and Zone 1 in Figure 7.4 are much reduced compared to the flat roof cases at the same wind angle. In addition, the flow above the decked roof is less sensitive to the change in wind direction. The proposed methodology of mapping the wind resource above the roof of high-rise buildings with various shapes can easily be extended to other geometries/setups. Moreover, performance maps can also be drawn for other engineering applications, such as wind loading on secondary structural elements, antennas, solar panels, or the design of helipads for complex building shapes.

Regarding the impact of surrounding objects of buildings in clusters considered in three study cases, two optimal line locations parallel to the windward edge of the building are identified at $(-0.5B, 0, 1.025H)$ (line L1) and $(-0.25B, 0, 1.1H)$ (line L2) relative to the building orientation at 0° wind angle. These locations are determined through an extensive analysis of the wind

power density, turbulence intensities and skew angle across three study cases for 0° and 45° wind angles. The discussion is further enriched with an examination of a 90° wind angle. Additionally, the effective wind power density is analysed in relation to the harvesting mechanisms of three types of wind turbines—HAWTs, Lift-based VAWTs, and horizontally mounted VAWTs—across both identified lines.

Across the first line (L1), case C1 records high values of normalised WPD for both 0° and 45° wind angles, exceeding 1.5 and peaking at 2 for 0° across the entire line and at select locations for 45° . However, the WPD nears zero at 90° , except for a peak of 1.7 near the windward edge. Cases C2 and C3 vary significantly due to upstream building positions and the approaching wind angle. Specifically, the C2 case records the highest normalised WPD of approximately 2.5 at 45° , while for the C3 case, the 0° wind angle is found to be the most favourable, with results comparable to the C1 case. For other wind angles in the C2 and C3 cases, WPD remains below 1. The significant contribution of the vertical (U_w) component to the total wind energy is underlined across all cases and wind angles.

For the second line (L2), the C1 case is marked as the most promising for wind energy harvesting when considering all three wind angles. Here, the normalised WPD surpasses 1 for all wind directions, with a maximum of around 2.2 recorded for 0° . Cases C2 and C3 exhibit the same pattern as found in line L1 regarding the favourable wind angle. Though results for other wind angles slightly improve compared to those for line L1, they still remain below desirable. Across the line L2, the dominance of the horizontal (U_u) component of the velocity vectors is evident.

Regarding the choice of a wind turbine, VAWTs are the most beneficial type regarding the effective WPD at both line locations, while HAWTs also provide desirable results for the second location (L2).

8 Evaluation of wind-induced loads on high-rise buildings

After examining wind flow around high-rise buildings in Chapter 6 and investigating favourable wind effects in urban areas such as wind energy harvesting potentials in Chapter 7, this chapter analyses a less favourable wind effect, that is, wind loading. The focus is on examining the accuracy of LES in predicting peak pressure coefficients, incorporating uncertainty quantification from experimental measurements as proposed in [131, 132].

The investigation covers the impact of different methodologies for the estimation of peak pressure, the duration of the pressure signal, and the complexity of the wind flow on the prediction of peak pressure coefficients on the flat roof of a high-rise building. The adopted methodology is also verified on the results over the ring around the facade. Two configurations are considered: an isolated high-rise building (C1) and a group configuration (C2), examined under various wind angles. Different modelling requirements for peak pressure reflected in the maximal Courant number values around one resulted in completely new LES simulations compared to the wind energy assessment, as described in Section 4.3.

The topic is introduced through a description of the methodology for evaluating peak pressure coefficients in Section 8.1. Experimental results of statistical treatment of peak pressure coefficients with uncertainty quantification are presented in Section 8.2. Built upon these results, Section 8.3 is devoted to numerical results and their validation. In the end, a summary of the main findings and implications of the study is given in Section 8.4. The results presented in this chapter have already been published in [42].

8.1 Methodology for evaluating peak pressure coefficients

The analysis employs statistical methods to describe the distribution of the peak pressure for the stationary pressure signals. Stationarity of the pressure signal has been examined previously in Section 5.1. The estimated values of the peak pressure coefficient with a specific probability are determined by fitting a statistical model to the observed data. Two statistical methods are employed for estimating peak pressure coefficients:

- the traditional “epochal” approach [186] and
- the peaks over threshold (POT) method in the form given in [187].

The first, the traditional approach, has been chosen due to its prevalence in the literature on the one hand and reliability and accuracy, demonstrated in [132] on the other. An extensive review of this method is given in [131] with a suggested procedure for calculating the uncertainty of the estimated local peak pressure values on the low-rise buildings. The second, the POT method, is a modern approach described in [187], which can be used for estimation of the extreme wind speeds with the desirable return period and surface peak pressure. Its main advantage regarding the peak pressure estimation is setting the optimal threshold value. Analysing only the data above the threshold aims to overcome the possible biased estimates of the first method. Also, it allows extrapolation of the results from shorter to longer duration of the signal, which is particularly desirable for numerical simulations. The software implementation of the POT method applicable for pressure analyses is available online at <https://github.com/usnistgov/potMax>. It is named *potMax* and is created in the R environment for statistical computing and graphics [188]. The details of the procedure are given in [189].

The uncertainty quantification of the estimated peak pressure coefficients is conducted on 11-hour equivalent full-scale (EFS) experimental data. The optimal set of key parameters which minimise the uncertainty for the predefined signal duration is determined for both methods. Negative peak pressure coefficients with a 20% probability of exceedance are reported, except for the windward sides of the facade, where emphasis is placed on the positive peak pressure coefficients with the same probability. Length, time and velocity scaling adopted in the experiments and numerical simulations are reported in Table 8.1.

Table 8.1. Scaling in the experimental and numerical part of the study.

| Full scale | | | Experiments | | | LES | | |
|---------------|-------------|-------------------|---------------|-------------|-------------------|---------------|-------------|-------------------|
| Length [m] | Time [s] | Velocity [m/s] | Length [m] | Time [s] | Velocity [m/s] | Length [m] | Time [s] | Velocity [m/s] |
| 1 | 1 | 1 | 1/300 | 1/300 | 1 | 1/300 | 1/235 | 1/1.275 |
| 120 | 600 | 16 | 0.4 | 2 | 16 | 0.4 | 2.55 | 12.6 |

The section is further divided into two subsections which provide the basics of both methods: Subsection 8.1.1 is devoted to the traditional “epochal” approach, while Subsection 8.1.2 addresses the POT method.

8.1.1 Traditional “epochal” approach

The traditional “epochal” approach, as detailed in [186], involves the following steps

- **Creating epochs:** The pressure signal from experiments and numerical simulations is divided into n_{ep} equal subintervals or ‘epochs’ of duration Δt .
- **Observing peak pressure coefficients for fitting:** For each epoch, the largest peak pressure coefficient is identified, creating a new dataset $C_{p,PEAK}$ comprising n_{ep} peak pressure coefficient values.
- **Fitting distribution model:** An appropriate extreme values fitting model is chosen. The estimated distribution of the peak pressure coefficients is constructed by fitting the model to the observed peak pressure coefficients.
- **Determining reference duration:** Define the target reference duration for one epoch (ΔT).

- **Conversion to reference duration:** For Δt less than the reference ΔT , apply the conversion of the obtained parameters of the distribution in order to approximate the reference duration of one epoch.
- **Estimating peak pressure coefficient:** Report the estimated peak pressure coefficient from the modified distribution with a specified probability of exceedance.

The key parameters of the traditional approach are the duration of one epoch (Δt), the reference-target length of one epoch (ΔT) and the number of epochs (n_{ep}).

While the procedure itself is simple, it encounters two possible challenges. The first challenge is how to define these key parameters. The length of the epoch Δt should be long enough to ensure the independence of their respective peak pressure coefficients. In addition, it should aim for the identical distribution of the peak pressure coefficients [186]. In the extensive review in [131] of the historical and current-state-of-practice analysis on the estimation of peak pressure coefficient, Δt ranges from 1–60 minutes in full-scale. The most dominant is the duration of 10 minutes, reported in more than 30 studies. In the design codes, it ranges from 10–60 min. On the other hand, the most frequently used number of epochs (n_{ep}) is six. Combined with a 10-minute duration, it results in a total pressure signal length of 60 minutes (in full-scale). Study in [131] set the desired—reference—duration for one epoch (ΔT) to be 60 minutes, making it consistent with literature and design codes. In another reference [132], 15 minutes window is used. For Δt less than the reference ΔT , they converted the obtained Gumbel parameters to approximate the reference one using the procedure defined in [190]. The same approach is used in this research, and the considered target length ΔT is set to 15 minutes in EFS.

The second challenge is the choice of the fitting model. Primarily, there are three types of distributions of extreme values summarised in [186]: Gumbel (also known as the Fisher-Tippett Extreme Value Type I—EV I distribution), Fréchet (EV II), and reverse Weibull (EV III) distributions. These distribution models are characterised by the length of the tail, which is infinite in the cases of Gumbel (EV I) and Fréchet (EV II) distributions and finite for reverse Weibull (EV III) distributions. The ASCE 7 Standard Committee on Loads, due to their characteristics and potential errors, abandoned the use of EV II and EV III distribution in favour of EV I distribution in the estimation of the extreme wind speeds. As a result, the Gumbel—EV I distribution is a commonly adopted and appropriate distributional model in wind engineering practice [186]. Based on this, the Gumbel distribution has been used to probabilistically describe the peak pressure coefficients.

The Cumulative Distribution Function (CDF) of the Gumbel distribution at a given value \check{C}_p is defined by:

$$F_I(\check{C}_p) = \exp \left[-\exp \left(-\frac{\check{C}_p - \mu}{\sigma} \right) \right] \quad (8.1)$$

where μ is the mode of the distribution (location parameter), and σ is the scale parameter related to the dispersion (spread) of the distribution (scale parameter). Inversion of the Equation (8.1) yields:

$$\check{C}_p(F) = \mu - \sigma \ln(-\ln F) \quad (8.2)$$

and \check{C}_p values for $F = 80\%$ are reported.

Methods for estimation of the Gumbel distribution parameters

The parameters of the Gumbel distribution are related to the standard deviation (C_p'') and mean pressure coefficient (\bar{C}_p) of the observed epoch through the following expressions:

$$\bar{C}_p = \mu + 0.5772\sigma \quad C_p'' = \frac{\pi}{\sqrt{6}}\sigma \quad (8.3)$$

Estimation of the parameters of Gumbel distribution from the Equation (8.3) is the traditional approach, known as the method of moments (MOM) in literature. Two other common methods are Lieblein's Best Linear Unbiased Estimator (BLUE) method [191] and the maximum likelihood (MLE). The basis of the BLUE method relies on attributing weight to every data point by implementing a series of coefficients of the 'best linear unbiased estimators'. Two series of coefficients are used: a_i , to estimate the mode μ , and b_i , to estimate the scale parameter σ . The dataset $C_{p,PEAK}$ needs to be arranged in ascending order ($\check{C}_{p1} \leq \check{C}_{p2} \leq \dots \leq \check{C}_{pn}$). Every estimator's value correlates to each rank (i), necessitating a unique set for every population (n). The estimated parameters of the Type I Extreme Value (EV I) distribution are obtained by multiplying each individual coefficient with the corresponding peak from the dataset $C_{p,PEAK}$ and subsequently summing these products according to the following expressions:

$$\mu = \sum_{i=1}^n a_i \check{C}_{pi} \quad \sigma = \sum_{i=1}^n b_i \check{C}_{pi} \quad (8.4)$$

The values of coefficients a_i and b_i , as well as the implementation in MATLAB software [192], are available at <https://www.nist.gov/wind> with the following documentation. The BLUE method is marked as more efficient than the traditional MOM in literature. Yet, its accuracy is affected by the number of epochs (n_{ep}) without recommendations for the optimal number n_{ep} [186]. All three methods (MOM, BLUE and MLE) are explored to distinguish the one that best fits the present investigation.

Regarding the extrapolation from the duration of Δt to the target $\Delta T = 15$ min, when $\Delta t < \Delta T$, the following correction of the parameters of Gumbel distribution, defined in [190], is applied:

$$\sigma_T = \sigma_t \quad \mu_T = \mu_t + \sigma_t \ln(\Delta T / \Delta t) \quad (8.5)$$

8.1.2 Peaks Over Threshold (POT) Method

The cornerstone of the POT method for estimating peak pressure coefficients proposed in [187] is a two-dimensional Poisson process. The probability that n events will occur during the time interval t is represented by:

$$p(n) = \frac{\lambda^n}{n!} \exp(-\lambda) \quad (8.6)$$

in which λ represents the average number of events in the given time interval t . The evaluation procedure using this method includes the following steps:

- **Determining time window:** Establish the time window Δt_{POT} for extracting peak pressure coefficients.
- **Stationarity test:** Conduct a stationarity test to confirm the stationarity of the pressure signal over the length Δt_{POT} .

- **Declustering:** Decluster the pressure signal to ensure the independence of extreme events.
- **Evaluating optimal threshold:** Identify the optimal threshold above which peak pressure coefficients are considered for analysis.
- **Fitting distribution model:** Choose the appropriate model for the intensity function λ and determine the its parameters. These parameters are inputs for the subsequent Monte-Carlo simulation.
- **Running Monte-Carlo simulations:** Construct the estimated distribution of peak pressure coefficients using Monte-Carlo simulations with inputs from the previous step. The target time window (Δt_{MC}) for Monte-Carlo simulations may differ from the original time window for peak pressure coefficient extraction (Δt_{POT}). A typical recommendation for Monte-Carlo simulations is 1000 samples. The resulting estimated distribution is the collection of the highest peak pressure coefficients recorded in every Monte-Carlo simulation.
- **Estimating peak pressure coefficient:** Report the estimated peak pressure coefficient with a specified probability of exceedance derived from the Monte-Carlo simulation-based distribution.

The key parameters of the POT method are the choice of the model for λ , duration of the signal (Δt_{POT}), optimal threshold and the target time window (Δt_{MC}) for Monte-Carlo simulations.

Regarding the choice of the model, *potMax* library includes two possible models for λ :

- *full*—the generalised extreme value distribution with the parameter of the tail length and
- *Gumbel*—with the tail length parameter approaching zero.

Details of both models are provided in [187]. This study will retain the assumption made in Subsection 8.1.1 that the value of peak pressure coefficient (\check{C}_p) can be described probabilistically by the Gumbel (EV I) distribution. Hence, the intensity function λ for time (t)–pressure (C_p) space is:

$$\lambda(t, C_p) = \frac{1}{\sigma_{POT}} \exp \left[-\frac{(\check{C}_p - \mu_{POT})}{\sigma_{POT}} \right] \quad (8.7)$$

Consequently, the resulting distribution of the peak pressure coefficients from the Monte-Carlo simulations is the Gumbel-like distribution due to the choice of the model (*Gumbel* Equation (8.7)). Additionally, the stationary time series assumption is made, implying the necessity of the stationarity test. Another critical assumption of the Poisson process is independence, accomplished through the declustering process included in the *potMax* library.

The selection of peak pressure coefficients from the predefined time window (Δt_{POT}) is made by setting the threshold value above which \check{C}_p are collected. Finding the optimal threshold value is the most challenging task in the POT method and should be determined separately for every pressure tap. Its impact on results can be significant. On the one hand, adopting it too low will result in larger data sets, while adopting a threshold value that is too high can result in insufficient observations. The procedure implemented in code *potMax* relies on prescribing the minimal and maximal number of observations from the selected time window. It has the option to set single or multiple thresholds. For the present investigation, a single threshold model is adopted.

The set of potential thresholds (d) is calculated from the defined criteria of minimal (n_{mn}) and maximal (n_{mx}) number of observations from one signal. The suggested minimal number of

observations is 10 for the adopted model, while the maximal number should be set high enough that the chosen threshold does not correspond to that specific number of observations, yet not excessively high to make execution times unmanageable [189]. In the present calculations, n_{mn} is set to 15 and n_{mx} to 100. For each potential threshold value d , the estimation of model parameters (μ and σ) to fit the model in Equation (8.7) is accomplished using the maximum likelihood method, which maximises the likelihood function given as follows:

$$L(\eta) = \left[\prod_{i=1}^I \lambda(t_i, C_{pi}) \right] \exp \left[- \int_V \lambda(t, C_p) dt dC_p \right] \quad (8.8)$$

In Equation (8.8), t_i and C_{pi} denote declustered values above the specific threshold d , and V refers to the domain of integration, which is the unbounded rectangle $[0, t'] \times [b, \infty)$ (t' is the time of the last observation). For the set of potential thresholds, the choice of the optimal one is made regarding the best fit of the data to the adopted model (Equation (8.7)), judged using the W-statistic plots [193].

The W-statistic is dimensionless and represents a data transformation. In an ideal scenario where the Poisson-process model is perfectly accurate, the transformed data (ordered W statistics versus exponential quantiles for the zero-tail) would follow exactly the 45° (diagonal) line, representing an exponential distribution with mean one. The W-statistic is defined by:

$$W_i = \frac{1}{\xi_{t_i}} \log \left[1 + \frac{\xi_{t_i}(C_{pi} - d)}{\sigma_{t_i} + \xi_{t_i}(d - \mu_{t_i})} \right] \quad (8.9)$$

in which $(t_i, C_{pi} - b)$ are the time and corresponding excess over the threshold (b) of C_{pi} . μ_{t_i} , σ_{t_i} and ξ_{t_i} are estimated location (mode), scale (dispersion) and shape parameters, respectively. Equation (8.9) is the most general form of the threshold model so far, and it is applicable to non-stationary signals [193]. In order to apply it to the present case, it is further modified by excluding time dependence of the estimated parameters (μ , σ), and $\xi \rightarrow 0$ which is in accordance with the adopted model (Equation (8.7)). Equation (8.9) is simplified into:

$$W_i = \frac{C_{pi} - d}{\sigma} \quad (8.10)$$

After generating the W-plots, the discrepancy from the 45° line for every potential d is calculated. The selected optimal threshold minimises the maximum absolute vertical distance from this line.

8.2 Experimental results: Evaluation of peak pressure coefficients with uncertainty quantification

The following section presents the analysis of peak pressure coefficients on the high-rise building's roof, evaluated from experimental measurements. Its primary aim is to supply data for LES modelling, processing numerical results and their validation in Section 8.3. The section determines the optimal set of previously defined key parameters that will be used in LES for two methods (the traditional “epochal” approach and the POT method) to minimise the uncertainty for the predefined signal length. Furthermore, analyses of various signal durations, defined in Subsection 5.1 on estimated peak pressure coefficients and associated uncertainties, are conducted. The following durations of the pressure signal are included in the examination: $150t^*$, $200t^*$, $300t^*$, $400t^*$ and $600t^*$ after the transient solution, equal to $T_{full} = \{18.5, 25, 37.5, 50, 75\}$ min in EFS.

Including uncertainty quantification in the validation process of LES is a vital step in evaluating the accuracy of numerical methods in assessing peak pressure coefficient values effectively. Considering the approaching wind angle, critical borderline cases of negative peak pressure coefficients on the roof are identified, which will be further employed for LES modelling.

The key steps in evaluating peak pressure coefficients with uncertainty quantification implemented in this study, based on the systematic and rigorous procedure exposed in [131, 132], are as outlined:

- **Building empirical benchmark—empirical peak pressure coefficient:** Construct the empirical distribution from the 11-hour EFS pressure signal. Assess the empirical peak pressure coefficient value ($\check{C}_{p,emp}$) with a specified probability of exceedance to serve as a benchmark for uncertainty quantification.
- **Estimating peak pressure coefficient:** Utilise statistical methods to evaluate the distribution of peak pressure coefficients for the obtained signal length. Report the estimated peak pressure coefficient ($\check{C}_{p,est}$) with a specified probability of exceedance. This step is iteratively performed for comprehensive uncertainty quantification.
- **Evaluating the performance metrics:** Compare the empirical and estimated peak pressure coefficients and calculate the performance metrics of the employed statistical methods to validate their accuracy and reliability.

Negative peak pressure coefficients relative to a 20% probability of exceedance are reported because of their practical importance in wind loading on the roof. The empirical distribution of peak pressure coefficients is outlined in Subsection 8.2.1 with the definition of empirical value. The subsection also encompasses the distribution of these values over the flat roof of the high-rise building from the experiments for two configurations and four approaching wind angles. Subsection 8.2.2 presents the estimated peak pressure coefficients and corresponding uncertainties using two statistical methods.

8.2.1 Empirical peak pressure coefficients

The empirical distribution of negative peak pressure coefficients is constructed to establish a benchmark for uncertainty quantification, following the methodology outlined in [131, 132]. In order to build empirical CDF, an 11-hour EFS pressure signal is split into 43-time windows, each representing a 15-minute EFS event, which is the adopted reference duration ΔT . The most negative value from every window is stored, resulting in the data set with a length of $n = 43$. The absolute values of the stored peak pressure coefficients are rearranged in ascending order, with the assigned probability of occurrence $1/n$. The CDF is defined by:

$$F_{emp}(\check{C}_p) = i/n \quad (8.11)$$

where i takes values from 1 to n . The empirical peak pressure coefficient ($\check{C}_{p,emp}$) at each measurement point is defined as the value with a 20% probability of exceedance.

The standard error (SE) of the 80% quantile of the empirical peak pressure coefficients ($\check{C}_{p,emp}$) is computed using the technique described in [194]. It extends the method for estimating the SE of a sample median in [195] to any quantile. The uncertainty bounds of the $\check{C}_{p,emp}$ are assumed to be equal to $\pm 2SE$, consistent with findings in [132]. Empirical values of peak pressure coefficient with these uncertainty bounds ($\pm 2SE$) are used as a benchmark for comparison with the estimated peak pressure coefficients in Subsection 8.2.2 (Figures 8.2 and 8.5).

The distribution of $\check{C}_{p,emp}$ over the roof of the high-rise building is illustrated in Figure 8.1 to identify the critical borderline cases for further numerical investigation. The analysis encompasses experimental data on negative peak pressure coefficients across two configurations: single, isolated high-rise building (C1) and group configuration (C2), at four approaching wind angles: 0° , 15° , 30° and 45° .

A consistent pattern emerges across all configurations and wind angles: the most significant negative peak pressure coefficients are predominantly near the windward edges. Notably, in the group configuration (C2), higher negative peak pressure coefficients in this zone are observed compared to the isolated building (C1), indicating the influence of neighbouring buildings. Moreover, for wind angles of 15° and more, the C2 configuration demonstrates a more extensive area of high negative peak pressure coefficients.

At 0° , a certain building arrangement causes a “sheltering” effect of the upstream building on the principal one. It results in more pronounced negative peak pressure coefficients \check{C}_p close to the windward edge recorded in the C2 configuration than in C1, followed by a steeper drop further downstream. This phenomenon is a consequence of the turbulent wake generated from the upstream building, which impacts the downstream one and triggers specific behaviour. In contrast, at 45° , the two upstream buildings do not overshadow the central one but form the channel, resulting in the Venturi effect and leading to the maximal negative peak pressure coefficient from the experimental measurements of $\check{C}_p = -6$ observed in this case.

Analysing the spatial distribution patterns of \check{C}_p , two critical borderline cases emerge based on the wind angle: 0° and 45° . These cases will be subjected to more intensive numerical investigation.

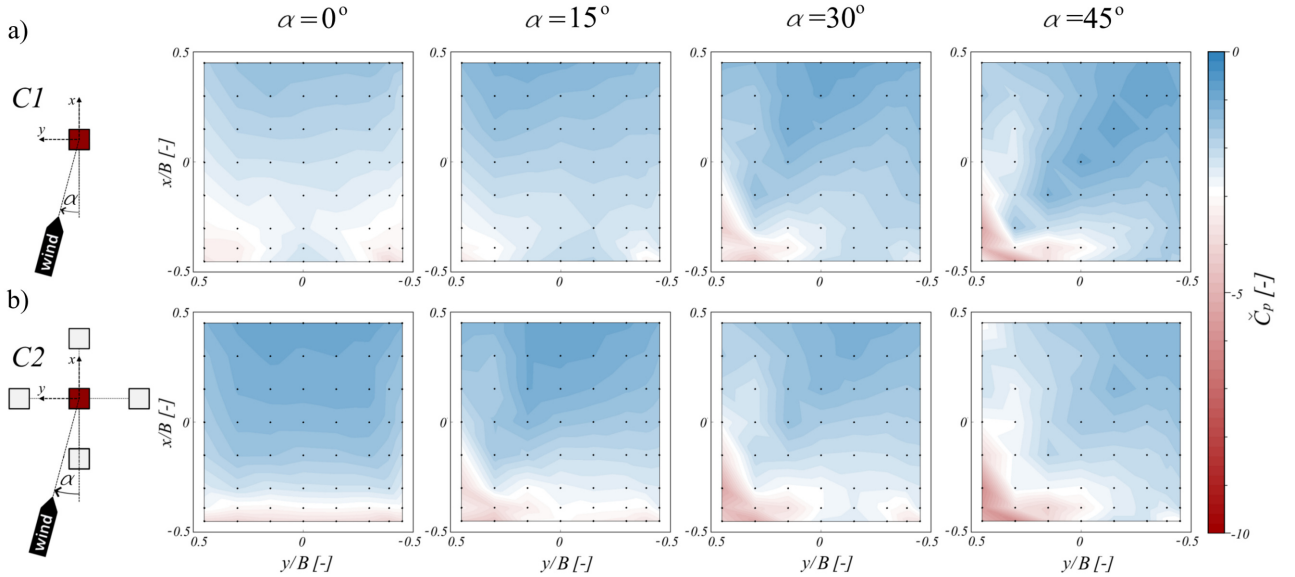


Figure 8.1. Experimental results of the minimum peak pressure coefficient over the roof for various wind directions: (a) single (C1) and (b) group (C2) configurations, adopted from [42].

8.2.2 Estimated peak pressure coefficients and corresponding uncertainties

Estimation of peak pressure coefficients with corresponding uncertainties is conducted using two statistical methods: the traditional “epochal” approach (Subsection 8.1.1) and the POT method (Subsection 8.1.2). The performance evaluations of the estimated peak pressure coefficients ($\check{C}_{p,est,i}$) compared to the empirical ones (from Subsection 8.2.1) for both methods are achieved using the normalised root mean squared error ($NRMSE$):

$$NRMSE = \sqrt{\frac{1}{n_{peak}} \sum_{i=1}^{n_{peak}} (NE_i)^2} \cdot 100 \quad [\%] \quad (8.12)$$

$$NE_i = \begin{cases} \frac{\check{C}_{p,est,i} - (\check{C}_{p,emp} + 2SE)}{\check{C}_{p,emp} + 2SE}, & \text{if } \check{C}_{p,est,i} > \check{C}_{p,emp} + 2SE \\ 0, & \text{if } \check{C}_{p,emp} - 2SE < \check{C}_{p,est,i} < \check{C}_{p,emp} + 2SE \\ \frac{(\check{C}_{p,emp} - 2SE) - \check{C}_{p,est,i}}{\check{C}_{p,emp} - 2SE}, & \text{if } \check{C}_{p,est,i} < \check{C}_{p,emp} - 2SE \end{cases} \quad (8.13)$$

where NE_i represents a normalised error. The mean and standard deviation (std.) considering all points on the roof of the $NRMSE$ obtained for each point are reported. Additionally, the $NRMSE$ of estimated peak pressure coefficients at the 95% confidence interval (95% CI), referred to as $NRMSE$ 95% CI, is considered, along with the maximal normalised error ($max.NE$ 95% CI) of these values. NE_i for the 95% CI in Equation (8.13) at one point is calculated as the maximal NE of $\check{C}_{p,est}$ at the boundaries of the 95% CI: 2.5% and 97.5% (more details on the process of evaluating certain CI for $\check{C}_{p,est}$ is given in the following). These last two statistical parameters aim to provide insight into the boundaries of the uncertainty of the experimental data, encompassing both normalised root mean squared error and maximal deviation for the 95% CI across all measuring points on the roof.

The research in [131] highlights the impact of statistical treatments of peak pressure values in Gumbel fitting models, particularly concerning the length and number of epochs, on the uncertainty in peak pressure estimation. They underlined the importance of a well-established procedure for the statistical treatment of peak pressures and the calculation of uncertainties where feasible. The available experimental data in the present study (11 hours EFS) provides a solid basis for the uncertainty quantification. The focus in this subsection is on single building configuration C1 for wind angles of 0° and 45°.

8.2.2.1 Traditional “epochal” approach

Calculating the estimated peak pressure coefficient using the traditional approach requires determining the parameters of the Gumbel distribution. The initial step involves selecting the method for estimating these parameters. In the first part of this subsection, the performance of various methods is evaluated, and the most appropriate one is chosen for further analyses of estimated peak pressure coefficients and uncertainty quantification, which will be addressed in the second part of the subsection.

Three methods have been tested: MOM, BLUE and MLE. The key parameters (n_{ep} and Δt) have been varied to tackle the performance of each method. Six different numbers of epochs are analysed, $n_{ep} = \{5, 6, 10, 15, 20, 30\}$, each associated with various epoch durations $\Delta t = \{1, 1.25, 1.5, 1.875, 2.5, 3, 3.75, 5, 6.25, 7.5, 10, 12.5, 15\}$ min in EFS. The specific choice of

n_{ep} and Δt will be employed for all analyses in this subsection, strategically selected to ensure their combinations align well with the 75-minute EFS time block.

Figure 8.2 demonstrates the performance evaluation process. Specifically, Figure 8.2(a) presents an example of the Gumbel distribution at point P4 (configuration C1 with a 0° wind angle) for a single time block of the duration $T_{full} = n_{ep}\Delta t$, applying all three parameter estimation methods (MOM, BLUE, MLE) on a semi-log plot which linearises the CDF of the Gumbel distribution. For this example, the epoch duration is set to $\Delta t = 5$ min in EFS, and the total number of epochs in one block is $n_{ep} = 10$. It results in a 50-minute EFS time block extracted from the pressure signal. In order to bring the duration of the epochs to the reference level ($\Delta T = 15$ min in EFS), the conversion of parameters of Gumbel distribution using Equation (8.5) is performed, and fitting lines are marked with grey colour on the plot in Figure 8.2(a). The uncertainty bounds for this specific combination of Δt and n_{ep} are calculated by shifting a 50-minute EFS time block by one Δt interval through the pressure signal and repeating the fitting process for each new time block. The results for all time blocks using the MLE method are illustrated in Figure 8.2(b). This figure indicates the mean of all distributions by a black dashed line. Peak pressure coefficients estimated to have a 20% probability of exceedance ($\check{C}_{p,est}$), along with their 95% confidence intervals (95% CI), are also marked. In addition, empirical peak pressure coefficients for point P4 are included in the plot for comparison.

This process has been replicated for each measurement point on the roof. For configuration C1 at a 0° wind angle, the results obtained from all three methods—MOM, BLUE and MLE—are represented in Figure 8.2(c). The plots include the performance metrics results for each method. They are comparable across all three methods, with the MLE method exhibiting slightly better performance in this particular case with the lowest values of all four parameters. The most noticeable improvement of the MLE method is achieved considering *max.NE* 95% CI, with an improvement of almost 7% compared to the MOM, and 2% compared to the BLUE. This trend aligns with observations from other combinations of Δt and n_{ep} , as well as across different configurations and wind angles. Based on these findings, further analyses will exclusively employ the MLE method for parameter estimation of the Gumbel distribution.

The second part of this subsection is dedicated to the analysis of the influence of various combinations of key parameters (n_{ep} and Δt) and durations of the pressure signal on the estimated peak pressure coefficients and associated uncertainty levels. The primary objective of this investigation is to identify the optimal combination of n_{ep} and Δt that minimises uncertainty within specified time blocks $T_{full} = \{18.5, 25, 37.5, 50, 75\}$ min in EFS, but also to address the uncertainty levels associated with the specific T_{full} .

Figure 8.3 represents the performance metrics across various combinations of n_{ep} (each n_{ep} is marked with a different bullet symbol in the scatter plot) and Δt . Additionally, data points which correspond to combinations $n_{ep}\Delta t$ equal to the specified T_{full} are connected with different line types and colours.

At both wind angles, performance metrics show a trend of decreasing uncertainty with increasing T_{full} , as expected due to the larger time window. However, for the same T_{full} , performance metrics vary across different combinations of n_{ep} and Δt . At a wind angle of 0° , a slight reduction in uncertainty is observed for smaller values of Δt , with the most desirable range between 2 and 3.75 min in EFS. Values of Δt less than 2 min in EFS increase uncertainty, suggesting that the minimal time window for peak pressure coefficient extraction should not be less than 2 min in EFS. At a 45° wind angle, the performance metrics are inconsistent with those for 0° . The uncertainty levels are higher in this case, particularly notable in the standard deviation

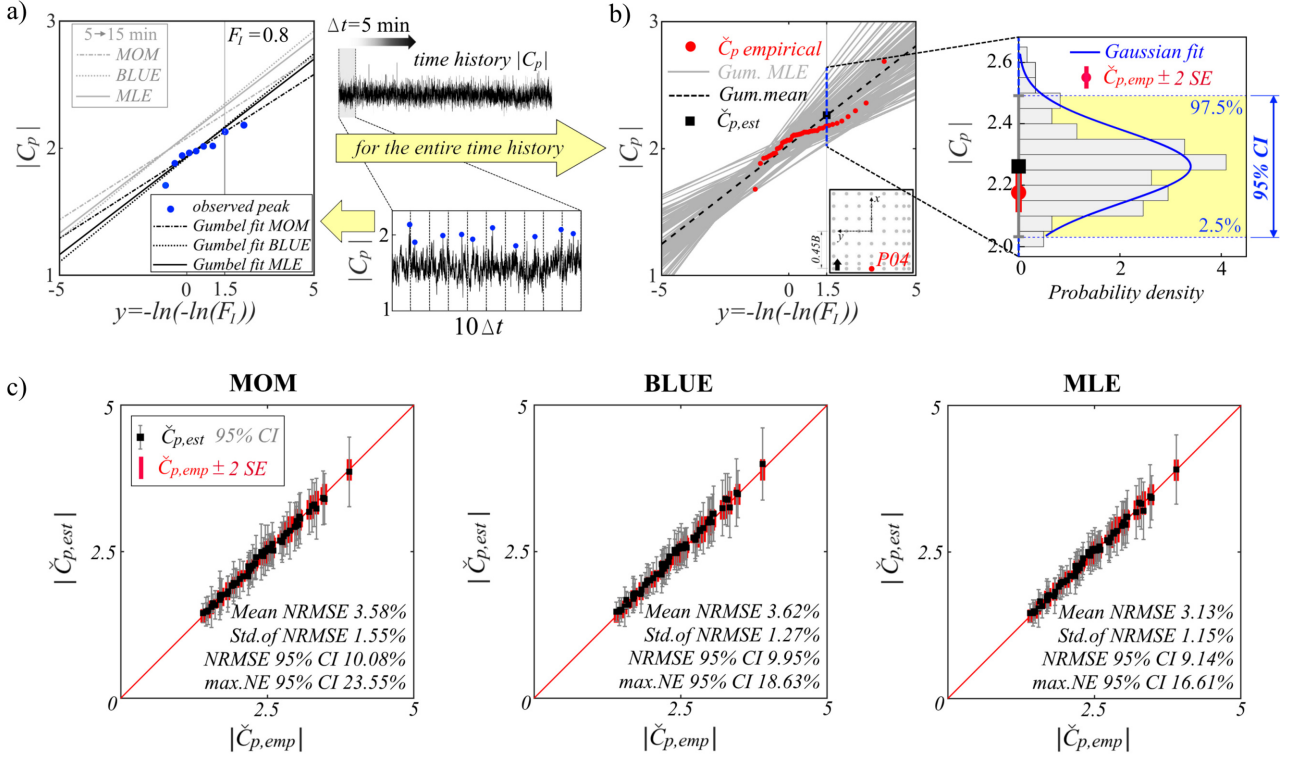


Figure 8.2. Procedure for estimation of peak pressure coefficient from the experimental data using the Gumbel method in the traditional approach, demonstrated at point P4, location $(-0.45B, 0, H)$ in configuration C1, at 0° wind angle: (a) Gumbel fit using MOM, BLUE and MLE for the combination of $n_{ep} = 10$ and $\Delta t = 5$ min in EFS with conversion to $\Delta T = 15$ min in EFS and (b) Gumbel fit using MLE for all time blocks across the pressure signal with 95% confidence interval (95% CI) for the estimated peak pressure coefficient with a probability of exceedance of 20%; (c) performance metrics of MOM, BLUE and MLE method for all 64 points on the roof, adopted from [42].

of $NRMSE$ and $max.NE$ 95% CI for Δt less than 7.5 min in EFS. The best results in this scenario are obtained for $n_{ep} = 5$ and $\Delta t \geq 7.5$ min in EFS.

When considering uncertainty levels for different T_{full} values, mean $NRMSE$ of 5% or lower is achieved at $T_{full} \geq 25$ min in EFS at 0° and $T_{full} \geq 37.5$ min in EFS at 45° . The accompanying standard deviation of $NRMSE$ remains below 3% in almost all combinations of n_{ep} and Δt for both wind angles. One of the most reliable indicators of uncertainty, $NRMSE$ of 95% CI , remains below 15% in these cases. However, the maximal NE of 95% CI goes up to 30% for $T_{full} \geq 25$ min in EFS at 0° and $T_{full} \geq 37.5$ min in EFS at 45° . These performance metrics can serve as threshold values. As such, $T_{full} = \{25, 37.5, 75\}$ min in EFS durations will be employed for further investigation and comparison with numerical results.

In a supplementary analysis, an additional third parameter, the number of time blocks (n_{bl}), is introduced. This parameter is crucial when $n_{ep}\Delta t$ is less than T_{full} , allowing for multiple blocks to be accommodated within a specific duration. In such scenarios, the mean of the distributions from two or more blocks, determined by how many can fit into the T_{full} window, is the representative distribution for the entire T_{full} period. Graphical representation of performance metrics for various combinations of n_{ep} , Δt and n_{bl} is given in Figure 8.4 for configuration C1 at 0° and 45° wind angle. Again, each n_{ep} is marked with a different bullet symbol in the plot and data points with specific T_{full} duration are connected with different line types and colours in the same manner as in Fig. 8.3.

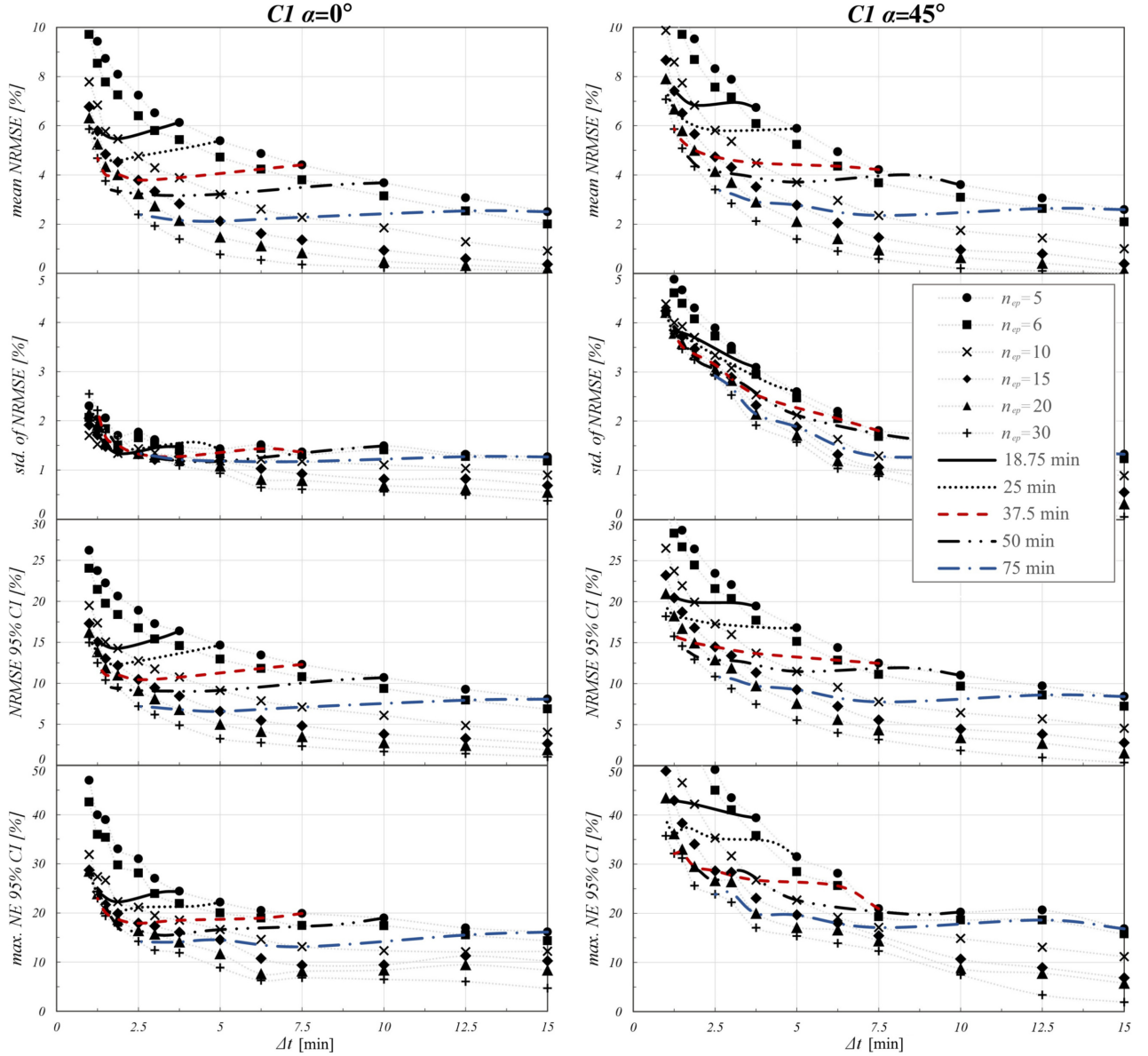


Figure 8.3. Graphical representation of performance metrics of experimental data for various combinations of n_{ep} and Δt ; each n_{ep} is marked with a different bullet symbol in the scatter plot, and data points which correspond to combinations $n_{ep}\Delta t$ equal to the specified T_{full} are connected with different line types and colours, adopted from [42].

For all analysed $T_{full} = \{25, 37.5, 75\}$ min in EFS durations, the increase in n_{bl} within a fixed duration Δt leads to a decline in all four statistical performance metrics. The trend remains consistent across both wind angles. Another important observation is that Δt of 1 minute EFS time window is linked to less favourable performance metrics, especially at 45° wind angle, implying a preference for a Δt of 2 min in EFS or greater. Regarding the number of epochs within a single block, n_{ep} , the most favourable outcomes are observed for $n_{ep}=5$, yet the minor variations across different Δt values are recorded.

Within the scope of this specific study, it is concluded that the optimal performance for analysed T_{full} (especially for $T_{full} = 25$ min in EFS) is achieved for a combination of $n_{ep}=5$, $\Delta t=2.5$ min in EFS and corresponding n_{bl} considering the mean $NRMSE$ and $NRMSE$ of 95% CI . However, the differences in performance metrics across the same T_{full} for different sets of parameters are

minor (within a few per cent). Consequently, different combinations of key parameters will not be subject to estimating peak pressure coefficients from the LES.

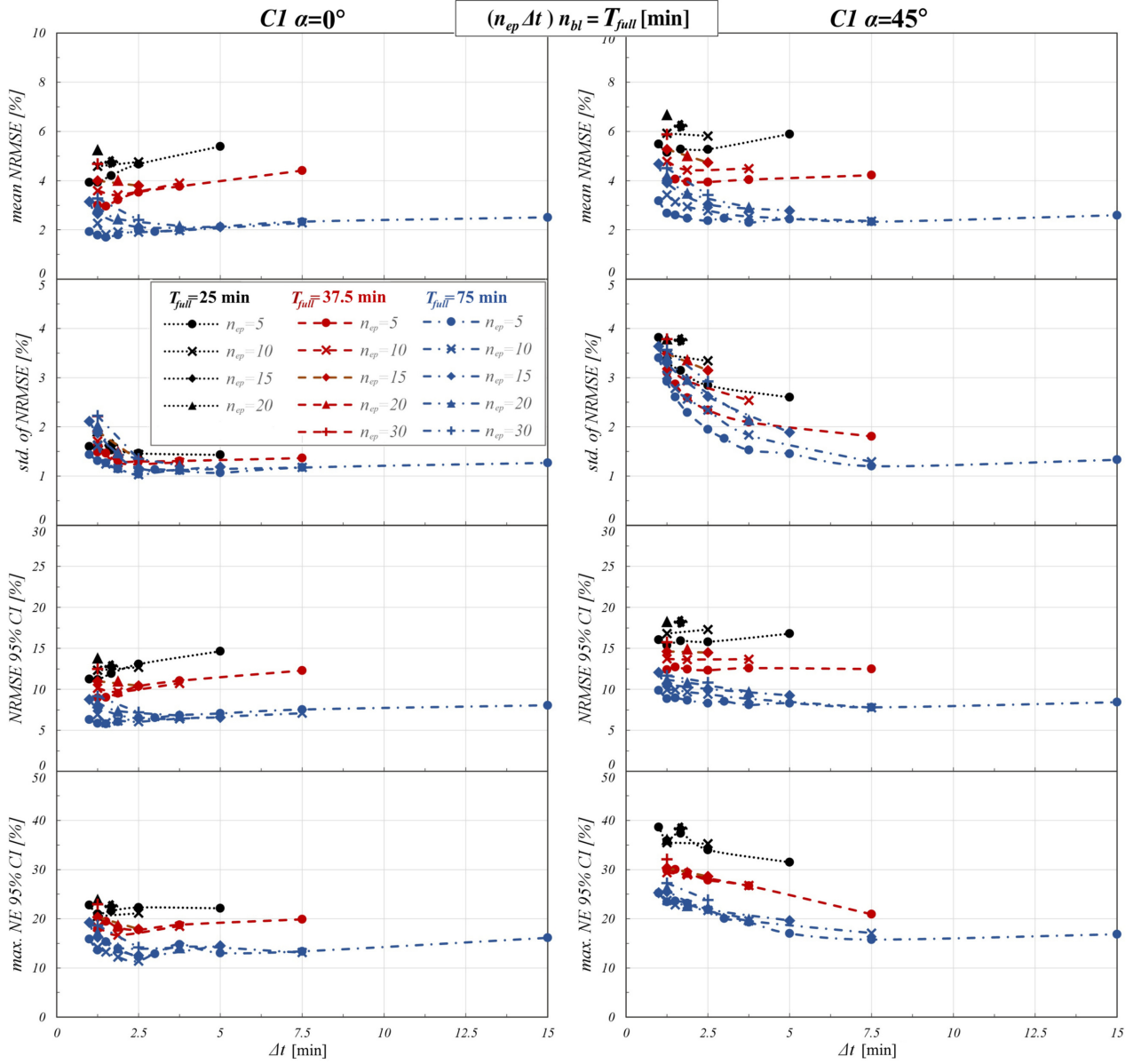


Figure 8.4. Graphical representation of performance metrics of experimental data for various combinations of n_{ep} , Δt and n_{bl} , resulting in $T_{full} = \{25, 37.5, 75\}$ min in EFS; each n_{ep} is marked with a different bullet symbol in the scatter plot, while points corresponding to the same T_{full} are connected with different line types and colours, adopted from [42].

In summary, the MLE method for parameter estimation of the Gumbel distribution outperforms the MOM and BLUE methods across various metrics. Through the analysis of key parameter combinations in the traditional “epochal” approach, an optimal set ($n_{ep} = 5$, $\Delta t = 2.5$ min in EFS, and corresponding n_{bl}) has been identified. This set minimises uncertainty in peak pressure coefficient estimation and will be employed for the statistical treatment of peak pressure coefficients in LES. The subsequent step involves further comparison with numerical results, with a focus on different durations ($T_{full} = \{25, 37.5, 75\}$ min in EFS) in Section 8.3.

8.2.2.2 POT method

Unlike the traditional method, calculating the estimated peak pressure coefficient using the POT method does not depend on n_{ep} , Δt and n_{bl} . The parameters of interest in this method are the length of the time window for peak pressure coefficient extractions Δt_{POT} , the minimal and maximal number of peak pressure coefficients from a single time window for finding the optimal threshold and the target time window for Monte-Carlo simulations (Δt_{MC}). In [189], a general recommendation is a minimum of 10 observations. Simultaneously, in [189], they suggested that the maximum should be sufficiently large to ensure that the chosen threshold does not correspond to that specific number of observations. However, it should also avoid being too high to make execution times unmanageable [189]. For the current analyses, n_{mn} is set to 10 and n_{mx} to 60, which corresponds to the number of peak pressure coefficients in the traditional approach when $\Delta t=1.25$ min in EFS. This study investigates the performance of extrapolating the results from a shorter time window Δt_{POT} to a longer one, which is particularly important for numerical simulations. The target time Δt_{MC} is set to 75 min in EFS, while four different durations for Δt_{POT} are considered, namely $\Delta t_{POT} = \{18.75, 37.5, 75, 150\}$ min in EFS.

Figure 8.5 provides a graphical description of the performance metrics results for the POT method for configuration C1, 0° and 45° wind angle, in the same manner as done for the traditional approach. The mean and standard deviation of NRMSE are used again as a measure of the quality of an estimator. Results for both wind angles are consistent. Initially, it is observed that the POT method tends to overestimate the peak pressure coefficient slightly compared to empirical data. This overestimation is attributable to the POT method's selection of the highest peak pressure coefficients within the entire window Δt_{POT} , unlike the traditional approach, which extracts only a single peak pressure coefficient from each Δt window, potentially overlooking higher peak pressure coefficients from adjacent intervals. Next, an analysis of uncertainty levels reveals a noticeable decrease as the time window Δt_{POT} is extended. Nevertheless, the uncertainty remains higher than in the traditional approach, primarily due to the overestimation mentioned above, indicated by the higher performance metrics. Namely, the mean and standard deviation of *NRMSE* are around 11% and 4%, respectively, at both wind angles, compared to around 2% of both statistical metrics in the traditional approach (illustrated in Figure 8.4) for $\Delta t_{POT} = T_{full} = 75$ min in EFS. Metrics for 95% CI follow the same trend with *NRMSE* around 25% and maximal *NE* reaching almost 45% at 45° .

Considering the extrapolation from shorter durations ($\Delta t_{POT} = \{18.75, 37.5\}$ min in EFS) to the target time $\Delta t_{MC}=75$ min in EFS, the results are promising. Namely, an increase in uncertainty is evident as expected and observed. However, the mean values of estimated peak pressure coefficients with the probability of exceedance of 20% are closely aligned with the values obtained for $\Delta t_{POT} = 75$ min in EFS. Notably, when employing a Δt_{POT} of 150 min in EFS, transitioning from a longer to a shorter duration appears to reduce uncertainty, as shown in Figure 8.5.

To summarise, the POT method tends to slightly overestimate the peak pressure coefficient due to its selection of the highest peak pressure coefficients within the entire Δt_{POT} . Promising results are seen when extrapolating from shorter to longer time windows, showing alignment in mean values and an increase in uncertainty with shortening durations. However, uncertainties remain higher than in the traditional approach. This method is included in processing LES results with the traditional one, too, with parameters $n_{mn}=10$, $n_{mx}=60$, $\Delta t_{MC}=\Delta t_{MC}=75$ min in EFS.

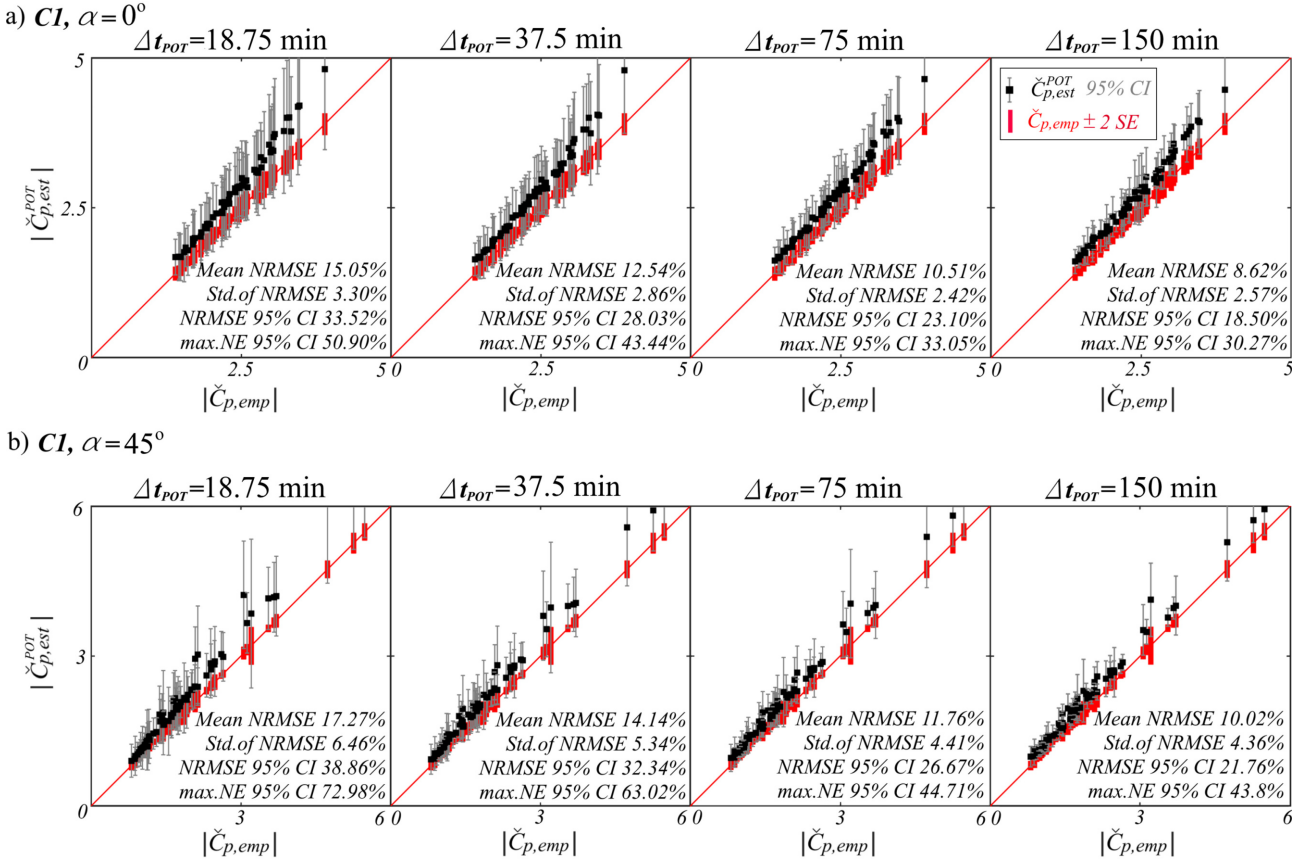


Figure 8.5. Graphical representation of performance metrics of experimental data for POT method in representing the 75-minute EFS event for C1 configuration at (a) 0° and (b) 45° wind angles, adopted from [42].

8.3 Evaluation of LES prediction capacities of peak pressure coefficients

In wind engineering, LES serves as a valuable numerical method, but it cannot stand alone; validation through experiments is essential [27]. This chapter delves into its predictive power regarding peak pressure coefficients, focusing on four selected cases from Subsection 8.2.1: configurations C1 and C2 at wind angles of 0° and 45° .

The section is structured into two subsections. Firstly, Subsection 8.3.1 compares LES results on peak pressure coefficients on the roof of the high-rise building using two statistical methods. It aims to identify a more reliable approach through validation against experimental results from Subsection 8.2.2. Following this, in Subsection 8.3.2, the chosen method is applied to different durations of LES pressure signals, and the results are compared with corresponding experimental data. This part examines how varying pressure signal durations impact the estimated peak pressure coefficients from LES. Furthermore, verification of the methodology is extended to include the facade of high-rise buildings, in addition to the roof zone.

To enrich the discussion, the link between the distribution of peak pressure coefficients on the roof for four study cases and flow mechanisms in this zone, relying on the flow characteristics presented in Chapter 6, are incorporated. This analysis offers a valuable perspective on how flow complexity influences LES results and whether simpler, isolated building benchmark cases can reliably validate more intricate group configurations regarding peak pressure coefficients.

8.3.1 Traditional vs. POT method

The performance of two statistical methods, the traditional and POT methods, in estimating peak pressure coefficients from LES are assessed through the comparison with experimental results from Subsection 8.2.2 in the roof zone. Each method's performance is evaluated based on the percentage deviations of LES results from the experimental ones within the 10%, 20% and 30% range. Additionally, the mean normalised bias, defined in Equation (5.2), is calculated to measure the relative error between numerical and experimental data with slight modification. Namely, in order to include the uncertainty bounds of experimental results from Subsection 8.2.2, Equation (5.2) is modified so that performance metrics for \check{C}_p are determined relative to these upper (superscript UP) and lower (superscript DN) uncertainty bounds. The modified version of Equation (5.2) is:

$$MNB = \frac{1}{N} \sum_{i=1}^N Q_i, \text{ where} \quad (8.14)$$

$$Q_i = \begin{cases} \left(\frac{q_{i,EXP}^{UP} - q_{i,NUM}}{q_{i,EXP}^{UP}} \right) \cdot 100[\%], & \text{if } q_{i,NUM} > q_{i,EXP}^{UP} \\ 0, & \text{if } q_{i,EXP}^{DN} < q_{i,NUM} < q_{i,EXP}^{UP} \\ \left(\frac{q_{i,EXP}^{DN} - q_{i,NUM}}{q_{i,EXP}^{DN}} \right) \cdot 100[\%], & \text{if } q_{i,NUM} < q_{i,EXP}^{DN} \end{cases} \quad (8.15)$$

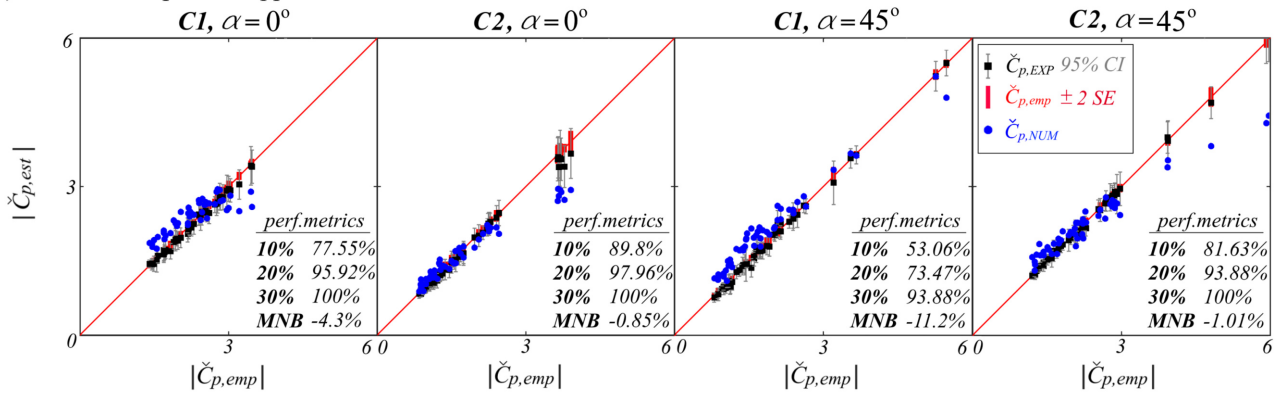
Figure 8.6 presents performance metrics for both methods in evaluating peak pressure coefficients. The absolute values of the negative peak pressure coefficients are reported. Plots include comparisons of estimated peak pressure coefficients ($\check{C}_{p,est}$) from the experimental (labelled with EXP) and numerical (labelled with NUM) results with empirical ($\check{C}_{p,emp}$) ones for a 75-minute EFS event. The empirical results are plotted along the x axis with the corresponding uncertainties, while the related estimated experimental results with their uncertainties and numerical results are plotted along the y axis. Both methods (traditional in Figure 8.6(a) and POT in Figure 8.6(b)) for peak pressure coefficient estimation are employed with optimal setup and uncertainties defined in Subsection 8.2.2. Percentage deviations related to upper and lower uncertainty bounds are calculated, as well as MNB and plots in Figure 8.6 are supplemented with a table view of performance metrics for each case.

Analysing the performance of the traditional “epochal” approach in estimating peak pressure coefficient from numerical results given in Figure 8.6(a), the match with experimental ones is very good. Three out of four cases have around 80% of the results, which fall within a range of less than 10% deviation from the uncertainty window of the $\check{C}_{p,EXP}$ and absolute MNB values are below 5%. Again, like for C_p'' , configuration C1 at 45° demonstrates lower performance metrics compared to the others. Still, more than 90% of data are within a tolerance range of up to 30%. An important observation is that in all cases, higher values of $|\check{C}_p|$ are close to the lower uncertainty bounds of experimental estimations or even underpredicted by LES, despite the MNB values, which are negative in all four cases and suggest an overprediction by LES. This can be attributed to the methodology of the particular approach and possibly biased results toward smaller values of peak pressure coefficients, as described in Subsection 8.2.2.

In examining the results of the POT method, a notable observation is the larger uncertainty bounds from the experimental results and also higher values of $|\check{C}_p|$. It is accompanied by a higher dispersion of numerical data compared to those from the traditional approach, especially at 0°.

It results in lower performance metrics at 0° wind angle in both configurations. However, at 45° , certain trends are not preserved. Namely, the performance metrics of the numerical results from the POT method are comparable to those obtained using the traditional approach, as shown in Figure 8.6. The reason lies in less dispersed results in combination with larger uncertainty bounds. More specifically, the results of estimated peak pressure coefficients using two statistical methods do not show a large discrepancy, as is the case at 0° , and larger uncertainty bounds compared to the traditional approach give comparable performance metrics with both methods. In all, a deviation of less than 10% is achieved for approximately 50% to 85% of the data, varying by case. The POT method's tendency to overestimate peak pressure coefficient values is also evident in LES results. While the *MNB* parameter is predominantly negative, indicating an overall overestimation, it is noteworthy that higher peak pressure coefficients are more accurately captured. Despite this, certain deviations and underpredictions persist, albeit less frequently than in the traditional approach.

a) Traditional “epochal” approach



b) POT method

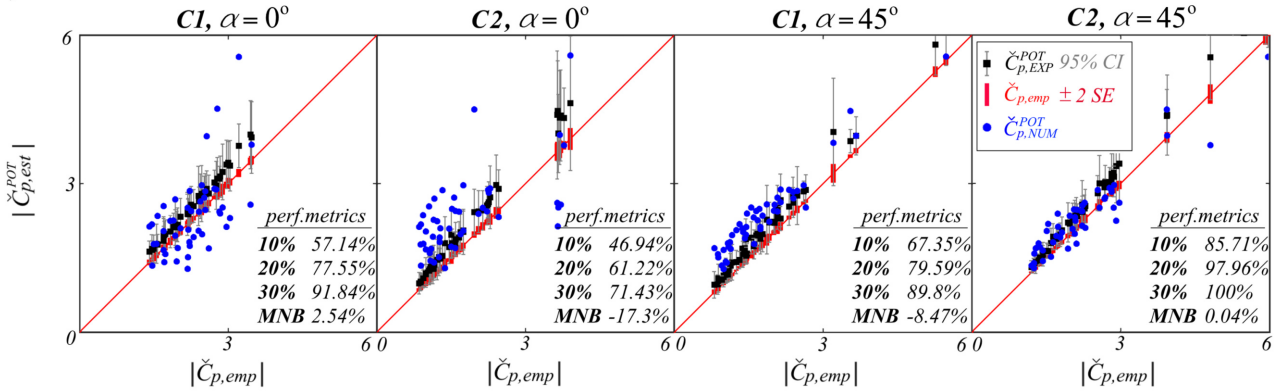


Figure 8.6. Scatter plots with error bars of negative peak pressure coefficient with the table view of performance metrics for four study cases: comparison of the empirical results and corresponding estimated experimental and numerical results using (a) traditional “epochal” approach and (b) POT method, adopted from [42].

Summarising the results of the performance metrics for two statistical methods for estimating peak pressure coefficients, it is clear that both traditional and POT methods provide valuable insights, yet with distinct characteristics. The traditional approach reliably matches experimental data, offering consistent and less dispersed results. On the other hand, despite broader uncertainty bounds and a tendency for overestimation, the POT method notably excels in capturing higher peak pressure coefficients, which are commonly underestimated by the traditional approach. However, considering the superior performance metrics and lower dispersion, the traditional approach has been chosen for the statistical treatment of peak pressure coefficient

values in interpreting numerical results, which will be discussed in the following Subsection 8.3.2.

8.3.2 Effect of signal duration on LES peak pressure coefficients

The focus of this subsection is on the LES results under different durations of the pressure signal ($T_{full} = \{25, 37.5, 75\}$ min in EFS). Besides, analyses of the influence of flow complexity on the accuracy of LES results are also included. The methodology employed for estimating the distribution of peak pressure coefficients is the traditional approach, albeit with slight modifications for optimal setup, as presented in Subsection 8.2.2.1. First, results on the roof are analysed in Subsection 8.3.2.1. Next, in Subsection 8.3.2.1, the investigation is extended to the facade.

8.3.2.1 Peak pressure coefficients on the roof

Figures 8.7 and 8.9 show the distribution of the mean \bar{C}_p , RMS C_p'' and peak \check{C}_p pressure coefficients for both configurations ((a) C1 and (b) C2) along two predefined lines on the roof at 0° and 45° wind angles, respectively. They provide numerical results considering various durations of the pressure signal (T_{full}) and demonstrate its impact on the related pressure statistics throughout the comparison with the corresponding experimental data. Uncertainty bounds of the 95% CI for the estimated peak pressure coefficients ($\check{C}_{p,est}$), obtained in Subsection 8.2.2.1 from experimental measurements, are also included for each T_{full} , as well as the empirical results ($\check{C}_{p,emp}$). The first line, marked as $L1$ in plots, is the one close to the lateral edge at $y_0 = 0.45B$, and the second one, marked as $L2$, is the local central line on the roof at $y_0 = 0$.

In addition, the surface plots of pressure statistics on the roof from LES are given in Figures 8.8 and 8.10 for two configurations ((a) C1 and (b) C2) at 0° and 45° wind angles, respectively, focusing solely on $T_{full} = 75$ min in EFS. These figures represent the distributions of negative peak pressure coefficients \check{C}_p , alongside the mean \bar{C}_p and RMS C_p'' values of the pressure coefficient. Moreover, these plots are partly overlapped with the mean velocity streamlines in the vicinity of the roof. Due to the symmetrical nature of the flow above the roof, these streamlines are depicted on just one side of the roof, originating from the symmetry plane.

Wind approaching at 0°

Results in Figure 8.7 reveal the impact of the decrease in T_{full} on pressure statistics at 0° wind angle. Regarding the configuration C1 (Figure 8.7(a)), numerical results of \bar{C}_p and C_p'' over both lines ($L1$ and $L2$) match perfectly for all analysed values of T_{full} , without any noticeable discrepancy. While generally achieving good agreement with experimental results, slightly higher differences are observed across line $L1$, particularly near the upwind corner, where LES slightly underestimates both \bar{C}_p and C_p'' .

Examining the peak pressure coefficients reveals more pronounced differences across various T_{full} values in Figure 8.7(a). Notably, the experimental results demonstrate an increase in the uncertainty bounds of the 95% CI with decreasing T_{full} . In contrast, the discrepancy in LES predictions between T_{full} values of 37.5 and 75 min in EFS is negligible, with both lines on the graph overlapping entirely and falling within the range of experimental results. However, for T_{full} equal to 25 min in EFS, slight discrepancies emerge, although they remain minor and

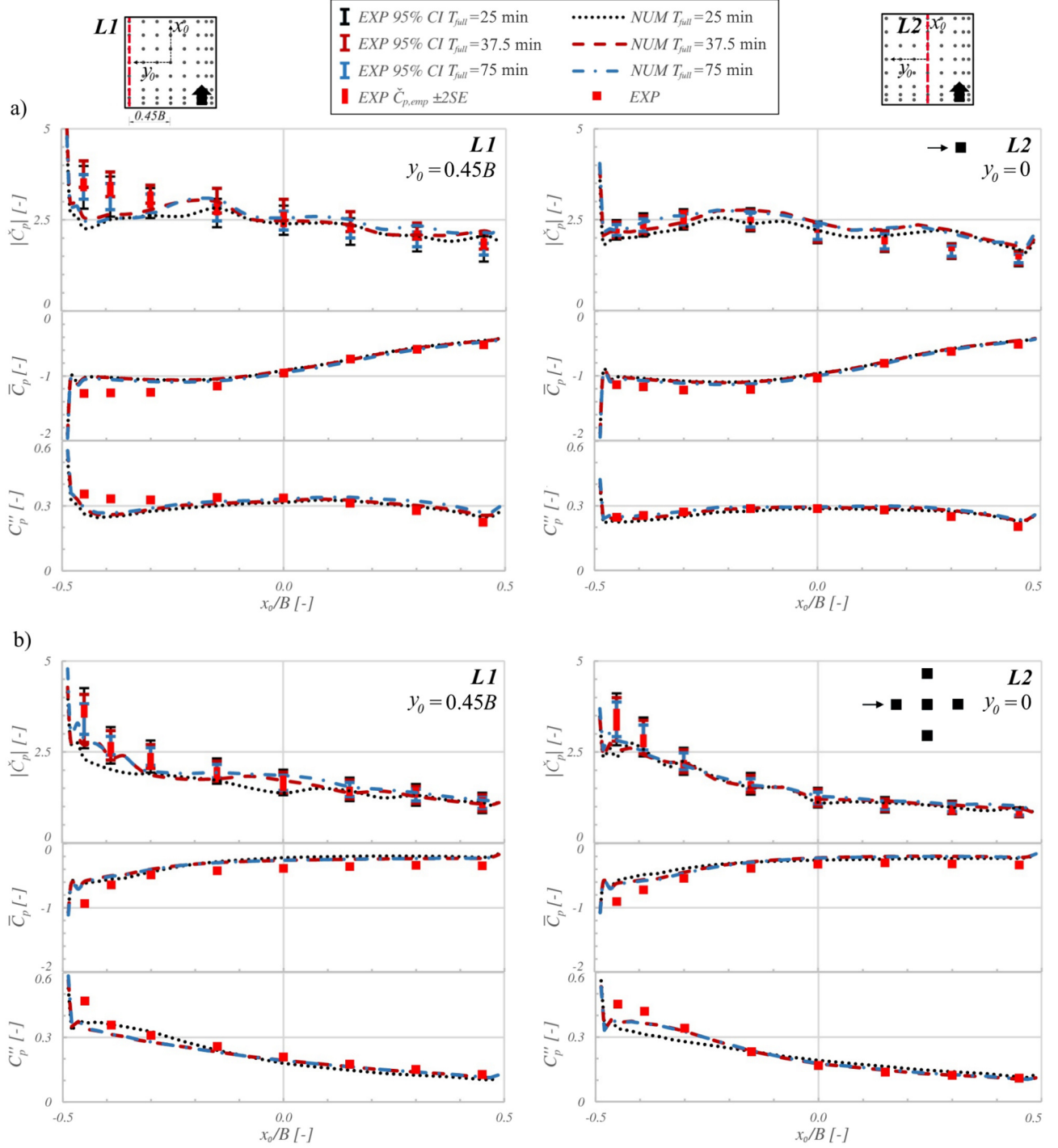


Figure 8.7. Pressure statistics along two predefined lines on the roof for various durations of pressure signal (T_{full}) at 0° for configuration (a) C1 and (b) C2, adopted from [42].

align with the corresponding uncertainty range. The largest deviation between estimated peak pressure coefficients from LES and empirical ones occurs in the same region as observed for \bar{C}_p and C_p'' , near the upstream corner along line $L1$. Again, results from LES are underestimated compared to the empirical ones and even slightly below the uncertainty bounds of the estimated values from the experimental data.

It's worth noting that the uncertainty bounds in the experimental data exhibit wider variability over line $L1$ compared to line $L2$ despite the values of the peak pressure coefficients mostly falling

within the same range. This underscores the importance of accurate uncertainty estimation, as no universal rule can be applied to all measurement locations, even within the same case.

Placing the building in group configuration C2 (Figure 8.7(b)) has not resulted in significant changes in the outcome compared to configuration C1. Consistently, similar levels of agreement are observed across all reported pressure statistics for various T_{full} values, whether considering LES results exclusively or in comparison with experimental data. The only deviation from the previous findings is noticed in the results for C_p'' where discrepancies emerge for $T_{full} = 25$ min in EFS compared to those obtained for 37.5 and 75 min in EFS.

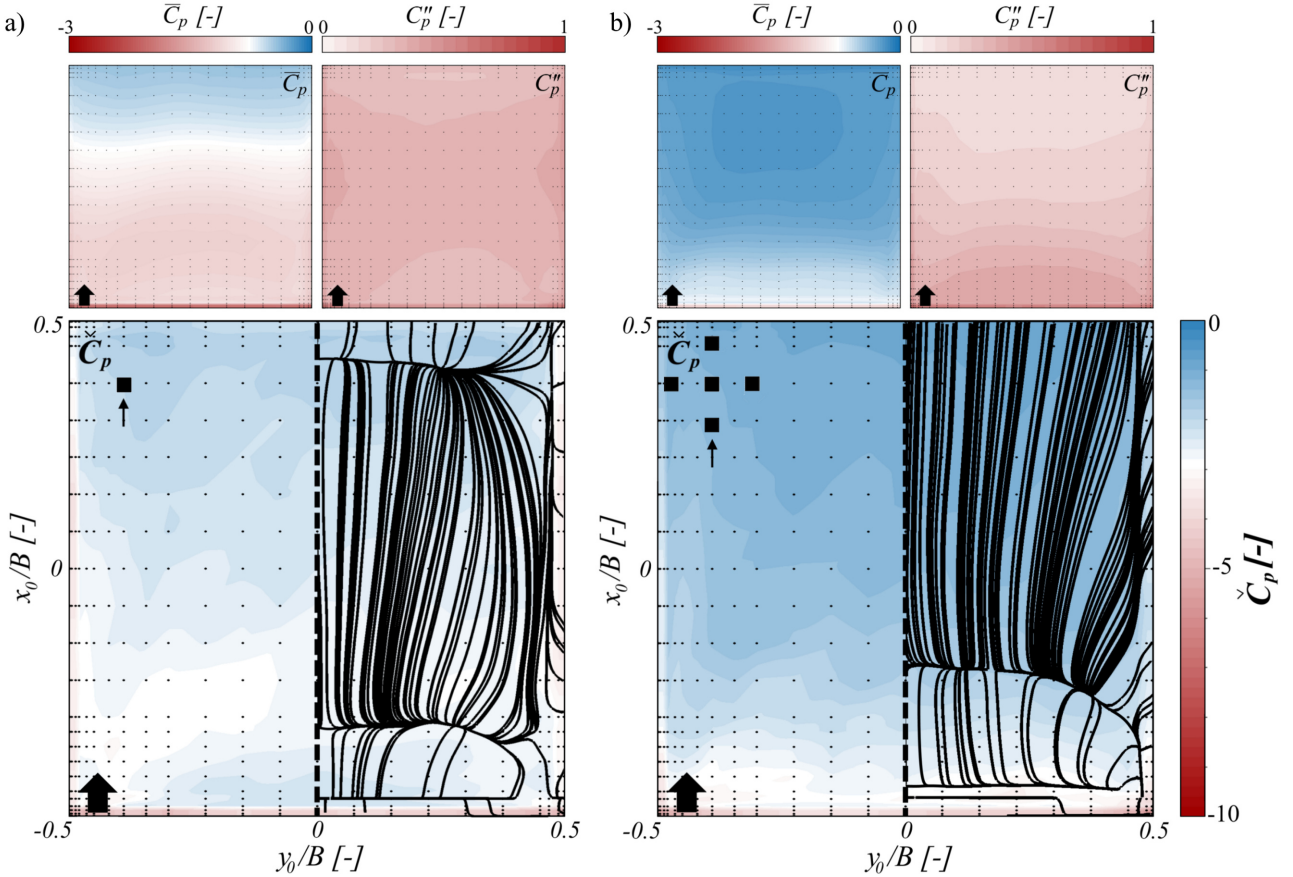


Figure 8.8. Pressure statistics on the roof with mean flow structures at 0° : Surface plots of mean, RMS and peak pressure coefficients overlapped with streamlines of mean velocity in the vicinity of the roof and marked pressure probes (black dots) for configuration (a) C1 and (b) C2, adopted from [42].

Regarding the surface distribution of peak pressure coefficients on the roof, in the C1 configuration, the most pronounced negative peak pressure coefficients are observed near the upstream and lateral edges of the roof, as depicted in Figure 8.8(a). Here, peak pressure coefficients reach values of up to $\check{C}_p = -5.2$ near the upstream corners. These findings coincide with the high values of the mean and RMS values of the pressure coefficient in particular zones. In the roof's central region, there is a notable increase in negative peak pressure coefficients in the zone between the reattachment line of the thin recirculation region near the upstream edge and the upstream part of the primary vortex above the roof reaching the maximal negative peak pressure coefficients in the central part of the roof of around -2.5. In this area, a modest increase in the RMS values of the pressure coefficient is also noted. As one moves towards the lateral edges, this area expands and merges with the upstream corners, highlighting the three-dimensional nature of the flow.

In the C2 configuration, the distribution of the pressure coefficients is dominantly influenced by the turbulent wake generated from the upstream building, as noted in Chapter 6. Unlike a large separation region above the roof in configuration C1, a small recirculation region followed by the reattachment is clearly visible in Figure 8.8(b) in the streamlines plot. The most negative peak pressure coefficients are concentrated in the area close to the windward edge. The values in the corner zones are even slightly higher than those obtained for the C1 configuration, reaching values of $\check{C}_p = -5.4$. These peak pressure coefficients decrease moving downstream following the same pattern as C_p'' , which is elevated in the upstream region due to the incoming turbulent flow but diminishes further downstream. The \bar{C}_p distribution exhibits mild suction across the roof.

Wind approaching at 45°

Results presented in Figure 8.9 show the pressure statistics along lines $L1$ and $L2$ at a 45° wind angle. Across both configurations, minimal discrepancies in LES results are observed for different T_{full} values, encompassing \bar{C}_p , C_p'' , and \check{C}_p . However, the alignment with experimental data varies between the two configurations. In configuration C1 (Figure 8.9(a)), notable discrepancies near the upstream corner along line $L1$ are evident in \bar{C}_p and C_p'' , although improvements are noted along line $L2$. Nevertheless, peak pressure coefficients along both $L1$ and $L2$ exhibit good agreement of LES results compared to both empirical ones and estimated uncertainty bounds from experimental data.

In configuration C2 (Figure 8.9(b)), significant underestimation across all pressure statistics is observed near the upstream corner along line $L1$ in all cases. Discrepancies in predicting C_p'' reach up to 40%, while for \bar{C}_p and \check{C}_p , they are slightly lower, around 30% and 25%, respectively. Transitioning from $L1$ to $L2$, results improve and align more closely with those of configuration C1. Similar to the 0° wind angle case, wider uncertainty bounds of 95% CI are observed near the upstream corners along $L1$ for both configurations.

The shift from a 0° to a 45° wind angle significantly transforms the flow structures above the roof, resulting in a pair of cone vortexes. This change remarkably influences the peak pressure coefficient distribution on the roof. As depicted in Figure 8.10(a,b), the most substantial negative peak pressure coefficients for both configurations are observed in the upstream corner zone. Specifically, these peak pressure coefficients reach up to -9.8 and -9.2 values in the C1 and C2 configurations, respectively, and decrease as the vortexes extend downstream.

There is a noticeable difference in the distributions of all the mean, RMS and peak pressure coefficients between the two configurations. Namely, the change in pressure statistic values in the C1 configuration is sharply defined, contrasting with the C2 configuration, where this transition is smoother but broader. This variation arises from the buildings' arrangement in the C2 configuration, where the four surrounding buildings compress the wind flow around the primary central building. That leads to an increase in the size of cone vortexes in C2 configuration but also slightly different shapes visible in the streamlines plot in Figure 8.10(b). In the central plane of the flow, the area is subject to slight mean suction, and the C_p'' values are also relatively low. It is attributed to the wind flow attached to the roof.

8.3.2.2 Peak pressure coefficients on the facade

The distribution of the mean \bar{C}_p , RMS C_p'' and peak \check{C}_p pressure coefficients for both configurations (C1 and C2) and wind angles (0° and 45°) along the facade ring at $z = 0.75H$ is illustrated

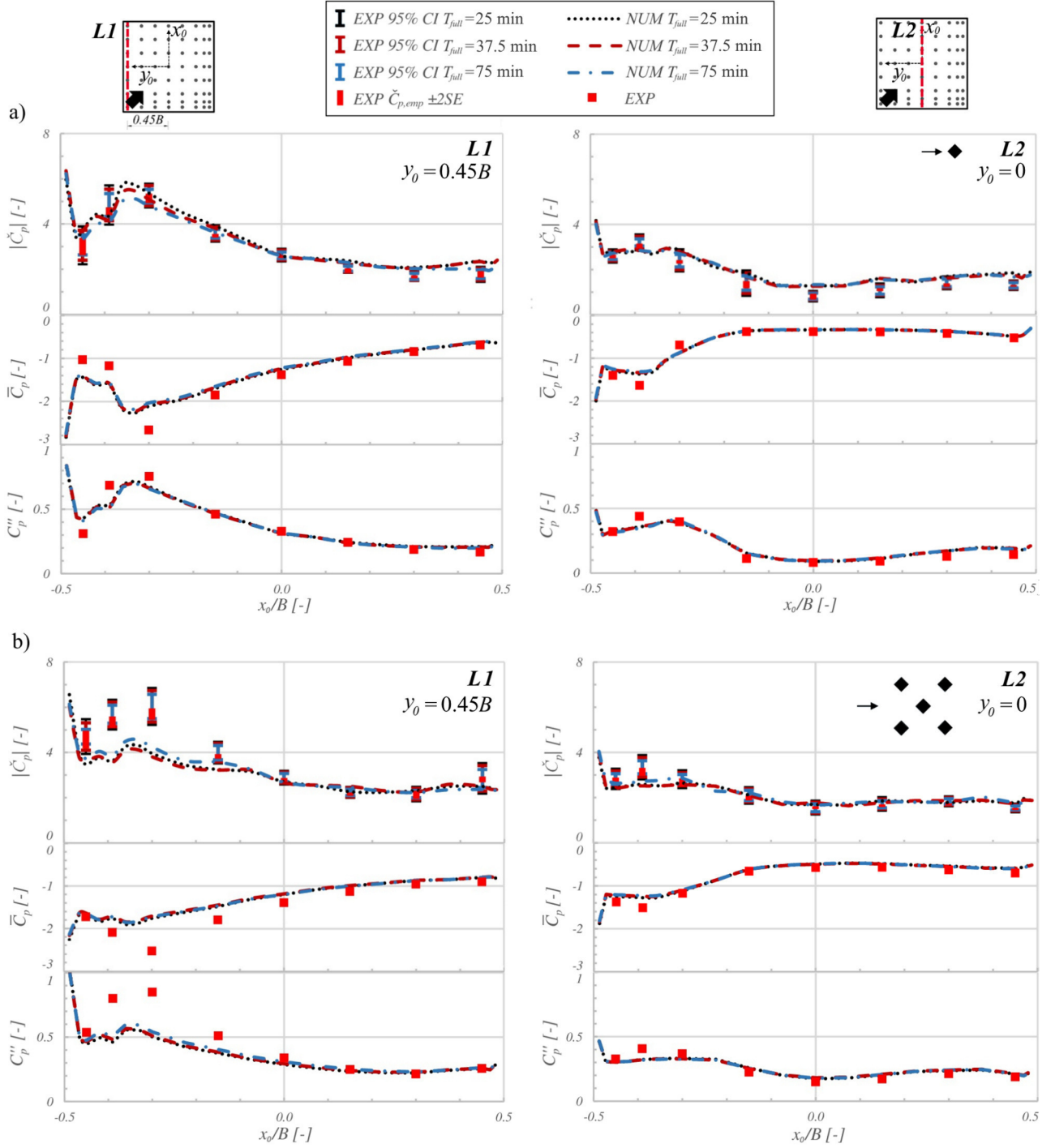


Figure 8.9. Pressure statistics along two predefined lines on the roof for various durations of pressure signal (T_{full}) at 45° for configuration (a) C1 and (b) C2, adopted from [42].

in Figure 8.11. Results are presented in the same manner as it is done in Figures 8.7 and 8.9 in Subsection 8.3.2.1, with one adjustment. Unlike focusing solely on negative peak pressure coefficients on the roof, the analysis extends to include positive peak pressure coefficients on the windward sides of the facade (indicated with the light red background on plots in Figure 8.11), while negative peak pressure coefficients are examined on the leeward sides.

Numerical results of the first- and second-order statistics of pressure coefficients reveal a very good alignment with experimental results across all analysed configurations and wind angles. No noticeable deviation among different T_{full} values is observed. Comparing the level of

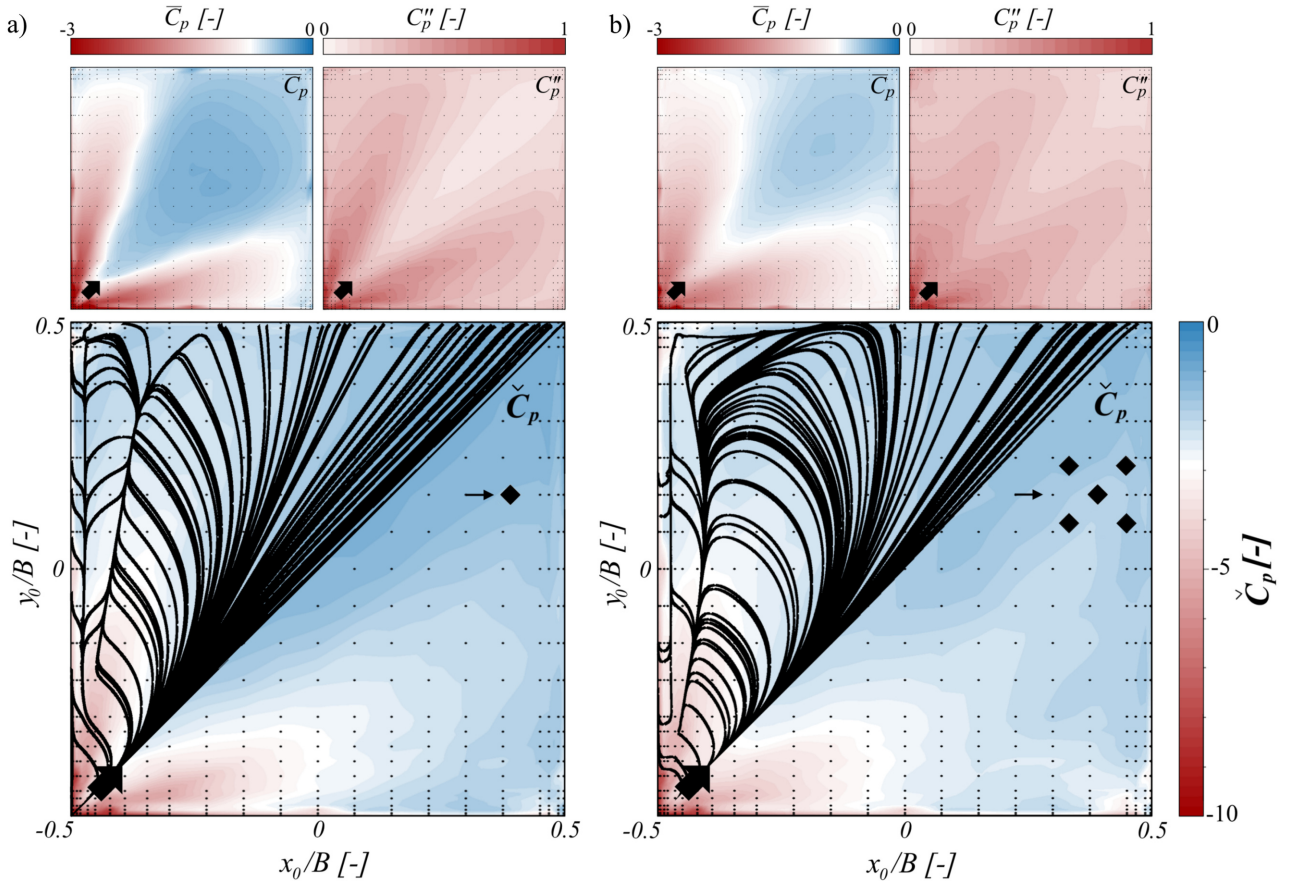


Figure 8.10. Pressure statistics on the roof with mean flow structures at 45° : Surface plots of the mean, RMS and peak pressure coefficients overlapped with streamlines of mean velocity in the vicinity of the roof and marked pressure probes (black dots) for configuration (a) C1 and (b) C2, adopted from [42].

agreement between results for the two configurations, a slight underestimation of C_p'' is observed in configuration C2 at both wind angles in the LES compared to the experimental data. It is particularly pronounced on the leeward sides of the facade. However, concerning peak pressure coefficients, LES results fall within the uncertainty bounds of the experiments, except for configuration C2 at 45° , where a discrepancy on the leeward sides is evident in Figure 8.11(b). Once more, the influence of analysed signal durations on estimated peak pressure coefficients from LES appears minimal.

Summing up findings for both high-rise building roof and facade and all analysed T_{full} , the difference in LES prediction of \bar{C}_p , C_p'' and \check{C}_p is negligible and is in overall a good agreement with the experimental results for all four cases. The highest mismatch between the numerical and experimental results is recorded near the upwind corner on the roof, which also coincides with the maximal uncertainty range of 95% confidence interval from the experimental results, causing these zones to be particularly challenging to predict due to the significant discrepancies in results.

Even though the grid and setup are consistent across all four cases, the results pointed out the importance of individual treatment and validation of each case, as no unique rule can be applied to all. It is demonstrated first in the experimental results on the roof where, for normalised error, different performance metrics are obtained for 0° and 45° wind angles. Next, the numerical results presented in this section show variations in the ability to reproduce certain

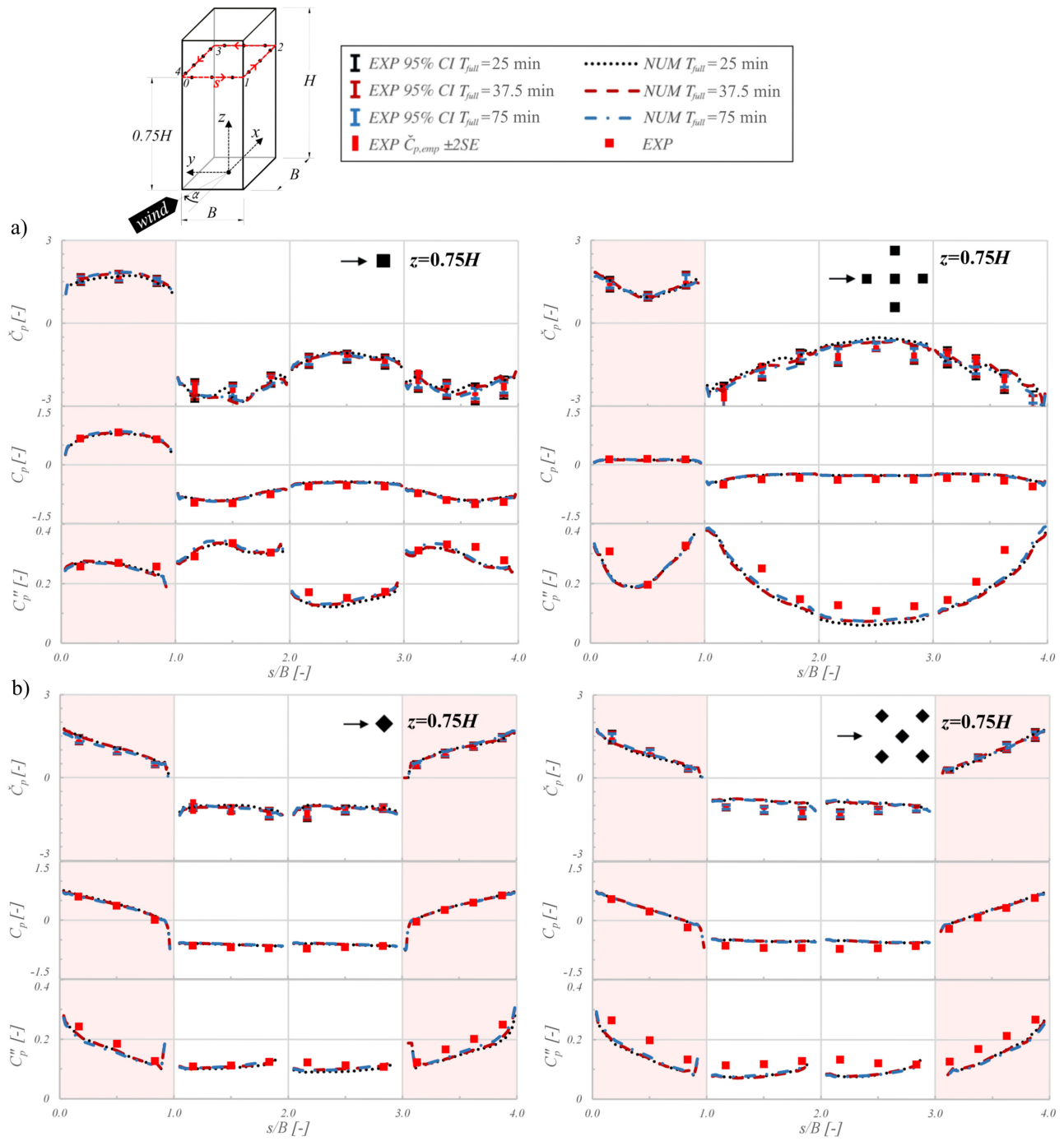


Figure 8.11. Pressure statistics over the ring on the facade for various durations of pressure signal (T_{full}) for configurations C1 and C2 at (a) 0° and (b) 45° wind angles; positive peak pressure coefficients are reported on the windward sides of the building (indicated with a light red background on the plot) and negative on the leeward sides, adopted from [42].

flow mechanisms and pressure statistics, marking configuration C2 at a 45° wind angle as the most difficult case for numerical modelling, observed on the roof and facade as well.

8.4 Conclusions

The results presented in this chapter indicate wind-induced loading, targeting the peak pressure coefficient mainly on the roof and only superficially on the facade of the high-rise buildings in two configurations, C1 and C2. A dual approach is employed, combining wind tunnel experiments with LES methods. The 11-hour EFS experimental data are processed using the traditional “epochal” approach and the POT. Peak pressure coefficients with a 20% probability of exceedance are reported. The analyses of various signal durations are used in the uncertainty quantification of estimated peak pressure coefficients from the experiments, while for numerical simulations, a duration of 25, 37.5 and 75 min in EFS are retained. The process of uncertainty quantification ensures a comprehensive understanding of the limitations and reliability of the findings.

Results indicate that the traditional approach yields higher performance metrics than the POT method, offering more reliable, consistent, and less dispersed results. However, the POT method notably excels in capturing higher peak pressure coefficients, which the traditional approach underestimates. The transparent evaluation procedure has also defined the optimal setup for studied cases for the traditional approach.

The section on experimental results reported the distribution of peak pressure coefficients on high-rise buildings, highlighting variations across four different wind angles (0° , 15° , 30° and 45°) and two configurations. It identifies two critical approaching wind angles, 0° and 45° , for further in-depth numerical analysis.

Uncertainty bounds of the estimated value of the peak pressure coefficient, associated with different signal durations, reveal that the mean deviation within a 95% confidence interval for a signal duration of 25 min in EFS is less than 20%, while the maximum deviation is approximately 40%. These metrics vary across different wind angles, highlighting different flow complexity. Extending the signal to 50 min in EFS reduces uncertainty levels, with mean values around 15% and maximum deviations dropping below 20%.

Comparative analysis of the LES results against experimental data confirmed the reliability of the traditional “epochal” approach, offering consistent and less dispersed results compared to the POT method. Therefore, the traditional approach with a predefined optimal setup is utilised in processing the numerical results.

Numerical results of the LES prediction of the peak pressure coefficients on the roof and facade, as well as the first- and second-order pressure statistics, exhibit negligible differences across all analysed durations. This suggests that a duration of 25 min in EFS serves as a reliable representation of the entire signal, and numerical results align well with experimental ones. However, notable discrepancies are observed near the upwind corner on the roof, coinciding with wider uncertainty intervals in the experimental data. These differences highlight challenges in predicting accuracy for these specific areas.

9 Concluding remarks

9.1 Summary

This dissertation explores the application of the LES method to study wind flow in urban areas. The research is conducted across three key areas. First, the dynamics of wind flow and specific flow mechanisms are examined. Second, the results obtained are utilised to assess wind energy potential. Finally, a comprehensive analysis of wind-induced surface pressure is performed in the wind loading study.

The focus is on the wind flow around high-rise buildings in three configurations:

- Configuration C1—an isolated high-rise building with flat and decked roof shapes;
- Configuration C2—a group configuration of five geometrically identical high-rise buildings with flat roofs, arranged in a regular circular cluster with four buildings surrounding a central one in a “cross” arrangement;
- Configuration C3—a group configuration with the same building geometry as in C2 but arranged in an “x” pattern.

All configurations are analysed at two approaching wind angles, 0° and 45° . The accuracy of the numerical simulations is assessed through validation using available experimental data.

The study of wind flow and energy assessment includes all three configurations, focusing on two aspects:

- The influence of roof shape in configuration C1, comparing flat and decked roof shapes;
- The impact of nearby high-rise buildings and their arrangement, combining results from all three configurations for the central building.

The roof zone receives special attention due to its specific flow characteristics and favourable location for wind energy exploitation.

The wind loading study incorporates available wind tunnel measurements with the LES method, primarily targeting the peak pressure coefficient on the roof and, to a lesser extent, on the facade of high-rise buildings in configurations C1 and C2. Two main topics are investigated:

- The selection of the optimal statistical setup for estimating the peak pressure coefficient with the desired probability and minimal uncertainty. It includes two methods: the traditional “epochal” approach and the POT method, alongside the complex parametric analyses;

- The uncertainty bounds of the estimated peak pressure coefficient associated with different pressure signal durations from the 11-hour experimental signal (in EFS). These bounds serve as a cornerstone for validating the LES method and examining its performance.

9.2 Main contributions

This dissertation makes several contributions to the field of wind engineering, particularly in the application of the LES method to study wind flow in urban environments. The research provides new insights into wind flow dynamics around high-rise buildings, advances the assessment of wind energy potential, and improves the understanding of wind-induced surface pressures. These contributions are detailed below across the three primary areas of investigation: wind flow dynamics, wind energy assessment, and wind loading analysis.

Wind flow dynamics

Wind flow around an isolated high-rise building in configuration C1 reveals significant reductions in flow separation above the roof when switching from a flat to a decked roof shape. Moreover, the decked roof shape shows insensitivity to changes in wind direction, providing more stable aerodynamic performance.

Placing the high-rise building in the cluster, surrounded by four buildings, demonstrates a significant influence of buildings' arrangement on the wind flow. In the "cross" shape configuration (C2), a sheltering effect of the upstream building at a 0° wind angle reduces wind speed around the central one and increases turbulence, which further dumps the separation. On the other hand, at 45° , the Venturi effect boosts wind velocity by up to 50%, compared to the reference free-stream value. Similar patterns of aerodynamic behaviour are observed in the "x" shaped arrangement (configuration C3) but for opposite wind angles. This consistency reinforces the robustness of the findings and underscores the importance of building orientation and prevailing wind direction in urban planning and design.

Urban wind energy

The analyses demonstrate that decking the roof reduces flow disturbances compared to flat roofs, leading to a more stable flow above the roof and favourable wind energy potential in the zone close to the rooftop. This finding advances the understanding of how roof shapes influence wind patterns and suggests that decked roofs are more suitable for urban wind energy exploitation. The proposed methodology of mapping wind resources above various roof shapes can be extended to different geometries and applications, indicating its broad potential.

The research identifies optimal line locations for wind energy harvesting above the roof, with two key lines parallel to the windward edge of the building. The study reveals notable variations in WPD due to building arrangements and wind angles. For instance, in the "cross" shape configuration (C2), the highest normalised WPD is recorded at a 45° wind angle, while the isolated building configuration (C1) shows high WPD values at both 0° and 45° . These findings indicate that the arrangement of buildings and their orientation relative to the wind are critical factors in optimising wind energy exploitation.

Another important factor is the type of wind turbine. The completed analysis highlights the significant contribution of the vertical wind velocity component to total wind energy, suggesting

that VAWTs are particularly effective in urban environments. However, results also show that HAWTs perform well at specific locations, emphasising the need for strategic turbine placement based on detailed wind flow analyses. This comprehensive approach advances the potential for wind energy exploitation by providing a framework to maximise wind energy capture in complex urban landscapes.

Wind loads on high-rise buildings

The investigation employs advanced methods, including the traditional “epochal” approach and the POT method, to analyse wind-induced peak pressure coefficients on high-rise buildings. It demonstrates that while the traditional approach offers reliable and consistent results, the POT method excels in capturing higher peak pressures, highlighting the importance of method selection based on specific structural design needs. Moreover, parametric analyses reveal the optimal set of parameters that reduces the uncertainty in the predefined time window.

The comparative analysis of LES results against experimental data confirms the reliability of the traditional “epochal” approach. The research demonstrates that a 25-minute EFS duration reliably represents the entire signal, with numerical results that align well with experimental data. This validation supports the use of LES methods in predicting wind-induced surface pressure, strengthening their application in structural design.

Despite generally aligned results between numerical simulations and experiments, discrepancies near the upwind roof corners underscore challenges in predicting localised pressures in a particular zone. Moreover, the varying performance metrics between wind angles of 0° and 45° in the experimental part of the study, as well as the distinct levels of agreement of numerical results across different cases compared to the experimental findings, highlights the need to treat and validate each case individually.

In conclusion, LES has proven to be effective as a numerical method to simulate complex flows in urban environments accurately. It has broad applications across various engineering disciplines. The research aims to promote its broader adoption in similar studies, hoping that increased application will pave the way for LES to become a stand-alone tool in wind engineering.

9.3 Recommendations for future work

This dissertation explores various aspects of the numerical LES method for studying wind effects in urban areas, including urban wind energy assessment and wind-induced loading on high-rise buildings. However, several research directions remain open for further development. First, the approximations and limitations of this study are identified, along with potential extensions of these topics. Then, considering current trends in numerical modelling, particularly in LES, ideas for future research are proposed.

The first approximation made in the present study is the geometry of the building model, which is adopted as the idealised square-base cuboid high-rise. However, a realistic high-rise building features additional geometric details, such as various corner zone shapes on the facade, the existence of balconies and parapets, and modifications in the roof shape. These features affect the wind flow structures and may contribute to creating the separation and recirculation zones. Although some research papers on this topic already exist, they mostly rely on low-fidelity numerical methods. Further investigations using high-fidelity numerical methods are needed

to systematically assess how different levels of geometric detail influence flow patterns and, consequently, wind energy potentials and wind loading. It would be interesting to formulate these findings as guidelines, identifying which approximations have minimal impact on the wind flow and which should be avoided to realistically represent a building in an urban area.

Regarding the layout of the surrounding structures, this study is limited to a group of five buildings arranged in two different configurations. While numerous studies have examined wind effects in various building arrangements, only a few focus on real urban blocks, and even fewer consider wind energy. Future research should synthesise the existing knowledge on urban wind flow and try to reinterpret it in the context of wind energy. This study has shown that certain building arrangements at specific prevailing wind angles can create desirable effects, such as flow acceleration due to the Venturi effect. Therefore, based on synthesised knowledge of wind flow, developing recommendations for urban planners and decision-makers on optimising building arrangements and geometric modifications to enhance urban wind energy potential would be of great interest.

The limitations in the wind loading study presented in this research, beyond the geometric approximations mentioned earlier, are primarily related to the statistical treatment of the peak pressure coefficient. First, the exploration of alternative probability distribution models for describing negative peak pressures, such as the Fréchet and reverse Weibull distributions, should be considered. Next, this study only analysed the uncertainty associated with the statistical treatment of peak pressure coefficients from wind tunnel experiments. A valuable extension would be to apply the same procedure to pressure signals from LES to evaluate their consistency. This would require a long-duration LES signal to provide a robust statistical foundation. In addition, there is a notable lack of studies investigating the impact of the Reynolds number on peak pressure coefficients since Reynolds independence applies only to mean values. Further research on this topic would improve the reliability of peak pressure predictions.

Considering the development of the LES method, it is vital to establish official guidelines for creating and validating numerical simulations to determine the standard practice in the field. This research contributes to this effort by proposing a validation strategy for comparing two signals of different durations. However, many other aspects still need to be addressed, including guidelines for grid creation. These should define optimal mesh refinement strategies, considering the definition of refinement zones, the minimum cell size relative to the object of interest, and the characteristic flow structures that need to be captured. Another important topic is the definition of boundary conditions at the inlet, as there is currently no consensus on the most appropriate approach, and this remains an area of ongoing research.

Regarding the validation of LES, further development can be done by specifying minimal validation criteria. Namely, the main idea behind numerical methods is to extend the scope of the experiments, as discussed in the first chapter of this dissertation. This includes modifications to building model geometries and configurations that go beyond those tested in wind tunnels. However, the findings of this study indicate that the accuracy of LES results is highly dependent on the complexity of the wind flow. Therefore, it is necessary to determine the minimal scope of wind tunnel experiments (such as configurations, approaching wind angles, and other relevant factors) that must be considered to validate LES in a given study. Additionally, building an open-access database of experimental data used for LES validation would be extremely valuable. The guidelines for LES validation should also define acceptable accuracy levels for specific variables, enabling a clear assessment of LES performance.

Recent advancements in artificial intelligence have led to its rapid integration across various scientific disciplines, including computational wind engineering. The potential applications of artificial intelligence in this field are diverse, though, in this context, the focus will be on the LES method. One approach is enhancing the LES method itself through the advancements of existing SGS turbulence models or the development of new inlet boundary conditions, with an emphasis on data-driven technologies. Additionally, artificial intelligence could offer a fresh perspective on existing correlations and assist in discovering new ones from experimental data. Achieving this would be particularly beneficial, as it would deepen our understanding of wind behaviour and, consequently, improve the accuracy of numerical models.

Another promising direction for future research is the application of machine learning to reduce the computational burden of numerical simulations. One such approach involves error correction in solutions obtained from coarse-grid, low-fidelity RANS simulations using machine learning models trained on high-fidelity LES data. Several aspects can be explored, such as determining the minimal number of LES simulations required to achieve satisfactory RANS results or evaluating the applicability of the machine learning model to various modifications in building geometries and arrangement of surrounding structures. Research on this topic can provide a powerful tool for practitioners in both wind energy harvesting and wind loading assessments. Namely, the solution to the specific problem covered by the trained machine learning model can be reached on a computer in a few minutes. Furthermore, the potential for advancing and expanding these models to address a wider range of problems is unlimited.

*While there is much work ahead
And the journey has just begun,
With the wind at our back,
we are flying like a bird in the sun.*

-

Bibliography

- [1] N. Info, *Beograd nakon nevremena*, <https://n1info.rs/vesti/video-foto-beograd-nakon-nevremena-steta-na-vise-lokacija-u-gradu/>, 2024, (accessed: 01.12.2024).
- [2] Britannica, *Tacoma Narrows Bridge*, <https://www.britannica.com/topic/Tacoma-Narrows-Bridge>, 2007, (accessed: 01.12.2024).
- [3] USDA, *Derecho damage in Iowa*, <https://disasterphilanthropy.org/resources/derecho/>, 2020, (accessed: 01.12.2024).
- [4] G. B. News, *UGE Harnesses Urban Wind Energy*, <https://greenbuildingnews.com/2014/09/17/uge-harnesses-urban-wind-energy/>, 2014, (accessed: 01.12.2024).
- [5] A. Ray, *Concurrent Calamities*, <https://www.linkedin.com/pulse/ships-semiconductors-skills-concurrent-calamities-amitabh-ray/>, 2024, (accessed: 01.12.2024).
- [6] E. Straža, *Pollution Dispersion in Belgrade*, <https://ekostraza.com/>, 2024, (accessed: 01.12.2024).
- [7] U. N. United Nations, *World urbanization prospects 2018: highlights*, New York: Department of Economic and Social Affairs, Population Division, 2019, ISBN: 978-92-1-148318-5.
- [8] IRENA, *Renewable capacity highlights*, <https://www.irena.org>, 2022, (accessed: 01.07.2024).
- [9] T. Stathopoulos et al., “Urban wind energy: Some views on potential and challenges”, *Journal of Wind Engineering and Industrial Aerodynamics* 179 (2018), pp. 146–157, DOI: 10.1016/j.jweia.2018.05.018
- [10] A. Kc, J. Whale, T. Urmee, “Urban wind conditions and small wind turbines in the built environment: A review”, *Renewable Energy* 131 (2019), pp. 268–283, DOI: 10.1016/j.renene.2018.07.050.
- [11] M. Intelligence, <https://www.mordorintelligence.com/industry-reports/small-wind-turbine-market>, 2024, (accessed: 01.07.2024).
- [12] Z. Tasneem et al., “An analytical review on the evaluation of wind resource and wind turbine for urban application: Prospect and challenges”, *Developments in the Built Environment* 4 (2020), p. 100033, DOI: 10.1016/j.dibe.2020.100033
- [13] L. C. Pagnini, M. Burlando, M. P. Repetto, “Experimental power curve of small-size wind turbines in turbulent urban environment”, *Applied Energy* 154 (2015), pp. 112–121, DOI: 10.1016/j.apenergy.2015.04.117.
- [14] B. Blocken et al., “Numerical Study on the Existence of the Venturi Effect in Passages between Perpendicular Buildings”, *Journal of Engineering Mechanics* 134.12 (2008), pp. 1021–1028, DOI: 10.1061/(ASCE)0733-9399(2008)134:12(1021).

- [15] B. Blocken, T. Stathopoulos, J. Carmeliet, “Wind Environmental Conditions in Passages between Two Long Narrow Perpendicular Buildings”, *Journal of Aerospace Engineering* 21.4 (2008), pp. 280–287, DOI: 10.1061/(ASCE)0893-1321(2008)21:4(280).
- [16] B. Blocken, “Smart Cities: a Wind Engineering Perspective”, *Presented at INVENTO 2016, XIV Conference of the Italian Association for Wind Engineering*, Terni, Italy, 2016.
- [17] Council on Tall Buildings and Urban Habitat, *Bahrain World Trade Center*, <http://www.skyscrapercenter.com/building/bahrain-world-trade-center1/998>, 2024, (accessed: 01.12.2024).
- [18] J. Mortimer, *Elephant & Castle tower block turbines barely move because of how loud they are*, <https://www.mylondon.news/news/south-london-news/elephant-castles-iconic-strata-tower-23551686>, 2023, (accessed: 01.12.2024).
- [19] NOAA, *U.S. Billion-Dollar Weather and Climate Disasters*, tech. rep., NOAA National Centers for Environmental Information (NCEI), 2023, DOI: 10.25921/stkw-7w73, (accessed: 01.11.2024).
- [20] A. K. Jay et al., “Overview: Understanding risks, impacts, and responses”, *Fifth National Climate Assessment*, ed. by A. Crimmins et al., Washington, DC, USA: U.S. Global Change Research Program, 2023, chap. 1, DOI: 10.7930/NCA5.2023.CH1.
- [21] D. M. Overend, K. Zammit, “Wind loading on cladding and glazed façades”, *International Symposium on the Application of Architectural Glass, ISAAG*, 2006.
- [22] A. Kareem, “Performance of cladding in Hurricane Alicia”, *Journal of Structural Engineering* 112(12) (1986), pp. 2679–2693.
- [23] E Maruta, M Kanda, J Sato, “Effects on surface roughness for wind pressure on glass and cladding of buildings”, *Journal of Wind Engineering and Industrial Aerodynamics* 74-76 (1998), pp. 651–663, DOI: 10.1016/S0167-6105(98)00059-2
- [24] W. Kim, Y. Tamura, A. Yoshida, “Interference effects on local peak pressures between two buildings”, *Journal of Wind Engineering and Industrial Aerodynamics* 99.5 (2011), pp. 584–600, DOI: 10.1016/j.jweia.2011.02.007.
- [25] H. Montazeri, B. Blocken, “CFD simulation of wind-induced pressure coefficients on buildings with and without balconies: Validation and sensitivity analysis”, *Building and Environment* 60 (2013), pp. 137–149, DOI: 10.1016/j.buildenv.2012.11.012
- [26] N. J Cook, *The designer’s guide to wind loading of building structures Part 1: Background, damage survey, wind data and structural classification*, vol. 7, Sevenoaks, Kent, GB: Butterworths (for) Building Research Establishment, Department of the Environment, 1985, ISBN: 0 408 00870 9.
- [27] B. Blocken, “50 years of Computational Wind Engineering: Past, present and future”, *Journal of Wind Engineering and Industrial Aerodynamics* 129 (2014), pp. 69–102, DOI: 10.1016/j.jweia.2014.03.008
- [28] B. Blocken, “Computational Fluid Dynamics for urban physics: Importance, scales, possibilities, limitations and ten tips and tricks towards accurate and reliable simulations”, *Building and Environment* 91 (2015), pp. 219–245, DOI: 10.1016/j.buildenv.2015.02.015.
- [29] B. Blocken, “LES over RANS in building simulation for outdoor and indoor applications: A foregone conclusion?”, *Building Simulation* 11.5 (2018), pp. 821–870, DOI: 10.1007/s12273-018-0459-3.

- [30] F. Toja-Silva, “Urban wind energy: empirical optimization of high-rise building roof shape for the wind energy exploitation”, PhD thesis, Escuela Tecnica Superior de Ingenieros Aeronauticos, Universidad Politecnica de Madrid (UPM), Spain, 2015.
- [31] G. Vita et al., “On the assessment of pedestrian distress in urban winds”, *Journal of Wind Engineering and Industrial Aerodynamics* 203 (2020), p. 104200, DOI: 10.1016/j.jweia.2020.104200.
- [32] AIJ, *Architectural Institute of Japan, Guidebook for CFD Predictions of Urban Wind Environment*, tech. rep., 2007, (accessed: 01.07.2024).
- [33] J. Franke et al., *Best Practice Guideline for the Cfd Simulation of Flows in the Urban; Environment COST Action 732*, COST action 732: Quality Assurance and Improvement of Microscale Meteorological Models, 2007, ISBN: 3-00-018312-4.
- [34] S. B Pope, *Turbulent flows*, Cambridge; New York: Cambridge University Press, 2000, ISBN: 978-1-316-17947-5 978-0-511-84053-1.
- [35] D. Micallef, G. van Bussel, “A Review of Urban Wind Energy Research: Aerodynamics and Other Challenges”, *Energies* 11.9 (2018), p. 2204, DOI: 10.3390/en11092204.
- [36] A. Rezaeiha, H. Montazeri, B. Blocken, “A framework for preliminary large-scale urban wind energy potential assessment: Roof-mounted wind turbines”, *Energy Conversion and Management* 214 (2020), p. 112770, DOI: 10.1016/j.enconman.2020.112770.
- [37] G. Lamberti, C. Gorié, “Sensitivity of LES predictions of wind loading on a high-rise building to the inflow boundary condition”, *Journal of Wind Engineering and Industrial Aerodynamics* 206 (2020), p. 104370, DOI: 10.1016/j.jweia.2020.104370.
- [38] T. Potsis, Y. Tominaga, T. Stathopoulos, “Computational wind engineering: 30 years of research progress in building structures and environment”, *Journal of Wind Engineering and Industrial Aerodynamics* 234 (2023), p. 105346, DOI: 10.1016/j.jweia.2023.105346.
- [39] J. Xing et al., “Early stages wind load assessment using Computational Fluid Dynamics: The new Bologna Stadium roof”, *Structures* 47 (2023), pp. 1912–1926, DOI: 10.1016/j.istruc.2022.11.089.
- [40] K. Kostadinović Vranešević et al., “Furthering knowledge on the flow pattern around high-rise buildings: LES investigation of the wind energy potential”, *Journal of Wind Engineering and Industrial Aerodynamics* 226 (2022), p. 105029, DOI: 10.1016/j.jweia.2022.105029.
- [41] K. Kostadinović Vranešević, S. Ćorić, A. Šarkić Glumac, “LES study on the urban wind energy resources above the roof of buildings in generic cluster arrangements: Impact of building position”, *Journal of Wind Engineering and Industrial Aerodynamics* 240 (2023), p. 105503, DOI: 10.1016/j.jweia.2023.105503.
- [42] K. Kostadinović Vranešević, A. Šarkić Glumac, “Peak pressures on high-rise buildings roof: A dual approach through validated LES and wind tunnel experiments with uncertainty quantification”, *Journal of Wind Engineering and Industrial Aerodynamics* 250 (2024), p. 105784, DOI: 10.1016/j.jweia.2024.105784.
- [43] H. Hemida et al., “On the Flow over High-rise Building for Wind Energy Harvesting: An Experimental Investigation of Wind Speed and Surface Pressure”, *Applied Sciences* 10.15 (2020), p. 5283, DOI: 10.3390/app10155283.

- [44] K. Kostadinović Vranešević, A. Šarkić Glumac, S. Bordas, “The influence of exposure on wind flow characteristics around a high-rise building”, *The 8th European-African conference on wind engineering (8EACWE)*, Bucharest, Romania, 2022, ISBN: 978-973-100-532-4.
- [45] K. Kostadinović Vranešević, A. Šarkić Glumac, “Impact of surroundings on the local peak pressure in high-rise building clusters”, *The 16th International Conference on Wind Engineering (ICWE16)*, Florence, Italy, 2023.
- [46] K. Kostadinović Vranešević, A. Šarkić Glumac, “Peak Pressure Evaluation on High-Rise Buildings: Insights from Experimental and LES Analyses”, *The 9th International Colloquium on Bluff Body Aerodynamics and Applications (BBAA9)*, Birmingham, UK, 2024.
- [47] R. B. Stull, *An Introduction to Boundary Layer Meteorology*, Dordrecht: Springer Netherlands, 1988, ISBN: 978-90-277-2769-5.
- [48] I. Orlanski, “A Rational Subdivision of Scales for Atmospheric Processes”, *Bulletin of the American Meteorological Society* 56.5 (1975), Publisher: American Meteorological Society, pp. 527–530, (accessed: 01.07.2024).
- [49] J. F. Barlow, “Progress in observing and modelling the urban boundary layer”, *Urban Climate* 10 (2014), pp. 216–240, DOI: 10.1016/j.uclim.2014.03.011
- [50] EN1991-1-4, *Eurocode 1: Actions on Structures-Part 1-4: General Actions-Wind Actions*, The European Committee for Standardization (CEN): Brussels, Belgium, 2005.
- [51] American Society of Civil Engineers, *Wind Tunnel Testing for Buildings and Other Structures*, Reston, VA: American Society of Civil Engineers, 2022, ISBN: 978-0-7844-1574-0 978-0-7844-8336-7, DOI: 10.1061/9780784415740.
- [52] E. U. of Technology, *ABL wind tunnel*, <https://www.tue.nl/en/research/research-labs/wind-tunnel>, 2024, (accessed: 01.12.2024).
- [53] D. Guttridge, *Wind Tunnel at the Imperial College London*, <https://www.imperial.ac.uk/aeronautics/research/facilities/10x5-wind-tunnel/>, 2024, (accessed: 01.12.2024).
- [54] M. S. Thordal et al., “Engineering approach for a CFD inflow condition using the precursor database method”, *Journal of Wind Engineering and Industrial Aerodynamics* 203 (2020), p. 104210, DOI: 10.1016/j.jweia.2020.104210.
- [55] M. S. Thordal, J. C. Bennetsen, H. H. H. Koss, “Review for practical application of CFD for the determination of wind load on high-rise buildings”, *Journal of Wind Engineering and Industrial Aerodynamics* 186.December 2018 (2019), pp. 155–168, DOI: 10.1016/j.jweia.2018.12.019
- [56] M. S. Thordal et al., “Towards a standard CFD setup for wind load assessment of high-rise buildings: Part 1 – Benchmark of the CAARC building”, *Journal of Wind Engineering and Industrial Aerodynamics* 205 (2020), p. 104283, DOI: 10.1016/j.jweia.2020.104283
- [57] T. S. Lund, X. Wu, K. D. Squires, “Generation of Turbulent Inflow Data for Spatially-Developing Boundary Layer Simulations”, *Journal of Computational Physics* 140.2 (1998), pp. 233–258, DOI: 10.1006/jcph.1998.5882
- [58] T. Nozu et al., “Mesh-adaptive LES for wind load estimation of a high-rise building in a city”, *Journal of Wind Engineering and Industrial Aerodynamics* 144 (2015), pp. 62–69, DOI: 10.1016/j.jweia.2015.05.007.

- [59] Y. Cao, T. Tamura, H. Kawai, “Investigation of wall pressures and surface flow patterns on a wall-mounted square cylinder using very high-resolution Cartesian mesh”, *Journal of Wind Engineering and Industrial Aerodynamics* 188 (2019), pp. 1–18, DOI: 10.1016/j.jweia.2019.02.013.
- [60] S. H. Huang, Q. S. Li, J. R. Wu, “A general inflow turbulence generator for large eddy simulation”, *Journal of Wind Engineering and Industrial Aerodynamics* 98.10 (2010), pp. 600–617, DOI: 10.1016/j.jweia.2010.06.002
- [61] H. G. Castro, R. R. Paz, “A time and space correlated turbulence synthesis method for Large Eddy Simulations”, *Journal of Computational Physics* 235 (2013), pp. 742–763, DOI: 10.1016/j.jcp.2012.10.035
- [62] Y. Kim, I. P. Castro, Z. T. Xie, “Divergence-free turbulence inflow conditions for large-eddy simulations with incompressible flow solvers”, *Computers and Fluids* 84 (June 2013), pp. 56–68, DOI: 10.1016/j.compfluid.2013.06.001
- [63] H. Aboshosha et al., “Consistent inflow turbulence generator for LES evaluation of wind-induced responses for tall buildings”, *Journal of Wind Engineering and Industrial Aerodynamics* 142 (2015), pp. 198–216, DOI: 10.1016/j.jweia.2015.04.004
- [64] T. Potsis, T. Stathopoulos, “A Novel Computational Approach for an Improved Expression of the Spectral Content in the Lower Atmospheric Boundary Layer”, *Buildings* 12.6 (2022), p. 788, DOI: 10.3390/buildings12060788
- [65] L. Patruno, M. Ricci, “A systematic approach to the generation of synthetic turbulence using spectral methods”, *Computer Methods in Applied Mechanics and Engineering* 340 (2018), pp. 881–904, DOI: 10.1016/j.cma.2018.06.028
- [66] L. Patruno, S. de Miranda, “Unsteady inflow conditions: A variationally based solution to the insurgence of pressure fluctuations”, *Computer Methods in Applied Mechanics and Engineering* 363 (2020), p. 112894, DOI: 10.1016/j.cma.2020.112894
- [67] B. Blocken et al., “Application of computational fluid dynamics in building performance simulation for the outdoor environment: an overview”, *Journal of Building Performance Simulation* 4.2 (2011), pp. 157–184, DOI: 10.1080/19401493.2010.513740
- [68] R. P. Hosker, W. R. Pendergrass, *Flow and Dispersion Near Clusters of Buildings*, NOAA technical memorandum ERL ARL; 153; ATDL contribution file; no. 84/34, Environmental Research Laboratories (U.S.); United States, Environmental Protection Agency, 1987.
- [69] J. Peterka, R. Meroney, K. Kothari, “Wind flow patterns about buildings”, *Journal of Wind Engineering and Industrial Aerodynamics* 21.1 (1985), pp. 21–38, DOI: 10.1016/0167-6105(85)90031-5.
- [70] Y. Tamura, X. Xu, Q. Yang, “Characteristics of pedestrian-level Mean wind speed around square buildings: Effects of height, width, size and approaching flow profile”, *Journal of Wind Engineering and Industrial Aerodynamics* 192 (2019), pp. 74–87, DOI: 10.1016/j.jweia.2019.06.017.
- [71] H. Kawai, “Structure of conical vortices related with suction fluctuation on a flat roof in oblique smooth and turbulent flows”, *Journal of Wind Engineering and Industrial Aerodynamics* 69-71 (1997), pp. 579–588, DOI: 10.1016/S0167-6105(97)00188-8
- [72] R. Marwood, C. Wood, “Conical vortex movement and its effect on roof pressures”, *Journal of Wind Engineering and Industrial Aerodynamics* 69-71 (1997), pp. 589–595, DOI: 10.1016/S0167-6105(97)00189-X

- [73] D Banks et al., “Flow visualization of conical vortices on flat roofs with simultaneous surface pressure measurement”, *J. Wind Eng. Ind. Aerodyn.* (2000), p. 21, DOI: 10.1016/S0167-6105(99)00044-6.
- [74] A. Šarkić Glumac, H. Hemida, R. Höffer, “Wind energy potential above a high-rise building influenced by neighboring buildings: An experimental investigation”, *Journal of Wind Engineering and Industrial Aerodynamics* 175 (2018), pp. 32–42, DOI: 10.1016/j.jweia.2018.01.022.
- [75] F. Ricciardelli, S. Polimeno, “Some characteristics of the wind flow in the lower Urban Boundary Layer”, *Journal of Wind Engineering and Industrial Aerodynamics* 94.11 (2006), pp. 815–832, DOI: 10.1016/j.jweia.2006.06.003.
- [76] P. Louka, S. Belcher, R. Harrison, “Modified street canyon flow”, *Journal of Wind Engineering and Industrial Aerodynamics* 74-76 (1998), pp. 485–493, DOI: 10.1016/S0167-6105(98)00044-0.
- [77] P. Kastner-Klein, E. Fedorovich, M. Rotach, “A wind tunnel study of organised and turbulent air motions in urban street canyons”, *Journal of Wind Engineering and Industrial Aerodynamics* 89.9 (2001), pp. 849–861, DOI: 10.1016/S0167-6105(01)00074-5.
- [78] A. To, K. Lam, “Evaluation of pedestrian-level wind environment around a row of tall buildings using a quartile-level wind speed descriptor”, *Journal of Wind Engineering and Industrial Aerodynamics* 54-55 (1995), pp. 527–541, DOI: 10.1016/0167-6105(94)00069-P.
- [79] A. Hagishima et al., “Aerodynamic Parameters of Regular Arrays of Rectangular Blocks with Various Geometries”, *Boundary-Layer Meteorology* 132.2 (2009), pp. 315–337, DOI: 10.1007/s10546-009-9403-5.
- [80] H. Cheng et al., “Flow over cube arrays of different packing densities”, *Journal of Wind Engineering and Industrial Aerodynamics* 95.8 (2007), pp. 715–740, DOI: 10.1016/j.jweia.2007.01.004.
- [81] T. R. Oke, “Street design and urban canopy layer climate”, *Energy and Buildings* 11.1 (1988), pp. 103–113, DOI: 10.1016/0378-7788(88)90026-6.
- [82] S. Murakami, K. Uehara, H. Komine, “Amplification of wind speed at ground level due to construction of high-rise building in urban area”, *Journal of Wind Engineering and Industrial Aerodynamics* 4.3 (1979), pp. 343–370, DOI: 10.1016/0167-6105(79)90012-6.
- [83] Y. Du, C. M. Mak, B.-s. Tang, “Effects of building height and porosity on pedestrian level wind comfort in a high-density urban built environment”, *Building Simulation* 11.6 (2018), pp. 1215–1228, DOI: 10.1007/s12273-018-0451-y.
- [84] Y. Tominaga, M. Shirzadi, “Wind tunnel measurement of three-dimensional turbulent flow structures around a building group: Impact of high-rise buildings on pedestrian wind environment”, *Building and Environment* 206 (2021), p. 108389, DOI: 10.1016/j.buildenv.2021.108389.
- [85] A. Elshaer et al., “Variations in wind load on tall buildings due to urban development”, *Sustainable Cities and Society* 34 (2017), pp. 264–277, DOI: 10.1016/j.scs.2017.06.008.
- [86] A. Sohankar, “A LES study of the flow interference between tandem square cylinder pairs”, *Theoretical and Computational Fluid Dynamics* 28.5 (2014), pp. 531–548, DOI: 10.1007/s00162-014-0329-2.

- [87] H. Sakamoto, H. Haniu, “Aerodynamic forces acting on two square prisms placed vertically in a turbulent boundary layer”, *Journal of Wind Engineering and Industrial Aerodynamics* 31.1 (1988), pp. 41–66, DOI: 10.1016/0167-6105(88)90187-0.
- [88] R. J. Martinuzzi, B. Havel, “Turbulent Flow Around Two Interfering Surface-Mounted Cubic Obstacles in Tandem Arrangement”, *Journal of Fluids Engineering* 122.1 (2000), pp. 24–31, DOI: 10.1115/1.483222.
- [89] W. Kim, Y. Tamura, A. Yoshida, “Simultaneous Measurement of Wind Pressures and Flow Patterns for Buildings with Interference Effect”, *Advances in Structural Engineering* 16.2 (2013), pp. 287–305, DOI: 10.1260/1369-4332.16.2.287.
- [90] Y. Hui et al., “Pressure and flow field investigation of interference effects on external pressures between high-rise buildings”, *Journal of Wind Engineering and Industrial Aerodynamics* 115 (2013), pp. 150–161, DOI: 10.1016/j.jweia.2013.01.012.
- [91] T. Mara et al., “Aerodynamic and peak response interference factors for an upstream square building of identical height”, *Journal of Wind Engineering and Industrial Aerodynamics* 133 (2014), pp. 200–210, DOI: 10.1016/j.jweia.2014.06.010.
- [92] M. Shirzadeh Gerami, H. Eimani Kalehsar, “Numerical investigation of interference effects on the critical wind velocity of tall buildings”, *Structures* 30 (2021), pp. 239–252, DOI: 10.1016/j.istruc.2021.01.013.
- [93] Z. Xie, M. Gu, “Simplified formulas for evaluation of wind-induced interference effects among three tall buildings”, *Journal of Wind Engineering and Industrial Aerodynamics* 95.1 (2007), pp. 31–52, DOI: 10.1016/j.jweia.2006.05.003.
- [94] J. Liu et al., “LES for pedestrian level wind around an idealized building array—Assessment of sensitivity to influencing parameters”, *Sustainable Cities and Society* 44 (2019), pp. 406–415, DOI: 10.1016/j.scs.2018.10.034.
- [95] G. Vita et al., “On the Wind Energy Resource above High-Rise Buildings”, *Energies* 13.14 (2020), p. 3641, DOI: 10.3390/en13143641.
- [96] Y.-H. Juan et al., “CFD assessment of wind energy potential for generic high-rise buildings in close proximity: Impact of building arrangement and height”, *Applied Energy* 321 (2022), p. 119328, DOI: 10.1016/j.apenergy.2022.119328.
- [97] R. Yoshie et al., “Cooperative project for CFD prediction of pedestrian wind environment in the Architectural Institute of Japan”, *Journal of Wind Engineering and Industrial Aerodynamics* 95.9 (2007), pp. 1551–1578, DOI: 10.1016/j.jweia.2007.02.023.
- [98] B. Blocken, J. Carmeliet, “Pedestrian Wind Environment around Buildings: Literature Review and Practical Examples”, *Journal of Thermal Envelope and Building Science* 28.2 (2004), pp. 107–159, DOI: 10.1177/1097196304044396.
- [99] Y. Zhang, Z. Gu, C. W. Yu, “Impact Factors on Airflow and Pollutant Dispersion in Urban Street Canyons and Comprehensive Simulations: a Review”, *Current Pollution Reports* 6.4 (2020), pp. 425–439, DOI: 10.1007/s40726-020-00166-0.
- [100] H. Mittal, A. Sharma, A. Gairola, “A review on the study of urban wind at the pedestrian level around buildings”, *Journal of Building Engineering* 18 (2018), pp. 154–163, DOI: 10.1016/j.jobe.2018.03.006.
- [101] CEDVAL, *Compilation of Experimental Data for Validation of Microscale Dispersion Models*, <https://mi-pub.cen.uni-hamburg.de/index.php?id=628>, 2007, (accessed: 01.07.2024).
- [102] H. Hemida, A. Šarkić, *Final Report of a Short Term Scientific Mission COST Action TU1304: Wind tunnel tests - air flow around buildings*, tech. rep., 2014, (accessed: 01.07.2024).

- [103] “Design requirements”, ed. by I. E. Commission, Edition 4.0, Wind energy generation systems / International Electrotechnical Commission part 1, Geneva, Switzerland: International Electrotechnical Commission, 2019, ISBN: 978-2-8322-6253-5.
- [104] T. Ishugah et al., “Advances in wind energy resource exploitation in urban environment: A review”, *Renewable and Sustainable Energy Reviews* 37 (2014), pp. 613–626, DOI: 10.1016/j.rser.2014.05.053
- [105] F. Toja-Silva, “A review of computational fluid dynamics (CFD) simulations of the wind flow around buildings for urban wind energy exploitation”, *Journal of Wind Engineering* (2018), p. 22, DOI: 10.1016/j.jweia.2018.07.010
- [106] I. Abohela, N. Hamza, S. Dudek, “Effect of roof shape, wind direction, building height and urban configuration on the energy yield and positioning of roof mounted wind turbines”, *Renewable Energy* 50 (2013), pp. 1106–1118, DOI: 10.1016/j.renene.2012.08.068
- [107] F. Balduzzi et al., “Feasibility analysis of a Darrieus vertical-axis wind turbine installation in the rooftop of a building”, *Applied Energy* 97 (2012), pp. 921–929, DOI: 10.1016/j.apenergy.2011.12.008
- [108] L. Lu, K. Y. Ip, “Investigation on the feasibility and enhancement methods of wind power utilization in high-rise buildings of Hong Kong”, *Renewable and Sustainable Energy Reviews* 13.2 (2009-02-01), pp. 450–461, DOI: 10.1016/j.rser.2007.11.013
- [109] A. Dilimulati, T. Stathopoulos, M. Paraschivoiu, “Wind turbine designs for urban applications: A case study of shrouded diffuser casing for turbines”, *Journal of Wind Engineering and Industrial Aerodynamics* 175 (2018), pp. 179–192, DOI: 10.1016/j.jweia.2018.01.003
- [110] L. Ledo, P. B. Kosasih, P. Cooper, “Roof mounting site analysis for micro-wind turbines”, *Renewable Energy* 36.5 (2011), pp. 1379–1391, DOI: 10.1016/j.renene.2010.10.030
- [111] Y. Tominaga et al., “Air flow around isolated gable-roof buildings with different roof pitches: Wind tunnel experiments and CFD simulations”, *Building and Environment* 84 (2015), pp. 204–213, DOI: 10.1016/j.buildenv.2014.11.012
- [112] B. Wang et al., “Estimation of wind energy of a building with canopy roof”, *Sustainable Cities and Society* 35 (2017), pp. 402–416, DOI: 10.1016/j.scs.2017.08.026
- [113] L. Lu, K. Sun, “Wind power evaluation and utilization over a reference high-rise building in urban area”, *Energy and Buildings* 68 (2014), pp. 339–350, DOI: 10.1016/j.enbuild.2013.09.029.
- [114] F. Toja-Silva et al., “An empirical–heuristic optimization of the building-roof geometry for urban wind energy exploitation on high-rise buildings”, *Applied Energy* 164 (2016), pp. 769–794, DOI: 10.1016/j.apenergy.2015.11.095
- [115] P. Larin, M. Paraschivoiu, C. Aygun, “CFD based synergistic analysis of wind turbines for roof mounted integration”, *Journal of Wind Engineering and Industrial Aerodynamics* 156 (2016), pp. 1–13, DOI: 10.1016/j.jweia.2016.06.007.
- [116] F. Balduzzi, A. Bianchini, L. Ferrari, “Microeolic turbines in the built environment: Influence of the installation site on the potential energy yield”, *Renewable Energy* 45 (2012), pp. 163–174, DOI: 10.1016/j.renene.2012.02.022
- [117] D. Romanic, A. Rasouli, H. Hangan, “Urban wind resource assessment in changing climate: Case study”, *Wind Engineering* 41.1 (2017), pp. 3–12, DOI: 10.1177/0309524X16653486
- [118] D. Romanić, A. Rasouli, H. Hangan, “Wind Resource Assessment in Complex Urban Environment”, *Wind Engineering* 39.2 (2015), pp. 193–212, DOI: 10.1260/0309-524X.39.2.193.

- [119] M. Zabarjad Shiraz, A. Dilimulati, M. Paraschivoiu, “Wind power potential assessment of roof mounted wind turbines in cities”, *Sustainable Cities and Society* 53 (2020), p. 101905, DOI: 10.1016/j.scs.2019.101905.
- [120] T. Kono, T. Kogaki, T. Kiwata, “Numerical Investigation of Wind Conditions for Roof-Mounted Wind Turbines: Effects of Wind Direction and Horizontal Aspect Ratio of a High-Rise Cuboid Building”, *Energies* 9.11 (2016), p. 907, DOI: 10.3390/en9110907.
- [121] T. Kono, T. Kogaki, “Numerical Investigation of Wind Conditions over a Rectangular Prism-Shaped Building for Mounting Small Wind Turbines”, *Wind Engineering* 36.2 (2012), pp. 111–121, DOI: 10.1260/0309-524X.36.2.111.
- [122] J. Millward-Hopkins et al., “The predictability of above roof wind resource in the urban roughness sublayer: Urban wind resource prediction”, *Wind Energy* 15.2 (2012), pp. 225–243, DOI: 10.1002/we.463.
- [123] H. Zhu et al., “Wind engineering for high-rise buildings: A review”, *Wind and Structures* 32.3 (2021), pp. 249–265, DOI: 10.12989/WAS.2021.32.3.249.
- [124] G. Pomaranzi et al., “Wind tunnel pressure data analysis for peak cladding load estimation on a high-rise building”, *Journal of Wind Engineering and Industrial Aerodynamics* 220 (2022), p. 104855, DOI: 10.1016/j.jweia.2021.104855.
- [125] Y. Tamura, A. Kareem, eds., *Advanced structural wind engineering*, Tokyo ; New York: Springer, 2013, ISBN: 978-4-431-54336-7.
- [126] Y. Cao et al., “Wind peak pressures on a square-section cylinder: Flow mechanism and standard/conditional POD analyses”, *Journal of Wind Engineering and Industrial Aerodynamics* 222 (2022), p. 104918, DOI: 10.1016/j.jweia.2022.104918.
- [127] G. Giangaspero et al., “High-order scale-resolving simulations of extreme wind loads on a model high-rise building”, *Journal of Wind Engineering and Industrial Aerodynamics* 230 (2022), p. 105169, DOI: 10.1016/j.jweia.2022.105169.
- [128] R. Ong et al., “Numerical simulation of wind-induced mean and peak pressures around a low-rise structure”, *Engineering Structures* 214 (2020), p. 110583, DOI: 10.1016/j.engstruct.2020.110583.
- [129] T. N. Geleta, G. Bitsuamlak, “Validation metrics and turbulence frequency limits for LES-based wind load evaluation for low-rise buildings”, *Journal of Wind Engineering and Industrial Aerodynamics* 231 (2022), p. 105210, DOI: 10.1016/j.jweia.2022.105210.
- [130] T. Potsis, T. Stathopoulos, “Wind induced peak pressures on low-rise building roofs via dynamic terrain computational methodology”, *Journal of Wind Engineering and Industrial Aerodynamics* 245 (2024), p. 105630, DOI: 10.1016/j.jweia.2023.105630.
- [131] E. Gavanski, K. R. Gurley, G. A. Kopp, “Uncertainties in the Estimation of Local Peak Pressures on Low-Rise Buildings by Using the Gumbel Distribution Fitting Approach”, *Journal of Structural Engineering* 142.11 (2016), p. 04016106, DOI: 10.1061/(ASCE)ST.1943-541X.0001556.
- [132] X. Peng et al., “A comparison of methods to estimate peak wind loads on buildings”, *Journal of Wind Engineering and Industrial Aerodynamics* 126 (2014), pp. 11–23, DOI: 10.1016/j.jweia.2013.12.013.
- [133] D. Duthinh, A. L. Pintar, E. Simiu, “Influence of Wind Tunnel Test Duration on Wind Load Factors”, *Journal of Structural Engineering* 144.11 (2018), p. 06018005, DOI: 10.1061/(ASCE)ST.1943-541X.0002202.

- [134] T. Stathopoulos, “The numerical wind tunnel for industrial aerodynamics: Real or virtual in the new millennium?”, *Wind and Structures* 5 (2002), pp. 193–208, DOI: 10.12989/was.2002.5.2_3_4.193
- [135] H. Tennekes, J. L. Lumley, *A first course in turbulence*, Cambridge, Mass: MIT Press, 1972, 300 pp., ISBN: 978-0-262-20019-6.
- [136] O. Reynolds, “An experimental investigation of the circumstances which determine whether the motion of water shall be direct or sinuous, and of the law of resistance in parallel channels”, *Philosophical Transactions of the Royal Society of London* 174 (1883), pp. 935–982, DOI: 10.1098/rstl.1883.0029.
- [137] L. F. Richardson, *Weather Prediction by Numerical Process*, Cambridge University Press, 1922.
- [138] A. N. Kolmogorov, “The Local Structure of Turbulence in Incompressible Viscous Fluid for Very Large Reynolds Numbers”, *Doklady Akademii Nauk SSSR* 30 (1941), pp. 301–305.
- [139] E. DeVilliers, “The Potential of Large Eddy Simulation for the Modeling of Wall Bounded Flows”, PhD thesis, London, UK: Imperial College of Science, Technology and Medicine, Department of Mechanical Engineering, Thermofluids Section, 2006.
- [140] J. Hinze, *Turbulence: An Introduction to Its Mechanism and Theory*, First edition, McGraw-Hill series in mechanical engineering, McGraw-Hill Book Company, 1959, ISBN: 978-0-07-029038-9.
- [141] S. K. Robinson, “Coherent Motions in the Turbulent Boundary Layer”, *Annual Review of Fluid Mechanics* 23 (1991), pp. 601–640, DOI: 10.1146/annurev.fl.23.010191.003125
- [142] J. Franke, “Introduction to the Prediction of Wind Loads on Buildings by Computational Wind Engineering (CWE)”, *Wind Effects on Buildings and Design of Wind-Sensitive Structures*, ed. by T. Stathopoulos, C. C. Baniotopoulos, Vienna: Springer Vienna, 2007, pp. 67–103, ISBN: 978-3-211-73076-8, DOI: 10.1007/978-3-211-73076-8_3
- [143] J. H. Ferziger, M. Perić, *Computational Methods for Fluid Dynamics*, 3rd Edition, Springer Berlin, Heidelberg, 2002, ISBN: 3-540-42074-6.
- [144] The Clay Mathematics Institute of Cambridge, Massachusetts (CMI), *The Millennium Prize Problems*, <https://www.claymath.org/millennium-problems/>, (accessed: 01.07.2024).
- [145] P. Sagaut, *Large eddy simulation for incompressible flows: an introduction*, 3rd ed, Scientific computation, Berlin ; New York: Springer, 2006, 556 pp., ISBN: 978-3-540-26344-9.
- [146] J. Smagorinsky, “General circulation experiments with the primitive equations. Part I: The basic experiment”, *Monthly Weather Review* 91.3 (1963), pp. 99–164, DOI: 10.1126/science.27.693.594.
- [147] E. R. Van Driest, “On Turbulent Flow Near a Wall”, *Journal of the Aeronautical Sciences* 23.11 (1956), pp. 1007–1011, DOI: 10.2514/8.3713.
- [148] P. Moin, J. Kim, “Numerical investigation of turbulent channel flow”, *Journal of Fluid Mechanics* 118.-1 (1982), p. 341, DOI: 10.1017/S0022112082001116
- [149] M. Germano et al., “A dynamic subgrid-scale eddy viscosity model”, *Physics of Fluids A* 3.7 (1991), pp. 1760–1765, DOI: 10.1063/1.857955.
- [150] D. K. Lilly, “A proposed modification of the Germano subgrid-scale closure method”, *Physics of Fluids A: Fluid Dynamics* 4.3 (1992), pp. 633–635, DOI: 10.1063/1.858280.

- [151] F. Nicoud, F. Ducros, “Subgrid-Scale Stress Modelling Based on the Square of the Velocity Gradient Tensor”, *Flow, Turbulence and Combustion* 62.3 (1999), pp. 183–200, DOI: 10.1023/A:1009995426001.
- [152] Y. Tominaga et al., “AIJ guidelines for practical applications of CFD to pedestrian wind environment around buildings”, *Journal of Wind Engineering and Industrial Aerodynamics* 96.10-11 (2008), pp. 1749–1761, DOI: 10.1016/j.jweia.2008.02.058
- [153] H. Jasak, “Error Analysis and Estimation for the Finite Volume Method with Applications to Fluid Flows”, PhD thesis, Imperial College of Science, Technology and Medicine, Department of Mechanical Engineering, Thermofluids Section, 1996, DOI: 10.1016/S0020-7683(02)00168-3.
- [154] H. Nilsson, ed., *Proceedings of CFD with OpenSource Software*, Chalmers University of Technology, Göteborg, Sweden, 2019, DOI: 10.17196/OS_CFD#YEAR_2019.
- [155] S. V. Patankar, *Numerical heat transfer and fluid flow*, Series in computational methods in mechanics and thermal sciences, New York, NY Hamburg: McGraw-Hill [u.a.], 1980, 197 pp., ISBN: 978-0-07-048740-6.
- [156] R. Issa, “Solution of the implicitly discretised fluid flow equations by operator-splitting”, *Journal of Computational Physics* 62.1 (1986), pp. 40–65, DOI: 10.1016/0021-9991(86)90099-9.
- [157] H. K. Versteeg, W. Malalasekera, *An introduction to computational fluid dynamics: the finite volume method*, 2nd ed, Harlow, England ; New York: Pearson Education Ltd, 2007, 503 pp., ISBN: 978-0-13-127498-3.
- [158] T. Marić, J. Höpken, K. Mooney, *The OpenFOAM technology primer*, Duisburg: Sourceflux, 2014, 442 pp., ISBN: 978-3-00-046757-8.
- [159] A. Šarkić Glumac, H. Hemida, R. Höffer, *Wind Tunnel Experimental Data for Flow Characteristics above the Roof of High-rise Buildings in Group Arrangement for Wind Energy Harvesting, Mendeley Data v2*, 2017, DOI: 10.17632/cxc4w2myyw.2
- [160] A. Šarkić Glumac et al., *Wind Tunnel Experimental Data for Flow Characteristics above the Roof of Isolated High-rise Building for Wind Energy Harvesting Considering Two Shapes of the Roof, Flat Roof and Deck Roof, Mendeley Data v1*, 2020, DOI: 10.17632/jp7vc8tf7w.1.
- [161] H. Weller, “Controlling the Computational Modes of the Arbitrarily Structured C Grid”, *Monthly Weather Review* 140 (2012), 3220–3234, DOI: 10.1175/MWR-D-11-00221.1
- [162] A. Hunt, “Wind-tunnel measurements of surface pressures on cubic building models at several scales”, *Journal of Wind Engineering and Industrial Aerodynamics* 10.2 (1982), pp. 137–163, DOI: 10.1016/0167-6105(82)90061-7.
- [163] H. Tieleman, R. Akins, “THE EFFECT OF INCIDENT TURBULENCE ON THE SURFACE PRESSURES OF SURFACE-MOUNTED PRISMS”, *Journal of Fluids and Structures* 10.4 (1996), pp. 367–393, DOI: 10.1006/jfls.1996.0024.
- [164] S. Murakami, “Overview of turbulence models applied in CWE-1997”, *Journal of Wind Engineering and Industrial Aerodynamics* 74-76 (1998), pp. 1–24, DOI: 10.1016/S0167-6105(98)00004-X.
- [165] M. Ricci et al., “Towards LES as a design tool: Wind loads assessment on a high-rise building”, *Journal of Wind Engineering and Industrial Aerodynamics* 180 (2018), pp. 1–18, DOI: 10.1016/j.jweia.2018.07.009

- [166] Y. Dai, C. Mak, Y. Ai, “Flow and dispersion in coupled outdoor and indoor environments: Issue of Reynolds number independence”, *Building and Environment* 150 (2019), 119–134, DOI: 10.1016/j.buildenv.2019.01.008
- [167] T. Kajishima, K. Taira, *Computational Fluid Dynamics*, Cham: Springer International Publishing, 2017, ISBN: 978-3-319-45302-6 978-3-319-45304-0, DOI: 10.1007/978-3-319-45304-0.
- [168] L. Bruno et al., “3D flow around a rectangular cylinder: A computational study”, *Journal of Wind Engineering and Industrial Aerodynamics* 98 (2010), 263–276, DOI: 10.1016/j.jweia.2009.10.005
- [169] T. V. Karman, *Progress in the Statistical Theory of Turbulence*, tech. rep., 1948, 530–539.
- [170] M. J. Morrison, G. A. Kopp, “Effects of turbulence intensity and scale on surface pressure fluctuations on the roof of a low-rise building in the atmospheric boundary layer”, *Journal of Wind Engineering and Industrial Aerodynamics* 183 (2018), pp. 140–151, DOI: 10.1016/j.jweia.2018.10.017.
- [171] F. Jorgensen, *How to measure turbulence with hot-wire anemometers*, tech. rep., 2002, DOI: 10.1046/j.1540-8167.2004.04138.x
- [172] B. Blocken, T. Stathopoulos, J. Carmeliet, “CFD simulation of the atmospheric boundary layer: wall function problems”, *Atmospheric Environment* 41.2 (2007), pp. 238–252, DOI: 10.1016/j.atmosenv.2006.08.019
- [173] J. Ahrens, B. Geveci, C. Law, *ParaView: An End-User Tool for Large Data Visualization, Visualization Handbook*, Elsevier, 2005, ISBN: 9780123875822.
- [174] F. Haan, “The Effects of Turbulence on the Aerodynamics of Long-span Bridges”, PhD thesis, University of Notre Dame, Notre Dame, Indiana, 2000.
- [175] M. Kiya, K. Sasaki, “Free-stream turbulence effects on a separation bubble”, *Journal of Wind Engineering and Industrial Aerodynamics* 14.1 (1983), pp. 375–386, DOI: 10.1016/0167-6105(83)90039-9.
- [176] B. Bienkiewicz, Y. Sun, “Local wind loading on the roof of a low-rise building”, *Journal of Wind Engineering and Industrial Aerodynamics* 45.1 (1992), pp. 11–24, DOI: 10.1016/0167-6105(92)90003-S.
- [177] J. Wang et al., “Characteristics of conical vortices and their effects on wind pressures on flat-roof-mounted solar arrays by LES”, *Journal of Wind Engineering and Industrial Aerodynamics* 200 (2020), p. 104146, DOI: 10.1016/j.jweia.2020.104146
- [178] J. Jeong, F. Hussain, “On the identification of a vortex”, *Journal of Fluid Mechanics* 285 (1995), pp. 69–94, DOI: 10.1017/S0022112095000462
- [179] S. J. Daniels, I. P. Castro, Z.-T. Xie, “Peak loading and surface pressure fluctuations of a tall model building”, *Journal of Wind Engineering and Industrial Aerodynamics* 120 (2013), pp. 19–28, DOI: 10.1016/j.jweia.2013.06.014
- [180] A. Tummala et al., “A review on small scale wind turbines”, *Renewable and Sustainable Energy Reviews* 56 (2016), pp. 1351–1371, DOI: 10.1016/j.rser.2015.12.027.
- [181] N. Carpman, *Turbulence Intensity in Complex Environments and its Influence on Small Wind Turbines*, Department of Earth Sciences Geotryckeriet, Uppsala University, Uppsala, 2011.
- [182] B. Belabes, M. Paraschivoiu, “Numerical study of the effect of turbulence intensity on VAWT performance”, *Energy* 233 (2021), p. 121139, DOI: 10.1016/j.energy.2021.121139.

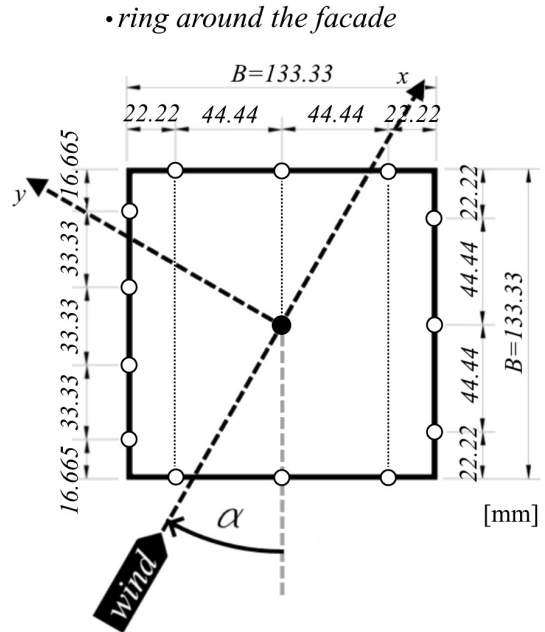
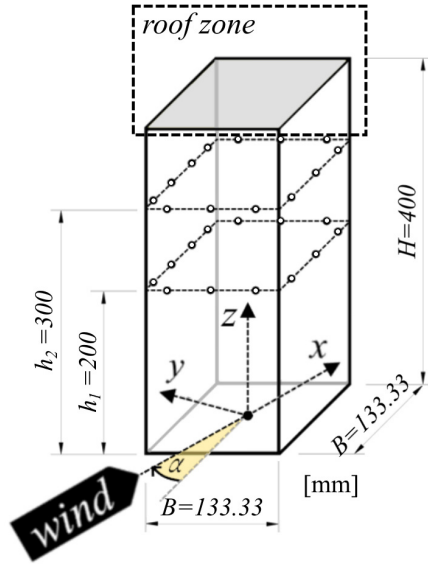
- [183] S. Mertens, G. van Kuik, G. van Bussel, “Performance of an H-Darrieus in the Skewed Flow on a Roof”, *Journal of Solar Energy Engineering* 125.4 (2003), pp. 433–440, DOI: 10.1115/1.1629309.
- [184] J. Cace et al., *Urban wind turbines. Guidelines for small wind turbines in the built environment*, tech. rep., 2007, (accessed: 01.07.2024).
- [185] IEC, *Design requirements, Edition 4.0., Wind energy generation systems / International Electrotechnical Commission*. International Electrotechnical Commission, Geneva, Switzerland, 2019.
- [186] E. Simiu, D. Yeo, *Wind effects on structures: modern structural design for wind*, Fourth edition, Hoboken, NJ: John Wiley & Sons, 2019, ISBN: 978-1-119-37590-6 978-1-119-37593-7.
- [187] D. Duthinh, A. L. Pintar, E. Simiu, “Estimating Peaks of Stationary Random Processes: A Peaks-over-Threshold Approach”, *ASCE-ASME Journal of Risk and Uncertainty in Engineering Systems, Part A: Civil Engineering* 3.4 (2017), p. 04017028, DOI: 10.1061/AJRUA6.0000933.
- [188] R Core Team, *R: A Language and Environment for Statistical Computing*, <https://www.R-project.org>, Vienna, Austria: R Foundation for Statistical Computing, 2015.
- [189] A. Pintar, *potMax - Estimating the distribution of the maximum of time series using peaks-over-threshold models*, tech. rep., 2016, (accessed: 01.07.2024).
- [190] N. J. Cook, J. R. Mayne, “A novel working approach to the assessment of wind loads for equivalent static design”, *Journal of Wind Engineering and Industrial Aerodynamics* 4.2 (1979), pp. 149–164, DOI: 10.1016/0167-6105(79)90043-6
- [191] J. Lieblein, *Efficient methods of extreme-value methodology*, en, tech. rep., Washington, DC, 1974, (accessed: 01.07.2024).
- [192] T. M. Inc., *MATLAB version: 9.13.0 (R2022b)*, <https://www.mathworks.com>, Natick, Massachusetts, United States, 2022.
- [193] R. L. Smith, *Statistics of Extremes, with Applications in Environment, Insurance, and Finance*, ed. by B. Finkenstadt, H. Rootzen, 1st Edition, Chapman and Hall/CRC, 2003, ISBN: 978-0-429-20451-7.
- [194] R. R. Wilcox, *Introduction to robust estimation and hypothesis testing*, 3rd ed, Statistical modeling and decision science, Amsterdam ; Boston: Academic Press, 2012, 690 pp., ISBN: 978-0-12-386983-8.
- [195] J. S. Maritz, R. G. Jarrett, “A Note on Estimating the Variance of the Sample Median”, *Journal of the American Statistical Association* 73.361 (1978), pp. 194–196, DOI: 10.1080/01621459.1978.10480027.

Appendices

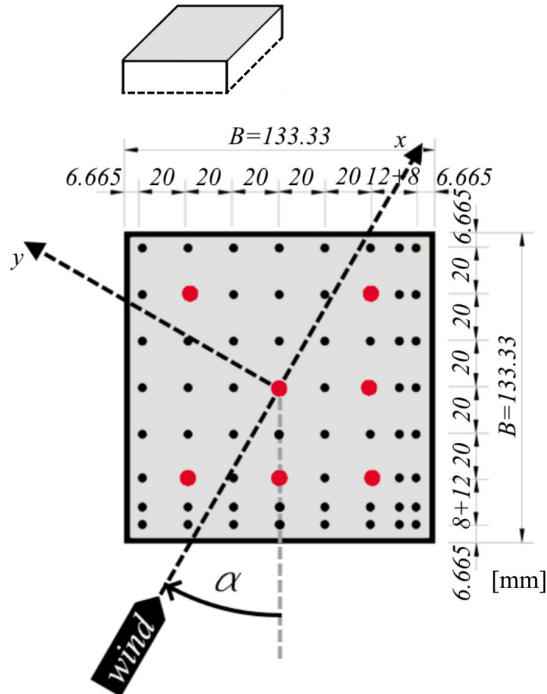
A Experimental setup: Position of the pressure taps

Appendix A gives the exact location of the pressure taps at the surface of the building model in the wind tunnel experiments. These locations are given in [102] and presented in Figure A.1. The pressure taps on the flat and decked roofs are marked with filled black circles, while the taps on two rings around the facade are marked with empty black circles. In addition, the pressure taps on the roof above which the velocity data was collected, are marked with filled red circles.

High-rise building model



• flat roof



• decked roof

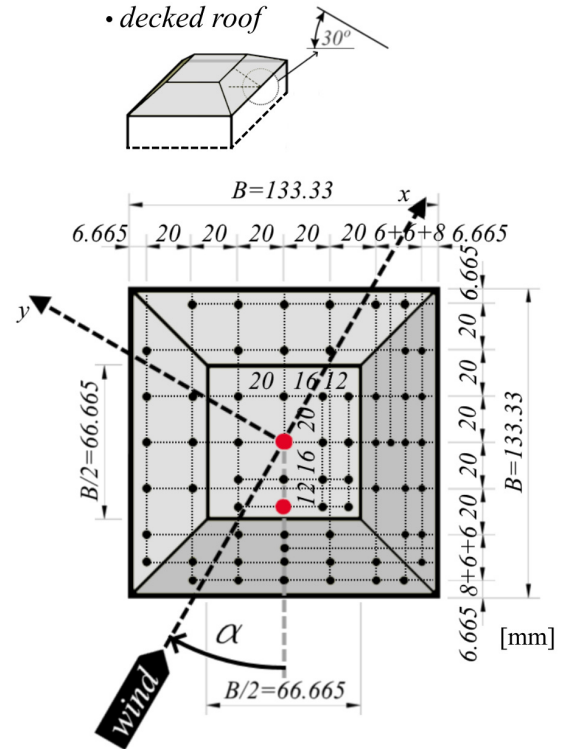


Figure A.1. Schematic presentation of the distribution of the pressure taps on the building model in the wind tunnel experiments.

B Numerical setup

Appendix B provides more details on the flow modelling. It gives two sets of numerical schemes used in the research in B.1. B.2 gives details of the grid creation process using `snappyHexMesh`. Specifics of the modelling of the precursor domain are shown in B.3. Appendix B aims to reflect the navigation through the complexities of grid creation and flow modelling in LES during this research.

B.1 Numerical schemes: Setup from OpenFOAM® `fvSchemes` file

Given the lack of best-practice guidelines for the LES method and the high computational demands of the numerical process, one is often left to learn through a trial-and-error approach. Although there is no perfect combination of numerical schemes for discretising the N-S equations, preferable choices are documented in the literature. However, each simulation is unique, depending on the specific issues it aims to address. Based on the considerations above, two numerical setups are used in the present investigation.

The first setup is implemented in the wind energy assessment simulations and is shown in Figure B.1. Wind energy study simulations are more stable and can handle a high Courant number (up to 4). A slight modification of the schemes for wind loading is made, the second setup given in Figure B.2. Namely, the choice of schemes is identical, with modification of limiters only. In OpenFOAM®, the blending factor, selected in a range from 0 to 1, doses the boundedness, and hence the stability, of a certain scheme for higher values. The main difference is in a scheme for the advective term, where in the first case `unlimitedGrad(U)` is used and in the second `grad(U)`. This change is associated with the discretisation of the velocity gradient term. Here, a slightly more diffusive `cellLimited` limiter is used in the second setup, compared to `cellMDLimited` limiter in the first.

During the run, it was noticed that the simulations for wind energy assessment were more stable and capable of handling higher values of the Courant number. On the other hand, simulations for the wind loading study have demonstrated instabilities and braked down at $CFL > 2$. It is hard to distinguish one parameter and say the reason for a certain behaviour since the grid was also different, and it can be caused either by modifications of schemes or by a single problematic cell.

```

/*-----*-- C++ --*-----*/
| =====|
|  \ \ /  | F ield      | OpenFOAM: The Open Source CFD Toolbox|
|  \ \ /  | O peration | Version: 4.1|
|  \ \ /  | A nd       | Web: www.OpenFOAM.org|
|  \ \ /  | M anipulation|
/*-----*--*/
FoamFile
{
    version      2.0;
    format       ascii;
    class        dictionary;
    location     "system";
    object       fvSchemes;
}
// ***** //

ddtSchemes
{
    default backward;
}

gradSchemes
{
    default      cellMDLimited Gauss linear 0.5;
    grad(U)      cellMDLimited Gauss linear 0.3;
}

divSchemes
{
    default      Gauss linear;
    div(phi,U)   Gauss LUST unlimitedGrad(U);
    div(phi,k)   Gauss limitedLinear 1;
    div(phi,nuTilda) Gauss limitedLinear 1;
    div((nuEff*dev(T(grad(U))))) Gauss linear;
}

laplacianSchemes
{
    default      Gauss linear limited 1;
}

interpolationSchemes
{
    default      linear;
}

snGradSchemes
{
    default      limited 1;
}

// ***** //

```

Figure B.1. OpenFOAM® fvSchemes file for wind energy assesment.

B.2 SnappyHexMesh: Creating computational grid

SnappyHexMesh is the OpenFOAM® built-in meshing utility that generates three-dimensional grids composed predominantly of hexahedral cells. It relies on the base grid, usually created using `blocMesh`, the main meshing utility in OpenFOAM®. The following steps outline the process of creating a grid using SnappyHexMesh:

- **Create geometry:** Design a three-dimensional surface model for every object in the computational domain (e.g., building, roughness field, spires, ramp) using programmes

```

/*-----*-- C++ -*-----*\
| =====|
| \\      / F ield      | OpenFOAM: The Open Source CFD Toolbox
| \\      / O peration  | Version: 4.1
| \\      / A nd        | Web: www.OpenFOAM.org
|  \\    / M anipulation|
\*-----*--\
FoamFile
{
    version      2.0;
    format       ascii;
    class        dictionary;
    location     "system";
    object       fvSchemes;
}
// * * * * *

ddtSchemes
{
    default backward;
}

gradSchemes
{
    default      cellLimited Gauss linear 0.5;
    grad(U)      cellLimited Gauss linear 0.3;
}

divSchemes
{
    default      Gauss linear;
    div(phi,U)   Gauss LUST grad(U);
    div(phi,k)   Gauss limitedLinear 0.5;
    div(phi,nuTilda) Gauss limitedLinear 0.5;
    div((nuEff*dev(T(grad(U))))) Gauss linear;
}

laplacianSchemes
{
    default      Gauss linear limited 1;
}

interpolationSchemes
{
    default      linear;
}

snGradSchemes
{
    default      limited 1;
}

// *****

```

Figure B.2. OpenFOAM® fvSchemes file for wind loading.

like AutoCAD or Salome. NOTE: It is recommended that one model be formed, with all objects included, paying attention to the origin of the coordinate system.

- **Triangulate faces:** Use Salome or similar software to triangulate the surfaces of each object. NOTE: Aim for a fine triangular grid to enhance SnappyHexMesh's ability to accurately capture the geometry's features.
- **Export STL file:** Export the triangulated geometry files for each object or group separately (e.g., building, roughness field, spires, ramp) as an STL file—this is the input

for SnappyHexMesh. Place the STL file in the `constant/triSurface` directory of the OpenFOAM® case.

- **Extract feature edges:** Utilise the `surfaceFeatureExtract` utility in OpenFOAM® to extract feature edges from the STL file. This step helps to preserve sharp edges during the meshing process.
- **Create a base grid with `blockMesh`:** Define a base grid using the `blockMesh` utility, specifying the outer dimensions of the computational domain, typically a cuboid. NOTE: Ensure that the base grid cells are as close to cubes as possible, avoiding skewed cells and high aspect ratios to maintain grid quality.
- **Configure `snappyHexMeshDict`:** Set up the `snappyHexMeshDict` file located in the `system/` directory of the case. This dictionary controls various parameters of the meshing process, including geometry definition, refinement levels, snapping controls, and layer addition.
- **Run `SnappyHexMesh`:** Execute the `snappyHexMesh` utility to generate the grid. The process involves:
 - **Castellation:** Refine the base grid into predefined zones.
 - **Snapping:** Adjusting grid points to align with the surface geometry.
 - **Layer addition (optional):** Adding surface boundary layers for better resolution near surfaces. NOTE: Layer addition can be performed separately from castellation and snapping, which is recommended for complex grids.
- **Check grid quality:** After meshing, assess grid quality to ensure it meets the desired requirements.

Detailed guidance on each of these steps can be found in the official OpenFOAM® User Guide (available at <https://www.openfoam.com/documentation/user-guide>), as well as in [158]. An example of the `snappyHexMeshDict` file used for the grid generation for the wind loading study, configuration C2, at 0 ° is provided below.

snappyHexMeshDict file—the grid for the wind loading study (C2, at 0°)

```

1  /*-----* C++ *-----*/
2  | ===== |
3  |  \ \      /  F i e l d      | OpenFOAM: The Open Source CFD Toolbox |
4  |  \ \      /  O p e r a t i o n | Version: 4.1 |
5  |  \ \      /  A n d              | Web: www.OpenFOAM.org |
6  |  \ \      /  M a n i p u l a t i o n | |
7  /*-----*/
8  FoamFile
9  {
10     version      2.0;
11     format        ascii;
12     class         dictionary;
13     object        snappyHexMeshDict;
14  }
15  // * * * * *
16
17  castellatedMesh false;
18  snap           false;
19  addLayers      true;
20
21  geometry
22  {
23
24     HR-C1-a0_BUILDING.stl
25     {
26     name BUILDING;
27     type triSurfaceMesh;
28     }
29
30     HR-C2-a0_DUMMY.stl
31     {
32     name DUMMY;
33     type triSurfaceMesh;
34     }
35
36     buildingZone
37     {
38     name buildingZone;
39     type searchableBox;
40     min (-0.13333 0 -0.13333);
41     max ( 0.26666 0.46666 0.13333);
42     }
43
44     rotTable
45     {
46     name rotTable;
47     type searchableCylinder;
48     point1 (0 0 0); // Height
49     point2 (0 0.53333 0); // Vector
50     radius 0.6;
51     }
52
53     zone1
54     {
55     name zone1;
56     type searchableBox;
57     min (-10 0 -1);
58     max (1.2 1 1);
59     }
60
61     zone2
62     {
63     name zone2;
64     type searchableBox;
65     min (-10 0 -0.6);
66     max ( 1 0.8 0.6);
67     }
68
69     ELEMENTS_STSM_new.stl

```

1/7

```

70     {
71         name ELEMENTS;
72         type triSurfaceMesh;
73     }
74
75     SPIRES_MID.stl
76     {
77         name SPIRES_MID;
78         type triSurfaceMesh;
79     }
80
81     SPIRES_SIDE.stl
82     {
83         name SPIRES_SIDE;
84         type triSurfaceMesh;
85     }
86
87     RAMP.stl
88     {
89         name RAMP;
90         type triSurfaceMesh;
91     }
92
93     zone3spires
94     {
95         name zone3spires;
96         type searchableBox;
97         min (-7 0 -0.6);
98         max (-5.4 1.6 0.6);
99     }
100
101     zone4floor
102     {
103         name zone4floor;
104         type searchableBox;
105         min (-6.2 0 -1);
106         max (0 0.08 1);
107     }
108
109 };
110
111 castellatedMeshControls
112 {
113     locationInMesh (-1 0.1 0.5);
114
115     maxLocalCells 30000000; //max cells per CPU core
116
117     maxGlobalCells 100000000; //max cells to use before mesh deletion step
118
119     nCellsBetweenLevels 5; // expansion factor between each high & low refinement zone
120
121     minRefinementCells 0; //if minRefinementCells ≥ number of cells to be refined,
    surface refinement stops
122
123     maxLoadUnbalance 0.5; //maximum processor imbalance during refinement, i.e., if
    the number of vertices on one
124         //processor differs from average number of vertices on another processor
    by more than
125         //maxLoadUnbalance $ \times 100\%$, then re-balancing algorithm is
    performed
126
127     resolveFeatureAngle 20; //the local curvature refinement - The higher the value, the
    less features it captures
128
129     planarAngle 30; // Angle used to detect opposite surfaces; for higher refinement in
    small gaps and between close features
130
131     allowFreeStandingZoneFaces true; //Allowing zone faces that share the same owner and
    neighbour cell zone;

```

```

132                                     //Not used if there are no faceZones
133     features
134     (
135     {file "HR-C1-a0_BUILDING.eMesh"; level 5;}
136     {file "HR-C2-a0_DUMMY.eMesh"; level 4;}
137     {file "ELEMENTS_STSM_new.eMesh"; level 4;}
138     {file "SPIRES_MID.eMesh"; level 3;}
139     {file "SPIRES_SIDE.eMesh"; level 3;}
140     {file "RAMP.eMesh"; level 2;}
141     );
142
143     refinementSurfaces
144     {
145
146     BUILDING
147     {
148         level (5 5);
149         patchInfo
150         {
151             type wall;
152         }
153     }
154
155     DUMMY
156     {
157         level (4 4);
158         patchInfo
159         {
160             type wall;
161         }
162     }
163
164     ELEMENTS
165     {
166         level (4 4);
167         patchInfo
168         {
169             type wall;
170         }
171     }
172
173     SPIRES_MID
174     {
175         level (3 3);
176         patchInfo
177         {
178             type wall;
179         }
180     }
181
182     SPIRES_SIDE
183     {
184         level (3 3);
185         patchInfo
186         {
187             type wall;
188         }
189     }
190
191     RAMP
192     {
193         level (2 2);
194         patchInfo
195         {
196             type wall;
197         }
198     }
199
200

```

```

201     }
202
203     refinementRegions //Region wise refinement
204     {
205
206         buildingZone
207         {
208             mode inside;
209             levels ((1E15 4)); // refinement level 1 (1E15 entry ignored)
210         }
211
212         rotTable
213         {
214             mode inside;
215             levels ((1E15 3)); // refinement level 1 (1E15 entry ignored)
216         }
217
218         zone1
219         {
220             mode inside;
221             levels ((1E15 1)); // refinement level 1 (1E15 entry ignored)
222         }
223
224         zone2
225         {
226             mode inside;
227             levels ((1E15 2));
228         }
229
230         zone3spires
231         {
232             mode inside;
233             levels ((1E15 1));
234         }
235
236         zone4floor
237         {
238             mode inside;
239             levels ((1E15 3));
240         }
241     }
242 }
243
244
245 snapControls
246 {
247     nSmoothPatch    5; //number of patch smoothing iterations before finding
correspondence to surface (typically 3)
248
249     tolerance        1.5; //ratio of distance for points to be attracted by surface
feature point or edge, to local maximum edge length (typically 2.0)
250
251     nSolveIter       100; // number of mesh displacement relaxation iterations (typically
30-100);
252
253     nRelaxIter        5; //nRelaxIter: maximum number of snapping relaxation iterations
(typically 5)
254         //Increase this value to improve the quality of the body fitted mesh - can
result the high skewness
255
256 // Feature snapping
257
258 // Number of feature edge snapping iterations; Highly experimental and wip
259 // Leave out altogether to disable
260 nFeatureSnapIter 10;
261
262 explicitFeatureSnap    true; // Use castellatedMeshControls::features (default =
true)
263

```



```

264     implicitFeatureSnap    false; // Detect (geometric only) features by sampling the
      surface (default=false)
265
266     multiRegionFeatureSnap false; // Detect features between multiple surfaces (only for
      explicitFeatureSnap, default = false)
267 }
268
269 addLayersControls
270 {
271     //Global parameters
272     relativeSizes          false; //use false when defining firstLayerThickness
273     expansionRatio          1.1; //other combinations of parameters are also available
274     firstLayerThickness     5E-4;
275     minThickness           1E-10; //minimum layer thickness below which the layer is not
      added
276
277     layers
278     {
279
280         BUILDING
281         {
282             nSurfaceLayers 10;
283             expansionRatio  1.05;
284             firstLayerThickness 0.8E-4;
285             minThickness 1E-10;
286         }
287
288         DUMMY
289         {
290             nSurfaceLayers 5;
291         }
292
293         FLOOR
294         {
295             nSurfaceLayers 5;
296         }
297     }
298
299     nGrow                0; //number of layers of connected faces that are not
      grown if points do not get extruded;
301     //helps convergence of layer addition close to features
302     //very experimental - best results with value 0
303
304     featureAngle          180; //Specification of feature angle above which layers
      are collapsed automatically
305
306     maxFaceThicknessRatio 0.5; // Stop layer growth on highly warped cells
307
308     // Patch displacement
309
310     nSmoothSurfaceNormals 10; // Number of smoothing iterations of surface normals
311
312     nSmoothThickness      10; // Smooth layer thickness over surface patches
313
314     // Medial axis analysis
315
316     minMedialAxisAngle    90; // Angle used to pick up medial axis points
317
318     maxThicknessToMedialRatio 0.3; // Reduce layer growth where ratio thickness to
      medial distance is large
319
320     nSmoothNormals        15; // Number of smoothing iterations of interior mesh
      movement direction
321
322     // Mesh shrinking
323
324     slipFeatureAngle       90; // Optional: at non-patched sides allow mesh to slip
      if extrusion

```

5/6

```

325                                     // direction makes angle larger than
326                                     slipFeatureAngle. Default is
327                                     // 0.5*featureAngle.
328     nLayerIter                        40; // Overall max number of layer addition iterations.
329     The mesher will
330                                     // exit if it reaches this number of iterations;
331                                     possibly with an
332                                     // illegal mesh
333     nRelaxedIter                      25; // Maximum number of snapping relaxation iterations
334     Should stop
335                                     // before upon reaching a correct mesh.
336     nRelaxIter                        10; //maximum number of snapping relaxation iterations
337     (typcially 5)
338     nBufferCellsNoExtrude             0; // Create buffer region for new layer terminations
339     // Additional reporting: if there are just a few faces where there
340     // are mesh errors (after adding the layers) print their face centres.
341     // This helps in tracking down problematic mesh areas
342
343     additionalReporting               true;
344
345 }
346
347 meshQualityControls
348 {
349     /*
350         maxNonOrtho 60;
351         maxBoundarySkewness 4; //deactivated (-1)
352         maxInternalSkewness 4; //deactivated (-1)
353         maxConcave 80;
354         minFlatness 0.7;
355         minVol 1e-13;
356         minTetQuality 1e-15; // very small value (1E-30)
357         minArea 1e-10;
358         minTwist 0.05;
359         minDeterminant 0.001;
360         minFaceWeight 0.05;
361         minVolRatio 0.01;
362         minTriangleTwist -1;
363     */
364     */
365     //Try to deactivate all the mesh quality controls for the layer insertion
366
367     maxNonOrtho 70;
368     maxBoundarySkewness 20;
369     maxInternalSkewness 4;
370     maxConcave 180;
371     minVol -1;
372     minTetQuality -1;
373     minArea -1;
374     minTwist -1;
375     minDeterminant 0.001;
376     minFaceWeight -1;
377     minVolRatio -1;
378     minTriangleTwist -1;
379
380     // Advanced
381
382     nSmoothScale 4;
383     errorReduction 0.75;
384 }
385
386 }
387
388 writeFlags

```

6/7

```
389  (  
390      scalarLevels  
391      layerSets  
392      layerFields  
393  );  
394  
395  mergeTolerance 1e-6;  
396  
397  // *****  
398
```

B.3 Incoming wind profile: Modelling precursor domain

Modelling turbulent incident wind flow is a challenging task in LES. The approach used in this research is modelling the whole precursor domain from the wind tunnel, with all turbulent elements. The common boundary condition prescribed at the inlet for this approach is usually a constant, uniform velocity without any turbulence, which is the closest approximation of the experimental setup. The accuracy of the incident wind profile is highly dependent on the grid refinement in the precursor domain. Two important processes need to be covered. The first is resolving the separation and recirculating regions around turbulent elements. This is particularly important in the roughness field region where elements are small, and the grid needs to be very fine to capture turbulent structures developed at separating edges of the small cubes and prisms (roughness elements). The second segment is the energy cascade, in particular, transferring energy from large energy-containing eddies to smaller ones. It can be challenging with a too-coarse grid, which smoothes the smaller scales and prevents breaking these large turbulent structures.

In the present research, two grid refinements, illustrated in Figure B.3, and three inlet boundary conditions are analysed and summed up in the three setups:

- Setup 1 (NUM S1)—grid 1 (G1) used for wind energy study, presented in Figure B.3(a), with the uniform constant velocity profile at the inlet $U(15, 0, 0)$ [m/s]
- Setup 2 (NUM S2)—grid 2 (G2) used for wind loading study, presented in Figure B.3(b), with the uniform constant velocity profile at the inlet $U(12, 0, 0)$ [m/s]
- Setup 3 (NUM S3)—grid 2 (G2) used for wind loading study, same as in setup 2, with a constant incident velocity profile from the experiment approximated by the power law function with an exponent of 0.20 at the inlet $U = U^*(z/H)^{0.2}$ and $U^* = U(inlet, H) = 12$ [m/s]

The base grid for G1 has a cell size $\delta/H = 8.75 \times 10^{-2}$, while for G2, it equals $\delta/H = 16.67 \cdot 10^{-2}$. The base grid has been further refined by the cell-splitting method. An additional five rows of cells are inserted in the boundary layer of roughness elements in G1 and G2, as well as on the floor after the roughness field. Different refinement levels in the roughness field zone in the first place, but also reduction of the refinement close to the lateral walls of the tunnel and concentration on the central part are the main reasons for the significant reduction of cell count in G2 compared to G1. The total cell number in G1 is $21.8 \cdot 10^6$, while in G2, the number has been reduced more than three times ($6.3 \cdot 10^6$).

Apart from grid and inlet velocity differences, the Courant number is the third distinct parameter in Setup 1 and Setups 2 and 3. In Setup 1, the maximum of $CFL = 2.5$ is reached, while it is below 0.5 in Setups 2 and 3. In addition, slight discrepancies in numerical schemes are also present, as explained in B.1.

Results of the normalised streamwise velocity and turbulence intensity profiles with velocity spectra at $(0, 0, H)$ are shown in B.4 for all three setups. The mean streamwise velocity profiles from all three numerical setups coincide very well with the experimental one. Considering turbulence intensities, slight overprediction of I_U in the zone below $z = 0.5H$ is notable in NUM S1 compared to the experiments, while the other two setups are aligned with the experiments. The velocity spectra in Figure B.4(b,c) demonstrate the grid's capability to capture the turbulent kinetic energy of the flow and distribute it among different scales. The cutoff frequency in all three setups is around 3. A slight shift between NUM S1 and NUM S3 after the cutoff frequency

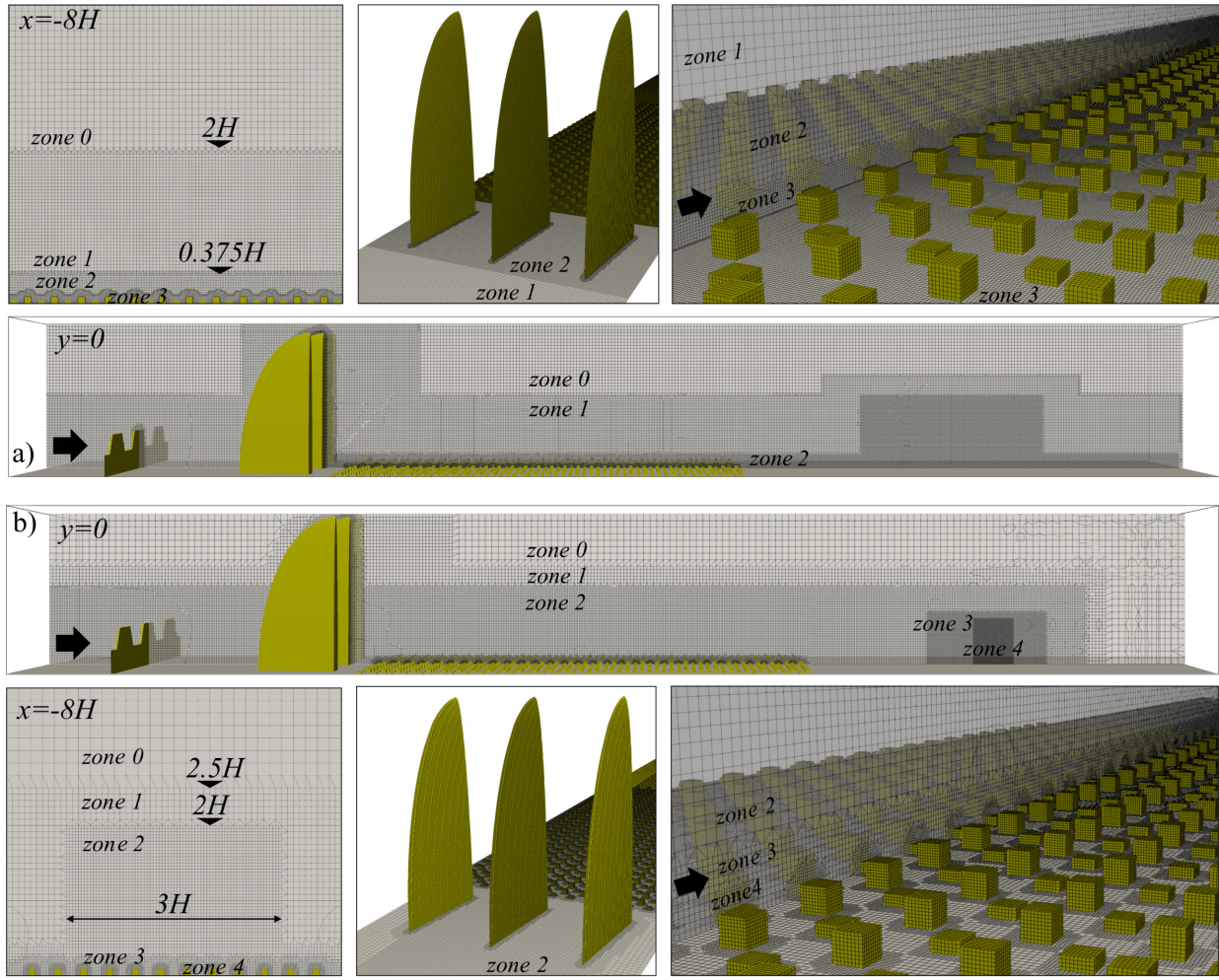


Figure B.3. Grid refinement of the precursor domain: (a) grid 1 (G1) used in wind energy study (NUM S1) and (b) grid 2 (G2) used in wind loading study (NUM S2 and NUM S3).

is attributed to the finer grid at the location of the high-rise building in NUM S3 compared to NUM S1. The differences in spectra of NUM S2 and NUM S3 are negligible. This implies that the change in the inlet velocity definition from uniform in NUM S2 to constant velocity profile in NUM S3 does not affect the incident wind profile as the dominant influence is made by turbulent features in the precursor domain. NUM S3 setup is also used in the wind load study in simulations with building models.

A comparison of the results for two grids, G1 and G2, highlights the great influence of one's experience in the field. Official guidelines can improve a certain aspect of flow modelling, and special attention should be paid to minimal criteria to avoid conservative recommendations such as the one given in [54].

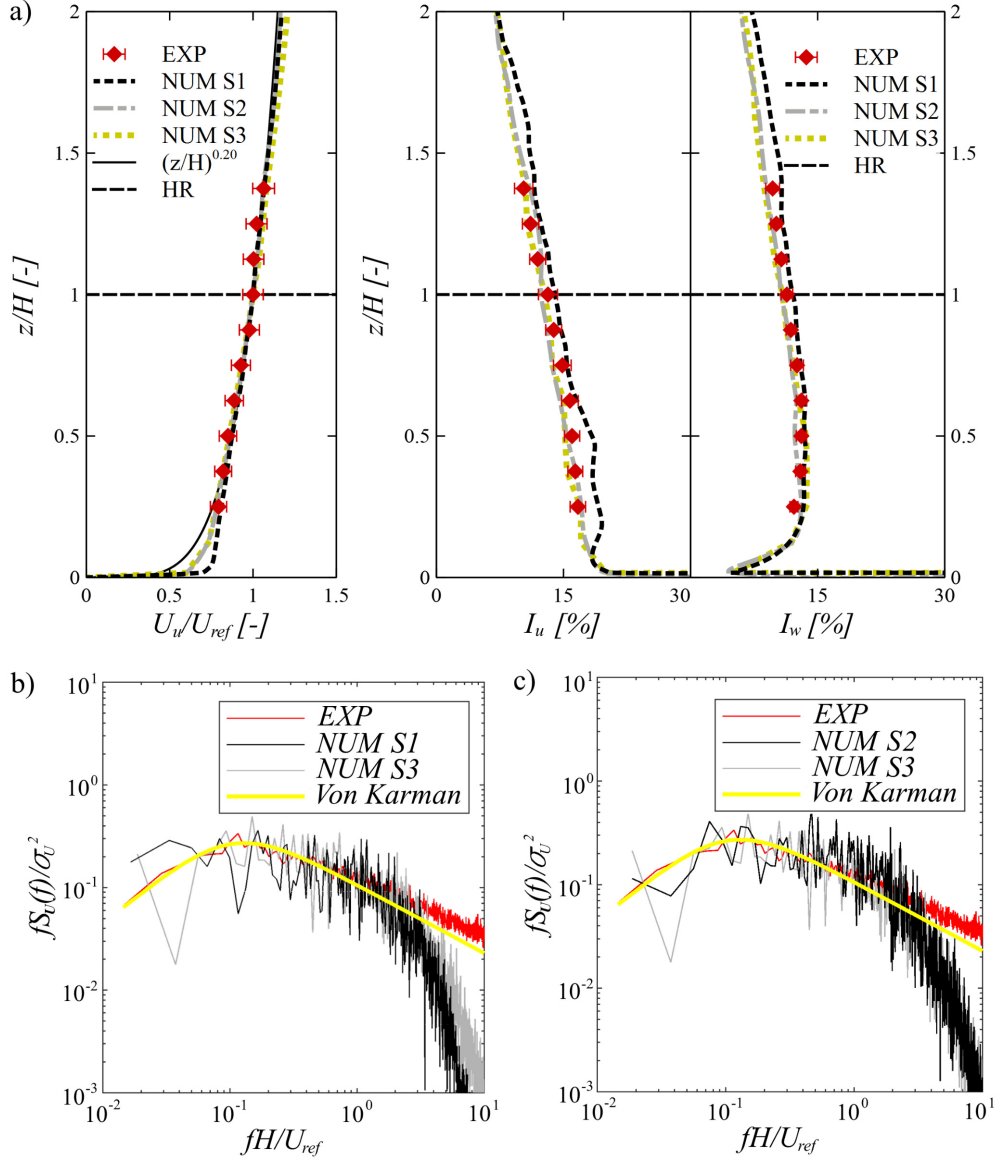


Figure B.4. (a) Incident wind profile at (0,0): mean velocity in the streamwise direction, turbulence intensity profiles in the streamwise and vertical directions for the three analysed setups; velocity spectra at (0, 0, H), comparison of (b) NUM S1 and NUM S3, and (c) NUM S2 and NUM S3, with the experimental results.

C Matlab code for the estimation of the peak pressure

This appendix provides the Matlab code used for estimating the peak pressure coefficient with uncertainty quantification. The example corresponds to a single measurement point and employs the traditional method for peak pressure estimation, assuming a Gumbel distribution. Uncertainty is quantified by calculating a 95% CI using Gaussian distribution.

Code Explanation:

- **Input parameters:** The code begins by defining the necessary parameters, including the number of epochs for peak extraction (*nEpochs*), the durations of the epochs (*tEpoch*), and the target duration (*targEpoch*) for extrapolation based on the Cook and Mayne method [190]. The probability of non-exceedance (*Fref*) and the number of pressure taps (*nProbe*) are also specified.
- **Data loading:** The code imports the time series data from a file in the *INPUT/* directory and extracts the pressure signal for the specified measurement point (*nProbe*).
- **Peak extraction and Gumbel fitting:** For each epoch duration in the specified range (*tEpoch*), the code segments the signal into smaller windows and extracts the minimal (negative) peaks from each window forming a dataset of peak values. A Gumbel distribution is then fitted to the specified number of peaks (*nEpochs*) repetitively, sliding through the dataset of peak values for one value forward. The location and scale parameters of the distributions are computed and corrected using the Cook and Mayne method [190] for time extrapolation.
- **Probability of non-exceedance calculation:** The code calculates the peak value corresponding to the target probability of non-exceedance (80% by default), both for the corrected and uncorrected cases.
- **Uncertainty quantification:** For each epoch duration, the mean and standard deviation of the peak values with the defined probability of non-exceedance are calculated. The 95% CI are computed using a Gaussian distribution.

The script provides a framework for estimating peak values and uncertainty quantification. It can be adapted to suit different datasets and configurations by modifying the input parameters or the data loading section as needed.

Matlab code for the peak pressure estimation with uncertainty quantification

```
1  % Statistical treatment of the PEAK Cp values
2  % Gumbel distribution with uncertainties for different signal durations
3  % and applying Cook and Mayne time conversion for parameters of Gumbel
4  % distribution (code works for negative peaks only)
5
6
7  close all
8  clc
9
10 % Path to the input folder
11 path1 = 'INPUT/';
12
13 % INPUT
14
15 % Number of epochs for peak extraction and their duration
16 nEpochs = 10; % Number of epochs for peak extraction and fitting
17 tEpoch = 1:1:15; % Epoch durations in seconds
18 targEpoch = 15; % Target duration  $\Delta T$  for extrapolation using Cook and Mayne
19
20 Fref = 80; % in [%] define the target probability of non-exceedance for PEAKS
21
22 nProbe = 18; % Number of pressure tap
23
24
25 % LOAD DATA
26
27 A_all = importdata([path1 'Cp_TimeHistory.txt'],' ', 0);
28 T = A_all(2:end,1); % Time
29 Ttot = T(end,1);
30 deltaT = (T(2) - T(1)); %Time step
31 A = A_all(2:end,nProbe); % Pressure signal at specific location
32
33
34 % CALCULATIONS
35
36 % Initialize storage for results
37 results = [];
38 % Initialize storage for uncorrected results
39 uncorrectedPeaks = [];
40
41 % Loop over each epoch duration
42 for duration = tEpoch
43
44     % Divide the signal into windows of specified duration
45     windowLength = round(duration / deltaT); % Convert duration to data points
46     numSeries = floor(length(A) / windowLength); % Determine the number of series for
47     % shorter durations
48
49     gumbelPeaks = [];
50     uncorrectedGumbelPeaks = [];
51
52     % OBSERVATIONS - collected peaks for fitting the Gumbel distribution
53     for series = 1:numSeries
54         startX = (series - 1) * windowLength + 1;
55         endX = startX + numSeries * windowLength - 1;
56
57         if endX > length(A)
58             continue; % Skip if the window exceeds signal length
59         end
60
61         signalSegment = A(startX:endX); % Subset of the signal
62         minPeaks = [];
63
64         % Extract minimal (negative) peaks from each window
65         for i = 1:numSeries
66             windowData = signalSegment((i-1)*windowLength+1 : i*windowLength);
67             minPeaks = [minPeaks; min(windowData)];
68         end
69     end
70 end
```

1/2


```

69         % GUMBEL fitting
70
71         numSteps = length(minPeaks) - nEpochs - 1; % Number of steps based on duration
72         for stepX = 1:numSteps
73
74             % Extract peaks within the current window
75             peakGUM = minPeaks(stepX:(stepX+nEpochs-1));
76
77             % Fit the minimal peaks to Gumbel distribution using MLE
78             pd = evfit(peakGUM); % Gumbel distribution in MATLAB
79             mu_t = pd(1,1); % Location parameter
80             sigma_t = pd(1,2); % Scale parameter
81
82             % Apply the Cook and Mayne (1979) correction for ΔT
83             sigma_T = sigma_t; % Scale parameter remains the same
84             mu_T = mu_t - sigma_t * log(targEpoch / duration); % Adjusted location
                        parameter
85
86             % Compute the 80% non-exceedance value
87             probNonExceed = Fref/100;
88             peakValue_t = mu_t + log(-log(Fref/100))*sigma_t;
89             peakValue_T = mu_T + log(-log(Fref/100))*sigma_T;
90
91             % Store peak values
92             gumbelPeaks = [gumbelPeaks; peakValue_T]; % Corrected
93             uncorrectedGumbelPeaks = [uncorrectedGumbelPeaks; peakValue_t]; % Uncorrected
94         end
95     end
96
97     % Compute the mean of peaks across all series
98     meanPeakValue_T = mean(gumbelPeaks);
99     meanUncorrectedValue = mean(uncorrectedGumbelPeaks);
100
101     % Compute standard errors for corrected and uncorrected peaks
102     stdErr_T = std(gumbelPeaks); % standard deviation
103     stdErr_uncorrected = std(uncorrectedGumbelPeaks);
104
105     % Compute 95% confidence intervals (CI = mean ± 1.96 * SD)
106     % Gaussian distribution
107     confInt_T = 1.96 * stdErr_T;
108     confInt_uncorrected = 1.96 * stdErr_uncorrected;
109
110     % Store results
111     results = [results; duration, mean(mu_t), mean(sigma_t), mean(mu_T), sigma_T,
112               meanPeakValue_T, confInt_T];
112     uncorrectedPeaks = [uncorrectedPeaks; duration, meanUncorrectedValue,
113               confInt_uncorrected];
113 end
114
115 % Define the folder for export
116
117 path2 = 'RESULTS';
118 if ~isfolder(path2)
119     mkdir(path2);
120 end
121
122 % Save results to a CSV file
123 csvFName = [path2 '/PEAKS-GUM_probe' num2str(nProbe) '_targetT-' num2str(targEpoch)
124             '_nEpochs' num2str(nEpochs) '.csv'];
124 writematrix(results, csvFName, 'Delimiter', ',', 'WriteMode', 'overwrite');
125
126 % close all

```

Biography

Kristina Kostadinović Vranešević was born on 30 June 1988 in Užice, Republic of Serbia, Yugoslavia. Her family originates from the nearby village of Šljivovica.

She excelled in her early education, graduating as the valedictorian of her technical high school class in 2003. In 2007, she enrolled at the Faculty of Civil Engineering, University of Belgrade, specialising in Structures. She graduated in 2011 with an average grade of 9.04/10, completing a final project on “*Design of a Multi-Storey Concrete Building (B+G+9)*”. That same year, she enrolled in the Master’s programme in the same module, earning her MSc in 2013 with an average grade of 9.29/10. Her master thesis, “*Application of Lightweight Steel Structures: A Case Study of Sports Hall Design*”, reflected her expertise. She then pursued doctoral studies, passing all required exams with an average grade of 9.62/10.

Kristina began her professional career in May 2013 at DEL ING DOO, Belgrade, as a structural engineer, contributing to the design of steel, concrete, and timber structures. In November 2014, she was appointed as a Teaching Assistant at the University of Belgrade, Faculty of Civil Engineering, where she continues to work.

She is married to Filip Vranešević, also from Užice, and they have two children, Višnja and Anja. The family lives in Belgrade.

Kristina has published four articles in international journals indexed in the SCI list (M21-M22), one in the national journal of international significance (M24), and twelve conference papers, all detailed in Contributions.

Contributions

Journal articles:

- **Top international journal - M21**
 - **K. Kostadinović Vranešević**, A. Šarkić Glumac, “*Peak pressures on high-rise buildings roof: A dual approach through validated LES and wind tunnel experiments with uncertainty quantification*”, Journal of Wind Engineering and Industrial Aerodynamics 250 (2024), p. 105784, doi: 10.1016/j.jweia.2024.105784.
 - **K. Kostadinović Vranešević**, S. Ćorić, A. Šarkić Glumac, “*LES study on the urban wind energy resources above the roof of buildings in generic cluster arrangements: Impact of building position*”, Journal of Wind Engineering and Industrial Aerodynamics 240 (2023), p. 105503, doi: 10.1016/j.jweia.2023.105503.
 - **K. Kostadinović Vranešević**, G. Vita, S.P.A. Bordas, A. Šarkić Glumac, “*Furthering knowledge on the flow pattern around high-rise buildings: LES investigation of the wind energy potential*”, Journal of Wind Engineering and Industrial Aerodynamics 226 (2022), p. 105029, doi: 10.1016/j.jweia.2022.105029.
- **Prominent international journal - M22**
 - H. Hemida, G. Vita, **K. Kostadinović Vranešević**, R. Hoffer, A. Šarkić Glumac, “*On the Flow over High-rise Building for Wind Energy Harvesting: An Experimental Investigation of Wind Speed and Surface Pressure*”, Applied Sciences 10.15 (2020), p. 5283, doi: 10.3390/app10155283.
- **National journal of international importance - M24**
 - **K. Kostadinović Vranešević**, N. Gluhović, J. Dobrić, M. Spremić, “*Behaviour of thin-walled cylindrical and conical shells – carbon vs. stainless steel*”, Građevinski materijali i konstrukcije 1/2019 (2019), p. 27-41. ISSN 2217-8139, COBISS.SR-ID 188695820.

Conference papers:

- **International Conferences - M33**
 - **K. Kostadinović Vranešević**, A. Šarkić Glumac, “*Peak Pressure Evaluation on High-Rise Buildings: Insights from Experimental and LES Analyses*”, The 9th International Colloquium on Bluff Body Aerodynamics and Applications, University of Birmingham, UK (2024).
 - **K. Kostadinović Vranešević**, A. Šarkić Glumac, O. Jadhav, M. Jočković, S. Bordas, B. Blocken, “*Prediction of the wind flow patterns above different building roof shapes using machine learning techniques*”, The 9th International Colloquium on Bluff Body Aerodynamics and Applications, University of Birmingham, UK (2024).

-
- **K. Kostadinović Vranešević**, A. Šarkić Glumac, “*Impact of surroundings on the local peak pressure in high-rise building clusters*”, *The 16th International Conference on Wind Engineering (ICWE16)*, Florence, Italy, (2023).
 - **K. Kostadinović Vranešević**, A. Šarkić Glumac, S. Bordas, “*The influence of exposure on wind flow characteristics around a high-rise building*”, *The 8th European-African conference on wind engineering (8EACWE)*, Bucharest, Romania (2022), ISBN: 978-973-100-532-4.
 - **K. Kostadinović Vranešević**, A. Glumac, H. Hemida, “*Experimental investigation of wind load on low-rise industrial building*”, 7th International Conference: Contemporary Achievements in Civil Engineering, Conference proceedings, Subotica, Serbia (2019), p. 333-340, ISBN: 978-86-80297-78-1.
 - **K. Kostadinović Vranešević**, A. Glumac, H. Hemida, “*Experimental investigation of wind flow around low-rise tilted house*”, 7th International Conference: Contemporary Achievements in Civil Engineering, Conference proceedings, Subotica, Serbia (2019), p. 323-332, ISBN: 978-86-80297-78-1.
 - **K. Kostadinović Vranešević**, A. Glumac, U. Winkelmann, “*Pressure field analyses of a low-rise building model surrounded by neighbouring buildings in urban areas*”, 7th International Congress of Serbian Society of Mechanics, Proc. on CD, Sremski Karlovci, Serbia (2019).
 - A. Šarkić, **K. Kostadinović Vranešević**, D. Šumarac, “*Numerical investigations of the flow around a high-rise building*”, 5th International Congress of Serbian Society of Mechanics, Proc. on CD, Arandelovac, Serbia (2015), ISBN: 978-86-7892-715-7.
 - A. Šarkić, H. Hemida, **K. Kostadinović Vranešević**, R. Höffer, “*Experimental investigation of interference effect of high-rise buildings for wind energy extraction*”, WINERCOST Workshop “Trends and Challenges for Wind Energy Harvesting”, Proc. on CD, Coimbra, Portugal (2015), p. 57-66.
 - Ž. Lazić, **K. Kostadinović Vranešević**, Z. Koneski, J. Stanojević, “*Ultimate load of rectangular plate*”, International Conference: Contemporary Achievements in Civil Engineering, Conference proceedings, Subotica, Serbia (2015), p. 309-315, doi: 10.14415/konferencijaGFS2015.039.
 - **National Conferences - M63**
 - **K. Kostadinović Vranešević**, N. Gluhović, J. Dobrić, M. Spremić, “*Carbon steel vs. stainless steel behaviour of thin-walled cylindrical shells*”, 15th Congress of DGKS, Proc. on CD, Zlatibor, Serbia (2018), p 519-528, ISBN: 978-86-6022-069-3.
 - Z. Koneski, **K. Kostadinović Vranešević**, S. Kovačević, Ž. Lazić, “*The effect of transverse shear deformation on the bending of rectangular plates*”, 14th Congress of DGKS, Conference proceedings, Novi Sad, Serbia (2014), p. 205-214, ISBN: 978-86-85073-19-9.

Изјава о ауторству

Име и презиме аутора Кристина Костадиновић Вранешевић

Број индекса 909/13

Изјављујем

да је докторска дисертација под насловом

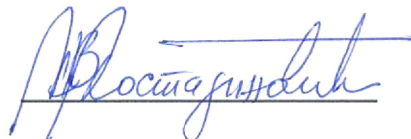
Validated large-eddy simulation method for wind effects in urban areas

Метода симулације великих вртлога за утицаје ветра у урбаним срединама

- резултат сопственог истраживачког рада;
- да дисертација у целини ни у деловима није била предложена за стицање друге дипломе према студијским програмима других високошколских установа;
- да су резултати коректно наведени и
- да нисам кршио/ла ауторска права и користио/ла интелектуалну својину других лица.

Потпис аутора

У Београду, 10.3.2025. године



Изјава о истоветности штампане и електронске верзије докторског рада

Име и презиме аутора Кристина Костадиновић Вранешевић

Број индекса 909/13

Студијски програм грађевинарство

Наслов рада Validated large-eddy simulation method for wind effects in urban areas

Ментор Доцент др Анина Глумац

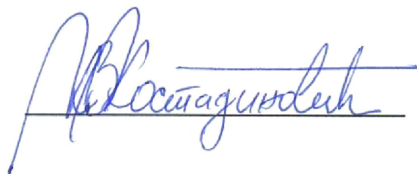
Изјављујем да је штампана верзија мог докторског рада истоветна електронској верзији коју сам предао/ла ради похрањивања у **Дигиталном репозиторијуму Универзитета у Београду**.

Дозвољавам да се објаве моји лични подаци везани за добијање академског назива доктора наука, као што су име и презиме, година и место рођења и датум одбране рада.

Ови лични подаци могу се објавити на мрежним страницама дигиталне библиотеке, у електронском каталогу и у публикацијама Универзитета у Београду.

Потпис аутора

У Београду, 10.3.2025. године



Изјава о коришћењу

Овлашћујем Универзитетску библиотеку „Светозар Марковић“ да у Дигитални репозиторијум Универзитета у Београду унесе моју докторску дисертацију под насловом:

Validated large-eddy simulation method for wind effects in urban areas

Метода симулације великих вртлога за утицаје ветра у урбаним срединама

која је моје ауторско дело.

Дисертацију са свим прилозима предао/ла сам у електронском формату погодном за трајно архивирање.

Моју докторску дисертацију похрањену у Дигиталном репозиторијуму Универзитета у Београду и доступну у отвореном приступу могу да користе сви који поштују одредбе садржане у одабраном типу лиценце Креативне заједнице (Creative Commons) за коју сам се одлучио/ла.

1. Ауторство (CC BY)

2. Ауторство – некомерцијално (CC BY-NC)

③ Ауторство – некомерцијално – без прерада (CC BY-NC-ND)

4. Ауторство – некомерцијално – делити под истим условима (CC BY-NC-SA)

5. Ауторство – без прерада (CC BY-ND)

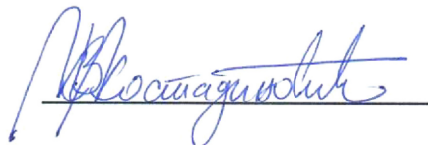
6. Ауторство – делити под истим условима (CC BY-SA)

(Молимо да заокружите само једну од шест понуђених лиценци.

Кратак опис лиценци је саставни део ове изјаве).

Потпис аутора

У Београду, 10.3.2025. године



1. **Ауторство.** Дозвољаваате умножавање, дистрибуцију и јавно саопштавање дела, и прераде, ако се наведе име аутора на начин одређен од стране аутора или даваоца лиценце, чак и у комерцијалне сврхе. Ово је најслободнија од свих лиценци.

2. **Ауторство – некомерцијално.** Дозвољаваате умножавање, дистрибуцију и јавно саопштавање дела, и прераде, ако се наведе име аутора на начин одређен од стране аутора или даваоца лиценце. Ова лиценца не дозвољава комерцијалну употребу дела.

3. **Ауторство – некомерцијално – без прерада.** Дозвољаваате умножавање, дистрибуцију и јавно саопштавање дела, без промена, преобликовања или употребе дела у свом делу, ако се наведе име аутора на начин одређен од стране аутора или даваоца лиценце. Ова лиценца не дозвољава комерцијалну употребу дела. У односу на све остале лиценце, овом лиценцом се ограничава највећи обим права коришћења дела.

4. **Ауторство – некомерцијално – делити под истим условима.** Дозвољаваате умножавање, дистрибуцију и јавно саопштавање дела, и прераде, ако се наведе име аутора на начин одређен од стране аутора или даваоца лиценце и ако се прерада дистрибуира под истом или сличном лиценцом. Ова лиценца не дозвољава комерцијалну употребу дела и прерада.

5. **Ауторство – без прерада.** Дозвољаваате умножавање, дистрибуцију и јавно саопштавање дела, без промена, преобликовања или употребе дела у свом делу, ако се наведе име аутора на начин одређен од стране аутора или даваоца лиценце. Ова лиценца дозвољава комерцијалну употребу дела.

6. **Ауторство – делити под истим условима.** Дозвољаваате умножавање, дистрибуцију и јавно саопштавање дела, и прераде, ако се наведе име аутора на начин одређен од стране аутора или даваоца лиценце и ако се прерада дистрибуира под истом или сличном лиценцом. Ова лиценца дозвољава комерцијалну употребу дела и прерада. Слична је софтверским лиценцама, односно лиценцама отвореног кода.